ADVERTIMENT. L'accés als continguts d'aquesta tesi doctoral i la seva utilització ha de respectar els drets de la persona autora. Pot ser utilitzada per a consulta o estudi personal, així com en activitats o materials d'investigació i docència en els termes establerts a l'art. 32 del Text Refós de la Llei de Propietat Intel·lectual (RDL 1/1996). Per altres utilitzacions es requereix l'autorització prèvia i expressa de la persona autora. En qualsevol cas, en la utilització dels seus continguts caldrà indicar de forma clara el nom i cognoms de la persona autora i el títol de la tesi doctoral. No s'autoritza la seva reproducció o altres formes d'explotació efectuades amb finalitats de lucre ni la seva comunicació pública des d'un lloc aliè al servei TDX. Tampoc s'autoritza la presentació del seu contingut en una finestra o marc aliè a TDX (framing). Aquesta reserva de drets afecta tant als continguts de la tesi com als seus resums i índexs.

ADVERTENCIA. El acceso a los contenidos de esta tesis doctoral y su utilización debe respetar los derechos de la persona autora. Puede ser utilizada para consulta o estudio personal, así como en actividades o materiales de investigación y docencia en los términos establecidos en el art. 32 del Texto Refundido de la Ley de Propiedad Intelectual (RDL 1/1996). Para otros usos se requiere la autorización previa y expresa de la persona autora. En cualquier caso, en la utilización de sus contenidos se deberá indicar de forma clara el nombre y apellidos de la persona autora y el título de la tesis doctoral. No se autoriza su reproducción u otras formas de explotación efectuadas con fines lucrativos ni su comunicación pública desde un sitio ajeno al servicio TDR. Tampoco se autoriza la presentación de su contenido en una ventana o marco ajeno a TDR (framing). Esta reserva de derechos afecta tanto al contenido de la tesis como a sus resúmenes e índices.

WARNING. Access to the contents of this doctoral thesis and its use must respect the rights of the author. It can be used for reference or private study, as well as research and learning activities or materials in the terms established by the 32nd article of the Spanish Consolidated Copyright Act (RDL 1/1996). Express and previous authorization of the author is required for any other uses. In any case, when using its content, full name of the author and title of the thesis must be clearly indicated. Reproduction or other forms of for profit use or public communication from outside TDX service is not allowed. Presentation of its content in a window or frame external to TDX (framing) is not authorized either. These rights affect both the content of the thesis and its abstracts and indexes.

Universitat Politècnica de Catalunya

Doctoral Program:

Thermal Engineering

Doctoral Thesis:

PERFORMANCE INDICATORS FOR THE DYNAMIC MODELING AND CONTROL OF PEMFC SYSTEMS

Attila Peter Husar

Directors:

Dr. Maria Serra i Prat and Dr. Jordi Riera i Colomer

January 2012

to my wonderful children

Acknowledgements:

First of all, I would like to thank Dr. Jordi Riera and Dr. Maria Serra for their guidance, inspiration and support throughout my research stay at the Institute.

I would like to give special thanks to Miguel Allué, technical leader of *the Laboratorio de Pilas de Combustible* at *the Institut de Robòtica i Informàtica Industrial*, whose help has made the construction, implementation and experimentation with the test stations possible.

I would especially like to thank Stephan Stahl and Cristian Kunusch for their patience and willingness to read and comment my dissertation.

Thanks to the whole controls group and the staff at the institute for putting up with all my odd yet hopefully interesting topics of discussion.

Finally, my family, without whom I would have never gotten this far in my education.
Thanks mom

Financial Support:
My research was partially funded by *Consejo Superior de Investigaciones Científicas* through the I3P doctoral scholarship fund.

The research was also partially funded by the following projects of *the Spanish Council of Science and Innovation*: DPI2004-06871-C02-01, DPI2007-62966, DPI2010-15274

PERFORMANCE INDICATORS FOR THE DYNAMIC MODELING AND CONTROL OF PEMFC SYSTEMS

Attila Peter Husar

Abstract:

Society is gradually becoming aware that the current energy industry, based on the use of fossil fuels, is inefficient, highly polluting and has a finite supply. Within the scientific community, there are indications that hydrogen (H2) as an energy vector, obtained from renewable energy sources, can represent a viable option to mitigate the problems associated with hydrocarbon combustion. In this context, the change from the current energy industry to a new structure with a significant involvement of H2 facilitates the introduction of fuel cells as elements of energy conversion. Polymer Electrolyte Membrane Fuel Cells (PEMFC) are gaining increased attention as viable energy conversion devices for a wide range of applications from automotive, stationary to portable. In order to optimize performance, these systems require active control and thus in-depth knowledge of the system dynamics which include fluid mechanics, thermal dynamics and reaction kinetics. One of the main issues, with respect to proper control of these systems, is the understanding of the water transport mechanisms through the membrane and the liquid water distribution. The thesis is based on the publication of nine international journal articles that are divided into 4 sub-topics: Dynamic fuel cell modeling, fuel cell system control-oriented analysis, identification of parameters and performance indicators and finally, fault and failure detection and system diagnosis. In the sub-topic of Dynamic Fuel cell modeling, experimentally validated Computational Fluid Dynamics (CFD) modeling is used to relate the effects of the physical phenomena associated with fluid mechanics and thermal dynamics, that occur inside the fuel cell [Alonso, 2009][Strahl, 2011], to water distribution. However, since these CFD models cannot be directly used for control, control-oriented models [Kunusch, 2008][Kunusch, 2011] have been developed in parallel. As well, another study is done in [Serra, 2006] which includes a controllability analysis of the system for future development and application of efficient controllers. The results of the above mentioned studies are limited because either they do not incorporate an electrochemical model or the model is not

experimentally validated. Moreover, these models do not take into account the voltage losses due to liquid water inside the fuel cell. Therefore, there is a need to properly relate the relevant effects of fluid mechanics and thermal dynamics, including liquid water, to the fuel cell voltage. Primarily, methodologies are needed to determine the relevant indicators associated to the effect of water on the fuel cell performance. The works published in [Husar, 2008] and [Husar, 2011] treats experimental parameter identification, mainly focused on water transport through the membrane and fuel cell voltage loss indicators respectively. The implementation of the indicators indirect measurement methodology provides an experimental way for the isolation of three main types of voltage losses in the fuel cell: activation, mass transport and ohmic losses. Additionally since these voltage loss indicators relate the fuel cell operating conditions to the fuel cell voltage, they can be utilized to calibrate and validate CFD models as well as employed in novel control strategies. On the other hand, to develop reliable systems, the controller should not only take into account performance variables during standard operation but should also be able to detect failures and take the appropriate actions. A preliminary study on failure indicators is presented in [Husar 2007] and fault detection methodologies are described in [de Lira 2011]. As a whole, the compilation of articles represented in this thesis applies a comprehensive experimental approach which describes the implementation of novel methodologies and experimental procedures to characterize and model the PEMFC and their associated systems taking into consideration control oriented goals.

PERFORMANCE INDICATORS FOR THE DYNAMIC MODELING AND CONTROL OF PEMFC SYSTEMS

Attila Peter Husar

Resum:

La societat s'està adonant que la indústria energètica actual, basada en l'ús de combustibles fòssils, és ineficient, molt contaminant i té un subministrament limitat. Dins de la comunitat científica, hi ha indicis que el hidrogen (H2) com vector energètic, obtingut a partir de fonts d'energia renovables, pot representar una opció viable per a mitigar els problemes associats amb la combustió d'hidrocarburs. En aquest context, el canvi de la indústria energètica actual a una nova estructura amb una important participació de el hidrogen exigeix la introducció de les piles de combustible com elements de conversió d'energia. Les piles de combustible de membrana polimèrica (PEMFC) estan tenint cada vegada més atenció com a dispositius viables de conversió d'energia per a una àmplia gamma d'aplicacions com automoció, estacionàries o portàtils. Amb la finalitat d'optimitzar el seu rendiment, les piles PEM requereixen un control actiu i per tant un coneixement profund de la dinàmica del sistema, que inclou la mecànica de fluids, la dinàmica tèrmica i la cinètica de les reaccions. Un dels temes principals relacionat amb el control adequat d'aquests sistemes és la comprensió dels mecanismes de transport d'aigua a través de la membrana i la distribució d'aigua líquida. Aquesta tesi es basa en nou articles publicats en revistes internacionals que es divideixen en 4 sub-temes: la modelització dinàmica de piles de combustible, l'anàlisi orientada al control del sistema, la identificació de paràmetres i d’indicadors de funcionament i, finalment, la detecció de fallades i la diagnosi dels sistemes. En el sub-tema de la modelització dinàmica de piles PEM, la modelització basada en la Dinàmica de Fluids Computacional (CFD) amb validació experimental s'ha utilitzat per a relacionar els efectes dels fenòmens físics de la mecànica de fluids i de la dinàmica tèrmica que es produeixen dintre de la pila [Alonso, 2009] [Strahl, 2011] amb la distribució d'aigua. No obstant això, com aquests models CFD no poden ser utilitzats directament per al control, s'han desenvolupat models orientats a control [Kunusch, 2008] [Kunusch, 2011] en paral·lel. A més, en un altre estudi [Serra, 2006] s'inclou

una anàlisi de control·labilitat del sistema per al desenvolupament i aplicació futurs de controladors eficaços. Però els resultats dels estudis esmentats anteriorment són limitats, ja sigui perquè no incorporen un model electroquímic o bé perquè no han estat validats experimentalment. A més, cap dels models té en compte les pèrdues de tensió degudes a l'aigua líquida dins de la pila de combustible. Per tant, hi ha una necessitat de relacionar adequadament els efectes rellevants de la mecànica de fluids i de la dinàmica tèrmica, incloent l'aigua líquida, amb el voltatge de la pila de combustible. Principalment, són necessàries metodologies per a determinar els indicadors rellevants associats a aquest efecte de l'aigua sobre el rendiment de la pila de combustible. Els treballs publicats en [Husar, 2008] i [Husar, 2011] tracten la identificació experimental de paràmetres, centrada en el transport d'aigua a través de la membrana i els indicadors de pèrdua de tensió, respectivament. L'aplicació d'una proposta de metodologia de mesura indirecte dels indicadors permet l'aïllament dels tres tipus principals de pèrdues de voltatge en la pila de combustible: l'activació, el transport de massa i les pèrdues ohmiques. Aquests indicadors de pèrdua de tensió relacionen les condicions d'operació amb el voltatge de la pila de combustible i per tant poden ser utilitzats per a calibrar i validar models CFD, així com per a definir noves estratègies de control. D'altra banda, per a aconseguir sistemes fiables, el controlador no només ha de considerar els indicadors de funcionament de l'operació normal, sinó que també ha de detectar possibles fallades per a poder prendre les accions adequades en cas de fallada. Un estudi preliminar sobre indicadors de fallades es presenta en [Husar 2007] i una metodologia de detecció de fallades completa es descriu en [Lira de 2011]. En el seu conjunt, el compendi d'articles que formen aquesta tesi segueix un enfocament experimental i descriu la implementació de noves metodologies i procediments experimentals per a la caracterització i el modelatge de piles PEM i els sistemes associats amb objectius orientats al control eficient d'aquests sistemes.

PERFORMANCE INDICATORS FOR THE DYNAMIC MODELING AND CONTROL OF PEMFC SYSTEMS

Attila Peter Husar

Resumen:

La sociedad se ésta dando cuenta de que la industria energética actual, basada en el uso de combustibles fósiles, es ineficiente, muy contaminante y tiene un suministro limitado. Dentro de la comunidad científica, hay indicios de que el hidrógeno (H2) como vector energético, obtenido a partir de fuentes de energía renovables, puede representar una opción viable para mitigar los problemas asociados con la combustión de hidrocarburos. En este contexto, el cambio de la industria energética actual a una nueva estructura con una importante participación de H2 exige la introducción de pilas de combustible como elementos de conversión de energía. Las pilas de combustible de membrana polimérica (PEMFC) están ganando cada vez más atención como dispositivos viables de conversión de energía para una amplia gama de aplicaciones como automoción, estacionarias o portátiles. Con el fin de optimizar su rendimiento, las pilas PEM requieren un control activo y por lo tanto un conocimiento profundo de la dinámica del sistema, que incluye la mecánica de fluidos, la dinámica térmica y la cinética de las reacciones. Uno de los temas principales relacionado con el control adecuado de estos sistemas, es la comprensión de los mecanismos de transporte de agua a través de la membrana y la distribución de agua líquida. Esta tesis se basa en la publicación de nueve artículos en revistas internacionales que se dividen en 4 sub-temas: el modelado dinámico de pilas de combustible, el análisis orientado a control del sistema, la identificación de parámetros e indicadores de desempeño y, por último, la detección de fallos y la diagnosis. En el sub-tema de la modelización dinámica de pilas PEM, el modelado basado en Dinámica de Fluidos Computacional (CFD) con validación experimental se ha utilizado para relacionar los efectos de los fenómenos físicos de la mecánica de fluidos y la dinámica térmica que se producen dentro de la pila [Alonso, 2009] [Strahl, 2011] con la distribución de agua. Sin embargo, como estos

modelos CFD no pueden ser utilizados directamente para el control, modelos orientados a control [Kunusch, 2008] [Kunusch, 2011] se han desarrollado en paralelo. Además, en otro estudio [Serra, 2006] se incluye un análisis de controlabilidad del sistema para el futuro desarrollo y aplicación de controladores eficaces. Pero los resultados de los estudios mencionados anteriormente son limitados, ya sea porque no incorporan un modelo electroquímico o bien porque no son validados experimentalmente. Además, ninguno de los modelos tiene en cuenta las pérdidas de tensión debidas al agua líquida dentro de la pila de combustible. Por lo tanto, hay una necesidad de relacionar adecuadamente los efectos relevantes de la mecánica de fluidos y la dinámica térmica, incluyendo el agua líquida, con la tensión de la pila de combustible. Principalmente, son necesarias metodologías para determinar los indicadores relevantes asociados al efecto del agua sobre el rendimiento de la pila de combustible. Los trabajos publicados en [Husar, 2008] y [Husar, 2011] tratan la identificación experimental de parámetros, centrada en el transporte de agua a través de la membrana y los indicadores de pérdida de tensió, respectivamente. La aplicación de una metodología propuesta de medición indirecta de los indicadores permite el aislamiento de los tres tipos principales de pérdidas de tensión en la pila de combustible: la activación, el transporte de masa y las pérdidas óhmicas. Éstos indicadores de pérdida de tensión relacionan las condiciones de operación con la tensión de la pila de combustible y por lo tanto pueden ser utilizados para calibrar y validar modelos CFD, así como para definir nuevas estrategias de control. Por otro lado, para conseguir sistemas fiables, el controlador no sólo debe considerar los indicadores de desempeño de la operación regular, sino que también debe detectar posibles fallos para poder tomar las acciones adecuadas en caso de fallo. Un estudio preliminar sobre indicadores de fallos se presenta en [Husar 2007] y una metodología de detección de fallos completa se describe en [Lira de 2011]. En su conjunto, el compendio de artículos que forman esta tesis sigue un enfoque experimental y describe la implementación de nuevas metodologías y procedimientos experimentales para la caracterización y el modelado de pilas PEM y los sistemas asociados con objetivos orientados al control eficiente de estos sistemas.

PERFORMANCE INDICATORS FOR THE DYNAMIC MODELING AND CONTROL OF PEMFC SYSTEMS

Table of Contents

1. Introduction

Society is gradually becoming aware that the current energy industry, based on the use of fossil fuels is inefficient, highly polluting and has a finite supply. Within the scientific community, there are indications that hydrogen (H2) as an energy vector, obtained from renewable energy sources, can represent a viable option to mitigate the problems associated with hydrocarbon combustion. In this context, the change from the current energy industry to a new structure with a significant involvement of H2 facilitates the introduction of fuel cells as elements of energy conversion. In fact, the VI and VII European Framework Programs and the US Department of Energy (DOE), clearly promote, for more than a decade, the development of technologies related to fuel cells, hydrogen production and hydrogen storage [FP6, 2002][FP7, 2007][DOE, 2005].

The articles presented in this thesis focus on Polymer Electrolyte Membrane Fuel Cells (PEMFC) technology. PEMFC are electrochemical devices that allow direct conversion of chemical energy from the catalytic oxidation of H2 into electricity. They are not subject to the Carnot principle and its limitations, which enables them to achieve high electrical efficiencies (in some actual systems close to 50%). In addition, the only by-products of the reaction in PEMFC are water and heat [Barbir, 2005]. Thus, it is possible to restrict the emissions only to the ones associated to the production of hydrogen, which in turn can be obtained from clean and renewable energies such as wind, solar or tidal energy.

The introduction of fuel cells to the market not only in stationary but also automotive applications has recently begun and is now part of major R&D programs of numerous important automotive companies (Daimler Chrysler, Ford, Volvo, General Motors, BMW, Renault, Hyundai and Nissan) [Ismail, 2009][Kazmi, 2009]. Despite current advances in PEMFC based technologies, high costs, moderate reliability and inadequate lifetime remain as major limitations. Hence, to extend current applicability and competitiveness of fuel cells (e.g. in comparison to internal combustion engines), it is necessary to improve reliability, efficiency, durability and safety, which implies the importance of the development and implementation of efficient controllers to these systems. The development of advanced control systems must be understood in a global way, taking into account sensors, actuators and local control schemes for each subsystem, as well as supervisory strategies, for optimal energy management under all operating condition.

During the last decade several model based control strategies have been reported, starting from classical problems such as temperature control, hydrogen consumption minimizing or oxygen stoichiometry control [Talj, 2010][Kunusch, 2009][Pukrushpan, 2004][Arce, 2010]. However, control problems do not end here, since there is still a diversity of variables to regulate and indexes to optimize which keeps being an important topic of current research. In particular, certain critical problems to be solved are improving the polymeric membranes hydration by active control of humidifiers [Hui, 2010], regulation of liquid water content that inhibit the uniform distribution of reactants and thus causing uneven electrical current densities over the active area of the cell [Mangold, 2010][Methekar, 2007][McCain, 2008]. Another related issue to address is the addition of optimized temperature control at different operating conditions [Riascos, 2009].

In the field of fuel cell control, cell or system modeling has played a decisive role in developing, optimizing and testing algorithms and strategies. However, modeling PEMFC based systems is a particularly challenging task due to the interactions between physical phenomena of different nature (thermal, electrical, mechanical, electrochemical, etc.), the presence of numerous nonlinear structures, the spatial distribution of phenomena, the sensitivity of the associated sensors and the limited accessibility of variables, to name some examples. In fact, PEMFC modeling has been studied by several authors and with different approaches [Amphlett, 1995][Mann, 2000][Rodatz, 2003][Pukrushpan, 2004]. However, many of these models have not been completely experimentally validated and there is still a lack of rigorous studies on parameters identification and their association with performance variables. Moreover, there are few models and methodologies specifically oriented to control design. The first published fuel cell models, as the ones presented in [Amphlett, 1995] and [Springer, 1991], are essentially electrochemical characterizations based on empirical relationships that do not consider gas dynamics. More recently some works have presented extended equations which include gas dynamics and temperature effects inside the cell. However, only a few works have proposed fully analytical control oriented system models. The model presented in [Rodatz, 2003] is specially developed for control engineering and is the basis of numerous works such as [Pukrushpan, 2004][Khan, 2005][Bao, 2006] [Grasser, 2007].

The subject of estimation of internal states and performance variables in PEMFC systems is still marginally explored, but with an increasing industrial interest, since its real time implementation involves reducing the number of sensors and their associated cost. [He, 2003] presents promising results in detecting electrode flooding with pressure drop measurements, resulting in a significant advance for developing controllers that may consider indexes related to the device performance. The observation of humidity and water content of the membranes and electrodes was studied by [McKay, 2004][Gorgun, 2006][Thawornkuno, 2008]. However, there are still limited experimental results that support the methodology.

In order to advance and contribute to the state-of-the-art of the fuel cell research topics stated above, this doctoral thesis is focused on performance indicators for the dynamic modeling and control of PEMFC systems. The involved research and its results have been presented in the following published manuscirpts.

First, experimentally validated dynamic Computational Fluid Dynamics (CFD) modeling is used to identify the effects of the physical phenomena associated with fluid mechanics and thermal dynamics that occur inside the fuel cell [Alonso, 2009][Strahl, 2011]. These models investigate the relation between temperature, reactant concentrations, system pressure and water distribution with the final aim of fuel cell system performance. However, since these CFD models cannot be directly used for control, control-oriented models [Kunusch, 2008][Kunusch, 2011] have been developed in parallel. [Serra, 2006] includes control oriented system analysis carried out for future development and application of efficient controllers and represent a preliminary view of the fundamental control strategies needed in a fuel cell system. The results of these studies are limited because either they use an electrochemical model that is not experimentally validated [Serra 2006] or experimental models that do not take into account the electrochemistry [Kunusch, 2008][Kunusch, 2011]. Moreover, these models do not consider the losses due to liquid water.

Therefore, there is a need to properly relate fluid mechanics and thermal dynamics relevant effects, including liquid water, to the fuel cell voltage. Primarily, methodologies are needed to extract (online if used for a control objective) the relevant indicators associated to the effect of water on the fuel cell performance. The works published in [Husar, 2008] and [Husar, 2011] treats experimental parameter identification, mainly focused on water transport through the membrane and fuel cell voltage loss indicators respectively. The implementation of the indicators' indirect measurement methodology allows for the isolation of three main types of voltage losses in the fuel cell: activation, mass transport and Ohmic losses. The voltage loss indicators relate the fuel cell operating conditions to the fuel cell voltage and thus can be utilized to calibrate and validate CFD models as well as employed in novel control strategies.

On the other hand, to develop reliable systems, the controller should not only take into account performance variables during standard operation but should also be able to detect failures and take the appropriate actions. In [Husar, 2007] and [de Lira, 2011] some fault indicators are described. These indicators are based on the obtained experience on fuel cell operation during the laboratory work [Husar, 2007] and the application of novel Fault Detection and Isolation (FDI) model-based techniques [de Lira, 2011].

The work done in this thesis, described in detail in the published articles attached in section 8, is based on a comprehensive experimental approach which describes the implementation of novel methodologies and experimental procedures to characterize and model the PEMFC and their associated systems taking into consideration control oriented goals related to performance enhancement.

The results and conclusions achieved from these works directly influenced the writing of a collaborative project proposal submitted to the European Commission 7th Framework Program for the specific call on "Improvement of PEMFC performance and durability through multi-scale modeling and numerical simulation”. This proposal has been approved and has moved into the negotiation phase.

2. Summary

The thesis is based on the publication of nine international journal articles that are divided into 4 sub-topics. First, the two articles published in the sub-topic of dynamic CFD fuel cell modeling are described. Second, the three articles in the field of fuel cell system control-oriented modeling and analysis are described. Third, in the sub-topic of identification of parameters and performance indicators two articles are described and finally, two articles in the field of fault and failure detection and system diagnosis are described.

2.1. Dynamic CFD fuel cell modeling

This section summarizes the two articles published in the field of fuel cell modeling. The presented numerical 2D and 3D macroscopic models are based on the finite elements and finite differences method, respectively. Although almost all imaginable physical phenomena occurring in a PEMFC can be incorporated in these computational fluid dynamics (CFD) models, it leads to results that are difficult to interpret due to large number of variables. Therefore, each model has certain assumptions and a specific focus related to the model's objectives.

[Alonso, 2009] describes a dynamic 3D non-isothermal single cell model for both the anode and cathode subsystems. Each subsystem contains energy and mass balance as well as a pressure drop sub-models which function in parallel. This model is focused on determining, if and where water condenses in the flow field channels and thus determines the critical current for a given operating condition. The critical current is defined as the maximum current at which water condenses in the cathode flow field, relative to the active area of the fuel cell. An interesting simulation result on the anode is that there is no significant temperature gradient, which could drive condensation along the channel because the gas temperature of pure hydrogen reaches the fuel cell temperature within the first node in most simulations.

One of the major results of this work is the introduction of a liquid water, effective channel cross-sectional area reduction factor that was experimentally calibrated and validated. The simulation also shows the sensitivity of condensation of water with respect to fuel cell temperature, dew point temperatures, current, and flow rates. For example a one degree change in the fuel cell temperature difference greatly affects the critical current. It should also be noted that not only stoichiometry but also the inlet dew point temperatures have a great effect on cathode pressure drop due to the reduction of the channel volume by droplet formation. However, water transport through the membrane is considered to be constant for all operating conditions.

A similar model, where water transport through the membrane by diffusion and Electro-Osmotic Drag (EOD) is investigated, was developed by [Strahl, 2011] for an open-cathode, self-humidified fuel cell system. The two-dimensional, non-isothermal, dynamic model determines the temperature, water vapor and reactant gas concentration distributions. The work is focused on water vapor management of open-cathode systems, which are sensitive to ambient conditions; however this model does not consider liquid water effects. The objective of the model is to simulate the effects of the dynamic control mechanisms for water management: cooling/oxygen supply fan flow rate, periodic hydrogen purge and short circuit. The aim is to learn how to operate the fuel cell by regulating the concentration of water vapor, the additional creation of water and heat due to the short circuit and water and heat removal from the stack in order to properly manage membrane hydration and fuel cell flooding.

Water is needed to maintain good proton conductivity and therefore has to be kept in the membrane, however liquid water on the catalyst reduces the active area, and in the Gas Diffusion Layer (GDL) it hinders the reactant gases from diffusing to the catalyst surface and thus reduces performance. The goal is to maintain an optimal water concentration in the membrane electrode assembly (MEA) by keeping a balance between the two conflicting requirements. Thus, to control water transport within a fuel cell system and thereby optimize the membrane hydration and diffusion at any operation point, proper dynamic water management strategies have to be developed. Using this model, various strategies can be tested and optimized. In order to characterize, understand and manipulate the water transport mechanisms, not only a mathematical model that describes the physical phenomena, but also experimental parameter identification is needed. Thus [Strahl, 2011] describes the performed experimental work, such as diffusion, EOD and temperature experiments.

The model has been validated by using the experimental data directly obtained from laboratory tests with the investigated fuel cell stack.

Although most physical phenomena occurring in a PEMFC can be incorporated in the macroscopic CFD models, it leads to time-consuming simulations with high computational costs, which makes them impossible to use in an on-board, model-based controller. Thus reduced, lumped parameter control-oriented models tailored for specific control objectives are developed.

2.2. Fuel cell system control-oriented models and their analysis

This section describes the three articles published in the field of control-oriented modeling and analysis. The first one [Serra, 2006] describes controllability associated to fuel cell systems efficiency, while article [Kunusch, 2008] and [Kunusch, 2011] describe lumped parameter control-oriented models.

The object of the study published in [Serra, 2006] is to compare the controllability to efficiency of a PEMFC at specific operating points. It considers the inputs to be the air compressor voltage and the hydrogen mass flow rate and the output to be the stack voltage and the anode-cathode pressure differential. The study is based on a ninth order non-linear model, which has been linearized at selected operating points. Different linear analysis tools, which include the Morari resiliency index (MRI), the condition number (CN), the relative gain array (RGA), the sensitivity function S and the complementary sensitivity function T, are applied to the linearized models and results show important controllability differences between operating points. The results show that decentralized control is easier in the operating points with lower efficiency. Moreover, the performance of diagonal control structures with PI controllers at different operating points is studied and a method for the tuning of these controllers is proposed and applied.

In [Kunusch, 2008] a linear identification of the system time constants on an experimental laboratory fuel cell system, under a specific operating condition, is obtained to develop a black box model of the system. The objective of the work is the development of an experimentally validated linear model of the fuel cell system that approximates the coupled dynamics with respect to the inputs and outputs. The two inputs are fuel cell stack current and cathode mass flow rate and the output are fuel cell stack voltage and cathode inlet pressure. The dynamics are determined using spectroscopy tests of the four different single-input single-output subsystems. With this initial information a controller could be designed in order to regulate the outputs. Moreover, the proposed analysis is also useful to study the system time constants that are necessary for the development of a comprehensive non-linear model.

From this, [Kunusch, 2011] applies a comprehensive methodology to develop a control-oriented model that reproduces the most typical features of a laboratory PEMFC system through ordinary non-linear differential equations. The methodology used to develop the model is based on a modular procedure, combining theoretical modeling techniques and empirical analysis based on experimental data. The obtained model is a fully validated analytical model of the PEMFC system's flow dynamics. The model can be easily adapted to other systems because its parameters maintain their physical significance. The model is used for the design of sophisticated control algorithms such as model based predictive control and variable structure control [Kunusch, 2010] [Kunusch, 2012].

2.3. Performance indicators and identification of parameters

This section describes the two articles published in the field of performance indicators and identification of parameters. Water management and distribution, related to fuel cell performance is one of the main issues that need to be dealt with in PEMFC stack and systems. Thus the topics addressed in these experimental works are water transport and the voltage loss dissection that can be related to mass transport limitations of oxygen due to water.

[Husar, 2008] experimentally isolates the three major water transport mechanisms through the membrane: diffusion, EOD and hydraulic permeation. This study establishes that diffusion and EOD drag are generally in the same order of magnitude. The hydraulic permeation is an order of magnitude lower than the other two mechanisms.

The in-situ determination of the effective water diffusion coefficient and the EOD coefficient is essential in order to obtain a representative mass transport model. However, to be able to describe the mass transport effects, such as concentration losses, on fuel cell performance, all major voltage losses have to be identified. Determination of these losses in an on-board diagnosis system would allow for the design of a robust controller for performance optimization.

[Husar, 2011] experimentally isolates the three major voltage loss indicators for the fuel cell. Which are activation, mass transport and Ohmic losses. The methodology used in this work could be directly applied to a real world system with minimal added cost.

These indicators can be extracted by using some of the naturally occurring system specific dynamics (e.g. actuation of the purge valve, change of set points) together with some forced dynamics (e.g. current interrupt) can be used to relate electrical as well as mechanical measurements to the previously stated indicators. Electrical small signal and large signal dynamics in conjunction with the global measurements of temperature, pressure and reactant flow rates will facilitate the determination of these indicators. With these new indicators the control objectives will be defined, coexisting with conventional objectives, such as pressure, temperature, or humidity regulation, and may also replace a few.

The data analysis from these works suggests that one of the main controller objectives should be to minimize mass transport losses due to liquid water in the catalyst and the diffusion layer because this directly affects the performance of the fuel cell.

2.4. Fault and Failure detection and analysis

Alternatively from the performance indicators, to know if the fuel cell is operating in proper conditions and/or if some failure has occurred can be determined by Fault Detection and Isolation (FDI) techniques. A FDI system can be based on rules given by an expert. However, when the number of possible failures and their combination is large a mathematically structured alarm system is required [de Lira 2011]

This section describes two articles published in the field of diagnosis and failure analysis. [Husar, 2007] describes the failure of a 7 cell stack. Three failure indicators are found for crossover leak detection provoked by a gasket failure. The indicators of the failure are: an unanticipated rise in the stack temperature, unanticipated loss in stack pressure and instability in a single cell's voltage which is induced when the anode pressure is larger than the cathode pressure.

In [de Lira 2011] a new LPV model-based fault diagnosis methodology is presented and applied to a PEMFC system. The approach takes into account model parameter variation with the operating point and includes a fault isolation algorithm based on the relative fault sensitivity concept. The model has been obtained through a Jacobian linearization of a PEMFC non-linear dynamic model that was calibrated using laboratory data. A case study is performed with a set of common fault scenarios, which could appear during a normal PEMFC operation, such as hydrogen leakage due to seal degradation or compressor malfunction due to an increase in shaft friction. It has been shown that the developed diagnosis method is able to isolate all the analyzed faults.

3. Discussion of Results

The design and validation of the two macroscopic CFD dynamic models has provided valuable insight on the non-measurable dynamics of the phenomena occurring internal to the fuel cell. The single cell 3D non-isothermal model, from [Alonso, 2009] for instance, shows where liquid water is condensing in the cathode flow field channels and describes an effective channel cross-sectional area reduction factor which is related to the pressure drop in the flow field. This model also demonstrates the sensitivity of condensation to both fuel cell temperature and reactant dew point temperature and allows determining the critical current at which water will condense. With this knowledge controllers can be designed to estimate the liquid water content in the flow field by measuring the pressure drop and thus adjust the conditions accordingly. A possible control objective could be to avoid liquid water droplet formation in the gas channels by controlling fuel cell temperature and/or reactant flows depending on fuel cell stack current. The 2D dynamic, non-isothermal CFD model of an open cathode fuel cell from [Strahl, 2011] describes the system dynamics associated to the three control actions of an open cathode fuel cell system: hydrogen purge, cathode fan flow rate and short circuit. Since the model is designed to simulate the dynamics of the reactants and water vapor concentrations, it provides the necessary fundamental insight for determining the meaningful variables that may be estimated by future observers (i.e. reactant concentrations at the catalyst surface). However, the model can still be improved by including charge transfer, two-phase flow characteristics as well as temperature driven water transport. Moreover, further experiments are needed to analyze the dynamic effect of liquid water storage in the membrane and GDL’s.

In regards to control oriented issues, initial results from [Serra 2006] show that the system controllability changes with the operating point. Specifically, controllability is higher at lower efficiencies within a wide range of operating conditions. This result will be relevant if we want to use simple decentralized control structures.

The work presented in [Kunusch, 2011] represents a novel contribution in the field of control-oriented model, because it proposes a systematic methodology to develop models and its corresponding validation procedure. The final complete model is represented by seven nonlinear differential equations that capture the flow subsystem dynamic behavior, while maintaining the physical meaning, which allows for the future coupling of thermal and/or electrochemical models. Based on this model, a comprehensive analysis is currently being done in order to study its algebraic observability. Meanwhile, advanced works are under development in the field of finite-time convergence observers based on Super Twisting algorithms [Moreno, 2011]. In particular, three novel approaches are being proposed to estimate the membrane water transport based on the dynamic anode model of [Kunusch, 2011].

Advances have been made in identifying some of the crucial coefficients for water transport, namely the effective diffusion and the EOD coefficient that are determined experimentally, based on a novel in-situ methodology proposed and implemented in the work of [Husar 2008]. A notable result from [Husar, 2008] is that the effective water diffusivity increases with fuel cell temperature and decreases with total system pressure. On the other hand the EOD coefficient not only increases with temperature but also with current density, which is different from what is published in the literature [Springer, 1991] but is in accordance with the experimental parameter determination in [Strahl, 2011]. This indicates that further studies are still needed for proper understanding of the effect of current on the EOD coefficient. It is important to stress that this coefficient drives approximately fifty percent of the water transport through the membrane.

The control-oriented models analyzed and developed in [Serra, 2006], [Kunusch, 2008] and [Kunusch, 2011] present some first necessary steps needed to develop robust system controllers. However, the relationship between the fluid dynamics and the electrochemistry for both the CFD and control-oriented models is still needed. The connection between the fuel cell voltage and the CFD model is being made by experimentally determining the following critical parameters needed to define the reaction kinetics and electric properties: Tafel slope, exchange current density, cathode mass transport resistance and membrane resistance as described in

[Husar, 2011]. The methodology can also be applied to calibration and validation of the fluid mechanics and the thermal dynamic models with the electrochemical fuel cell model. With the automation and implementation of voltage loss indicators into system one of the main controller objective should be to minimize mass transport losses due to liquid water in the catalyst and the diffusion layer. However this objective could be in conflict with a durability objective. Most likely, certain amount of liquid water has to be maintained in the catalyst for proper membrane hydration.

Incorporating the obtained performance indicators for monitoring fuel cell degradation is another possible application of this technique. Degradation of the catalysts layer should present itself as an increase in the activation losses, whereas the degradation of the hydrophobic agent in the gas diffusion layer can be observed by an increase in the mass transport losses due to a build-up of liquid water in the GDL. Finally degradation in the membrane should present itself as an increase in the membrane resistance. These degradation losses may be detected in a long-term study and can be used for fault and failure prediction. Besides MEA degradation, mechanical and material failures are also crucial aspects to be dealt with during fuel cell operation. Specially, gasket failures can be detected by a future supervisory controller incorporating the indicators reported in [Husar, 2007]. For instance, a safe shutdown protocol could be developed, based on these results. The relationship among symptoms, failures, faults and system degradation has to be studied. Thus, more research is required in the field of fault detection and isolation as is introduced in [de Lira, 2011].

4. Conclusions and Contributions

Modeling of PEMFC dynamics behavior, performance and internal state is a very useful tool for improving not only the mechanical design but also controller design. For the implementation of novel all-inclusive controllers that improve the efficiency of the system into real world applications, it is necessary to identify and control relevant variables of the fuel cell. These variables like liquid water in the diffusion layer are internal to the cell and generally cannot be directly measured. Thus, in this thesis models and online measurement techniques have been developed that allow for accurate performance simulations of PEMFC system for the development of control strategies.

A representative model has to be properly validated using experimental data. The articles presented in this thesis are firmly based on experimental validation and data analysis. To obtain this data for the works, several fuel cell test stations were custom designed and built to accommodate for the specific goal for each article throughout this thesis. It should be noted that any experimental work always adds a certain level of complexity and time to the research. The value given by the experimental data has been instrumental and this data has enabled the studies to be conclusive and have sound results.

Moreover, an array of experimental methodologies and techniques, combining time and frequency analysis, has been used to obtain relevant parameters and indicators for determining the internal state of the fuel cell. These include: automated rapid current sweeps, current interrupt, electrochemical impedance spectroscopy and pressure drop analysis.

The parameters found for the effective diffusion coefficient and the EOD coefficient of water through the membrane have given a more complete expression, in operating fuel cell, than that found in literature. The indicators found allow for the separation of the main voltage losses in a fuel cell (i.e. activation loss, mass transport loss and Ohmic losses), the calibration and validation of CFD reaction kinetics models, the on-line monitoring of fuel cell internal state, and finally the implementation of novel control strategies. Other indicators have been proposed for fault and failure detection. The particular indicators of interest are the ones associated to gasket failure. With the FDI technique they should be detectable.

In regards to fault and failure diagnosis, other indicators have been proposed. Specifically, indicators to recognize gasket failure have been described. Moreover, it has been shown that the application of new FDI techniques would allow the diagnosis of a specific fault among a large set of faults.

As a whole, the compilation of articles represented in this thesis applies a comprehensive experimental approach which describes the implementation of novel methodologies and experimental procedures to characterize and model the PEMFC and their associated systems taking into consideration control oriented goals.

5. Future Work

As indicated in the results and discussion, this work has initiated some complementary research activities. There are, two new relevant future works that will be investigated in the near future:

The implementation of an improved 2D open cathode model which includes the Butler-Volmer electrochemical sub-model and liquid water effects on fuel cell voltage. The model will include voltage loss indicators and show there effects of fan flow rate, hydrogen purge, short circuit on fuel cell performance. The final objective would be to design and implement an effective high performance controller. This work is currently in progress as a Ph.D. thesis.

The second project is to improve the current models with the integration of multi-scale aspects of the relevant phenomena not only pertaining to fuel cell system performance but also to degradation phenomena that occur inside the fuel cell. This work will be part of the three year 2.3 M€ EU-FP7 project entered into the negotiation stage, named: "*Physical bottom Up Multi-scale Modelling for Automotive PEMFC Innovative performance and Durability optimization*" (PUMA-MIND), with the following work package objectives:

- to develop a control oriented model described by ordinary differential equations (ODE) based on the mathematical reduced version developed in previous work packages for real-time diagnostic purposes
- to develop and implement on-board monitoring tools to determine fuel cell performance and degradation indicators based on the mathematical model
- to develop model based control strategies with the purpose of enhancing the PEMFC performance and durability. Dynamic observers will be designed for the estimation of states and performance variables in the PEMFC.

6. References

[Amphlett, 1995] Amphlett, J.C., Baumert, R.M., Mann, R.F., Peppley, B.A. and Roberge, P.R. Performance modelling of the Ballard Mark IV solid polymer electrolyte fuel cell. Journal of Electrochemical Society, 142(1):9–15, 1995.

[Arce, 2010] Arce, A., Real, A.J., Bordons, C. and Ramírez, D.R. Real-Time Implementation of a Constrained MPC for Efficient Airflow Control in a PEM Fuel Cell. IEEE Tran. on Industrial Electronics, Vol 57, No.6: 1892-1905, 2010.

[Bao, 2006] Bao, C., Ouyang, M., and Yi, B. Modeling And Control of Air Stream and Hydrogen Flow with Recirculation in a PEM Fuel Cell System–I. Control-Oriented Modeling. International Journal of Hydrogen Energy, 31(13):1879–1896, 2006.

[Barbir, 2005] F. Barbir. PEM fuel cells: theory and practice. Elsevier, 2005.

[DOE, 2005] Department of Energy. Hydrogen, Fuel Cells And Infrastructure Technologies Program: Multi-Year Research, Development And Demonstration Plan: Planned program activities for 2005–2015. DOE Website. Section 3.4 Fuel Cells, 2005.

[FP6, 2002] The Sixth Framework Programme, Community Activities in the Field of Research, Technological Development and Demonstration (RTD) for the period 2002 to 2006. 2002.

[FP7, 2007] The Seventh Framework Programme, Competitive European Regions through Research and Innovation. Practical Guide to EU Funding Opportunities for Research and Innovation for the period 2007 to 2013. 2007.

[Gorgun, 2006] Gorgun, H., Arcak, M., Barbir, F. An Algorithm for Estimation of Membrane Water Content in PEM Fuel Cells. Journal of Power Sources 157: 389–394, 2006.

[Grasser, 2007] Grasser, F. and Rufer, A. A Fully Analytical PEM Fuel Cell System Model for Control Applications. IEEE Transactions on Industry Applications, 43(6):1499–1506, 2007.

[He, 2003] He, W., Lin, G. and Nguyen, T.V. Diagnostic Tool to Detect Electrode Flooding in Proton- Exchange-Membrane Fuel Cells. AIChE Journal, 49(12): 3221–3228, 2003.

[Hui, 2010] Hui, J. and Jie, H. Research of the Humidity Control System of PEM Fuel. International Conference on Intelligent Systems and Knowledge Engineering (ISKE), 2010.

[Ismail, 2009] A. F. Ismail, R. Naim and N. A. Zubir. Fuel Cell Technology Review. Chemistry and Materials Science. Polymer Membranes for Fuel Cells, pp. 27-49, 2009.

[Kazmi, 2009] Kazmi, I.H., Bhatti, A.I. and Iqbal, S.A. nonlinear observer for PEM fuel cell system. IEEE 13th International Multitopic Conference (INMIC), 2009.

[Khan, 2005] Khan, M.J. and Iqbal, M.T. Modelling And Analysis Of Electro-Chemical, Thermal, and Reactant Flow Dynamics for a Pem Fuel Cell System. Fuel Cells, 5(4):463–475, 2005.

[Kunusch, 2009] Kunusch, C., Puleston, P.F., Mayosky, M.A., and Riera, J. Sliding Mode Strategy for PEM Fuel Cells Stacks Breathing Control Using a Super-Twisting Algorithm. IEEE Transactions on Control Systems Technology, 17(1):167 – 174, 2009.

[Kunusch, 2010] Kunusch, C., Puleston, P.F., Mayosky, M.A., Davila, A., 2011. Efficiency Optimisation of an Experimental PEM Fuel Cell System via Super Twisting Control. 11th International Workshop on Variable Structure Systems (VSS 2010, Mexico), IEEE Xplore Digital Library.

[Kunusch, 2012] Kunusch, C., Puleston, P., Mayosky, M., 2012. Sliding-Mode Control of PEM Fuel Cells. Series of Advances in Industrial Control, Springer. ISBN 978-1-4471-2430-6.

[Mann, 2000] Mann, R., Amphlett, J., Hooper, M., Jensen, H., Peppley, B., Roberge, P. Development and Application of a Generalised Steady-State Electrochemical Model for a PEM Fuel Cell. J. of Power Sources, 86: 173–180, 2000.

[McKay, 2004] McKay, D. and Stefanopoulou, A.G. Parameterization and Validation of a Lumped Parameter Diffusion Model for Fuel Cell Stack Membrane Humidity Estimation. IEEE ACC, Vol 1: 816– 821, 2004.

[Mangold, 2010] Mangold, M., Bück, A., Hanke-Rauschenbach, R. Passivity Based Control of a Distributed PEM Fuel Cell Model. Journal of Process Control. 20: 292–313, 2010.

[McCain, 2008] McCain, B., Stefanopoulou, A. and Kolmanovsky, I. On the Dynamics And Control of Through-Plane Water Distributions in PEM Fuel Cells. Chemical Engineering Science 63 (2008) 4418- 4432, 2008.

[Methekar, 2007] Methekar, R., Prasad, V. and Gudi, R. Dynamic Analysis and Linear Control Strategies for Proton Exchange Membrane Fuel Cell Using a Distributed Parameter Model. J. of Power Sources 165 (2007) 152-170, 2007.

[Moreno, 2011] Moreno, J.A., 2011. Lyapunov Approach for Analysis and Design of Second Order Sliding Mode Algorithms. Springer. Chapter 4, 122-150.

[Pukrushpan, 2004] Pukrushpan, J.T., Stefanopoulou, A.G., and Peng, H. Control of Fuel Cell Power Systems. Springer, 2004.

[Riascos, 2009] Riascos, L., and Pereira, D. Optimal Temperature Control in PEM Fuel Cells. IEEE Annual Conference on Industrial Electronics (IECON), 2009.

[Rodatz, 2003] Rodatz, P.H. Dynamics of the Polymer Electrolyte Fuel Cell: Experiments and Model based Analysis. PhD thesis, Swiss Federal Institute of Technology Zurich, 2003.

[Springer, 1991] Springer, T.E., Zawodzinski, T.A., and Gottesfeld, S. Polymer electrolyte fuel cell model. Journal of Electrochemical Society, 138(8):2334–2342, 1991.

[Talj, 2010] Talj, R., Hissel, D., Ortega, R., Becherif, M., and Hilairet, M. Experimental Validation of a PEM Fuel-Cell Reduced-Order Model and a Moto-Compressor Higher Order Sliding-Mode Control. Industrial Electronics, IEEE Transactions on, 57(6):1906 – 1913, 2010.

[Thawornkuno, 2008] Thawornkuno, C., Panjapornpon, C. Estimation of Water Content in PEM Fuel Cell. Chiang Mai J. Sci., 35(1): 212-220, 2008.

7. Catalog of Published Articles

The citation data comes from Scopus on Dec 2011: https://www.scopus.com

The following is a list of the 5-year average of the Thomson Reuters Impact Factors (IF) for the journals in which the articles are published:

- 5 articles in *Journal of Power Sources* which has an IF of **4.644**
- 2 articles in *International Journal of Hydrogen Energy* with an IF of **4.411**
- 1 articles in IEEE Transactions on Energy Conversion with an IF of **2.489**
- 1 articles in Asia-Pacific Journal of Chemical Engineering with an IF of **0.583**

[Serra, 2006]: Maria Serra, **Attila Husar**, Diego Feroldi, Jordi Riera, *Performance of diagonal control structures at different operating conditions for polymer electrolyte membrane fuel cells*, Journal of Power Sources, Volume 158, Issue 2, 25 August 2006, Pages 1317-1323, ISSN 0378-7753, 10.1016/j.jpowsour.2005.10.092.
Citations 4

[Husar, 2007]: **Attila Husar**, Maria Serra, Cristian Kunusch, *Description of gasket failure in a 7 cell PEMFC stack*, Journal of Power Sources, Volume 169, Issue 1, 10 June 2007, Pages 85-91, ISSN 0378-7753, 10.1016/j.jpowsour.2007.01.078.
Citations 11

[Kunusch, 2008]: C. Kunusch, **A. Husar**, P.F. Puleston, M.A. Mayosky, J.J. Moré, *Linear identification and model adjustment of a PEM fuel cell stack*, International Journal of Hydrogen Energy, Volume 33, Issue 13, July 2008, Pages 3581-3587, ISSN 0360-3199, doi: 10.1016/j.ijhydene.2008.04.052.
Citations 12

[Husar, 2008]: **Attila Husar**, Andrew Higier, Hongtan Liu, *In situ measurements of water transfer due to different mechanisms in a proton exchange membrane fuel cell*, Journal of Power Sources, Volume 183, Issue 1, 15 August 2008, Pages 240-246, ISSN 0378-7753, 10.1016/j.jpowsour.2008.04.042.
Citations 9

[Alonso, 2009]: Javier Alonso Mora, **Attila Husar**, Maria Serra, Jordi Riera, *Numerical model for polymer electrolyte membrane fuel cells with experimental application and validation*, Asia-Pacific Journal of Chemical Engineering, Volume 4, Number 1, January **2009**, Pages 55-67, ISSN 1932-2143, 10.1002/apj.195.
Citations 1

[Strahl, 2011]: Stephan Strahl, **Attila Husar**, Maria Serra, *Development and experimental validation of a dynamic thermal and water distribution model of an open cathode proton exchange membrane fuel cell*, Journal of Power Sources, Volume 196, Issue 9, 1 May 2011, Pages 4251-4263, ISSN 0378-7753, 10.1016/j.jpowsour.2010.10.074.
Citations 0

[de Lira, 2011]: S. de Lira, V. Puig, J. Quevedo, **A. Husar**, *LPV observer design for PEM fuel cell system: Application to fault detection*, Journal of Power Sources, Volume 196, Issue 9, 2011, Pages 4298-4305, ISSN 0378-7753, doi: 10.1016/j.jpowsour.2010.11.084.
Citations 0

[Kunusch, 2011]: C. Kunusch, P.F. Puleston, M.A. Mayosky, **A. Husar**, *Control-Oriented Modeling and Experimental Validation of a PEMFC Generation System,*" Energy Conversion, IEEE Transactions on , vol.26, no.3, pp.851-861, ISSN: 0885-8969, 2011 doi:10.1109/TEC.2011.2124462.
Citations 0

[Husar, 2011]: **Attila Husar**, Stephan Strahl, Jordi Riera, *Experimental Characterization Methodology for Identification of Voltage Losses of PEMFC: Applied to an Open Cathode Stack,* International Journal of Hydrogen Energy, doi: 10.1016/j.ijhydene.2011.11.130
Accepted November 2011

8. Original Manuscripts

Available online at www.sciencedirect.com
ScienceDirect
Journal of Power Sources 158 (2006) 1317–1323
JOURNAL OF POWER SOURCES
www.elsevier.com/locate/jpowsour

Short communication

Performance of diagonal control structures at different operating conditions for polymer electrolyte membrane fuel cells

Maria Serra*, Attila Husar, Diego Feroldi, Jordi Riera

Institut de Robòtica i Informàtica Industrial, Universitat Politècnica de Catalunya,
Consejo Superior de Investigaciones Científicas, C. Llorens i Artigas 4, 08028 Barcelona, Spain

Received 5 August 2005; received in revised form 29 September 2005; accepted 26 October 2005

Abstract

This work is focused on the selection of operating conditions in polymer electrolyte membrane fuel cells. It analyses efficiency and controllability aspects, which change from one operating point to another. Specifically, several operating points that deliver the same amount of net power are compared, and the comparison is done at different net power levels. The study is based on a complex non-linear model, which has been linearised at the selected operating points. Different linear analysis tools are applied to the linear models and results show important controllability differences between operating points. The performance of diagonal control structures with PI controllers at different operating points is also studied. A method for the tuning of the controllers is proposed and applied. The behaviour of the controlled system is simulated with the non-linear model. Conclusions indicate a possible trade-off between controllability and optimisation of hydrogen consumption.

Keywords: PEMFC; Diagonal control; PI controllers; Operating conditions; Linear analysis; Efficiency

1. Introduction

Compared to other types of fuel cells, polymer electrolyte membrane fuel cells (PEMFC) have many advantages that make them suitable for a large number of applications. Some of these advantages are high power density, compactness, lightweight, low-operating temperature, solid electrolyte, long cell and stack life, low corrosion and high efficiencies [1]. PEMFC are regarded as ideally suited for transportation applications. However, important difficulties remain unsolved and a lot of research is being done in order to make the technology ready to implementation and commercialisation [2].

Advantages of different operating conditions for PEMFC have been described in the literature [3]. However, a comparison of the system controllability at different operating points is not found. A PEMFC can deliver the same amount of net power at different operating conditions. In order to chose the appropriate operating point, control aspects have to be taken into account, as well as efficiency aspects. Some works address the control of PEMFC [4–6], but only the efficiency is considered to determine the operating conditions. The objective of this work is to compare the controllability of a PEMFC operated at different operating conditions. The performance of the control system is evaluated implementing a diagonal structure with PI controllers in the control loops.

2. The model

In their study of the PEMFC flow dynamics, Pukrushpan et al. presented a control oriented model for an automotive application which has been the base for the model used in this work [4,7]. The transient phenomena captured in the model include the flow and inertia dynamics of the compressor, the manifold filling dynamics (both anode and cathode), reactant partial pressures and membrane humidity. On the other hand, the model neglects the extremely fast electrochemical and electrical dynamics, and temperature is treated as a constant parameter because its slow behaviour (time constant of 10^2 s) allows it to be regulated by its own controller. A constant cell temperature of 80 °C is assumed.

---

* Corresponding author. Tel.: +34 93 4015789; fax: +34 93 4015750.
E-mail address: maserra@iri.upc.edu (M. Serra).

doi:10.1016/j.jpowsour.2005.10.092

Nomenclature

I_{st}	stack current (A)
K_c	proportional constant of the PI controller
p_{ca}	cathode pressure (bar)
P_{net}	net power (W)
T_i	time constant of the PI controller (s)
v_{st}	stack voltage (V)
v_{cm}	compressor voltage (V)
$W_{an,in}$	anode inlet mass flow rate (kg s^{-1})

Greek letters

Δ_p	anode–cathode pressure difference (bar)
λ_{O_2}	oxygen stoichiometry

Mass and energy balance are the basic laws for the different volumes being modelled. Constant properties are assumed in all volumes. Flowrates from one volume to another are calculated as a function of the upstream and downstream pressures. Ideal gases are assumed.

Membrane hydration captures the effect of water transport across the membrane. Water transport is modelled through drag and diffusion effects. Both water content and mass flow are assumed to be uniform over the surface area of the membrane. This surface is of 280 cm^2.

Stack voltage is calculated as a function of stack current, cathode pressure, reactant partial pressures, fuel cell temperature, and membrane water content. Identical behaviour of each cell is assumed and the stack voltage is calculated as the individual cell voltage per the number of cells, in this case 381.

The air entering the cathode is impelled by a compressor the model of which consists of a dynamic part and a static part read from an experimental compressor map. The modelled compressor has the angular velocity limited to 100 krpm, the exit flow limited to 0.1 kg s^{-1}, and the pressure ratio limited to 4. The power consumed by the compressor is the only parasitic power taken into account. The net power, P_{net}, is therefore calculated as the electric power given by the fuel cell minus the power consumed by the compressor. Cooler and humidifier are also included. It is assumed that a static humidifier supplies the air with the desired relative humidity before entering the stack.

At the anode side, entering hydrogen comes from a pressurised tank and the hydrogen flow is assumed to be a manipulated input variable.

Only one modification is introduced, which is the existence of an anode exit flow. This exit is necessary to control the hydrogen pressure along the flow channels and to improve the power demand transient responses [2].

Some of the indexes used for the linear analysis depend on the model scaling. One of the controlled outputs is the difference of pressure between anode and cathode, Δ_p. It has been scaled with a variation of 0.1 bar. To scale the rest of the input and output variables, a maximum variation of 10% has been assumed. Hence, the scaled variables are the non-scaled increments divided by the maximum increments.

SIMULINK linearisation tools have been used to obtain the state space matrices of the system at the studied operating points.

3. Operating conditions

This work is based on the analysis of a set of selected operating points. Their operating conditions are summarised in Table 1. In Fig. 1, the operating points are located on the curves of net power versus stoichiometry at different current values. In a fuel cell, a certain amount of net power can be obtained at different currents. OP1 to OP5 deliver the same net power, P_{net} = 37,400 W, and the same happens with OP6 to OP8, with P_{net} = 30,000 W. OP1 and OP7 have the minimum amount of current for which P_{net} of 37,400 and 30,000 W can be, respectively, obtained. For example, it is not possible to obtain 37,400 W of net power with a current lower than 175 A, at any pressure or stoichiometry. These operating points are specially interesting because minimum current corresponds to the minimum hydrogen consumption if the hydrogen that does not react is recycled. Looking at the different curves of Fig. 1, it can be seen that for small λ_{O_2} P_{net} increases when λ_{O_2} increases, but this trend changes from a certain λ_{O_2} value. This is because when λ_{O_2} is high, to increase λ_{O_2} requires a compressor power increase larger than the electric power increase obtained from the fuel

Table 1
Studied operating points

	P_{net} (W)	I_{st} (A)	λ_{O_2}	v_{st} (V)	p_{ca} (bar)	Efficiency (%)	v_{cm} (V)
OP1	37390	175	2.15	242.7	1.99	42.5	158
OP2		187	1.60	217.8	1.78	40.7	135
OP3			3.20	261.2	2.56	37.4	217
OP4		200	1.41	201.8	1.73	38.3	130
OP5		280	1.29	149.7	1.89	27.3	151
OP6	30000	134	2.37	254.2	1.86	44.9	142
OP7		150	1.25	209.5	1.49	41.4	100
OP8			3.89	273.94	2.55	36.6	214.0

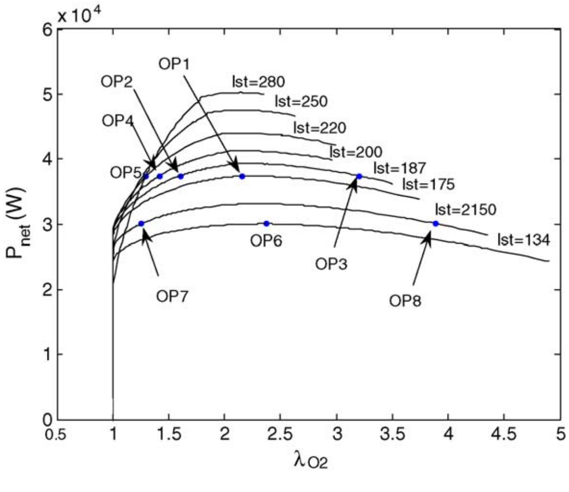

Fig. 1. Different operating points.

cell. Because of this power maximum, operating points with the same net power and current are possible (i.e. OP2 and OP3, or OP7 and OP8). It is interesting to compare these pairs of operating conditions that have different stoichiometries but the same net power and the same hydrogen consumption.

4. Control objectives

In this work, the stack current is considered a disturbance and there is a desired stack voltage, which depends on the required power. Therefore, the first control objective is to maintain v_{st} to the setpoint value. On the other hand, in order to prevent membrane damage, the difference in pressure between anode and cathode Δ_p needs to be small [8]. A small Δ_p will favour the membrane life time, and thus, the second control objective is to maintain Δ_p close to zero.

For certain applications, the required power is constant and there is a unique voltage setpoint. The selection of this setpoint (selection of operating conditions) is the main issue concerning this work. However, if the range of required power is large, different setpoint voltages will be necessary (even a desired operating curve), and what are the appropriate operating conditions will be questioned at every power level.

5. Structure of the control system

In this work, a decentralised PI based controller is implemented. Two output variables are controlled using two of the input manipulated variables giving a 2 × 2 control problem. The input control variable chosen to control v_{st} is v_{cm}. This control loop is called the first loop. To control Δ_p, $W_{\mathrm{an,in}}$ has been chosen. This is called the second loop. From all possible pairs of manipulated variables, v_{cm} and $W_{\mathrm{an,in}}$ have been chosen because this is what is found in the literature [4–6] and what is recommended after a controllability analysis by Serra et al. [9].

6. Tuning of PI controllers

The performance of the controlled system depends on the proportional and time constants of the PI controllers, K_{c} and T_{i}. In order to compare the behaviour of the proposed control structure at different operating points, it is important to employ the same tuning methodology. In this section, the used tuning methodology is described.

For the first loop, the control of v_{st}, Ziegler–Nichols tuning rules can be applied [10]. However, they are not appropriate for the second loop, the control of Δ_p, because the resulting tuning parameters provoke sudden changes in pressure that could damage the membrane. The tuning method used for the second loop permits to limit the pressure peaks. The tuning procedure consists of the following steps:

(a) *Tuning of the first control loop*. This tuning has been done with some tuning rules that can be viewed as a modification of the Ziegler–Nichols step response method: the Kappa–Tau tuning procedure [11]. These rules use three parameters to characterise the process dynamics instead of two, permitting substantial improvements in control performance while retaining much of the simplicity of the Ziegler–Nichols method.

(b) *Tuning of the second control loop*. The transfer function that relates Δ_p with $W_{\mathrm{an,in}}$ is of second order, but has a zero and a pole which almost cancel each other. Eliminating the zero and pole, an equivalent first order transfer function is obtained. The methodology employed was proposed by Rivera et al. for disturbance rejection of low-order processes [12]. The proportional constant of the PI controller is calculated as a function of the steady state gain of the process, the time constant of the process, and a parameter that has been chosen such that Δ_p peaks are no larger than 0.3 bar when current steps of $40\,\mathrm{A\,s^{-1}}$ and giving power increments of ±20% are applied.

Applying this tuning methodology to OP1, OP2, OP4 and OP5, the tuning parameters indicated in Table 2 are obtained.

7. Linear analysis

MIMO linear systems can be analysed using different analysis tools. These tools are mathematic operators applied to the transfer functions of the linear system. Some of them are applied to the process (without control) and characterise the controllability of the system as a property of the process itself. Others are applied to the controlled system and depend on the control structure and tuning. In this work, the following indexes and matrixes are considered in order to study the performance and controllability of the system: the Morari resiliency index (MRI), the condition number (CN), the relative gain array (**RGA**), the sensitivity function, **S**, and the complementary sensitivity function, **T**.

The MRI is the smallest singular value of the open-loop transfer function. It is the poorer gain of the process, poorer sensitivity, which corresponds to specific input and output directions. Large MRI over the frequency range of interest is preferred. The CN is the ratio of the maximum singular value to the minimum singular value. It indicates the sensitivity balance in a

Table 2
Scaled PI tuning parameters

	OP1		OP2		OP4		OP5	
	1st loop	2nd loop	1st loop	2nd loop	1st loop	2nd loop	1st loop	2nd loop
K_{c}	10.28	1.72	6.41	0.87	4.81	0.94	1.91	1.80
T_{i}	0.22	3.32	0.22	3.84	0.22	3.89	0.22	3.46

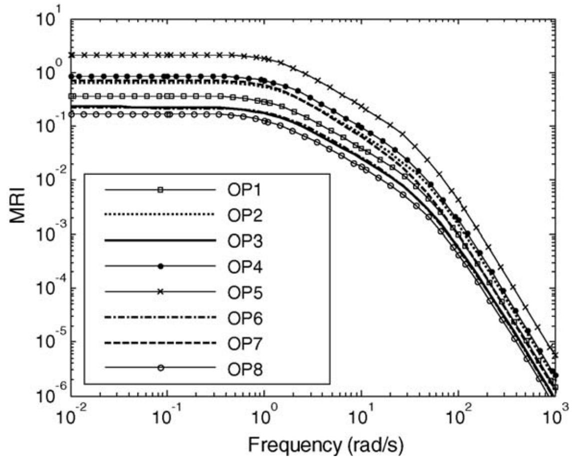

Fig. 2. MRI at the different operating points.

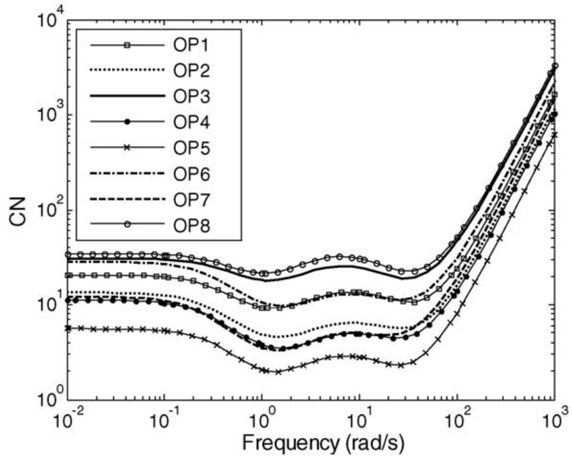

Fig. 3. CN at the different operating points.

multivariable system. Large CN indicate unbalanced sensitivity and also sensitivity to changes in process parameters. Therefore, small CNs are preferred. The **RGA** matrix is used to determine the interaction among control loops in a multivariable process. It is defined as the ratio of the open-loop gain for a selected output when all the other loops of the process are open, to its open-loop gain when all the other loops are closed. Pairings that have **RGA** close to unity matrix at frequencies around bandwidth are preferred. This rule favours minimal interaction between loops and prevents stability problems caused by interaction. Contrarily, large **RGA** elements indicate sensitivity to input uncertainty. **S** is a good indicator of the closed loop performance [13]. Typical specifications in terms of **S** include a large bandwidth frequency (frequency where the maximum singular value of **S** crosses 0.707) and a small peak of its maximum singular value. Large peaks indicate poor performance as well as poor robustness. Finally, **T** can be used to analyse the stability of the MIMO system [14]. The criterion require that the maximum value of its maximum singular value is small for robust stability. This maximum peak criterion can be insufficient for MIMO systems for which advanced tools considering uncertainty descriptions (μ-analysis) are needed. However, to have an idea of the stability robustness, this analysis can be useful.

The frequency range of interest is given by the bandwidth frequency, normally defined as the frequency up to which control is effective [13]. The range of frequencies analysed in this work is 0–10^3 rad s^{-1} because it is assumed that the bandwidth will be within this range. In Figs. 2–4, the MRI, CN and RGA(1,1)

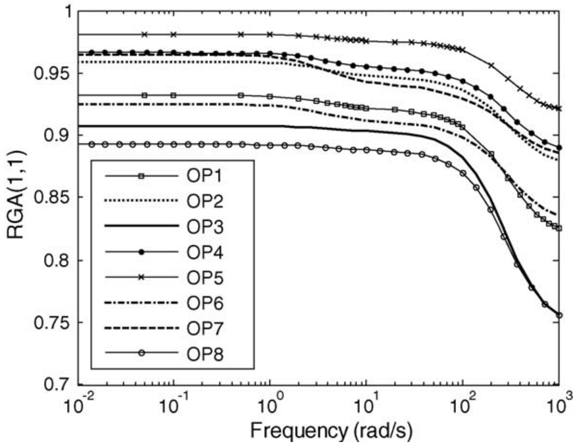

Fig. 4. **RGA** at the different operating points.

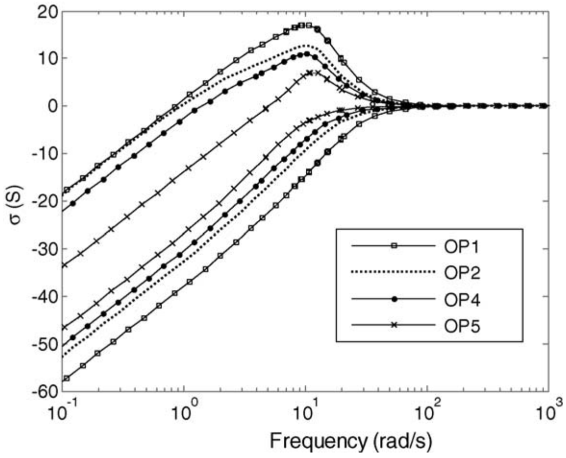

Fig. 5. Maximum and minimum **S** singular values.

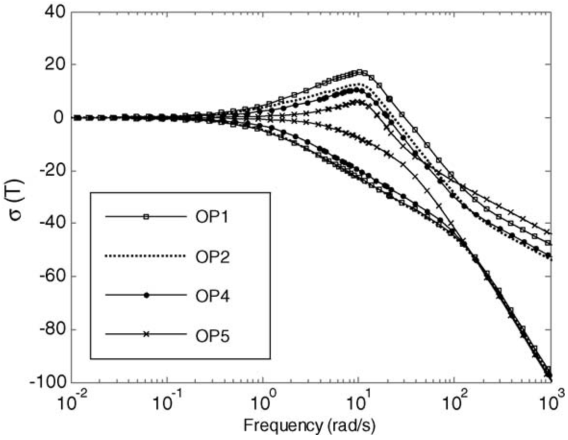

Fig. 6. Maximum and minimum **T** singular values.

of the 2X2 system are plotted. The three controllability indexes indicate the same trends: comparing OP1, OP2, OP4 and OP5, the controllability improves when the current increases. OP5 has the highest MRI, the lowest CN and the **RGA** closest to 1, followed by OP4, OP2 and OP1. Comparing these operating points with OP3, results indicate the poorest controllability at OP3. It can be seen that differences remain important all long the analysed frequency range.

If the analysis is repeated at a different P_{net} level, 30,000W, similar results are found: OP7 has better controllability than OP6, and OP8 has the poorest controllability of the three.

The sensitivity function, **S**, and the complementary sensitivity function, **T**, are also calculated for the controlled system at OP1, OP2, OP4 and OP5, using the tuning parameters indicated in Table 2. The maximum and minimum singular values of these matrixes are shown in Figs. 5 and 6. The following conclusions can be deduced from the Figures: the controlled system is faster at OP5 (higher bandwidth), and the peaks are lower for OP5, indicating better performance and robust stability. Therefore, from a control point of view, OP5 is the best, followed by OP4, OP2 and OP1.

8. Simulation results

In order to take into account the influence of the non-linearities, different simulations are done with the non-linear model. Figs. 7–14 show the behaviour of the controlled system in front of current and voltage setpoint step changes. Simulations are done around OP1 and OP5. All the combinations of 0 and ±10% increments in I_{st} and v_{st} setpoint are applied, covering eight equidistant directions of the bidimensional space defined by these two inputs. The dashed lines correspond to the ±10% current increments without v_{st} setpoint changes. Figs. 7, 9, 11 and 13 correspond to operation around OP1, and Figs. 8, 10, 12 and 14 correspond to operation around OP5.

One first general result is that at OP5 the system responds in a more regular manner in all directions. This confirms a lower system directionality at OP5. For instance, in Fig. 7, oscilatory behaviour is seen in the lower curves, which correspond to negative steps in the v_{st} setpoint, and not in the upper curves, which correspond to positive steps in v_{st} setpoint. In Fig. 8, small peaks are seen in the lower curves, which correspond to negative steps

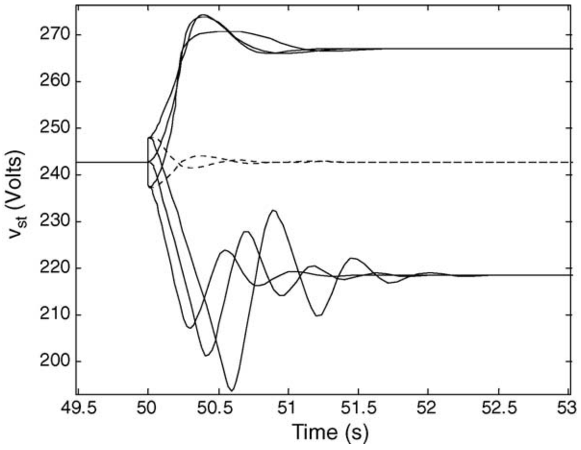

Fig. 7. v_{st} response at OP1.

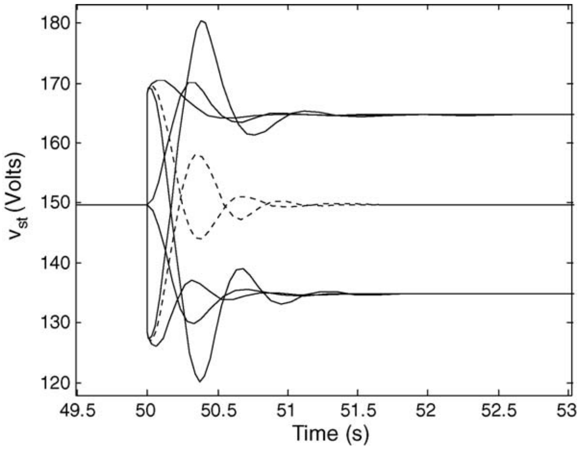

Fig. 8. v_{st} response at OP5.

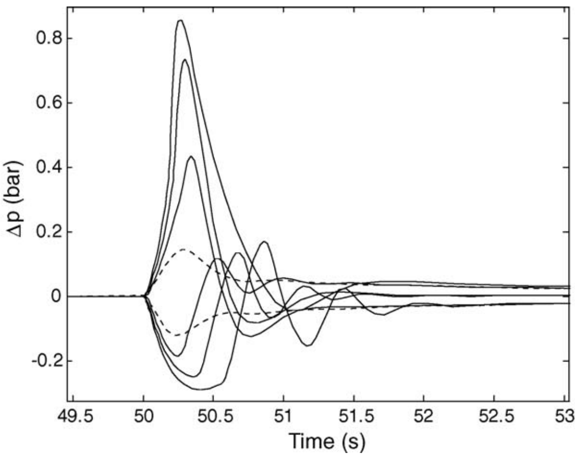

Fig. 9. Δ_p response at OP1.

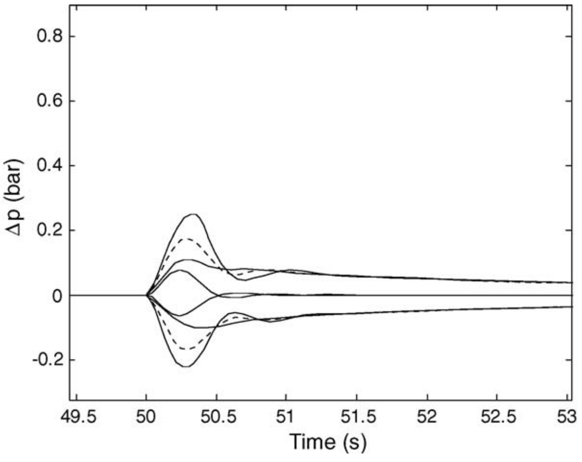

Fig. 10. Δ_p response at OP5.

in the v_{st} setpoint, and large peaks are seen in the upper curves, which correspond to positive steps in v_{st} setpoint. Comparing Figs. 7 and 8, while similar v_{st} peaks are found, a faster control is obtained at OP5. The worst oscillations are found at OP1. Looking at Δ_p, peaks are larger at OP1. In Figs. 11 and 12, it can be seen that v_{cm} has much larger increments and oscillations around OP1. Finally, in Figs. 13 and 14 a better behaviour is found around OP5 as well, with faster response, smaller peaks, and less oscillations.

To analyse the controlled system behaviour in front of larger disturbances around OP1 and OP5, current steps of −24 and +30% (corresponding to ±20% of net power) have been applied. Simulations show a similar behaviour of v_{st} and Δ_p at the two operating points, but both v_{cm} and $W_{\mathrm{an,in}}$ have larger peaks at OP1.

Therefore, simulation results agree with the linear analysis that the analysed fuel cell system has better control properties at OP5. Moreover, for the analysed variables and within the scope of this work, it can be said that the performance of the proposed control system around OP5 is satisfactory.

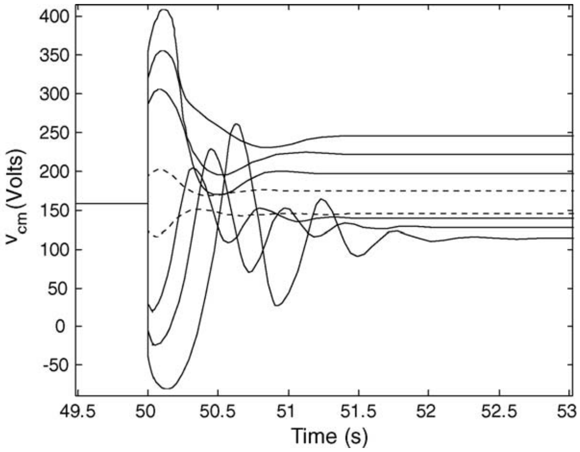

Fig. 11. v_{cm} response at OP1.

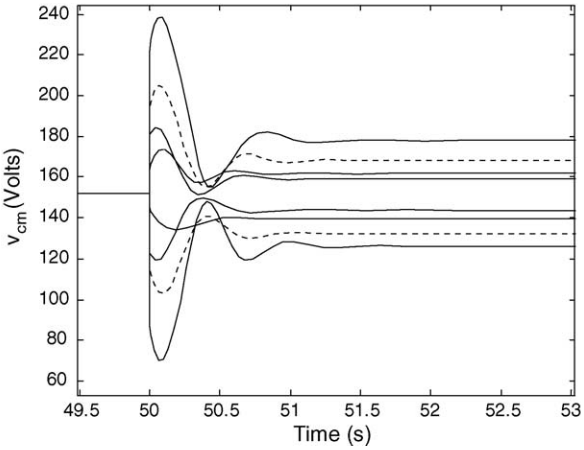

Fig. 12. v_{cm} response at OP5.

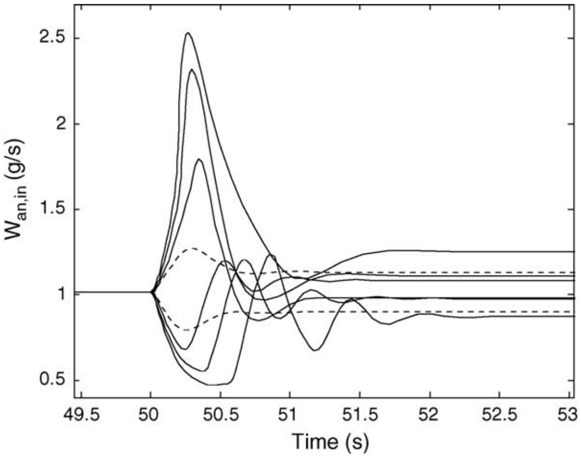

Fig. 13. $W_{\mathrm{an,in}}$ response at OP1.

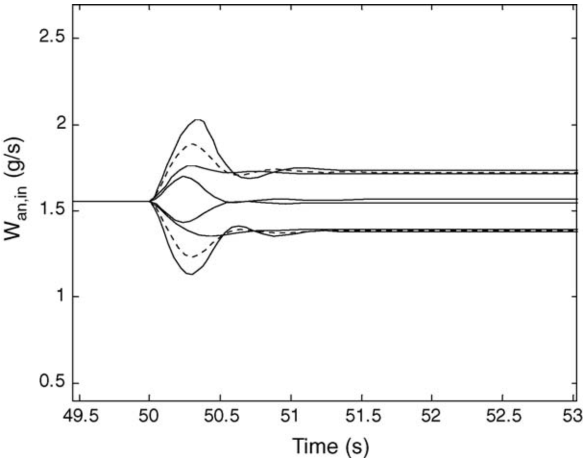

Fig. 14. $W_{\mathrm{an,in}}$ response at OP5.

9. Conclusions

Using three different controllability indexes (the MRI, the CN, and the RGA) to compare the controllability of a PEMFC at different operating points, it has been found that the higher the efficiency, the lower the controllability. Having done the comparative analysis at different net power levels, it can be said that the conclusion is valid in a wide operating range. Comparing operating points with the same current and net power but different stoichiometry and output voltage, the operating points with higher stoichiometry (higher output voltage) have the worst controllability. To continue the comparison, using some performance tools (the sensitivity functions S and T) results also indicate that it is easier to control the system when it is operated at the operating point with lower efficiency. Finally, some simulations done with a complete non-linear model show the same trend. Therefore, comparing the controllability and performance of a controlled PEMFC at different operating conditions, it has been found that there is a trade-off between controllability and efficiency within a wide operating region. The compressor has a key influence on the controllability and the efficiency of the system.

A diagonal control structure with PI controllers in the control loops is implemented and a tuning procedure has been proposed. For the analysed variables and within the scope of this work, it can be said that the performance of the proposed control system around OP5 is satisfactory.

Acknowledgments

This work has been funded partially by the projects CICYT DPI2002-03279 and CICYT DPI2004-06871-C02-01, of the Spanish Government.

References

[1] L. Carrette, K.A. Friedrich, U. Stimming, Fuel cells—fundamentals and applications, Fuel Cells 1 (2001) 1.
[2] W. Yang, B. Bates, N. Fletcher, R. Pow, Control challenges and methodologies in fuel cell vehicle development, in: International Congress of Transportation Electronics 98C054, 1998.
[3] J. Larminie, A. Dicks, Fuel Cell Systems Explained, John Wiley & Sons Ltd., 2003.
[4] J. Pukrushpan, A.G. Stefanopoulou, H. Peng, Control of fuel cell breathing, IEEE Control Systems Magazine (April) (2004).
[5] M. Grujicic, K. Chittajallu, J. Pukrushpan, Control of the transient behaviour of polymer electrolyte membrane fuel cell systems, Proc. Inst. Mech. Eng. Part D: J. Automobile Eng. 218 (2004).
[6] A. Vahidi, A. Stefanopoulou, H. Peng, Model predictive control for prevention starvation in a hybrid fuel cell system, in: Proceedings of the American Control Conference, vol. 1, 2004, pp. 834–839.
[7] J.T. Pukrushpan, H. Peng, A.G. Stefanopoulou, Control-oriented modeling and analysis for automotive fuel cell systems, Trans. ASME 126 (March) (2004).
[8] S. Yerramalla, A. Davari, Dynamic modelling and analysis of polymer electrolyte fuel cell, IEEE (2002).
[9] M. Serra, J. Aguado, X. Ansede, J. Riera, Controllability analysis of decentralised linear controllers for polymeric fuel cells, J. Power Sources 151 (2005) 93–102.
[10] K. Ogata, Modern Control Engineering, Prentice Hall, 2002.
[11] K. Astrom, T. Hagglund, PID Controllers: Theory, Design and Tuning, ISA, 1995.
[12] D. Rivera, S. Skogestad, M. Morari, Internal model control 4: PID controller design, Ind. Eng. Chem. Process Des. Dev. 25 (1986) 252–265.
[13] S. Skogestad, I. Postlethwaite, Multivariable Feedback Control, Analysis and Design, John Wiley & Sons, 1996.
[14] W. Luyben. Process Modeling, Simulation and Control for Chemical Engineers, 1990.

Available online at www.sciencedirect.com
ScienceDirect
Journal of Power Sources 169 (2007) 85–91
JOURNAL OF POWER SOURCES
www.elsevier.com/locate/jpowsour

Description of gasket failure in a 7 cell PEMFC stack☆

Attila Husar[a,*], Maria Serra[a], Cristian Kunusch[b]

[a] *Institut de Robòtica i Informàtica Industrial, Parc Tecnològic de Barcelona, Edifici U, C. Llorens i Artigas, 4-6, 2a Planta, 08028 Barcelona, Spain*
[b] *Laboratorio de Electrónica Industrial Control e Instrumentación, Facultad de Ingeniería, UNLP, Argentina*

Abstract

This article presents the data and the description of a fuel cell stack that failed due to gasket degradation. The fuel cell under study is a 7 cell stack. The unexpected change in several variables such as temperature, pressure and voltage indicated the possible failure of the stack. The stack was monitored over a 6 h period in which data was collected and consequently analyzed to conclude that the fuel cell stack failed due to a crossover leak on the anode inlet port located on the cathode side gasket of cell #2. This stack failure analysis revealed a series of indicators that could be used by a super visional controller in order to initiate a shutdown procedure.

Keywords: Polymer electrolyte membrane fuel cells; Stack failure; Gasket; Indicators

1. Introduction

Polymer electrolyte membrane fuel cell stacks fail generally due to: failure of the gasket, failure in the membrane, and/or failure of the catalyst. This article is going to examine both analytically and physically the failure of a gasket in a 7 cell stack.

The stack is an ElectroChem® 7 cell stack (Part #EFC-50-03-7-ST) with Nafion 115 MEA's, with a catalyst loading of 1 mg PT cm^{-2} and Toray carbon fiber paper as the gas diffusion layers (GDL). The gasket is a precision grade silicone material specially cut for the bipolar plate design and it should be able to maintain its integrity up to 220 °C [1].

The stack was being tested under a variety of pressures (1–4.5 bar_a), temperatures (25–60 °C), relative humidity (0–100%), and current (0–5 A). Both air and oxygen were used on the cathode and only pure hydrogen was used on the anode. The cell failed after approximately 20 h of operation. The test station that was used in these experiments was an ElectroChem® MTS-150 in combination with an HSA gas humidifier.

The stack design is based on a bipolar configuration where the cathode of one cell is electrically connected to the anode of the adjacent cell while the gas is connected in parallel through the bi-polar plates' flow fields. Fig. 1 shows a cross-sectional view of a generic bipolar configuration with the correct gas flows.

The main components of the stack are the membrane electrode assemblies (MEA), the catalyst in the center on the anode and cathode side of the membrane, the gaskets on the perimeter of the MEA with gas diffusion layers, and the graphite bipolar plates. The gasket generally has two sealing functions: overboard leak and crossover leak. An overboard leak is when the gas from either the anode or the cathode side escapes to the environment. A crossover leak is when the gas from one side of the membrane crosses over to the other side of the membrane. A crossover leak can occur in two ways: one is a leak between the gasket and the membrane in the inlet or outlet ports and the other is by passing through the membrane itself. There is an expected crossover leak rate of hydrogen and oxygen through the membrane due to diffusion through the membrane which can be estimated for any given stack based on the number of cells in the stack, active area, and type and thickness of the membrane assuming that the seals are perfect. This flow rate due to diffusion is measured in $cm^3\ s^{-1}$ and is also related to the partial pressure and temperature of the gas. However, the loss in voltage due to the hydrogen diffusion should only be seen at open circuit voltage because, as the current increases, the hydrogen partial pressure decreases on the anode side which reduces the driving force of the diffusion [2]. The oxygen crossover, on the other hand, should not be perceived in the open circuit voltage.

☆ This paper is presented at the 2nd National Congress on Fuels Cells, CONAPPICE 2006.

* Corresponding author at: Institut de Robòtica i Informàtica Industrial, Parc Tecnològic de Barcelona, Edifici U, C. Llorens i Artigas, 4-6, 2a Planta, 08028 Barcelona, Spain.

E-mail address: ahusar@iri.upc.edu (A. Husar).

0378-7753/$ – see front matter © 2007 Elsevier B.V. All rights reserved.
doi:10.1016/j.jpowsour.2007.01.078

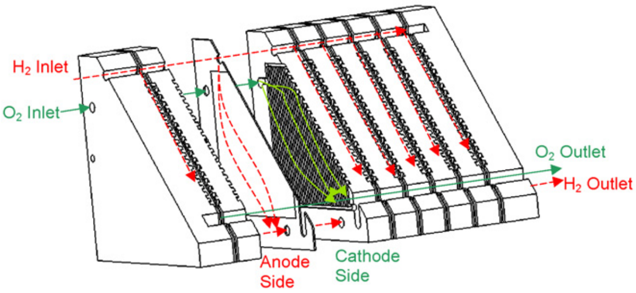

Fig. 1. A cross-sectional view of a typical parallel flow of the reactant gasses through a fuel cell stack.

The manufacturer recommended operating conditions for the stack are: H_2/O_2, 1.02 Stoichiometry for anode and cathode, 60 °C stack temperature, no humidification and a gas pressure of 4.50 bar_a (50 psi_g) for both the anode and cathode [3]. The data analyzed in this work were based on these conditions.

The stability of the stack over time with respect to individual cell voltage is shown in Fig. 2. As can be seen in this figure the stack was stable under these conditions. The variation in the cell voltage can be attributed to changes in the current due to impedance spectroscopy tests performed on the stack. Cell #7 of the stack had consistently showed a poor performance when compared to the other cells in the stack. However, this issue will not be analyzed in this work as it is unrelated to the ultimate failure of the stack.

As the testing went on, the cell voltages started to unexpectedly change and the pressure could not be maintained with the back pressure regulators. This marked the beginning of the end for this stack. The following section will describe the stack's final day of operation.

2. Gasket failure description

2.1. Analysis of data from the last day of operation

In the morning, an overboard leak check was performed on the stack using nitrogen on the anode and air on the cathode. A leak check was needed because on the previous run the pressure on the anode side could not be maintained. However, there were no other signs of failure. The procedure for the pressure decay leak check is as follows: a flow of nitrogen and air is applied to the stack, the system is pressurized to 4.5 bar_a, then the inlet and outlet to the stack are closed and the system left alone for a given amount of time. The pressure decay leak check is presented in Fig. 3. It was done in three sections. The first section of the test was done with anode and cathode pressures maintained at the same value (4.5 bar_a). The second part of the test was done with the cathode pressure left at 4.5 bar_a and the anode pressure reduced to 4.2 bar_a. The final part of the test was carried out in reverse order, the anode pressure was increased back up to 4.5 bar_a and the cathode pressure was reduced to 4.2 bar_a. The slope of each section of the test is indicated on the graph. Fig. 3 shows a positive slope of the lower pressure side of the membrane indicating that gas from the higher pressure side of the membrane is crossing over to the low pressure side. The exact rate is unknown because a true crossover leak check was not performed on this stack due to the lack of equipment. No com-

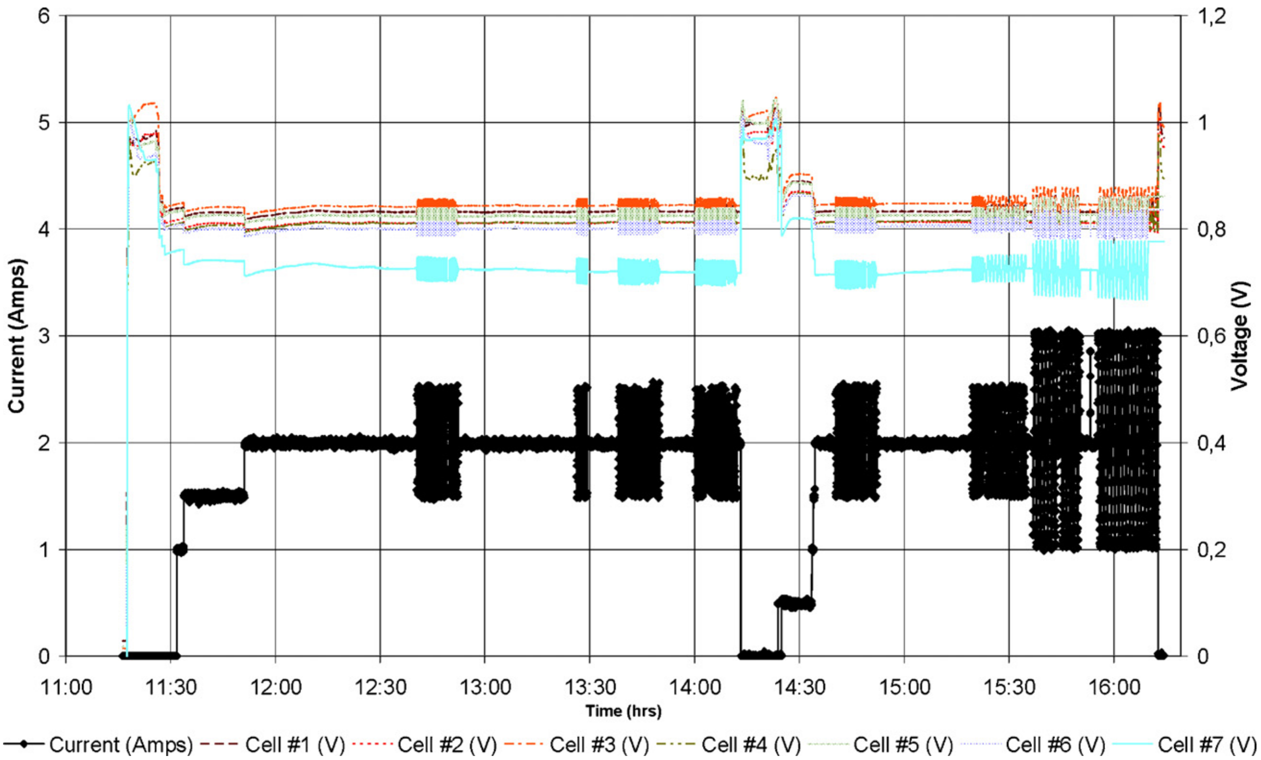

Fig. 2. Normal voltage current response of the 7 cell stack a few days before failing, H_2/O_2, 1.02 Stoichiometry for anode and cathode, 60 °C stack temperature, no humidification and a gas pressure of 4.50 bar_a (50 psi_g) for both the anode and cathode.

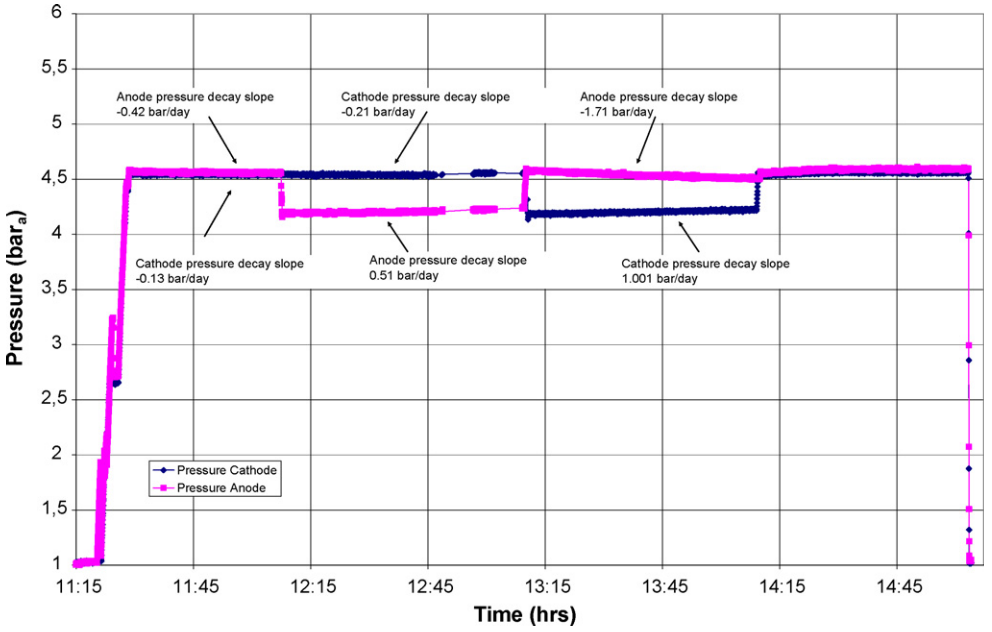

Fig. 3. Pressure decay leak check of stack at ambient temperature with air on the cathode and nitrogen on the anode.

bustion occurred during the leak test since nitrogen was being used on the anode.

After performing the pressure decay leak check it was decided to continue running the stack because the test did not show any overboard leaks and the crossover leak had not been identified nor quantified yet.

The stack temperature was the indicator that led to the final shutdown of the stack. The stack was being operated with oxygen and hydrogen and no humidification. The stack temperature reached 90 °C without current or resistance heaters enabled. The hot point in the stack was in the middle cells, which read a temperature of 91 °C. The pressure in the stack could not be maintained. Both of these symptoms indicated the presence of a crossover leak and combustion. So the stack was purged with nitrogen, and declared inoperable.

The data for these final hours with respect to pressure and temperature is shown in Fig. 4, which shows spikes in temperature as the pressures decayed. The cell temperature measurements were taken at eight different points throughout the stack located in the bipolar plates in between each cell. For simplicity purposes they were called measurements 1–8, where measurement 1 is located between the end plate and cell #1, where cell #1 is the first cell the gasses encounter when they enter the stack.

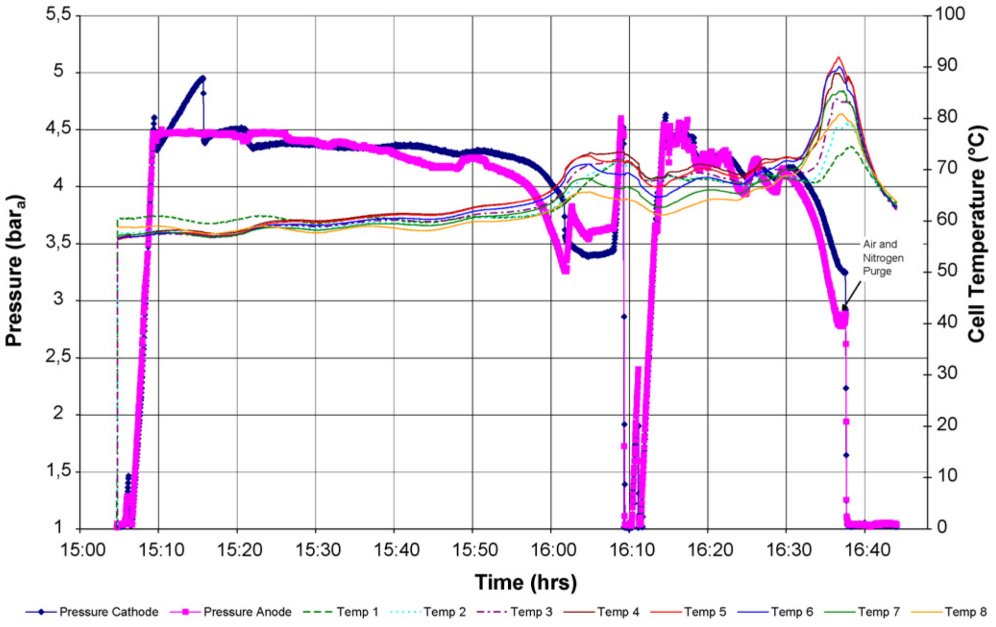

Fig. 4. Pressure of the reactant gasses vs. cell temperature during the last hours of operation. H_2/O_2, no humidification.

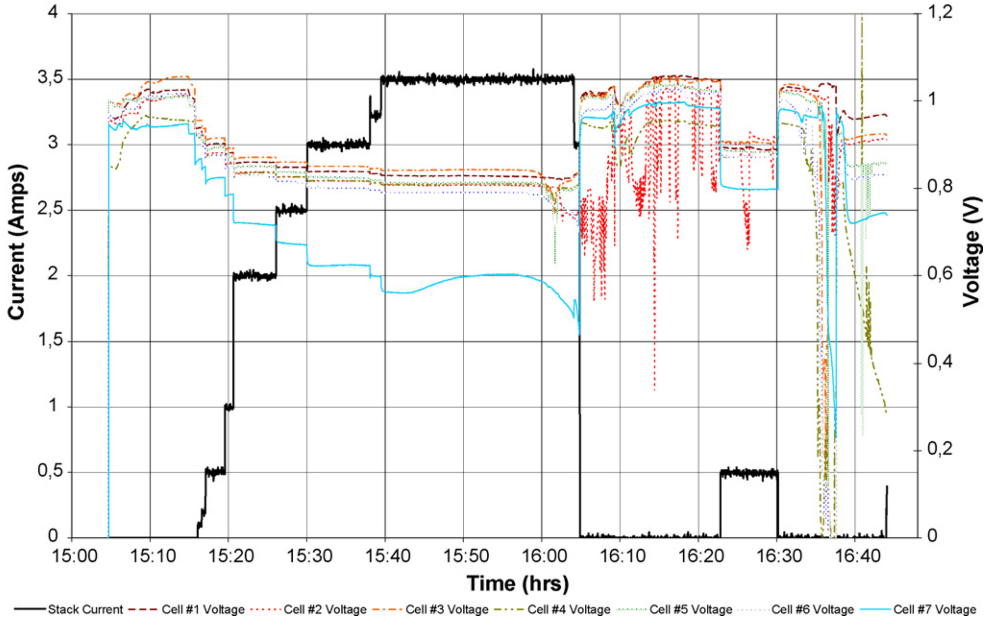

Fig. 5. Stack current vs. individual cell voltage during the last hours of operation, H_2/O_2, no humidification and a gas pressure.

In an attempt to stabilize the pressure the anode and cathode gas flows were increased. However, this attempt did not work and the pressures continued to fall.

Fig. 5 depicts the stack current versus the individual cell voltages. It shows how, after the current was reduced to 0 at around 16:05, the open circuit voltages became very unstable especially that of cell #2.

In Fig. 6 the time between 15:50 and 16:10 is examined with respect to pressure and cell temperature. When the load was removed from the stack at 16:05 the temperature measurements 4–8 started to decline, as was expected. However, the temperature measurements 1–3 continued to increase. This temperature rise showed signs of a breach possibly in cell #1 and/or #2.

Fig. 7 explains how a breach in one cell affects the flow of the reactant gases when the pressure of the anode is higher than the cathode. Hydrogen enters directly into the breached cell and combusts in the catalyst layer, therefore increasing the temperature for just that one cell.

At 16:09 there was a temporary shut down of the stack where the pressure was reduced to 1 bar_a.

In Fig. 8 the time between 16:30 and 16:45 is examined with respect to anode and cathode pressure and temperature. Initially both pressures were equalized. However, the anode pressure started to decline more rapidly than the cathode because hydrogen was being consumed at twice the rate of oxygen due to combustion which, in turn, caused more oxygen to be forced

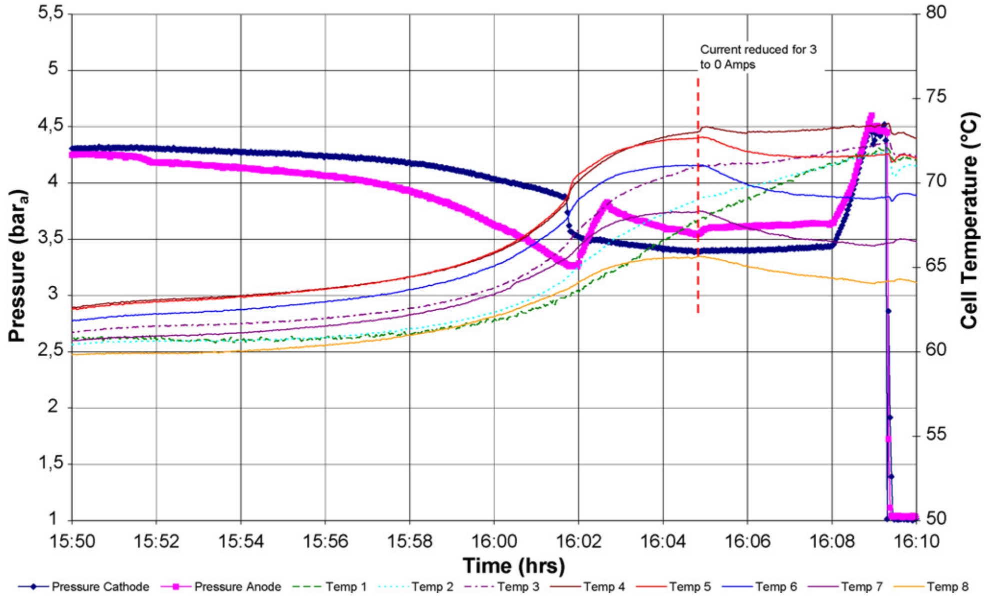

Fig. 6. Zoom of Fig. 4 between 15:50 and 16:10. Increase in temperature in cells #1 and #2 with no electric load or external heaters on the stack and an anode reactant pressure higher than the cathode pressure when the load was removed.

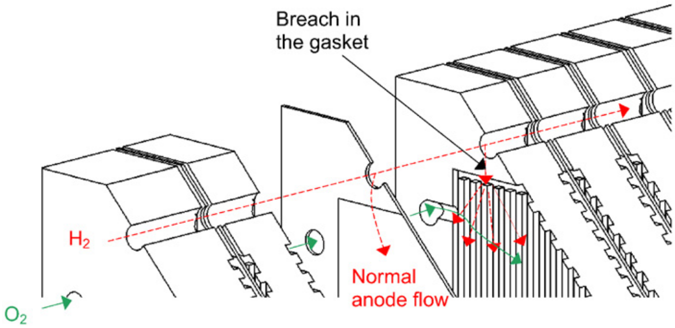

Fig. 7. Flow of the reactant gases when there is a breach in the seal at the anode inlet port that goes into the cathode flow field. Anode pressure is higher than the cathode's.

into the anode inlet port thus, increasing the rate of combustion in the cells located after the breach. Once the nitrogen purge was initiated on the anode and the air purge on the cathode the pressures began to stable out and the cell temperatures decreased. Shortly after, the pressure was reduced to atmospheric and the stack was declared inoperable.

Since the breach is reversible it should permit the oxygen to enter into the anode inlet port if the cathode pressure was higher than that of the anode as shown in Fig. 9. Therefore, the oxygen breach should only affect the subsequent cells.

Cell #2 in Fig. 10 showed a unique behavior when the anode pressure was higher than the cathode pressure. The cell lost about 20 mV and became unstable. Then, when the anode pressure was decreased to be lower than the cathode's the cell stabilized. This indicated the presence of a hydrogen crossover in cell #2.

Since the stack was declared inoperable it was disassembled to be physically examined.

Upon opening the stack it was clear that it was cell #2's cathode side gasket that had failed. Fig. 11 shows the cathode gasket and GDL for cell #2 while still attached to the bipolar plate. The interface between the gasket and the GDL is a white color indicating degradation.

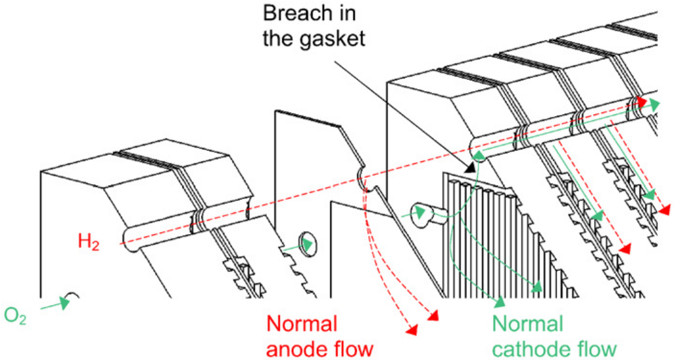

Fig. 9. Flow of the reactant gases when there is a breach in the seal at the anode inlet port. Oxygen is entering into the anode inlet port. Cathode pressure is higher than the anode's.

Interestingly, this was the only cell that had water droplets on the gas diffusion layer and a few of the droplets were brown in color which is a sign of contamination possibly from combustion on the cathode side.

Fig. 12 illustrates what a good cell with no degradation of the gasket looked like.

When the gasket and MEA were peeled off of the anode side of the bi-polar plate it revealed that there was severe degradation of the gasket material around the anode inlet port towards the GDL as shown in Fig. 13. There was also some degradation around the cathode inlet. This degradation occurred on the cathode gasket.

Finally, when the gasket was totally detached from the membrane it was discovered that a piece of the gasket material was fused to the membrane at the anode inlet port as seen in Fig. 14.

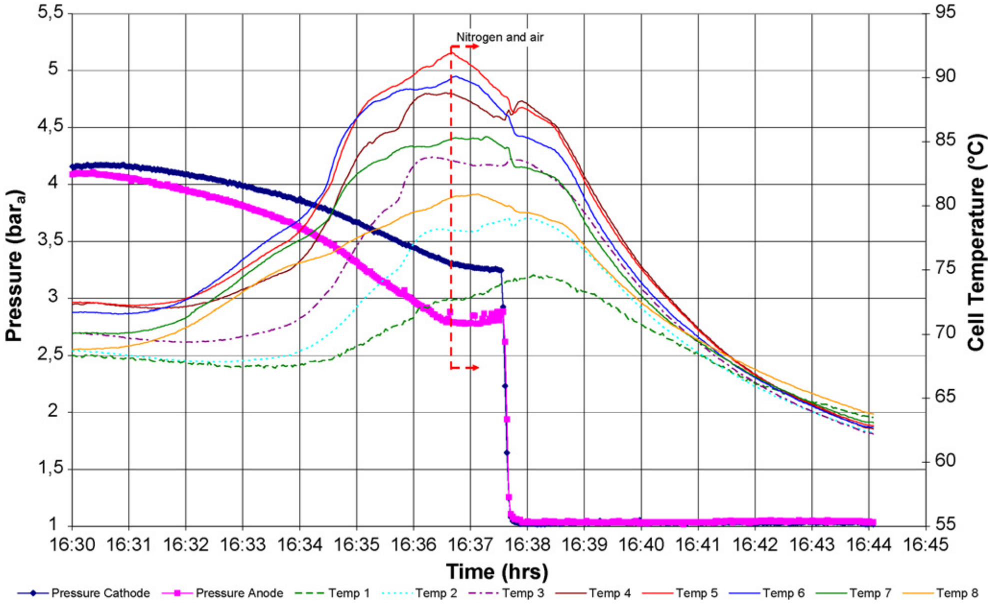

Fig. 8. Zoom of Fig. 4 between 16:30 and 16:45. Cathode pressure is higher than the anode's and the hot spots in the stack are from cell #3 to #6 indicating that the oxygen was entering into the hydrogen stream through the inlet port.

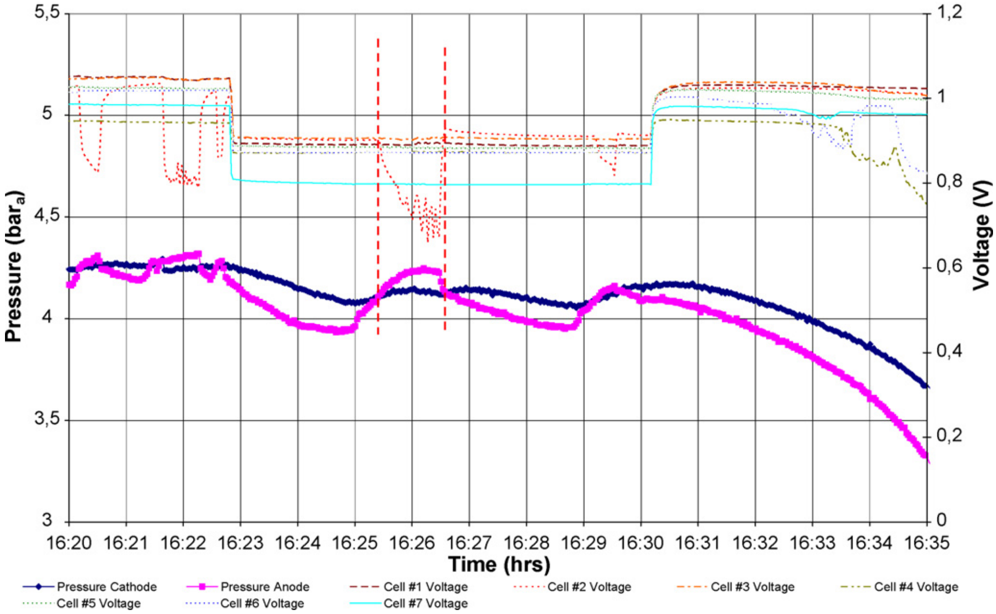

Fig. 10. Temporary instability of cell #2 when the anode pressure is higher than the cathode's. Hydrogen enters directly into the cathode flow field of the cell.

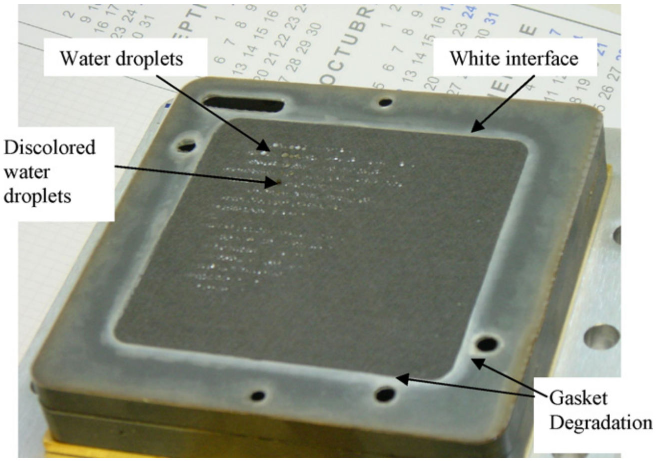

Fig. 11. Cathode GDL and gasket of cell #2 before it was removed from the bi-polar plate.

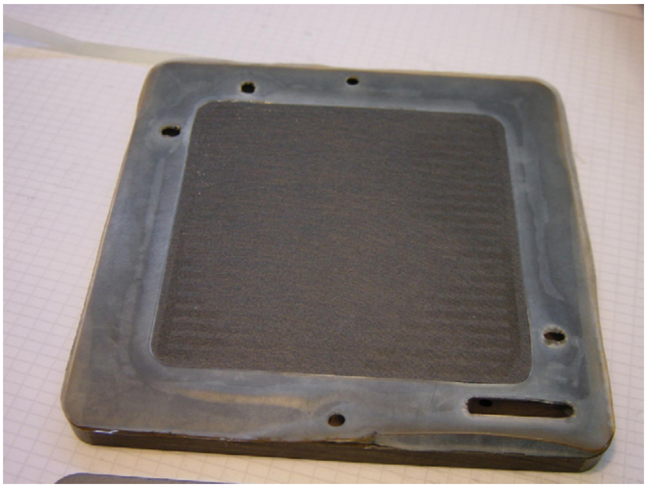

Fig. 12. Cell #5 gasket and diffusion layer which showed no degradation.

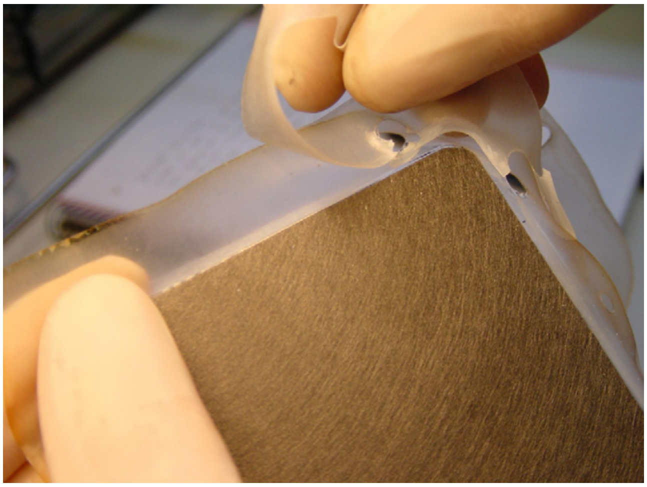

Fig. 13. Cell #2 cathode gasket degradation.

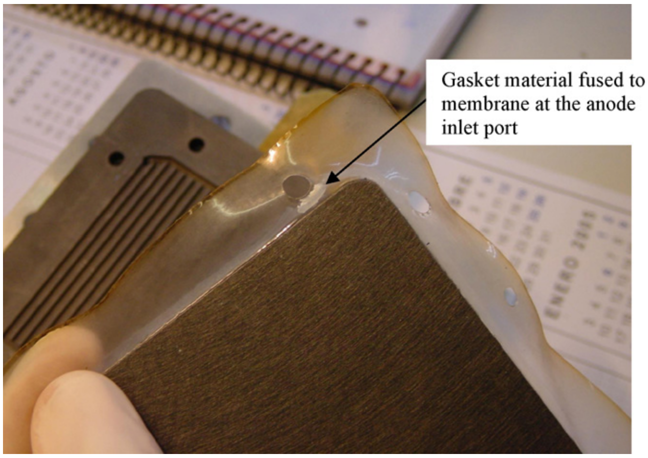

Fig. 14. Gasket material left on the membrane at the anode inlet port and on the cathode side of the membrane.

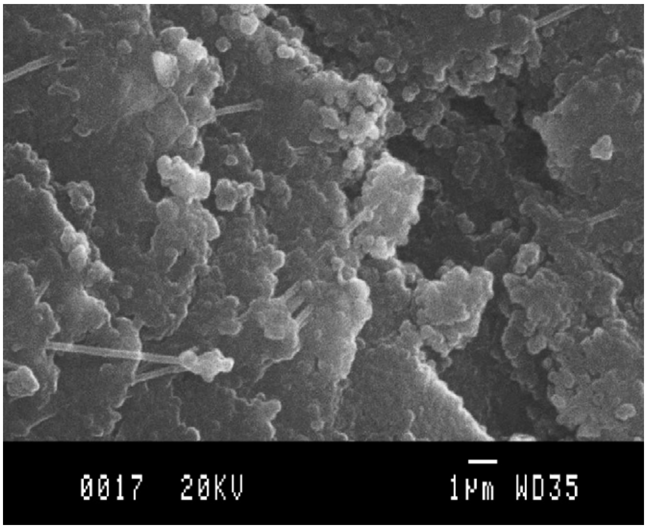

Fig. 15. Silicon gasket material that was exposed to the combustion from cell #2.

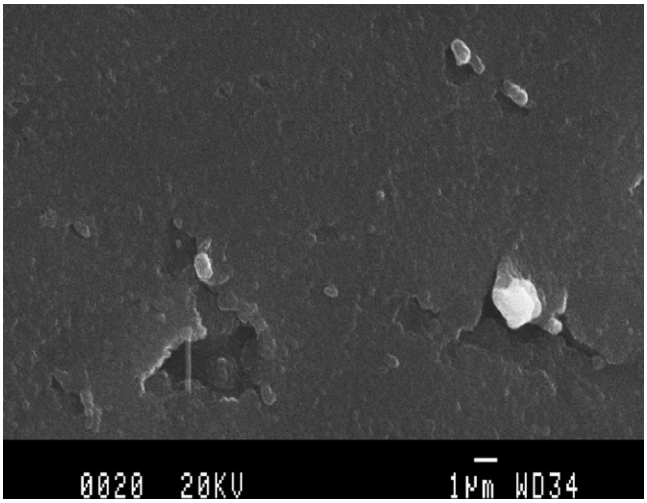

Fig. 16. Silicon gasket material that was not exposed to the combustion from cell #4.

This could be explained by the high temperature reached due to combustion that caused the gasket material to disintegrate and fuse to the membrane.

Cell #1 gasket also showed signs of degradation but not as severe as cell #2. The degradation can be noted by the discoloration of the gasket material around the edges of the GDL.

Figs. 15 and 16 show images of the silicon gasket material taken with the scanning electron microscope. In Fig. 15 shows the silicon gasket material from cell #2 that was exposed to combustion and Fig. 16 shows what the same material looks like under regular conditions.

The MEAs from cells #2 and #4 were also examined. An X-ray Energy Dispersing Spectroscopy was performed on both MEA samples which indicated the presence of both platinum and silicon. The presence of platinum was expected because it is used as a catalyst. However, the silicon indicated a possible contamination of the MEA.

3. Conclusion

The 7 cell stack failed due to a crossover leak on the cathode side gasket of cell #2. The main indicators of the failure were: an unexplainable rise in the stack temperature, pressures that could not be maintained, and the change in cell #2 voltage relative to anode and cathode pressure. The gasket failure occurred gradually over time which might have been started by loosening of the stack due to thermal cycling. Once started, the leak degraded the gasket further by exposing the gasket to the high temperature of combustion of hydrogen and pure oxygen. The combustion was initiated by the platinum catalyst on the membrane. Finally, the leak was so large that enough oxygen was able to crossover to the anode side causing the stack to heat up significantly.

Acknowledgment

This work has been partially funded by project CICYT DPI2004-06871-C02-01, from the Spanish MEC.

References

[1] Silicone. http://www.stockwell.com/newstuff/newpdfs/500_solid_silicone/510_cohr_9275_high_perf_clear_silicone.pdf.

[2] F. Barbir, PEM Fuel Cells Theory and Practice, Elsevier Academic Press, USA, 2005.

[3] Electro Chem Inc. website: http://www.fuelcell.com/pdfs/FuelCellStack.pdf (accessed May 2006).

Available at www.sciencedirect.com

ScienceDirect

journal homepage: www.elsevier.com/locate/he

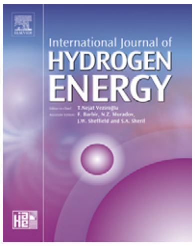

Linear identification and model adjustment of a PEM fuel cell stack

C. Kunusch[a,c,*], A. Husar[b], P.F. Puleston[a,c], M.A. Mayosky[a,d], J.J. Moré[a,c]

[a]LEICI, Departamento de Electrotecnia, Universidad Nacional de La Plata, calle 1 esq. 47 s/n, 1900 La Plata, Argentina
[b]Institut de Robòtica i Informàtica Industrial (CSIC-UPC), c/ Llorens i Artigas 4-6, 08028 Barcelona, España
[c]Consejo de Investigaciones Científicas y Técnicas (CONICET), Argentina
[d]Comisión de Investigaciones Científicas (CIC), Provincia de Buenos Aires, Argentina

ARTICLE INFO

Article history:
Received 21 December 2007
Received in revised form
23 April 2008
Accepted 28 April 2008
Available online 17 June 2008

Keywords:
PEMFC
Spectroscopy
Identification
MIMO linear model
Experimental tests

ABSTRACT

In the context of fuel cell stack control a mayor challenge is modeling the interdependence of various complex subsystem dynamics. In many cases, the states interaction is usually modeled through several look-up tables, decision blocks and piecewise continuous functions. Many internal variables are inaccessible for measurement and cannot be used in control algorithms.

To make significant contributions in this area, it is necessary to develop reliable models for control and design purposes. In this paper, a linear model based on experimental identification of a 7-cell stack was developed.

The procedure followed to obtain a linear model of the system consisted in performing spectroscopy tests of four different single-input single-output subsystems. The considered inputs for the tests were the stack current and the cathode oxygen flow rate, while the measured outputs were the stack voltage and the cathode total pressure. The resulting model can be used either for model-based control design or for on-line analysis and errors detection.

1. Introduction

Fuel cells (FC) are devices that convert hydrogen and oxygen electro-chemically into electrical energy and can be used in a wide variety of applications, from mobile and stationary power systems to portable appliances. The FC principles of operation were discovered in 1839, but only during the past two decades has the research activity in this field increased dramatically, which has improved FC flexibility, reliability and cost [1]. One of the most influential factors that motivated FC development is the environmental impact of fossil fuels. Considering that hydrogen production from water can be performed using renewable energy such as solar, wind or geothermal, polymer electrolyte membrane fuel cells (PEMFCs) are emerging as one of the most promising alternatives to reduce fossil fuel dependency [1].

Improvements in this field require interdisciplinary work and development of new technologies in many areas. One of the most important issues is related to the development of robust control strategies dealing with disturbances and model uncertainties in a systematic way. For instance, to avoid transient power deterioration and irreversible damage to the FC, an effective control algorithm for oxidant stoichiometry regulation inside the cells during variable load tracking is required [2].

---

*Corresponding author at: LEICI, Departamento de Electrotecnia, Universidad Nacional de La Plata, calle 1 esq. 47 s/n, 1900 La Plata, Argentina. Tel./fax: +54 221 4259306.
E-mail addresses: ckunusch@ing.unlp.edu.ar (C. Kunusch), ahusar@iri.upc.edu (A. Husar).

0360-3199/$ - see front matter © 2008 International Association for Hydrogen Energy. Published by Elsevier Ltd. All rights reserved.
doi:10.1016/j.ijhydene.2008.04.052

However, from the control point of view FC stacks represent a major challenge due to their associated subsystems that reveal complex dynamics and conflicting control objectives. For example, in the cathode subsystem dynamics of a hydrogen–oxygen fed stack the states interaction is usually described through several look-up tables and decision blocks. Many internal variables are inaccessible and therefore cannot be measured, thus cannot be used in control algorithms [3]. Besides, there are measurable and non-measurable disturbances that affect the system operation, as well as uncertainties in the model parameters [4].

Therefore, to make significant contributions in this area, it is necessary to develop reliable models for control and design purposes. Thus, a dynamic linear model of a 7-cell stack experimentally obtained is presented.

2. Materials and methods

2.1. FC stack and test station

The FC stack utilized is the EFC50-ST, which is a laboratory PEM FC stack designed for the fundamental study of membrane electrode assembly (MEA) and FC operation. This unit generates 50 W of power under normal operating conditions and can provide up to 100 W peak power [5].

The stack is an ElectroChem® 7-cell stack with Nafion 115 MEA's, with a catalyst loading of 1 mg/cm^2 of platinum and Toray carbon fiber papers as gas diffusion layers, 50 cm^2 of active area, eight graphite plates, fittings, gold plated copper current collectors and individual cell voltage and temperature measurement points (Fig. 1).

The power output of a single FC is limited. Therefore, in order to raise the amount of power coming from the FC, multiple cells are needed. FC stacks are multiple cells connected electrically in series, however, the gas flows are connected in parallel.

The EFC50ST can be operated at utilization levels for pure H_2 and O_2 close to 98%. The nominal recommended pressure by ElectroChem® for hydrogen and oxygen gases is 3.44 bar.

The test station (Fig. 2) is constituted by two humidifiers and two heated gas transfer lines. The temperatures are controlled by a power station via decentralized PID controllers, allowing for independent gas conditions to the stack.

The gases flow rates are controlled by Bronkhorst® EL-FLOW® controllers with an operating range of 0.03–1.5 SLPM. In addition, the different pressures are measured by piezo-resistive transmitters that have been designed for precision applications in industrial environments for pressures ranging from 0.2 to 6 bar. Finally, the AC-impedance measurements were performed by making use of the electronic load TDI RLB488 Dynaload®, in conjunction with the HP-35760A spectrum analyzer.

2.2. Operation range

The first step to perform a dynamic linear model of the FC system is to set the operating range. To this end, the stack temperature was set to 60 °C and the humidifiers temperatures were fixed at 50 °C, so the relative humidity inside the cells was 65%. The corresponding line heaters for the anode and cathode sides were both set to 60 °C. The anode and cathode nominal pressure was set to the recommended value of 3.44 bar, while the average current was 5 A. Finally, the hydrogen average flow rate was 1.5 SLPM and the oxygen average flow rate was 0.5 SLPM, thus the resulting stoichiometries of the stack were $\lambda_{an} = 5.63$ and $\lambda_{ca} = 3.77$.

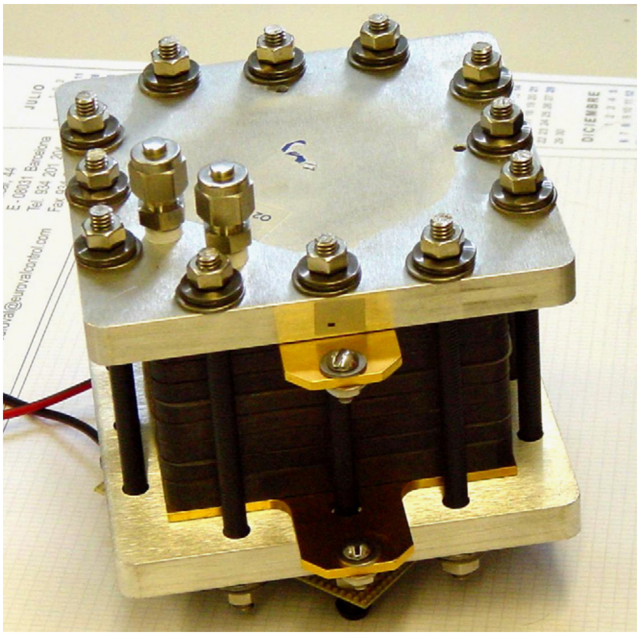

Fig. 1 – ElectroChem 7 MEA's stack (EFC50-ST).

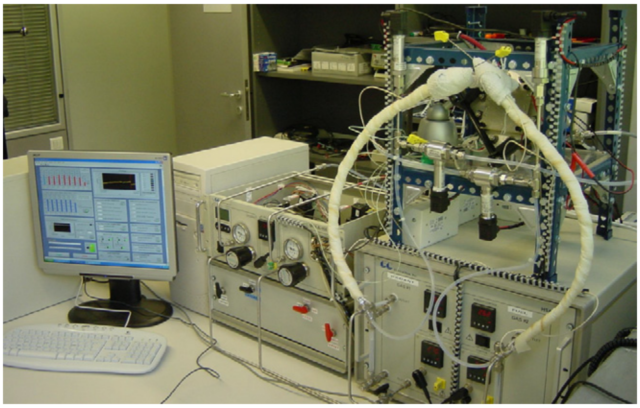

Fig. 2 – Fuel cell test bench at IRI (UPC).

2.3. Spectroscopy tests

The procedure followed to obtain a linear model of the system consisted of performing spectroscopy tests of four different single-input single-output subsystems. A spectroscopy test is based on exciting a dynamic system through sinusoidal signals of different frequencies. Then, after processing the resulting output data, a frequency diagram of the system response (Bode, Nyquist, Nichols, etc.) can be generated. Afterwards, different linear systems can be fitted to the data in order to develop a complete representative model. This well-known frequency-based tests are rather useful to develop accurate linear models off-line [6,7].

In this paper, four different identification tests were performed. The inputs were the stack current (I_{st} (A)) and the cathode flow rate (w_{ca} (SLPM)), while the measured outputs were the stack voltage (V_{st} (V)) and the cathode inlet pressure (p_{ca} (bar)).

The following subsections describe the technical specifications of the tests, as well as the corresponding results.

2.3.1. Test 1: $V_{st}(s)/I_{st}(s)$ submodel

Performing impedance measurements on FC can assist in identifying problems within the FC components, as well as track troubles in the FC assembly process. More specifically, such measurements can be helpful in identifying the kinetic and ohmic resistances of the FC stack, the electrolytic and the transport limitations of the reactants.

By imposing a sinusoidal perturbation in the stack current and measuring both the perturbed current and the voltage response, the AC impedance can be calculated. Repeating this procedure at different frequencies, an electrochemical impedance spectroscopy can be obtained. This test has been performed in the stack considering a frequency range from 100 mHz to 1 kHz, a mean stack current of 5 and 1 A amplitude, with a constant cathode flow rate of 0.5 SLPM.

The relationship between the stack current and the stack voltage is modeled through a transfer function, which is depicted by a Bode diagram in Fig. 3.

After obtaining the data, a parametric identification was conducted in order to fit the results to several linear time invariant (LTI) systems, as shown in Fig. 3. Some approximations and order reductions were made taking into account the existing tradeoff between model complexity and its accuracy to the real data. The best approximations were obtained fitting the raw data to parametric output error (OE) models through the least squares method. Among them, the most accurate model found for the V_{st}/I_{st} subsystem was

$$G_{11}(s) = V_{st}(s)/I_{st}(s) = \frac{-0.29971(s+189)}{(s+62.71)} \tag{1}$$

2.3.2. Test 2: $V_{st}(s)/w_{ca}(s)$ submodel

Another subsystem modeled was the dynamics between the cathode flow rate of oxygen and the resulting stack voltage generated at a given current. In this case, for the spectroscopy test, an oxygen flow rate sinusoidal perturbation was introduced to the system, while the stack current was set constant, at 5 A. The cathode flow rate frequency range was 10 mHz to 10 Hz, and using a mean value of 0.5 SLPM and an amplitude of 0.815 SLPM.

Several LTI models where fitted to the experimental data and the results are plotted in the Bode diagram in Fig. 4.

Finally, the most accurate model obtained to fit the subsystem was

$$G_{12}(s) = V_{st}(s)/w_{ca}(s) = \frac{0.023957}{(s+12.96)(s+0.1683)} \tag{2}$$

It is important to note that after the analysis it was found that the practical range of application where Eq. (2) accurately describes the $V_{st}(s)/w_{ca}(s)$ submodel is from 0 to 1 rad/s.

2.3.3. Test 3: $p_{ca}(s)/I_{st}(s)$ submodel

Another significant output to analyze is the inlet pressure of the cathode. The analysis of the p_{ca} behavior is a very important issue when a turbo compressor is connected to

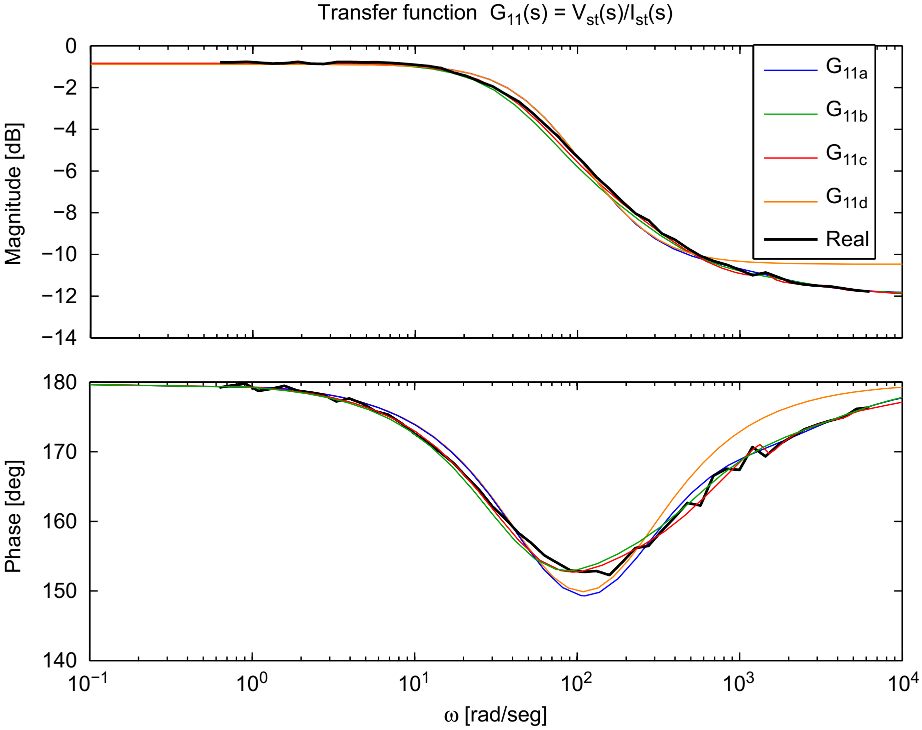

Fig. 3 – Different identification models of $G_{11}(s) = V_{st}(s)/I_{st}(s)$.

feed the stack, because it directly affects the voltage of the FC due the change in oxygen concentration.

A stack current sinusoidal perturbation was added to identify this subsystem dynamics in the settled operating range. The sinusoidal signal had a mean value of 5 A and an amplitude of 1 A, and its frequency ranged from 10 mHz to 10 Hz. The cathode flow rate was set constant at 0.5 SLPM.

In this particular stack, because of its open flow field design and the high inlet pressure, the pressure variation as a result of current change was rather small. Therefore, the signal to noise ratio of p_{ca} measure was poor, turning this test difficult to be conducted. However, some acceptable data was recorded and some representative models were obtained (Fig. 5). Among them, the most simple and accurate was the

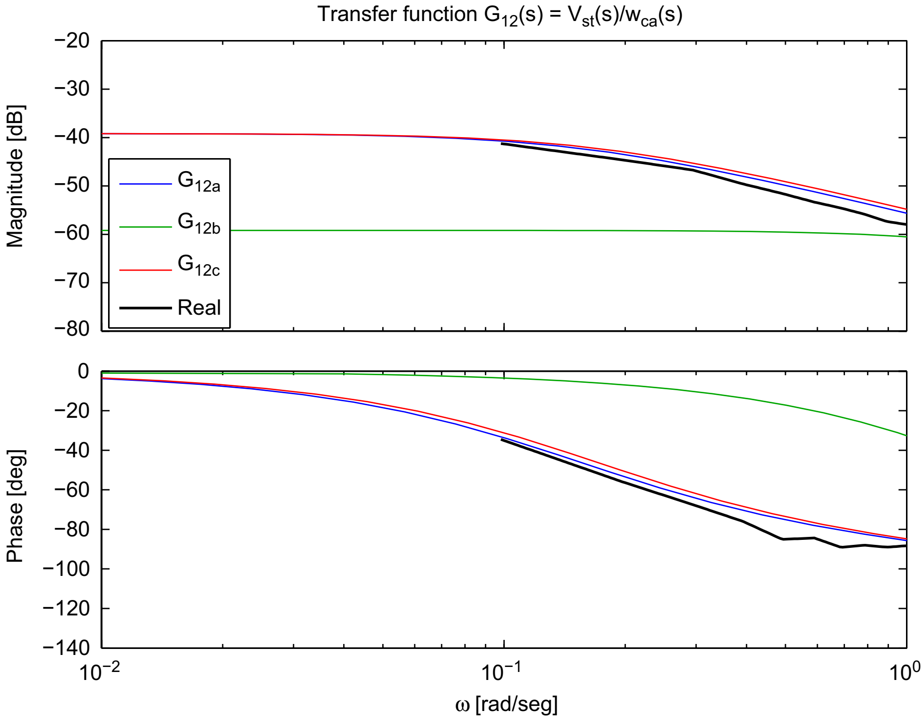

Fig. 4 – Different identification models of $G_{12}(s) = V_{st}(s)/w_{ca}(s)$.

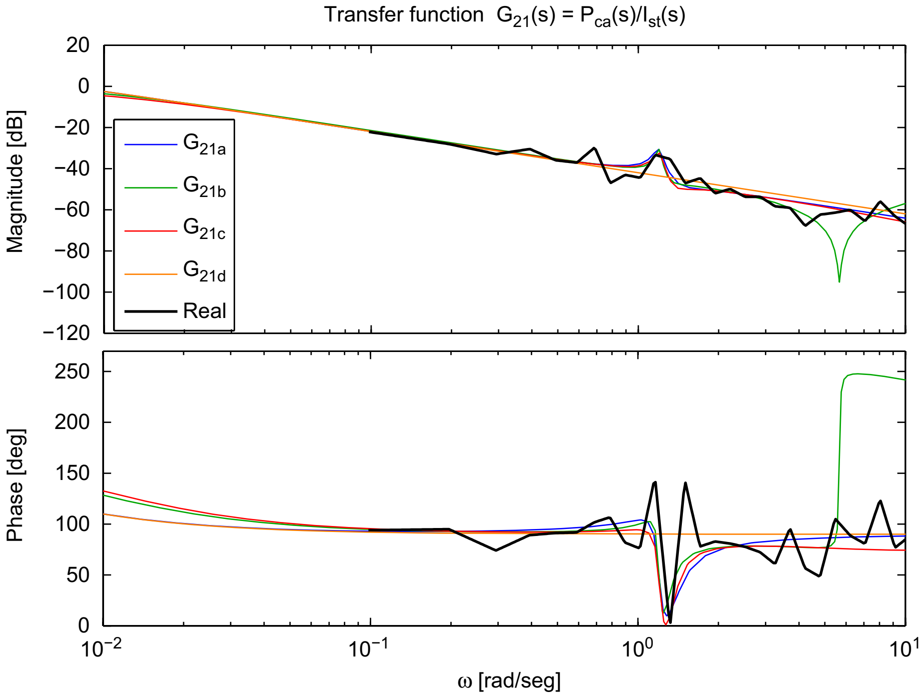

Fig. 5 – Different identification models of $G_{21}(s) = p_{ca}(s)/I_{st}(s)$.

following:

$$G_{21}(s) = p_{ca}(s)/I_{st}(s) = \frac{-0.0079596}{(s+0.003619)} \tag{3}$$

Note that in other stacks the pressure drop due to currents changes could be more significant. Thus, the signal to noise ratio would be higher and this procedure can retrieve more accurate results.

2.3.4. *Test 4: $p_{ca}(s)/w_{ca}(s)$ submodel*

Finally, the last subsystem to be identified is the corresponding flow-pressure cathode dynamics. The raw data of this model was also obtained via a spectroscopy test and then fitted to a suitable LTI model. The stack current was set constant at 5 A and the considered frequency range of the cathode flow rate sinusoidal perturbation was 10 mHz to 10 Hz, with a mean value of 0.5 SLPM and amplitude of 0.815 SLPM (see the results for different fits in Fig. 6).

The most accurate model found for this subsystem was

$$G_{22}(s) = p_{ca}(s)/w_{ca}(s) = \frac{0.041573}{(s+3.408)(s+0.1683)} \tag{4}$$

Similarly to the transfer function in Eq. (2), the experiments showed that the valid range of Eq. (4) is 0–1 rad/s.

3. Spectroscopy results

3.1. *Final model*

Gathering the results from Section 2.3, a representative multi-input multi-output (MIMO) model of the system was obtained (Fig. 7). The resulting linear model can be expressed as follows through four coupled single-input single output (SISO) systems that relate the different channels.

Furthermore, its minimal state-space realization can be denoted by the following expression:

$$\begin{aligned} \dot{x} &= Ax + Bu \\ y &= Cx + Du \end{aligned} \tag{5}$$

$$A = \begin{bmatrix} -0.003619 & 0 & 0 & 0 & 0 \\ 0 & -12.956 & 5.8495 & 0 & 7.7055 \\ 0 & 0 & -39.847 & 0 & 30.121 \\ 0 & 0 & 7.7055 & -3.408 & 10.151 \\ 0 & 0 & 30.121 & 0 & -23.034 \end{bmatrix}$$

$$B = \begin{bmatrix} 0.089216 & 0 \\ 0 & 0 \\ 4.8996 & 0.038696 \\ 0 & 0 \\ -3.7194 & 0.050974 \end{bmatrix}$$

$$C = \begin{bmatrix} 0 & 0.038696 & -4.8996 & 0 & 3.7194 \\ -0.089216 & 0 & 0 & 0.050974 & 0 \end{bmatrix}$$

$$D = 9\begin{bmatrix} -0.29971 & 0 \\ 0 & 0 \end{bmatrix}$$

Note that the proposed model can be used for control design, engineering analysis and prediction purposes.

4. Simulations

In the effort to fit detailed experimental results into a comprehensive model of the FC stack, the following proposed computer model was used to run the simulations (see Fig. 8).

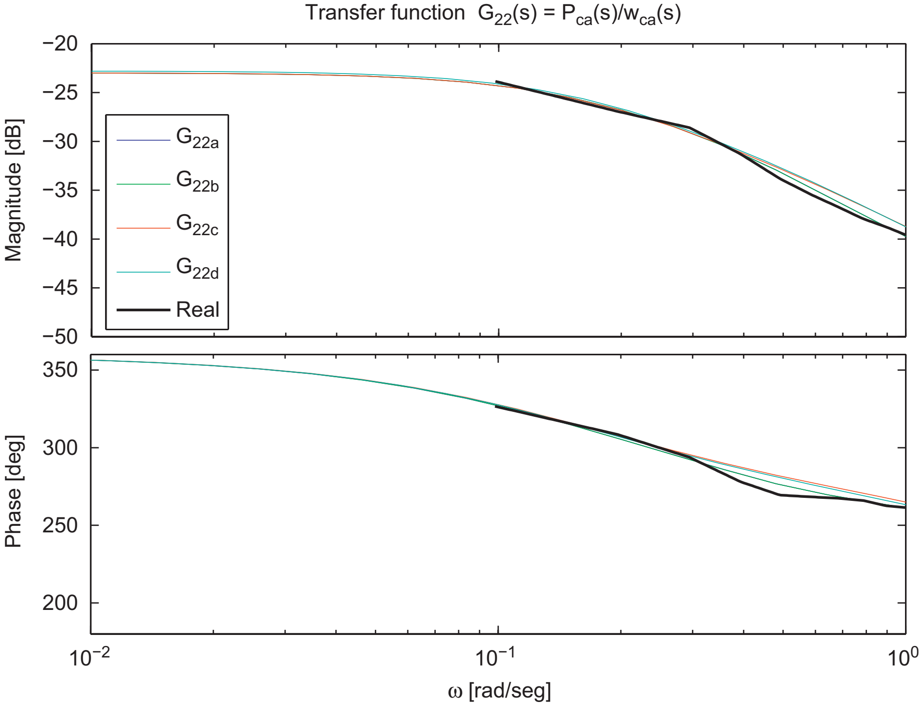

Fig. 6 – Different identification models of $G_{22}(s) = p_{ca}(s)/w_{ca}(s)$.

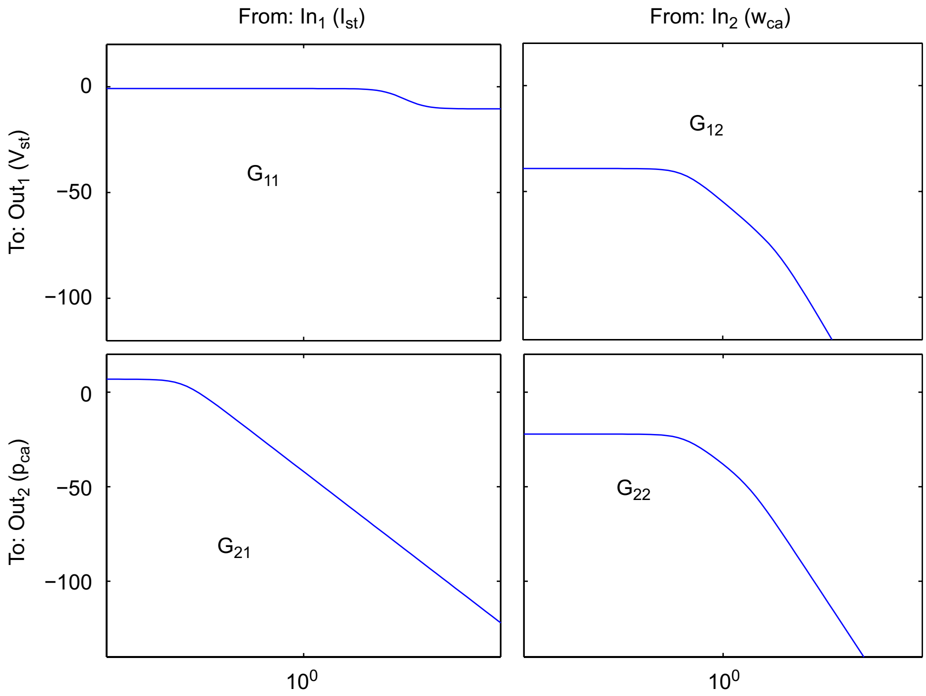

Fig. 7 – Input–output Bode diagrams.

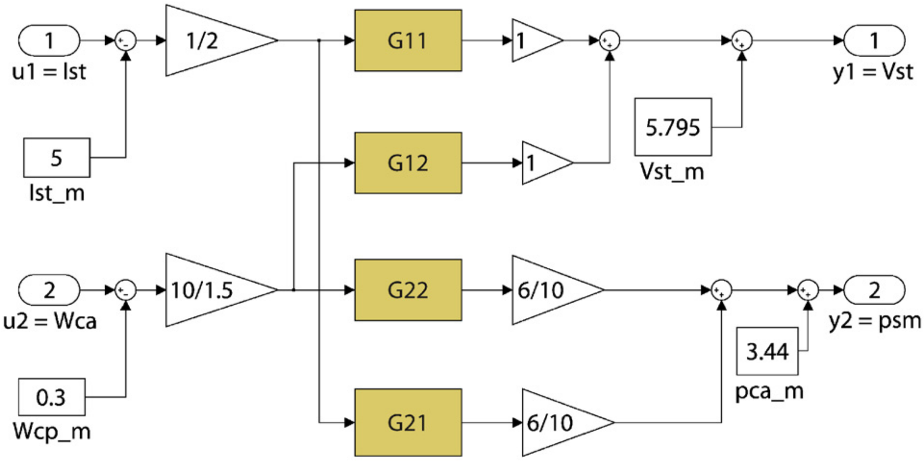

Fig. 8 – Simulink model of the stack.

Note that the models of Section 2.3 correspond to differential LTI systems at the specified operation point, so the mean value of each input and output must be included in the simulation model. In addition, the models in Section 2.3 were directly obtained from the raw data, therefore the sensors gains values have to be also added to make the simulations physically representative.

The resulting model shows the typical dynamic behavior of 7-cell stack working in the given operating point. Thus, it can be used for control design purposes as well as for analytical studies and for parameters identification.

Finally, Fig. 9 shows the changes in stack voltage and the cathode pressure when the two different inputs, namely the stack current (I_{st}) and the cathode air flow rate (w_{ca}) are excited. In addition, it shows the sensibility of the system when additive disturbances are present in the inputs (300–600 s).

5. Conclusions

A fuel cell system is complex and all phenomena involved in the process are difficult to be described. However, under certain assumptions based on the FC operation, a MIMO linear model based on experimental spectroscopy tests considering was developed in this paper. The proposed model represents the dynamic behavior of a hydrogen–oxygen PEM 7-cell stack, when humidity and temperature are kept controlled.

The simulations exhibit the dynamics in the neighborhood of the operation point when additive disturbances are added

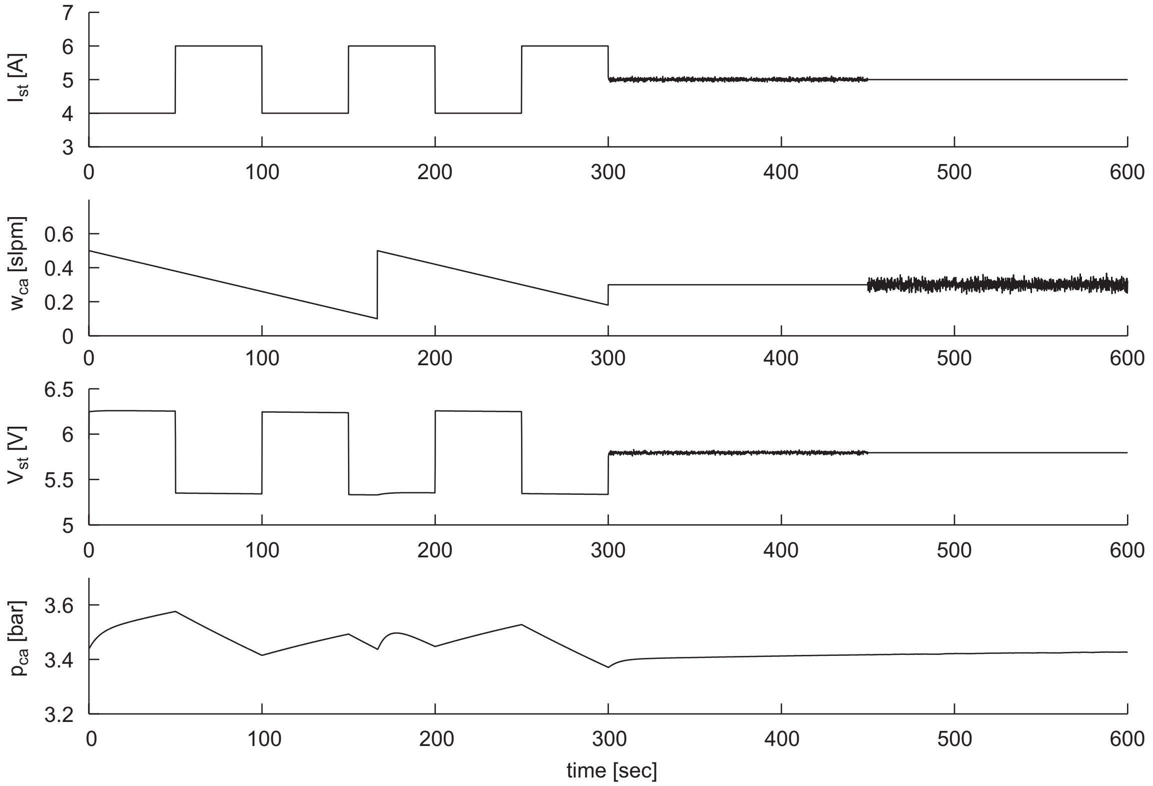

Fig. 9 – Simulation results.

to the inputs. This resulting MIMO model provides an accurate behavior and can be used either for model-based control design or for on-line analysis and errors detection.

Based on these results it is foreseen to continue working to develop an extended model of the system (i.e. considering more subsystems) at different working conditions.

Acknowledgments

This research has been funded by the Agencia Española de Cooperación Internacional (AECI), Universidad Nacional de La Plata (UNLP), Universitat Politècnica de Catalunya (UPC), Consejo de Investigaciones Científicas y Técnicas (CONICET) and the Ministerio de Educación y Ciencia (MEC) of Spain under the Contract DPI2007-62966.

REFERENCES

[1] Larminie J, Dicks A. Fuel cell systems explained. 2nd ed. New York: Wiley; 2003.

[2] Bao C, Ouyang M, Yi B. Modeling and control of air stream and hydrogen flow with recirculation in a PEM fuel cell system–I. Control-oriented modeling. Int J Hydrogen Energy 2006;31(13):1879–96.

[3] Pukrushpan JT, Stefanopoulou AG, Peng H. Control of fuel cell power systems. London: Springer; 2004.

[4] Kunusch C. Second order sliding mode control of a fuel cell stack using a twisting algorithm. Master's thesis, Electrical Department, National University of La Plata, March 2006.

[5] ElectroChem Inc website: 〈http://www.fuelcell.com/pdfs/FuelCellStack.pdf〉 [accessed May 2006].

[6] Yan X, Hou M, Sun L, Liang D, Shen Q, Xu H, et al. AC impedance characteristics of a 2 kW PEM fuel cell stack under different operating conditions and load changes. Int J Hydrogen Energy 2007;32(17):4358–64.

[7] Lai CM, Lin JC, Hsueh KL, Hwang CP, Tsay KC, Tsai LD, et al. On the electrochemical impedance spectroscopy of direct methanol fuel cell. Int J Hydrogen Energy 2007;32(17):4381–8.

Journal of Power Sources 183 (2008) 240–246

Contents lists available at ScienceDirect

Journal of Power Sources

journal homepage: www.elsevier.com/locate/jpowsour

In situ measurements of water transfer due to different mechanisms in a proton exchange membrane fuel cell

Attila Husar, Andrew Higier, Hongtan Liu*

Department of Mechanical and Aerospace Engineering, University of Miami, Coral Gables, FL 33124, United States

ARTICLE INFO

Article history:
Received 10 March 2008
Received in revised form 7 April 2008
Accepted 8 April 2008
Available online 26 April 2008

Keywords:
PEM
Fuel cell
Water transport
Water management
Electro-osmotic drag

ABSTRACT

Water management is of critical importance in a proton exchange membrane (PEM) fuel cell, in particular, those based on a sulfonic acid polymer, which requires water to conduct protons. Yet there are limited in situ studies of water transfer through the membrane and no data are available for water transfer due to individual mechanisms through the membrane in an operational fuel cell. Thus it is the objective of this study to measure water transfer through the membrane due to each individual mechanism in an operational PEM fuel cell. The three different mechanisms of water transfer, i.e., electro-osmotic drag, diffusion and hydraulic permeation are isolated by specially imposed boundary conditions. Therefore water transfer through the membrane due to each mechanism is measured separately. In this study, all the data is collected in an actual assembled operational fuel cell. The experimental results show that water transfer due to hydraulic permeation, i.e. the pressure difference between the anode and cathode is at least an order of magnitude lower than those due to the other two mechanisms. The data for water transfer due to diffusion through the membrane are in good agreement with some of the ex situ data in the literature. The data for electro-osmosis show that the number of water molecules dragged per proton increases not only with temperature but also with current density, which is different from existing data in the literature. The methodology used in this study is simple and can be easily adopted for in situ water transfer measurement due to different mechanisms in other PEM fuel cells without any cell modifications.

1. Introduction

In a PEM fuel cell, the most commonly used electrolyte is the Nafion® membrane or similar ionomer. Such membranes need to be well-hydrated in order to maintain high proton conductivity. Though water is produced during fuel cell operations, the anode side of the membrane and the anode catalyst layer are often de-hydrated due to the electro-osmotic drag effect. Thus, even though water is a product of a fuel cell, it often must be added to the gas streams to ensure proper hydration of the membrane and catalyst layers. Yet, too much water can cause flooding in the cathode catalyst layer, gas diffusion layers and the channels. Therefore, a delicate water balance is needed to ensure proper operation of a PEM fuel cell using the current membrane technology.

The difficulty of water balance in the PEM fuel cell lies in the interactions of three different mechanisms of water transfer through the membrane, diffusion, hydraulic permeation, and the so called electro-osmotic drag (EOD). Diffusion is caused by the difference in water concentrations between the anode and cathode sides; hydraulic permeation is due to pressure difference between anode and cathode; and EOD occurs when protons pull water molecules when transferring through the membrane. EOD will cause an increase in water content on the cathode side since the protons, and therefore the water, transfers from anode to cathode.

Most studies on water transfer in fuel cells are based on mathematical modeling. In most models, the correlations for water diffusivity and electro-osmotic drag coefficients used were mostly based on one correlation [1], which was based on ex situ measurement of water transfer in the Nafion® 117 membrane. For a Nafion® 117 membrane of 178 μm thickness, pretreated in boiling water, fully hydrated and in equilibrium with liquid water, the number of water molecules dragged per every proton was determined to be 2.5 ± 0.2. For a membrane which is not fully saturated the EOD coefficient was found to be approximately 0.9. Therefore the protonic drag coefficient was determined to be a function of the membrane hydration [2]. In the same study [2], the intra-diffusion coefficient was measured using the pulsed-field gradient spin-echo nuclear magnetic resonance (NMR) technique.

---

* Corresponding author. Tel.: +1 305 284 2019; fax: +1 305 284 2580.
E-mail address: hliu@miami.edu (H. Liu).

0378-7753/$ – see front matter © 2008 Elsevier B.V. All rights reserved.
doi:10.1016/j.jpowsour.2008.04.042

Nomenclature

A	area
c	water concentration
C	mass fraction
ΔC	water concentration difference
ΔC_{m}	log mean water concentration difference
D	effective diffusivity
K_{m}	effective hydraulic permeability
m	mass
$\dot{m}$	mass flow rate
M	molecular weight
n	number of water molecules transferred
p	pressure
q	water mass transfer flux through the membrane
Q	water mass transfer rate through the membrane
t	time
Greek symbols	
δ_{m}	dry membrane thickness
μ	dynamic viscosity
ρ_{m}	dry membrane density
Subscripts	
a	air
d	diffusion
e	exit/outlet
EOD	electro-osmotic drag
hyd	hydraulic permeability
in	inlet
m	membrane
out	outlet
sat	saturation
w	water
Superscripts	
a	anode
c	cathode
g	generation

In 2007 Dunbar and Masel [3] used MRI to measure water distribution in an assembled fuel cell using an MEA assembled from a Nafion 115 membrane. This study found that, at low current densities, water was transported from the cathode to the anode signifying that diffusion forces and hydrophobic capillary pressures appeared to dominate over the electro-osmotic forces. Trabold et al. [4] used in situ neutron radiography to investigate how and where water accumulates in a flow field and how different parameters such as humidification of reactants affected the water accumulation.

In 2000 Choi et al. [5] performed experimental studies to determine the net drag coefficient in Nafion 115, which was the resultant water transfer coefficient due to both EOD and diffusion. In 2001 Janssen and Overvelde [6] presented the measured results of the net drag coefficient for a Nafion 112 membrane under a wide range of operating conditions including temperature, pressure, stoichiometry and current density. The net water transfer through the membrane was measured using a condenser after the cell outlets. In 2006 in a study by Yan et al. [7] the net water flux through a Nafion 117 membrane at various temperatures and humidification was measured. This study measured the effects of concentration difference across the membrane as well as pressure difference across the membrane on the net water flux. They found that the net drag coefficient depended on current density and humidification of feed gasses and that the pressure difference across the membrane had less effect on the net water flux than concentration differences and EOD.

All of the above studies are either ex situ measurement of water transfer or measurement of the “net electro-osmotic drag”; what these papers refer to as “net EOD” is actually the net water transfer through the membrane due to both diffusion and EOD. There have been very limited studies focused on water transfer through the membrane due to individual transport mechanisms. Furthermore, water transfer due to EOD will be affected by the catalyst layers since a large volume fraction of the catalyst layer is ionomer. This means that EOD will also occur in the ionomer portion of the catalyst layer. To accurately calculate water diffusion transfer through the membrane, one must use the water contents of the membrane at the anode and cathode sides as boundary conditions. Yet covered with the catalyst layer and the GDL, it is almost impossible to know the water contents at these boundaries. Even though the diffusivity and EOD data for the membrane were accurate, direct application of such data to a real fuel cell may not be appropriate due to the fact that this data was collected ex situ. There is very limited data on water transfer due to hydraulic permeation. Besides, though measurement of total net water transfer through the membrane can be easily performed, such data have limited application to fuel cell design, operation and modeling since water transfer due to the three mechanisms are intertwined.

It is the objective of this study to separately measure water transfer due to the three water transport mechanisms in an operational fuel cell. Through specially imposed conditions, water transfer due to EOD, diffusion and hydraulic permeation were isolated so that in each experiment, water transfer due to only one mechanism could be measured. Such experiments will provide more realistic data for modeling practices. In addition, the applicability of the data obtained is greatly improved because it was obtained in an operational fuel cell.

2. Experimental system

There are four fundamental components in the fuel cell test system used for this study: (1) fuel cell test station, (2) single cell test fixture, (3) fuel cell thermal management system, and (4) reactant gas condenser and water collection equipment. Systematic calibrations were performed on the sub-systems to ensure accuracy of the experimental results. Schematic of the test station can be found in Fig. 1.

The fuel cell test station provides control over the reactant gas humidification temperature and cell operating pressure, as well as anode and cathode mass flow rates. The fuel cell temperature is controlled by an external thermal management system. The reactant gases are humidified by bubbling them through heated water tanks at both the anode and cathode sides. The fuel cell test fixture used in the experiments was designed and manufactured at the University of Miami. The fuel cell flow field used in these experiments was a serpentine single channel design with channel width 1.0 mm, channel height 1.0 mm, land width 1.1 mm and a length of 65.4 mm. The anode and cathode flow fields were identical. The diffusion layers used were carbon fiber cloth material manufactured by E-TEK® known as double-sided ELAT®, i.e. both sides of the carbon fiber cloth were coated with micro-diffusion layers. The catalyst loadings were 0.4 mg cm^{-2} platinum on both the anode and cathode sides. The membrane was Nafion® 115, which has an average thickness of 125 μm and the active area was 50 cm^2.

The temperature of the fuel cell is controlled by a thermal management system, in which the water glycol mixture at a preset

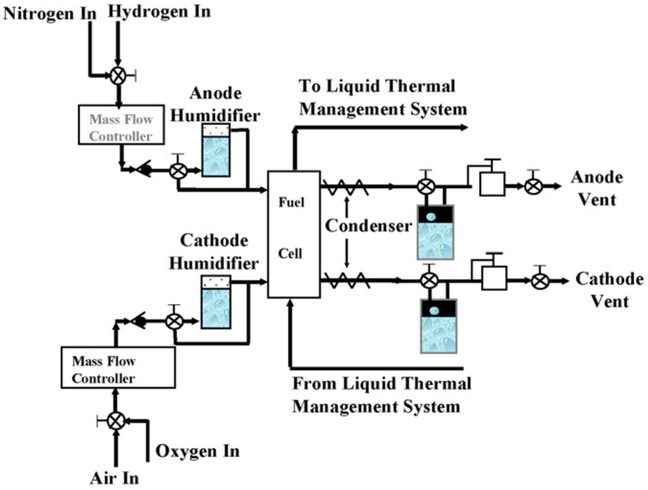

Fig. 1. Schematic of test system.

temperature flows though the cooling channels in the end plates of the cell fixture and the temperature of the fluid is controlled with a thermal bath. An in-house designed water vapor condenser was used to condense both the anode and cathode exit gas streams. In the condenser, the cooling fluid was supplied by an external cooler with a temperature control precision of 0.5 °C. A set of by-pass valves were installed before the condenser so that the exit gas streams could be switched easily either going through or bypassing the condenser. The condenser was connected to a cooling loop that uses automotive antifreeze coolant as the working fluid. The coolant loop is set to a constant temperature.

3. Experimental methodologies

The following experiments were designed to separately measure water transfer due to each of the three mechanisms: hydraulic permeation, diffusion and electro-osmotic drag.

3.1. Hydraulic permeation

To isolate hydraulic permeation, water transfer due to both EOD and diffusion must be eliminated. EOD can be eliminated by setting the cell current to zero. Diffusion can be eliminated by ensuring that both the anode and cathode sides have the same water content. This was done by filling the flow channels of both sides with de-ionized (DI) water. It may seem natural to use 100% humidified gas streams on both anode and cathode to measure hydraulic permeation, but such an approach was found to be extremely difficult due to the very large measurement error involved. Since water transfer rate due to hydraulic permeation is extremely low, the amount of water supplied by humidifying the gas streams at the inlets would be orders of magnitude higher than the permeation rate. As a result, the difference in the collected water from the two exit streams in the condenser would be so small that it would be impossible to accurately determine the hydraulic permeation rate. The exit of one side, anode side for example, is connected to the water collecting tube that is open to the atmosphere. The cathode side is pressurized to a pre-determined pressure. The amount of water increased in the anode side water collection tube during a specified period of time is the water transferred due to hydraulic permeation. Before the experiments, rigorous leak-checks of the system have been performed to ensure the accuracy of the experimental results.

3.2. Diffusion

In order to separately measure water transfer due to diffusion only, the effects of EOD and hydraulic permeation must be eliminated. The EOD can again be easily eliminated by setting the cell current to zero and the hydraulic permeation can be eliminated by ensuring both sides have the same pressure. Since, during this set of experiments, water will diffuse from the wet side (the anode side in this study) to the dry side, the water concentration of the wet side will generally decrease and that of the dry side will always increase along the channel. Thus the water concentration difference across the membrane and GDLs cannot be a constant along the channel. Knowledge of water concentration at the two inlets and two outlets can be used to determine the log mean concentration difference across the membrane, as is often used in heat exchanger designs [e.g. 9]. However, with water content varying on both sides, and because water diffusivity through the membrane depends on the water content in the membrane, without proper control of the water contents at these four points the experimental results would have large uncertainties. To improve accuracy, water content on the wet side was maintained constant throughout the cell. This was accomplished by over-saturating the wet side so much that wet side is always over-saturated throughout the cell. For any test run if the outlet gas of the wet side was found not to be over-saturated, the test results would be eliminated. At the dry side, completely dry gas was introduced to maximize water gradient across the membrane and to minimize experimental errors. Furthermore, to maintain consistency the outlet relative humidity was maintained in the vicinity of and less than 50%.

3.3. Electro-osmotic drag

In order to measure water transfer due to electro-osmotic drag, the fuel cell must be generating current and at the same time the driving forces for hydraulic permeation and diffusion must be eliminated. Hydraulic permeation can be easily eliminated by maintaining the same pressure at both the anode and cathode sides. To eliminate diffusion, the water vapor activities, and thus the water content, at both sides must be kept the same throughout the cell. This is achieved by ensuring both sides to be fully humidified throughout the cell at the same temperature. Since water will transfer from the anode side to the cathode side, water content would decrease along the anode channel and increase along the cathode channel. To ensure a fully humidified anode, it must be supplied with over-saturated gas stream and it must be ensured that its humidity level never drop below saturation until the exit. The air in the cathode side was also fully humidified, and the air flow rate was so chosen that excess liquid water must be able to be removed effectively to avoid significant flooding.

4. Results and discussions

In order to determine the amount of water transfer through the membrane the following must be calculated: the amount of water that is brought into the system by each gas stream, the amount of water produced by the reaction, and the amount of water that leaves the system through the two exhaust streams.

4.1. Hydraulic permeation

First, the mass transfer rate of liquid water Q from the higher pressure side (anode) to the lower pressure side (cathode) was measured and then the mass flux q is calculated by dividing Q by the active area of the membrane. From this mass flux q, the effective permeability of the membrane can be determined from

$$q_{\mathrm{hyd}} = C_{\mathrm{w}} \frac{K_{\mathrm{m}}}{\mu} \frac{\mathrm{d}p}{\mathrm{d}y} \tag{1}$$

where μ is the dynamic viscosity of water, K_{m} is the effective hydraulic permeability of the membrane and C_{w} is the mass fraction of water, which equals 1 here since the anode and cathode channels where filled with liquid water. Since the catalyst layers and the diffusion layers are porous, the values of their permeability must be several orders of magnitude greater than that of the membrane. Therefore, the hydraulic permeability obtained can be used as the effective permeability of the membrane.

The term $\mathrm{d}p/\mathrm{d}y$ represents the hydraulic pressure difference across the membrane divided by the nominal initial thickness of the membrane. The membrane used was Nafion® 115. Then from Eq. (1) the effective hydraulic permeability of the membrane can be determined from

$$K_{\mathrm{m}} = \frac{q_{\mathrm{hyd}} \delta_{\mathrm{m}} \mu}{\Delta p} \tag{2}$$

where δ_{m} represents the dry membrane thickness provided by the manufacturer, and Δp is the pressure difference between the anode and cathode sides. Mass flux of water is plotted against the pressure difference at three different cell temperatures in Fig. 2. It can be observed that a good linear relationship exists between mass flux and the pressure difference, as expected. It can be seen that the mass flux increases with temperature. Since water uptake of the membrane increases with temperature, there should be more nano-scale water channels [8]. The results of mass flux and hydraulic permeability are shown in Figs. 2 and 3. It can be seen that the hydraulic permeability varies slightly with pressure difference; while it decreases significantly with temperature.

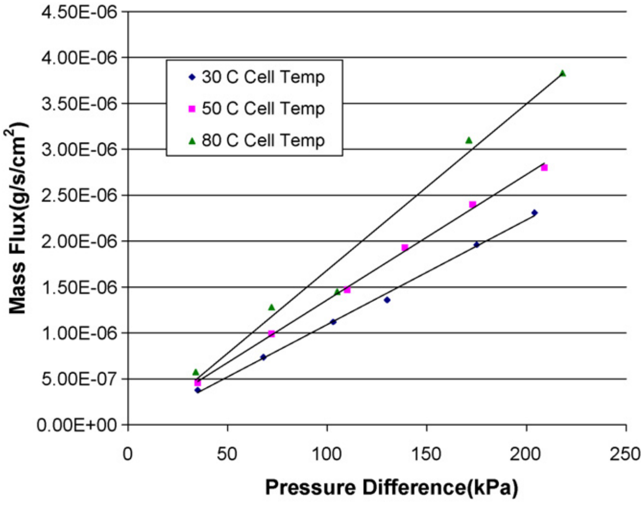

Fig. 2. Water mass transfer flux due to hydraulic permeation through the membrane versus pressure difference at different temperatures.

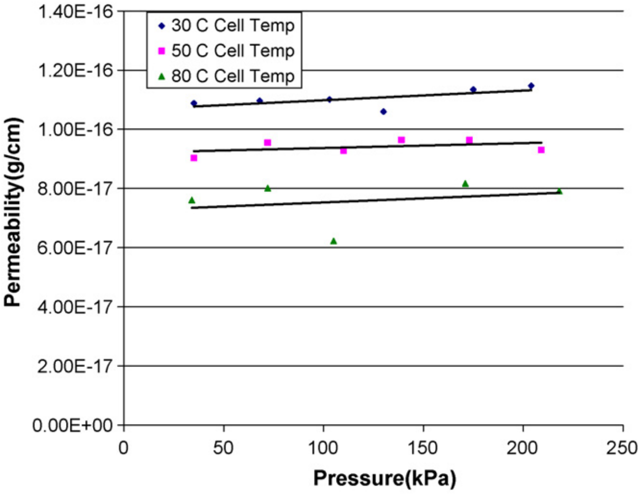

Fig. 3. Hydraulic permeability of water through the membrane at different temperatures.

4.2. Water diffusion

In this set of experiments, one side of the fuel cell (the anode) was supplied with nitrogen gas over-saturated with water while on the other side (the cathode) dry air was supplied. Since the inlet water flow rate at the dry side is zero, its exit water flow rate must equal the water transfer rate due to diffusion. This exit water flow rate equals the mass flow rate of water collected in the water trap plus the mass flow rate of water vapor in the exit air leaving the water trap. Assuming the air at the exit of the water trap is saturated at the exit temperature, the total water flow rate, thus the water diffusion rate, from the wet side to dry side can be calculated by

$$Q_{\mathrm{d}} = \frac{m_{\mathrm{w}}}{\Delta t} + \dot{m}_{\mathrm{a}} \frac{M_{\mathrm{w}} p_{\mathrm{sat}}}{M_{\mathrm{a}}(p - p_{\mathrm{sat}})} \tag{3}$$

where Q_{d} is the total mass diffusion rate, m_{w} is the mass of water collected in the water trap during the time period of Δt, $\dot{m}_{\mathrm{a}}$ is the dry air mass flow rate and p_{sat} is the vapor saturation pressure at the exit temperature of the water trap. Note that the exit temperature at the water trap was set at 4 °C, therefore the 2nd term in Eq. (3) is very small. Thus, even if the exit gas stream was not 100% saturated the error thus introduced would be extremely small. Once the total mass diffusion rate Q_{d} is obtained, the diffusion mass flux q_{d} can be calculated by dividing it by the cell active area and the effective diffusivity of the membrane can be determined by

$$D = \frac{q_{\mathrm{d}} \delta_{\mathrm{m}}}{\Delta C_{\mathrm{m}}} \tag{4}$$

where δ_{m} is the dry membrane thickness and ΔC_{m} is the log-mean water concentration difference, which can be calculated by

$$\Delta C_{\mathrm{m}} = \frac{\Delta C_{\mathrm{in}} - \Delta C_{\mathrm{out}}}{\ln(\Delta C_{\mathrm{in}}/\Delta C_{\mathrm{out}})} \tag{5}$$

where ΔC_{in} and ΔC_{out} are the water concentration differences between the wet side and the dry side at the inlet and outlet, respectively. The derivation of Eq. (5) is similar to that for the log-mean-temperature-difference (LMTD) used in heat exchanger designs [e.g. 9].

To calculate the water concentrations in the membrane the following correlation [10] was used:

$$c_{\mathrm{w}} = \frac{\rho_{\mathrm{m}}}{M_{\mathrm{m}}}[0.043 + 17.8a_{\mathrm{w}} - 39.85a_{\mathrm{w}}^2 + 36.0a_{\mathrm{w}}^3], \quad 0 \le a_{\mathrm{w}} \le 1 \tag{6}$$

where a_{w} is the water-vapor activity, ρ_{m} is the density of the dry membrane, and M_{m} is the equivalent weight of the dry membrane. Assuming the gas mixture is an ideal gas, the water vapor activity, denoted as a, can be replaced by the relative humidity. The exit gas of the wet side was also condensed and water mass flow rate determined. This was done to ensure that the wet side was kept over-saturated all the way to the exit. Data from any test runs with the wet side exit gas not fully saturated were removed. The diffusivities at different temperatures and different pressures are presented in Figs. 4 and 5. It can be seen from Figs. 4 and 5, the diffusivity increases with temperature and decreases with pressure.

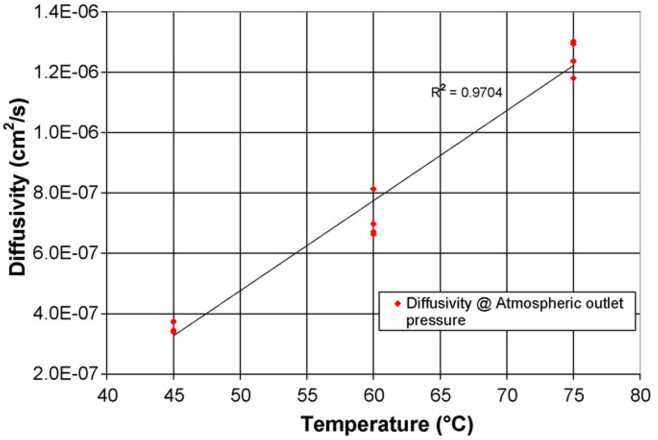

Fig. 4. Variation of effective water diffusivity through the membrane with temperature at atmospheric pressure.

Empirical equations for the diffusion coefficients have been proposed by Springer et al. [1], Nguyen and White [10], and Fuller and Newman [11], etc. However, the values of these coefficients vary widely. It is found that the results based on the correlations from Fuller and Newman [11] are at least an order of magnitude greater than all the others. Thus the measured results are compared only with those from Springer et al. [1] and Nguyen and White [10], as shown in Figs. 6–9. The best comparisons are with the results obtained from the correlation by Nguyen and White [10].

4.3. *Results on electro-osmotic drag*

In this set of experiments, the mass transfer rate through the membrane can be calculated from the water balance of the anode or the cathode. In this study, the mass transfer rates were calculated from the average of the results obtained from the anode and the cathode to minimize errors. For the anode side, the net water transfer rate equals to the inlet water mass flow rate minus the total outlet water mass flow rate. The total outlet water mass flow rate equals the mass of water collected in the water trap divided by the time period plus the water vapor mass flow rate from the exit of the water trap. It was also assumed that the gases that exited the water traps were fully saturated at the outlet. Thus the water mass flux due to electro-osmotic drag can be obtained as

$$q^{a}_{\mathrm{EOD}} = \frac{\dot{m}^{a}_{i} - m^{a}_{w}/\Delta t - \dot{m}^{a}_{e}}{A} \qquad (7)$$

where $\dot{m}^{a}_{i}$ is water inlet mass flow rate in the humidified hydrogen stream, m^{a}_{w} is the mass of water collected in the anode water trap during the time period of Δt, and $\dot{m}^{a}_{e}$ is the mass flow rate of water from the outlet of the anode water trap.

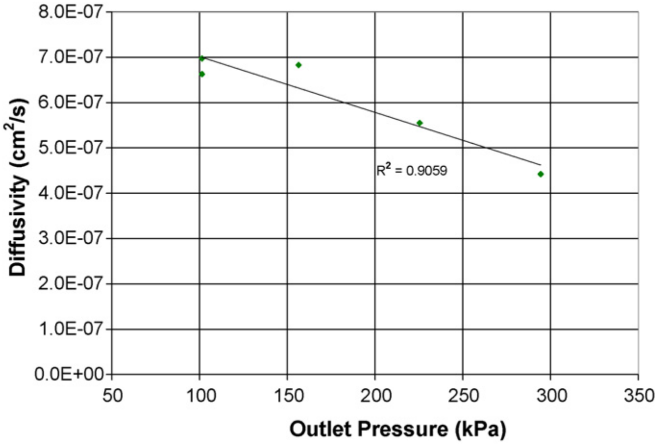

Fig. 5. Variation of effective water diffusivity through the membrane with pressures at 60 °C.

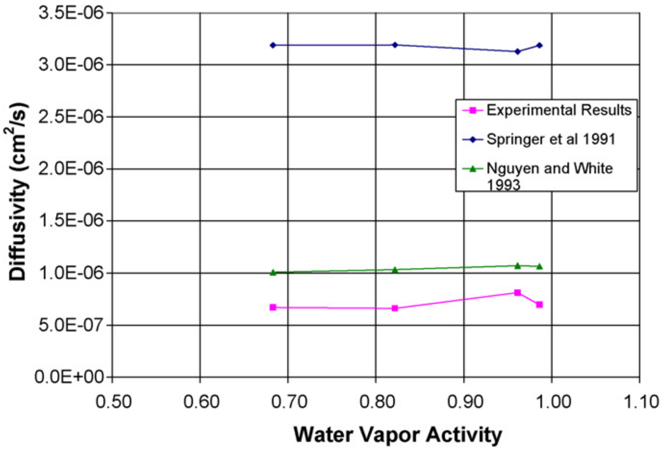

Fig. 6. Comparison of effective water diffusivity at different average water vapor activities at 60 °C.

For the cathode side, similar calculations can be performed. However the water generation rate in the fuel cell must be taken

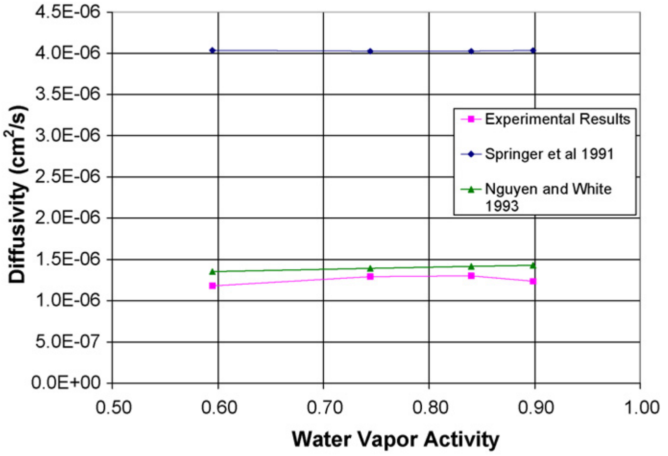

Fig. 7. Average water vapor activity vs. diffusivity comparisons at 75 °C.

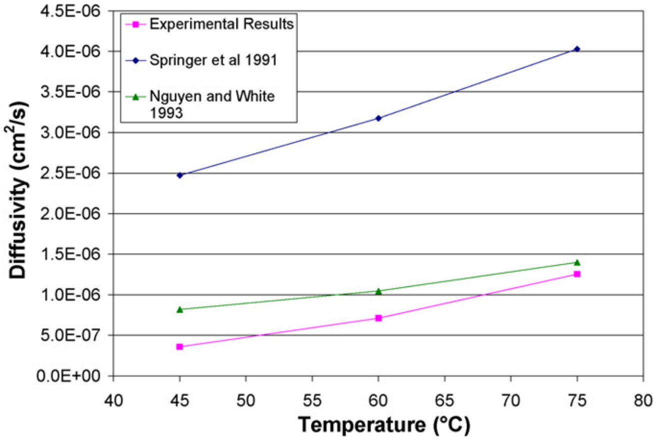

Fig. 8. Comparison of water diffusivity at different temperatures, at pressure 101 kPa.

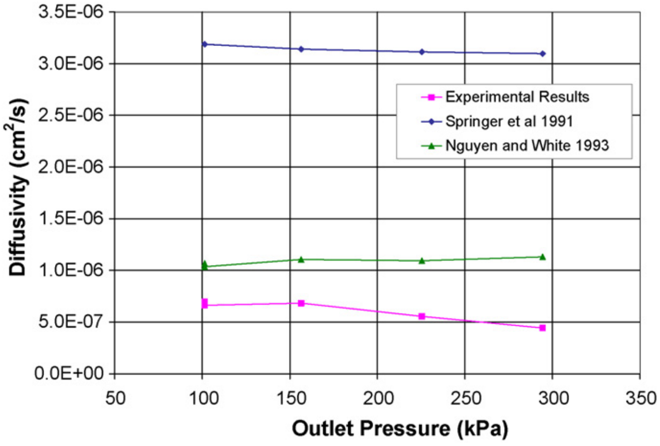

Fig. 9. Comparison of effective water diffusivity at different pressures.

into consideration, thus

$$q_{\mathrm{EOD}}^{\mathrm{c}}=\frac{m_{\mathrm{w}}^{\mathrm{c}}/\Delta t+\dot{m}_{\mathrm{e}}^{\mathrm{c}}-(\dot{m}_{\mathrm{i}}^{\mathrm{c}}+\dot{m}_{\mathrm{g}})}{A} \tag{8}$$

where $\dot{m}_{\mathrm{i}}^{\mathrm{c}}$ is water inlet mass flow rate in the humidified air stream, $\dot{m}_{\mathrm{g}}$ is the water generation rate in the fuel cell and can be calculated from the total cell current, $m_{\mathrm{w}}^{\mathrm{c}}$ is the mass of water collected in the cathode water trap during the time period of Δt, and $\dot{m}_{\mathrm{e}}^{\mathrm{c}}$ is the mass flow rate of water from the outlet of the cathode water trap. As mentioned above, to minimize uncertainties, the final effective water mass transfer flux due to EOD is taken to be the average of the results from anode and cathode sides

$$q_{\mathrm{EOD}}=\frac{1}{2}(q_{\mathrm{EOD}}^{\mathrm{a}}+q_{\mathrm{EOD}}^{\mathrm{c}}) \tag{9}$$

Since for every two protons transferred through the membrane, one water molecule is generated, the number of water molecules transferred due to EOD per proton transferred can be determined by

$$n_{\mathrm{EOD}}=\frac{2q_{\mathrm{EOD}}}{\dot{m}_{\mathrm{g}}} \tag{10}$$

Fig. 10 shows variations of the water mass flux due to EOD as function cell current density at two different temperatures of 40 °C and 60 °C. Data at higher cell temperatures could not be obtained since at higher temperatures, the anode exit gas stream could not be maintained fully saturated even if the anode inlet humidification temperature was set at the highest level. From Fig. 10 it can be observed that the water transfer flux due to electro-osmotic drag is much higher at higher temperatures and the rate of increase with current density is also higher at higher temperatures. This is reasonable since EOD depends on the water content in the membrane, which increases with temperature.

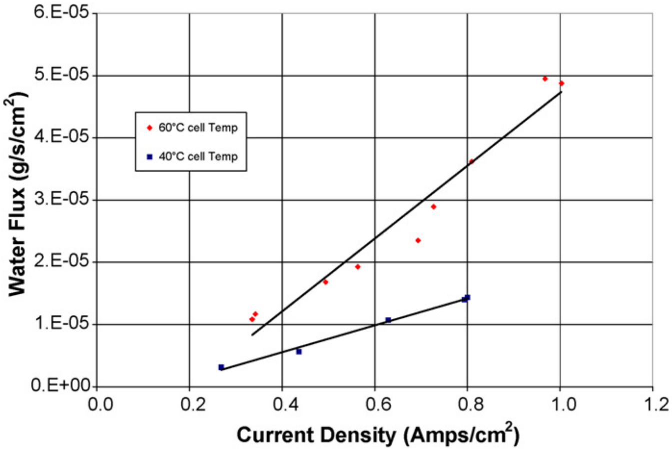

Fig. 10. Variations of effective water flux through the membrane due to electro-osmotic drag with current density at different temperatures.

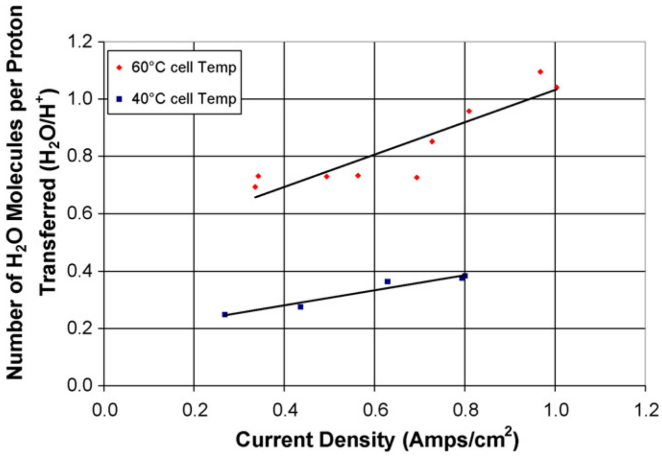

Fig. 11. Number of water molecules transferred through the membrane per proton due to electro-osmotic drag at different current densities.

Fig. 11 shows the results of number of water molecules transferred per proton. The classical work by Springer et al. [1] and Zawodzinski et al. [2] showed that for fully hydrated (immersed) Nafion® 117 membranes, a drag coefficient was between 2.5 and 2.9. With a partially hydrated membrane, the drag coefficient was determined to be 0.9. It can be seen that the experimental results from this study for 60 °C is in good agreement with their results. Note that the membrane used for this study was Nafion 115 while Zawodzinski et al. [2] used Nafion 117. However, Figs. 10 and 11 show that the electro-osmotic drag coefficient depends strongly on the cell current density as well as on temperature. The fact that the electro-osmotic drag coefficient increases with current density may indicate that our understanding of this phenomenon is not complete and there is a need to revisit the fundamental mechanisms.

5. Concluding remarks

The three different mechanisms of water transfer in an operational PEM fuel cell, i.e., electro-osmotic drag, diffusion and hydraulic permeation were isolated by specially imposed boundary conditions and thus in situ measurements of water transfer due to each individual mechanism were obtained. The measured results showed that water transfer due to hydraulic permeation, i.e. the pressure difference between the anode and cathode is at least an order of magnitude lower than those due to other two mechanisms. The measured effective diffusivity results compared well the correlation by Nguyen and White [10] and the results showed that the effective diffusivity increases with temperature and decreases with pressure. The experimental data on electro-osmosis compared relatively well with the ex situ measurement results for the membrane alone [1,2]. However, the data for electro-osmosis show that the number of water molecules dragged per proton increases not only with temperature but also with current density, which is different from existing data in the literature. The methodology used in this study is simple and can be easily adopted for in situ water transfer measurement due to different mechanisms in different PEM fuel cells without any cell modifications.

References

[1] T.E. Springer, T.A. Zawodzinski, S. Gottesfeld, J. Electrochem. Soc. 138 (8) (1991) 2334–2342.

[2] T.A. Zawodzinski, et al., J. Electrochem. Soc. 140 (4) (1993) 1041–1047.

[3] Z. Dunbar, R.I. Masel, J. Power Sources 171 (2007) 678–687.

[4] T.A. Trabold, J.P. Owejan, D.L. Jacobson, M. Arif, P.R. Huffman, Int. J. Heat Mass Transfer 49 (2006) 4712–4720.

[5] K.-H. Choi, D.-H. Peck, C.S. Kim, D.-R. Shin, T.-H. Lee, J. Power Sources 86 (2000) 197–201.

[6] G.J.M. Janssen, M.L.J. Overvelde, J. Power Sources 101 (2001) 117–125.

[7] Q. Yan, H. Toghiani, J. Wu, J. Power Sources 158 (2006) 316–325.

[8] A.Z. Weber, Newman, J. Electrochem. Soc. 150 (2003) A1008.

[9] S. Kakac, H. Liu, Heat Exchangers: Selection, Rating and Thermal Design, 2nd edition, CRC Press, 2002.

[10] T.V. Nguyen, R.E. White, J. Electrochem. Soc. 140 (8) (1993) 2178–2186.

[11] T.F. Fuller, J. Newman, J. Electrochem. Soc. 140 (5) (1993) 1218–1225.

ASIA-PACIFIC JOURNAL OF CHEMICAL ENGINEERING
Asia-Pac. J. Chem. Eng. 2009; **4**: 55–67
Published online 13 October 2008 in Wiley InterScience
(www.interscience.wiley.com) DOI:10.1002/apj.195

Special Theme Research Article

Numerical model for polymer electrolyte membrane fuel cells with experimental application and validation

Javier Alonso Mora, Attila P., Husar, Maria Serra and Jordi Riera*

Institute of Robotics and Industrial Informatics at Barcelona IRI (CSIC-UPC), Spain

Received 18 January 2008; Revised 3 March 2008; Accepted 21 May 2008

ABSTRACT: The aim of this paper is to present a simple 3D computational model of a polymer electrolyte membrane fuel cell (PEMFC) that simulates over time the heat distribution, energy, and mass balance of the reactant gas flows in the fuel cell including pressure drop, humidity, and liquid water. Although this theoretical model can be adapted to any type of PEMFC, for verification of the model and to present different analysis it has been adapted to a single cell test fixture. The model parameters were adjusted through a series of experimental tests and the model was experimentally validated for a well-defined range of operating conditions: H_2/air O_2 as reactants, flow rates of 0.5–1.5 SLPM, dew points and cell temperatures of 30–80 °C, currents 0–5 A and with/without water condensation. The model is especially suited for the analysis of liquid water condensation in the reactant channels. A key finding is that the critical current at which liquid water is formed is determined at different flows, temperatures, and humidity. © 2008 Curtin University of Technology and John Wiley & Sons, Ltd.

KEYWORDS: numerical modeling; PEM fuel cell; temperature distribution; pressure drop; parameter identification; experimental validation

INTRODUCTION

Polymer electrolyte membrane fuel cells (PEMFCs) have tremendous potential as energy conversion devices for a wide range of applications. However, there is a great deal to be learnt about the various interactions between the different physical phenomena that occur in the fuel cell. There are a vast number of studies in the literature that model the fuel cells with varying degrees of complexity. However most of them do not validate their model with experimental data. Static models, in particular, saw an important evolution in the 1990s. For instance, isothermal conditions are assumed by many authors such as Springer *et al*. (1991),[1] while others include thermal distribution (Nguyen, 1993)[2]. Spatial variation in only one dimension was considered initially (Springer, 1991)[1] while variation in two[17] and three dimensions was introduced later (Broka, 1997)[3] (Coppo, 2006)[4]. Some works do not model the two phases of water while others do (Bernardi, 1992)[5,15].

Dynamic models of physics and control solutions for PEMFC have evolved greatly in the past decade. However, the majority of these dynamic models have a low level of detail. Very few dynamic studies include essential characteristics, such as temperature distribution, formation of liquid water in different zones of the fuel cell, or pressure drop along the channels. Shan (2005)[6] and Um (2006)[7] present very complete models with heat distribution but their works do not take liquid water into account.

This study presents a dynamic model for PEMFC, which includes the computation of the thermal properties and temperature distribution of the fuel cell and the pressure drop in the reactant gases while taking into account the condensation of water, as well as the resulting effects on the flow and pressure fields. The experimental tests for parameter identification are described. The model is based on the numerical solution of heat transfer problems expressed as various equilibrium differential equations, using numerical iterative methods. In the section on Description of the Model, the model is described; sections on Application of the Model to a Single Cell Test Fixture and Experimental Methodology explain the application of the model to a specific single cell and the experimental methodology for the parameter identification and model validation; the section on Selected Results for the Single Cell Test Fixture collects the principal simulation results and emphasizes the features of the model. The main conclusions are summarized in the section on Conclusions.

**Correspondence to*: Maria Serra, Institute of Robotics and Industrial Informatics at Barcelona IRI (CSIC-UPC), Spain.
E-mail: maserra@iri.upc.edu

DESCRIPTION OF THE MODEL

The anode and cathode reactants are modeled separately from the stack and interact with it through convection heat transfer in the channels.[8] The pressure drop in the channels is experimentally determined using major and minor losses (for laminar flows).[9] Water and heat created inside the fuel cell due to the reaction are determined by commonly used equations which are explained in the section on Heat Transfer (Thermal Generation) at the Active Area and the section on Heat Transfer at the Channels and Active Area due to Reactant Flows.[10]

The model can be conceived as two submodels working together, a thermal and a pressure drop (the analytical nature of the thermal equation).

Thermal model

The thermal equilibrium equation (thermal generation plus heat transfer equal to energy stored per second) can be approximately solved by creating a mesh of the fuel cell, assuming constant temperature in each cuboid inside the mesh. Iterating with an adequate time interval, each cuboid is represented by a node situated at its midpoint. A correct mesh is crucial to obtain good results. As an example, the mesh used in our case is shown in the section on Model Assumptions (Fig. 2).

In this work, the following finite differences method is used for the simulation of the temperature field:

$$T_i^{k+1} = \frac{\Delta t}{C_i}\left[\sum_{j=1}^{N+1} K_{ij}^k T_j^k + (g_i^k V_i)\right] + \left[1 - \frac{\Delta t}{C_i}\sum_{j=1}^{N+1} K_{ij}^k\right] T_i^k \qquad (1)$$

where the thermal transfer coefficient between nodes K_{ij}^k can be obtained by the following equations: (0 for non adjacent nodes),

$$K_{ij}^k = \frac{A_{ij}}{\dfrac{l_i}{\lambda_i} + R_{\text{cont\_}ij} + \dfrac{l_j}{\lambda_j}} \qquad (2)$$

or

$$K_{ij}^k = \frac{A_{ij}}{\dfrac{l_i}{\lambda_i} + R_{\text{cont\_an}-\text{mem}} + \dfrac{l_{\text{mem}}}{\lambda_{\text{mem}}} + R_{\text{cont\_mem}-\text{cat}} + \dfrac{l_j}{\lambda_j}} \quad |i \in \text{ anode}, j \in \text{ cathod} \qquad (3)$$

for adjacent nodes, and

$$K_{i\infty} = h_i A_{i\infty} \qquad (4)$$

between a surface node and the exterior.

In order to ensure stability of the method, the time interval must be verified:[8]

$$\Delta t \le \frac{C_i}{\sum_{j=1}^{N+1} K_{ij}^k} \qquad (5)$$

For computation of the temperatures of each node at time k $[T\ (k)]$, it is beneficial to transform the above Eqn (1) to the matrix notation:[8]

$$T(k+1) = MC \cdot [MK \cdot T(k) + MH \cdot T_\infty + MG] + T(k) \qquad (6)$$

where

$$MC = \begin{bmatrix} \Delta t \big/ C_1 & 0 & \cdots & 0 \\ 0 & \ddots & \ddots & \vdots \\ \vdots & \ddots & \ddots & 0 \\ 0 & \cdots & 0 & \Delta t \big/ C_N \end{bmatrix} \qquad (7)$$

$$MK = \begin{bmatrix} -\sum_{j=1}^{N+1} K_{1j} & K_{12} & \cdots & K_{1(N-1)} & K_{1N} \\ K_{12} & -\sum_{j=1}^{N+1} K_{2j} & \cdots & K_{2(N-1)} & K_{2N} \\ \vdots & \vdots & \ddots & \vdots & \vdots \\ K_{1(N-1)} & K_{2(N-1)} & \cdots & -\sum_{j=1}^{N+1} K_{(N-1)j} & K_{(N-1)N} \\ K_{1N} & K_{2N} & \cdots & K_{(N-1)N} & -\sum_{j=1}^{N+1} K_{Nj} \end{bmatrix} \qquad (8)$$

The thermal conductivities between node i and ambient (∞) is:

$$MH = [K_{1\infty} \quad \ldots \quad K_{N\infty}]^t \qquad (9)$$

And the thermal generation at node i is:

$$MG = [(g_N^k V_1) \quad \ldots \quad (g_N^k V_N)]^t \qquad (10)$$

Although it seems to be a quadratic expression, it can be computed as a linear expression due to the matrix MC being diagonal and that MK has a maximum of seven nonzero values per row and column. This structure significantly reduces the computational time needed by the program.

The channels are included in the matrix representation as isolated nodes with all thermal properties equal to zero (literally holes). The heat transfer between the gases and the channel walls ($\dot{q}^k_{\mathrm{ch\_in/out}}$ and $\dot{q}^k_{\mathrm{ch\_aa}}$) is introduced as thermal generation inside the adjacent nodes (to the channels). The thermal generation ($\dot{q}^k_{\mathrm{g}}$) due to the load inside the active area is also introduced as thermal generation inside the adjacent nodes to the active area and distributed between them. The channels in the active area are in contact with their respective gas diffusion layer (3/4 of total surface)and active area (1/4), and the thermal generation due to the reaction is distributed between anode (K_{ga}) and cathode (K_{gc}); this heat is distributed in the model in the following manner:

$$\sum_i g_i^k = \dot{q}^k_{\mathrm{ch\_in/out}} \text{ for nodes in contact with in/out channels.} \tag{11}$$

$$\sum_i g_i^k = \frac{3}{4}\dot{q}^k_{\mathrm{ch\_aa}} \text{ for gas diffusion layer nodes in contact with active area channels.} \tag{12}$$

$$\sum_i g_i^k = \frac{1}{4}\dot{q}^k_{\mathrm{ch\_aa}} + \dot{q}^k_{\mathrm{g}} \text{ for nodes in active area (distributed between anode and cathode).} \tag{13}$$

Heat transfer (thermal generation) at the active area

The quantity of heat generated due to the reaction inside the fuel cell can be evaluated through its higher heating value efficiency, using the following equation:

$$\dot{q}^k_{\mathrm{g}} = \left(\frac{1}{\eta} - 1\right) V \cdot I \text{ where } \eta = \frac{V}{1.482} \tag{14}$$

The heat is assumed to be generated on the cathode active area, while the heat generation from the anode reaction is neglected.[11] In the literature, it is shown that the calculated heat generation due to the reaction is distributed between the anode, membrane and cathode for fully humidified gas streams in a proportion of 3, 4, and 93% respectively.[12]

Heat transfer at the channels and active area due to reactant flows

The heat transfer between the reactant gases and the channel walls is calculated as convection heat exchange inside circular channels for a laminar flow.[8]

It is assumed that both reactants and vapor behave as ideal gases; their partial pressures and/or vapor mass flow can be determined by Dalton's Law

$$\dot{m}_{\mathrm{vap}} = \dot{m}_{\mathrm{H_2}} \frac{M_{\mathrm{H_2O}}}{M_{\mathrm{H_2}}} \frac{P_{\mathrm{vap}}}{P - P_{\mathrm{vap}}} \text{ and relative humidity is } H_{\mathrm{r}} = P_{\mathrm{vap}}/P_{\mathrm{sat}}(T_{\mathrm{in}}) \leq 1. \tag{15}$$

Reactant consumption and water generation can be obtained by the equations

$$\dot{m}_{\mathrm{H_2\_out}} = \dot{m}_{\mathrm{H_2\_in}} - \frac{M_{\mathrm{H_2}} I}{2F} \tag{16}$$

$$\dot{m}_{\mathrm{O_2\_out}} = \dot{m}_{\mathrm{O_2\_in}} - \frac{M_{\mathrm{O_2}} I}{4F} \tag{17}$$

$$\dot{m}_{\mathrm{H_2O\_out\_an}} = \dot{m}_{\mathrm{H_2O\_in\_an}} + K_{\mathrm{wd1}} \frac{M_{\mathrm{H_2O}} I}{2F} \tag{18}$$

$$\dot{m}_{\mathrm{H_2O\_out\_cat}} = \dot{m}_{\mathrm{H_2O\_in\_cat}} + K_{\mathrm{wd2}} \frac{M_{\mathrm{H_2O}} I}{2F} \tag{19}$$

As stated in Ref. [10], $K_{\mathrm{wd1}} + K_{\mathrm{wd2}} = 1$ and can be determined by the equations shown in Ref. [1, 2].

Gas mixture properties are obtained from the data in NASA database,[13] evaluated at average conditions inside the channel and mixed according to the equations:

$$c_p = \sum_i c_{pi} \frac{\dot{m}_i}{\dot{m}} \tag{20}$$

$$\lambda = \sum_i \lambda_i \frac{\dot{m}_i}{\dot{m}} \tag{21}$$

The heat exchanged between gases and the channel can be obtained by an iterative method, explained in Ref. [8] with equations:

$$h_m = 3.66 \frac{\lambda_m}{D} \text{ (for laminar flow)} \tag{22}$$

$$T_{\mathrm{out}} = T_{\mathrm{ch}} + (T_{\mathrm{in}} - T_{\mathrm{ch}}) \cdot \exp\left(\frac{-h_m \cdot \mathrm{Per} \cdot L}{\dot{m}_m \cdot c_{pm}}\right) \tag{23}$$

and

$$\dot{q} = -h_m \cdot L \cdot Per \cdot LMTD \text{ where } LMTD = \frac{T_{\mathrm{out}} - T_{\mathrm{in}}}{\log\left(\dfrac{T_{\mathrm{ch}} - T_{\mathrm{in}}}{T_{\mathrm{ch}} - T_{\mathrm{out}}}\right)} \tag{24}$$

To this convective heat transfer, the heat generated/absorbed due to the water phase change is added; it can be obtained by the difference between liquid water in and out, and multiplied by the evaporation heat constant of water (h_{v}). Then, heat transfer between the channel and the gases ($\dot{q}^k_{\mathrm{ch\_in/out}}$ and $\dot{q}^k_{\mathrm{ch\_aa}}$) is obtained as the sum of both.

Pressure drop model

The pressure drop in the channel is influenced by the frictional losses in the channel and by the changing channel cross section due to the liquid water. In order to model pressure drop inside the fuel cell, two terms are required; the pressure drop produced by the mass flow and a term incorporating liquid water content inside the fuel cell channels.

Pressure drop related to mass flow

The pressure drop inside a channel can be modeled by calculating the major and minor losses, where the first equation depends linearly on mass flow and is modeled by

$$\Delta P_{\text{lin}} = -\frac{57}{\text{Re}}\frac{L}{D}\cdot\frac{\rho_m \cdot v^2}{2} = -\frac{57}{32}\frac{\mu_m}{\rho_m}L\frac{\text{Per}^2}{S^3}\dot{m}_m$$
$$= -K_{\text{lin}}\frac{\mu_m}{\rho_m}\dot{m}_m \qquad (25)$$

and where the second equation depends quadratically on the mass flow and is modeled by

$$\Delta P_{\text{sing}} = -K_{\text{sing}}\frac{1}{\rho_m}\dot{m}_m{}^2 \qquad (26)$$

An explanation of these equations can be found in Ref. [9]. Roughly, major losses are associated to pressure drop inside a straight channel, while the minor losses are produced in turns, entrances, and exits and are dependent on empirical data of a given geometry.

Properties of the gas mixtures can be obtained by the equations shown in the section on Thermal Model and the following:

$$\rho = \sum_i \rho_i \qquad (27)$$

$$\mu = \frac{\mu_1}{1+\psi_1\dfrac{M_2}{M_1}} + \frac{\mu_2}{1+\psi_2\dfrac{M_1}{M_2}} \text{ where } \psi_1$$
$$= \frac{\sqrt{2}}{4}\left(1+\left(\frac{\mu_1}{\mu_2}\right)^{0.5}\left(\frac{\dot{n}_1}{\dot{n}_2}\right)^{0.25}\right)^2\left(1+\frac{\dot{n}_2}{\dot{n}_1}\right)^{-0.5} \qquad (28)$$

Pressure drop related to liquid water content inside the fuel cell

When there are liquid water droplets present inside the channels, a greater pressure drop is detected in the fuel cell.[14] This extra pressure drop is accounted for in Eqn (26). We believe that this loss is directly associated to a narrowing of the effective cross section of the channels. The amount of restriction is related to the pressure drop induced in the channel due to the flow. The higher the pressure drop, the greater the force that is placed on the upstream side of the water droplet. This force needs to exceed the surface contact resistance of the droplet and that of the channel walls for the droplet to be removed. The dynamics associated with the buildup of water droplets in the channel is not taken into account in this model; however, a steady state constant is determined experimentally for the specific geometry and surface finish of the gas channels.

This effect, at least for the single cell, can be modeled as a special major loss with the equation:

$$\Delta P_W = -K_W \dot{m}_m \qquad (29)$$

Combined pressure drop in the case of liquid water inside the fuel cell

According to the previous section, the pressure drop is determined by

$$\Delta P = \Delta P_{\text{lin}} + \Delta P_{\sin\ g} + \Delta P_w$$
$$= -\left(K_{\text{lin}}\frac{\mu_m}{\rho_m} - K_w\right)\dot{m}_m - K_{\text{sing}}\frac{1}{\rho_m}\dot{m}_m{}^2 \qquad (30)$$

From Eqn (28) and by comparing it with Eqn (25), it is possible to obtain an approximate equation that models the effective cross section when liquid water appears. It is

$$K_{\text{lin}}\frac{\mu_m}{\rho_m} - K_w = \frac{57}{32}\frac{\mu_m}{\rho_m}L\frac{\text{Per}_{ww}{}^2}{S_{ww}{}^3} \qquad (31)$$

If it is assumed that the channel section at active area remains square, even if liquid water is accumulated, then the following equation is obtained.

$$S_{ww}{}^2 = \frac{2}{57}\frac{L}{\left(K_{\text{lin}} - K_w\dfrac{\rho_m}{\mu_m}\right)} \qquad (32)$$

The effective cross section has been found experimentally and is relatively constant for a wide range of operating conditions. Nevertheless, this may be true in the active area of the single cell because the experiments were done with very large stoichiometries; however, in a multicell stack it will require a more complex equation.

APPLICATION OF THE MODEL TO A SINGLE CELL TEST FIXTURE

Single cell test fixture description

The single cell test fixture modeled in this paper is an ElectoChem (model # EFC-05EFC-05-02-02) 5-cm^2 active area fuel cell. It is equipped with a Nafion 115 membrane with 1 mg Pt/cm^2 catalyst loading and Toray carbon fiber paper (Type TGP-H-060) gas diffusion layers, serpentine/straight channel flow field with groups of three channels that come back together at each turn in a uniting manifold. There are five straight

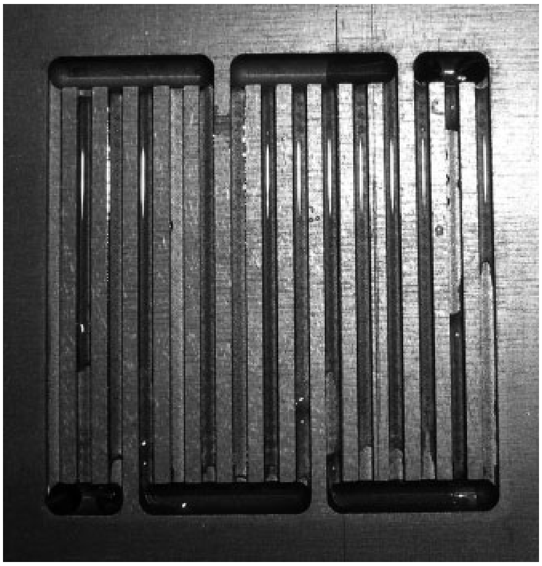

Figure 1. An image of the fuel cell channels configuration.

sections in the flow field, which make it similar to a five pass serpentine configuration, as shown in Fig. 1.

The channels are 0.78 mm wide, 0.78 mm deep, and the space between the channels is 0.78 mm (Table 1). The length of the straight section of a channel is 23.25 mm. The gases enter the flow field through two 1.6 mm diameter holes and exit through holes of the same size. The flow fields are machined into POCO graphite plates that are 19.1 mm thick. The Teflon fitting that connects the fuel cell to the test station is also screwed into the graphite plates. The current collector bus plates are gold-plated copper for enhanced surface conductivity. Resistive square planner 60-W heaters with adhesive are in the center of each bus plate with 50 mm width.

Model assumptions

The following assumptions are made in order to build a reliable, fast, and precise model.

1. One global convection coefficient for the whole cell: With the experimental setup it is impossible to obtain different coefficients for each surface; error committed is low.
2. Physical properties of the materials do not depend on temperature: Temperature range is small (40–80 °C) (Table 2).
3. Calculated properties (c_p, λ, ρ, μ) of dry air do not change very much due to oxygen depletion because of the very high stoichiometry.

Table 1. Dimensional properties of the cell.

		Dimensions					
	Material	x (mm)	y (mm)	z (mm)	Volume (m^3)	Convective area (m^2)	Contact area (m^2)
Heating sides	–	–	–	–	–	1.06E-02	–
Heaters	–	–	50.0	50.0	–	–	2.50E-03
Copper plates	Copper	3.3	95.5	111.0	3.50E-05	2.56E-03	9.09E-03
Graphite plates	graphite	19.35	95.5	95.2	1.76E-04	5.53E-03	9.09E-03
Diffusion layer	carbon paper	0.28	22.4	22.4	1.40E-07	–	5.00E-04
Gasket	Silicon	0.28	–	–	2.41E-09	–	8.59E-03
Membrane	NAFION	0.15	95.5	95.2	1.36E-06	–	9.09E-03
Lab. support	Acrylic	46.01	95.5	10.0	4.39E-05	4.39E-03	–

Table 2. Thermal properties of the cell.

	Thermal/physical properties		
	ρ density (kg/m^3)	c_p specific heat [J/(K·Kg)]	λ thermal conductivity [W/(m·K)]
Heating sides	–	–	–
Heaters	–	–	–
Copper plates	8954	384	395
Graphite plates	2200	980	120
Diffusion layer	1500	400	1.7
Gasket	710	440	0.4
Membrane	–	–	0.35
Lab. support	1460	1190	0.2

4. Properties of the flow inside the active area are determined for the average mass flow between entrance and exit.
5. Ideal gases are assumed.
6. It is assumed that $K_{\mathrm{wd1}} = 0.3$ and $K_{\mathrm{wd2}} = 0.7$; these constants have little effect on the simulations due to the high stoichiometries.
7. The channels in the active area are modeled as 3-parallel long straight tubes. This reduces precision and computational time. For a small single cell this assumption can be made.
8. No heat transfer by radiation: low temperature, nonlineal equation (thermal model is lineal); the determined convection coefficient includes radiation at a given temperature.

Fuel cell mesh

The mesh applied in the model of the single cell is shown in Fig. 2. It divides the different zones of the cell with the corresponding materials. Smaller cuboids are placed in the active area for higher precision.

Properties of the materials

Most of the constants were obtained from material suppliers, fuel cell supplier, or different reference books. They can be found in Tables 1 and 2.

EXPERIMENTAL METHODOLOGY

In this section we present the single cell test fixture, the experimental setups, and the LabView hardware and software used for data acquisition.

Experimental setup

The test station consists of two reactant (anode and cathode) gas subsystems. Each subsystem contains a Bronkhorst mass flow controller, membrane-based humidification with dew point sensors for control, inlet line heaters to prevent condensation, absolute pressure transducers at the inlet, differential pressure transducers between the inlet and outlet of each reactant, and back pressure regulator at the outlet of the fuel cell to control system pressure. The mass flow controllers are each calibrated for the specific gas (hydrogen for the anode and synthetic air for the cathode).

There are eight temperature sensors that come from the fuel cell by way of K type thermal couples. Four of the measurements are of the graphite plates (two in each plate) with one connected to a RedLion PID controller model #T4810105 that controls the temperature of the fuel cell. The cooling of the cell is attained mainly by natural convection. The other four temperature measurements are of the reactants inlets and outlets. The inlet temperature measurements are close to the outlet of the gas line heaters but still outside the cell. The outlet temperatures are measured inside the fuel cell in the outlet manifold. All the measurement and control are made in real time through LabView and are explained in more detail in the following section.

Two computers are used to define the data acquisition and control system. The first one is responsible for the user interface and in setting the operating conditions. This is done by means of a graphical interface developed by our laboratory through LabView. The second computer runs under a Real Time Operating System (RTOS) which works in deterministic mode offering consistent and stable functionality for

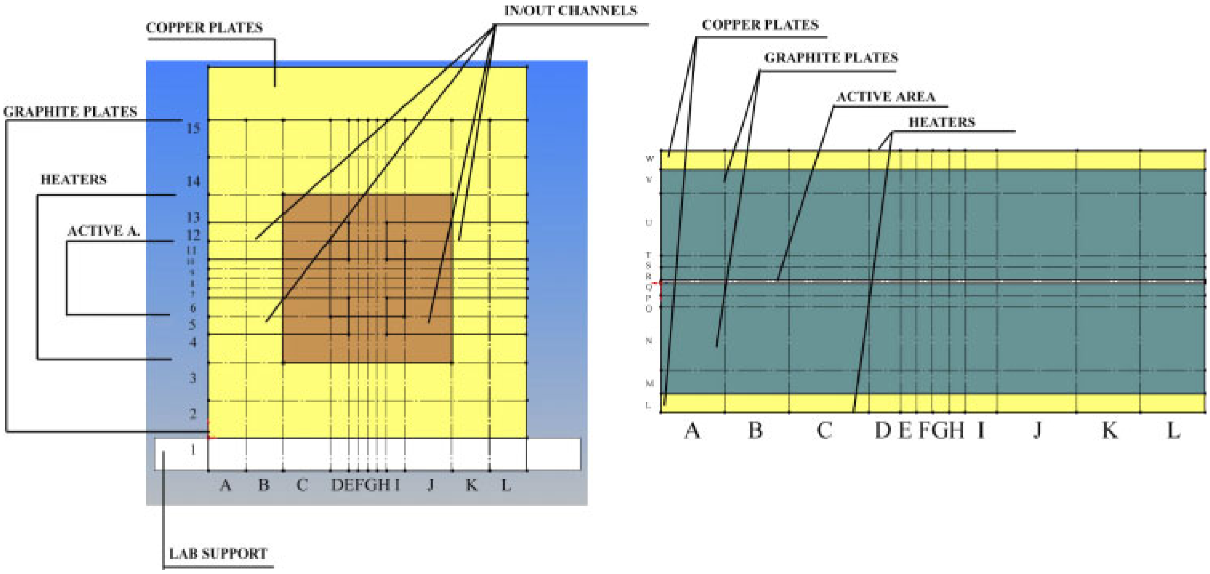

Figure 2. Single cell mesh. This figure is available in colour online at www.apjChemEng.com.

the implementation of controllers and to store the data. Inside a RTOS computer, there are CompactRIO cards with input/output modules that contain configurable signal conditioning, isolation, and screw terminals to provide direct connections to our sensors and actuators.

Experiments for parameter identification and verification

In order to adjust some unknown parameters such as global convective coefficient, internal contact resistances, and pressure drop constants to become known, and to verify the model, several experiments were performed, and simulated with the model (Fig. 3). These experiments were designed based on the data acquisition components and the fuel cell active area. All parameters were adjusted following a 'minimum global error' strategy.

The first set of experiments was designed to obtain the thermal constants (global convective coefficient and internal contact resistances) and check the thermal model (Tables 3 and 4). All of them were done without reactant flows. These experiments are divided into six groups:

- The flow of heaters current is adjusted in order to reach a thermal equilibrium inside the cell. This is done to calculate and verify the convection heat transfer parameter of the cell.
- The cell is heated using both heaters (no equilibrium is reached). This is done to calculate and verify convection parameter and heat capacity of the cell.
- The cell is cooled (no refrigeration system; no equilibrium is reached). This is done to verify all the previously stated parameters.
- The cell is heated using only one heater and the current flow is adjusted to reach thermal equilibrium inside the cell. This is to calculate and verify the convection parameter and internal contact resistances.
- The cell is heated with only one heater at maximum current (no equilibrium is reached). This is to verify all the previously stated parameters under different conditions.
- A temperature profile is followed turning the heaters on and off. This is done to verify all the previously stated parameters.

The adjusted parameters are given in Table 3.:

The second set of experiments was designed to check pressure drop inside the cell (Table 5), all of them were done with H_2/air, at different flow rates (0.5−1.5 SLPM), at different dew point and cell temperatures (30−80 °C), different currents (0−5 A), and with/without water condensation. It was impossible to work with low flow rates due to the extremely low pressure drops. Most of the experiments were done with flow rate 1.5 SLPM on both sides.

SELECTED RESULTS FOR THE SINGLE CELL TEST FIXTURE

This section presents selected results for the 2D temperature distribution snapshot as well as the temperature evolution in the cell.

Table 3. Thermal properties of the cell (adjusted).

	R_{ij} contact resistance ($W \cdot m^2/K$)	h convectivity ($W/(m^2 \cdot K)$)
Heating sides	–	12
Heaters	–	–
Copper plates	Copper−graphite 0	12
Graphite plates	Graphite−diffusion layer 0.00045	12
Diffusion layer	Dif. layer anode−membrane 0.00045	–
Gasket	Dif. layer cathode−membrane 0.00045	–
Membrane	–	–
Lab. support	–	9.23

Table 4. Heat balance for several experiments.

All measurements taken at two different temperature points	Two heaters: thermal equilibrium		Two heaters: full power		Two heaters: 1/4 power		One heater: thermal equilibrium	One heater: full power		No heaters	
$P_{heaters\_real}$ (W)	−15.12	−16,38	−100.28	−100.28	−28.50	−28.50	−16.38	−51.24	−51.24	0.00	0.00
P_{conv_mod} (W)	15.90	18.02	14.03	23.21	12.11	14.67	17.47	3.75	15.46	11.82	16.43
P_{stored_mod} (W)	0.00	0.00	95.32	67.28	13.29	12.37	0.00	51.66	36.10	−14.59	−15.82
Error (W)	0.78	1.64	9.07	−9.79	−3.10	−1.46	1.09	4.17	0.31	−2.77	0.62

DOI: 10.1002/apj

Table 5. Pressure drop constants (adjusted).

	H_2	Air
K_{lin} (s^2/m^3)	3.7×10^{12}	9×10^{12}
K_{sing} ($Pa \cdot s^2/kg \cdot m^3$)	1.8×10^{12}	1.9×10^{12}
K_w (Pa·s/kg)	2.8×10^7	7.5×10^7

The comparison between acquired data and simulated with the Matlab model is shown in Figure 3.

Temperature distribution inside the fuel cell at a fixed time

Figures 4–6 show the temperature distribution across the fuel cell and the change in the inlet and outlet reactant temperatures at a given time where every rectangle represents the temperature of a cuboid. This corresponds to a small fuel cell where the majority of the heat comes from two contact resistances, one on each side. It is critical to determine the thermal distribution because of its relationship with the phase change of water.

Evolution of fuel cell temperature over time

The model simulates the evolution over time of every cuboid temperature and temperature of the reactant. This allows for the simulation of nonequilibrium temperature pattern in the fuel cell. Figure 7 shows the temperature evolution through time, at a fixed location in the fuel cell while the heaters are cycled on and off.

Figure 8 shows relative humidity of the gases and liquid water content, through the anode and cathode. These illustrations are important in order to determine if and where water is condensing inside the fuel cell, which is a key factor in fuel cell efficiency and stability. In this case, on the anode side the hydrogen reaches its saturation temperature at the first node entering the fuel cell and starts condensing; however, on the cathode side the air reaches its saturation temperature at the third node.

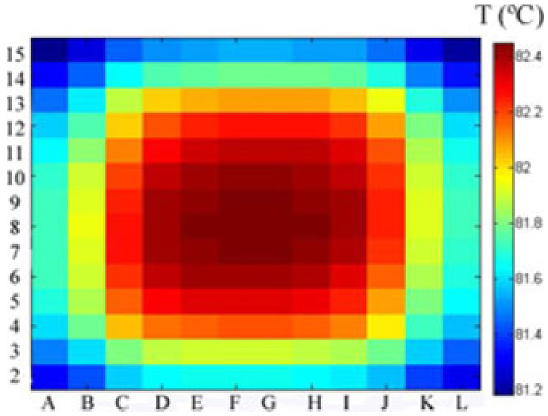

Figure 4. Longitudinal cut of the cell. This figure is available in colour online at www.apjChemEng.com.

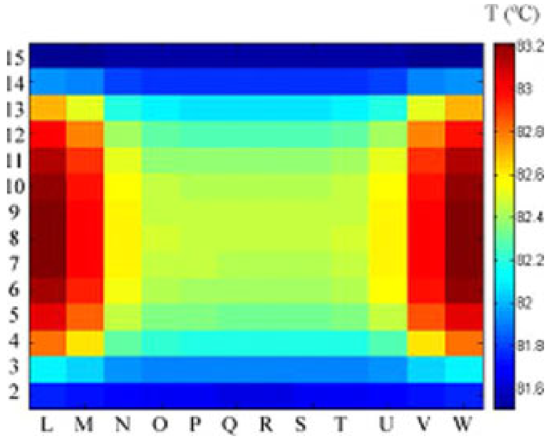

Figure 5. Transversal cut of the cell. This figure is available in colour online at www.apjChemEng.com.

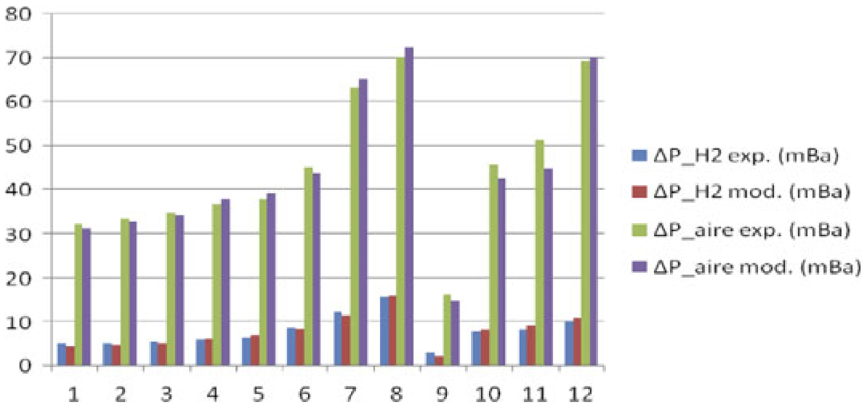

Figure 3. Pressure drop comparison of experimental data with simulated data. This figure is available in colour online at www.apjChemEng.com.

DOI: 10.1002/apj

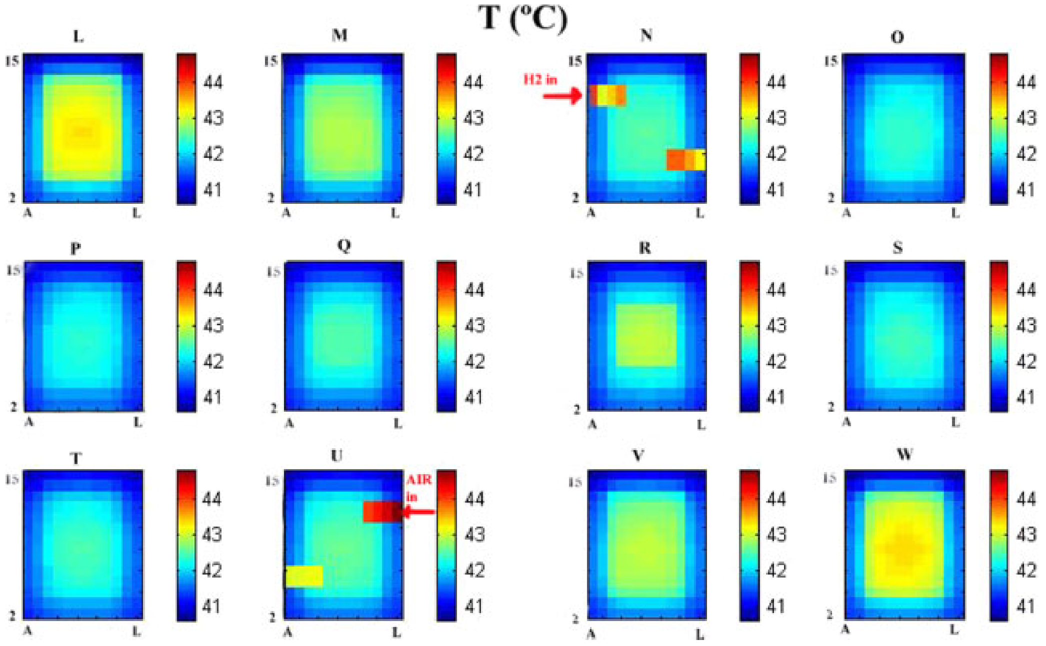

Figure 6. Longitudinal cuts through the cell at a given time. This figure is available in colour online at www.apjChemEng.com.

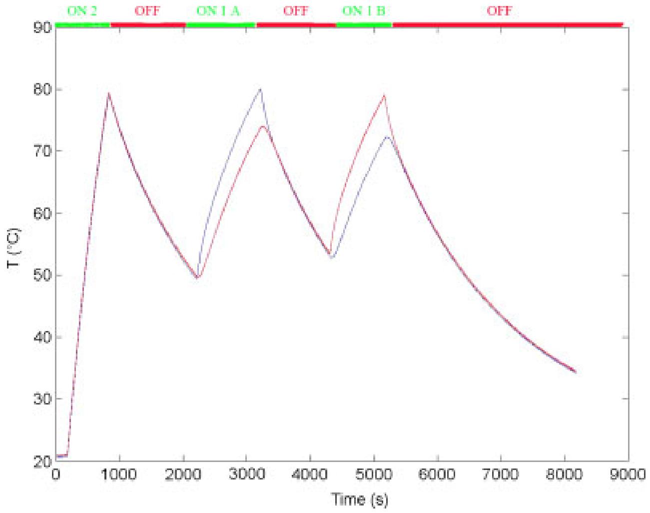

Figure 7. Temperature evolution with respect to time at two fixed points in the fuel cell. One in the anode side and one in the cathod side. This figure is available in colour online at www.apjChemEng.com.

Figure 9 shows the current at which water condenses inside the active area (critical current), for different temperatures and flow rates. Any point above each line will result in condensation in the flow field at the given conditions. Raising the current while all the other parameters remain constant will eventually lead to water condensation inside the active area. This model is designed to determine this critical maximum current.

Figure 10 shows the pressure drop in the channels for a fixed flow rate and the difference in temperature between the fuel cell and dew point while modifying the current. The discontinuity corresponds to the critical current. The simulation shows the sensitivity of condensation of water with respect to fuel cell and dew point temperatures, current, and flow rates. A one-degree change in the temperature difference greatly affects the critical current. Increasing overall temperature increases the capacity of the gases to remove water in the vapor form which, in turn, increases the critical current.

Figure 11 shows the pressure drop for the reactant gases with a fixed stoichiometry and temperature versus modifying the current. Increasing the current implies increasing the flow rate, which provokes a greater pressure drop inside the cell. It can be seen that both dew point temperature and stoichiometry have a great effect on the pressure drop. This is due to the quantity of water added to the cell.

CONCLUSIONS

In this work, a three-dimensional model of heat distribution and pressure drop for PEMFC was developed and experimentally tested. It includes a simple two-phase flow pressure drop model that is representative of the true effects of liquid water in the flow field. The model is especially suited for the analysis of liquid water condensation in the reactant channels.

The model was applied to a single cell test fixture and some of the parameters were adjusted through a series of experimental tests. The model was validated using experiments designed for this purpose. The

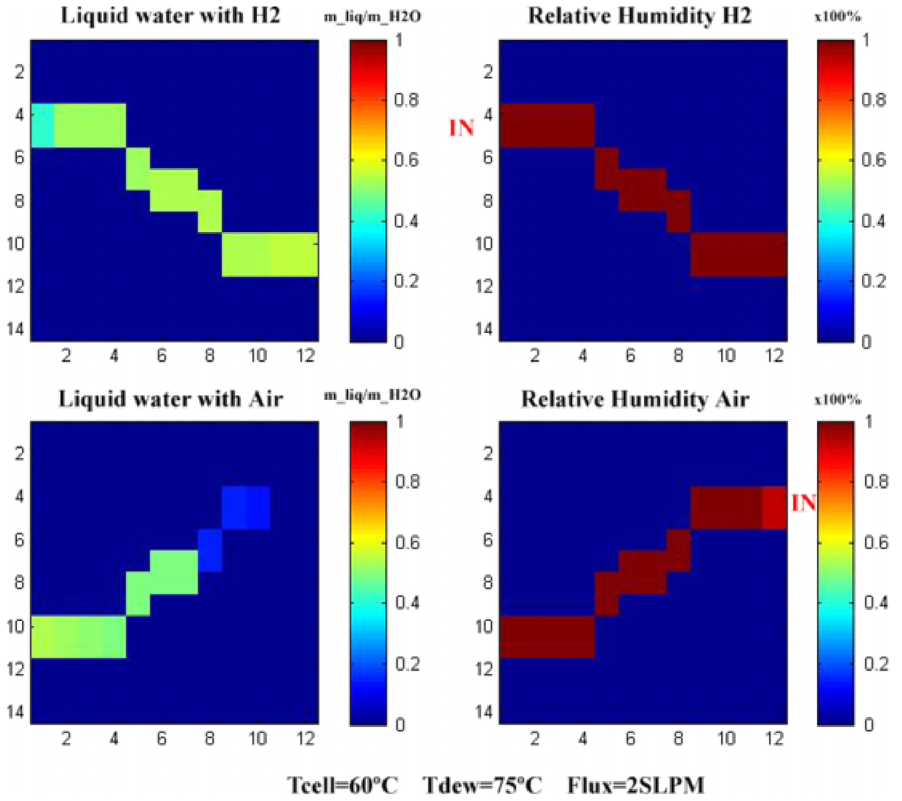

Figure 8. Relative humidity and liquid water content of the reactant gases through the cell. This figure is available in colour online at www.apjChemEng.com.

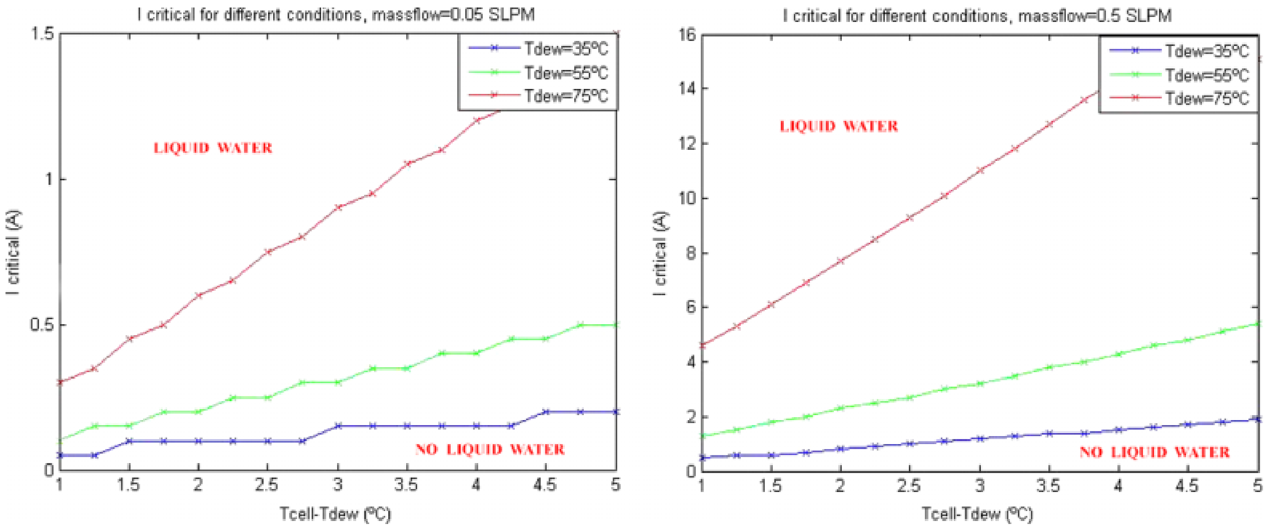

Figure 9. Critical current with respect to ΔT between fuel cell and reactant dew point. This figure is available in colour online at www.apjChemEng.com.

identified parameters are contact resistances, convective heat transfer coefficients, and pressure drop constants.

Several simulations were performed and analyzed. The results show that there is a step jump in the pressure drop when the critical current is reached. This determines the maximum current that should be applied to the fuel cell to avoid flooding of the catalyst layers and diffusion layers. Critical currents and the effects of liquid water and water vapor on the pressure drop of the fuel cell were evaluated for a range of operating conditions. The model shows that the current at which water condenses inside the reactant channels (or critical current) depends strongly on the flow rate and even more

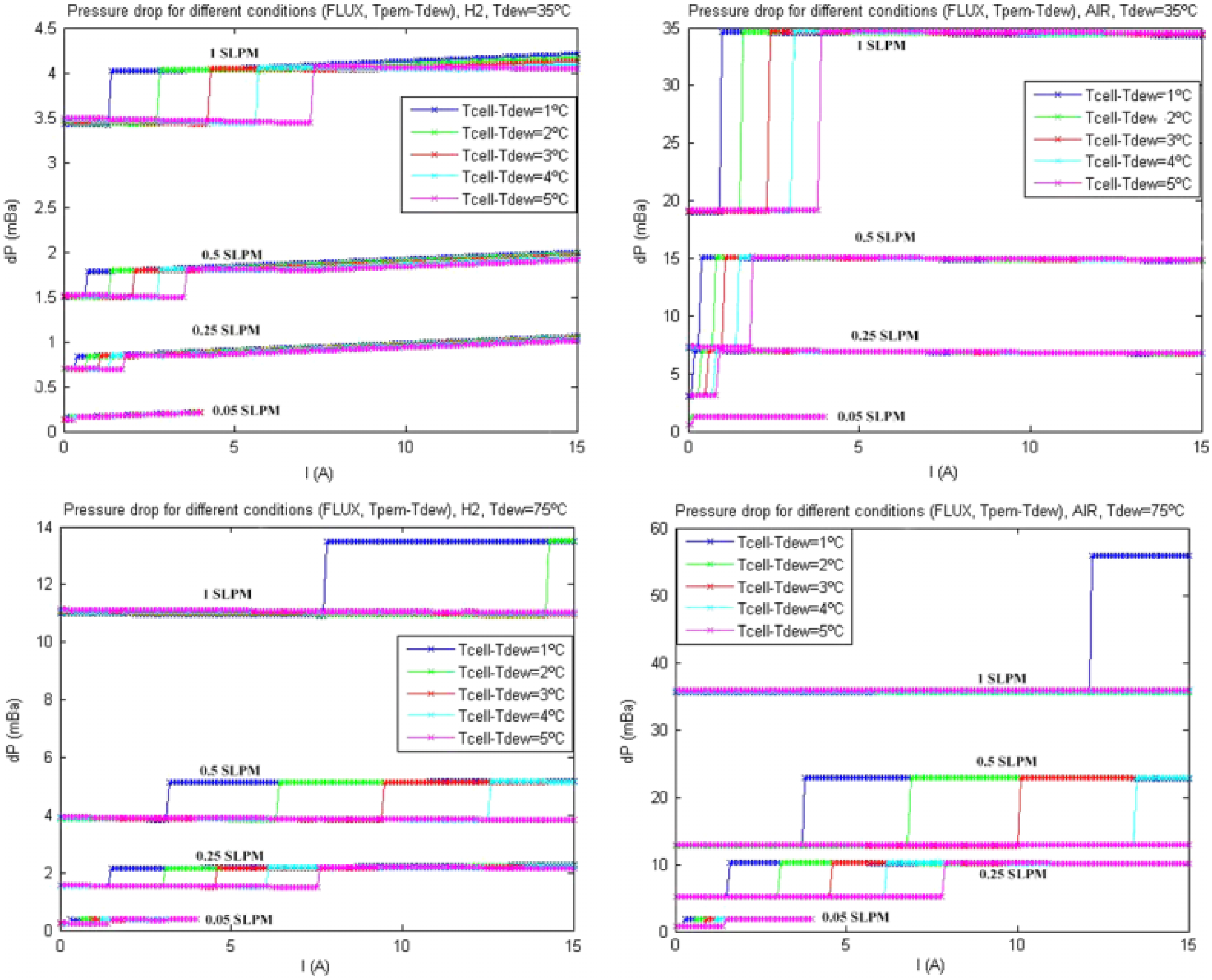

Pressure drop for different conditions (FLUX, Tpem-Tdew), H2, Tdew=35°C

Pressure drop for different conditions (FLUX, Tpem-Tdew), AIR, Tdew=35°C

Pressure drop for different conditions (FLUX, Tpem-Tdew), H2, Tdew=75°C

Pressure drop for different conditions (FLUX, Tpem-Tdew), AIR, Tdew=75°C

Figure 10. Pressure drop against current, fixed mass flow. This figure is available in colour online at www.apjChemEng.com.

on the temperature difference between the fuel cell and the reactant dew point. The model also shows that lower overall temperature gives a smaller critical current.

FUTURE WORK

Improvements in future versions of the model are the following:

- To apply the model to a fuel cell stack.
- to introduce more complex equations to model the pressure drop inside the cell. To achieve it, it is necessary to apply the model to a fuel cell (not single cell) with higher pressure drops and lower stoichiometry in order to have a greater range of possible experiments. For the operating range of the single cell in the lab, it has been confirmed that this simple model is quite enough.
- to introduce more complex equations to model water movements inside the active area. Once again, that will be necessary when modeling a fuel cell stack. As a reference, these equations can be found at Ref. [2].
- to introduce an electrical model, it is to say, a submodel which determines cell voltage at working conditions.

The following are some of the future objectives of research that will be conducted with more lab experiments and aids of models.

- To determine the quantity of liquid water that remains inside the cell dynamically and in steady state.
- To determine or verify the water movements inside the active area. It is related to figure 10.
- Create a more universal and precise approximation of section reduction due to liquid water formation inside the cell.

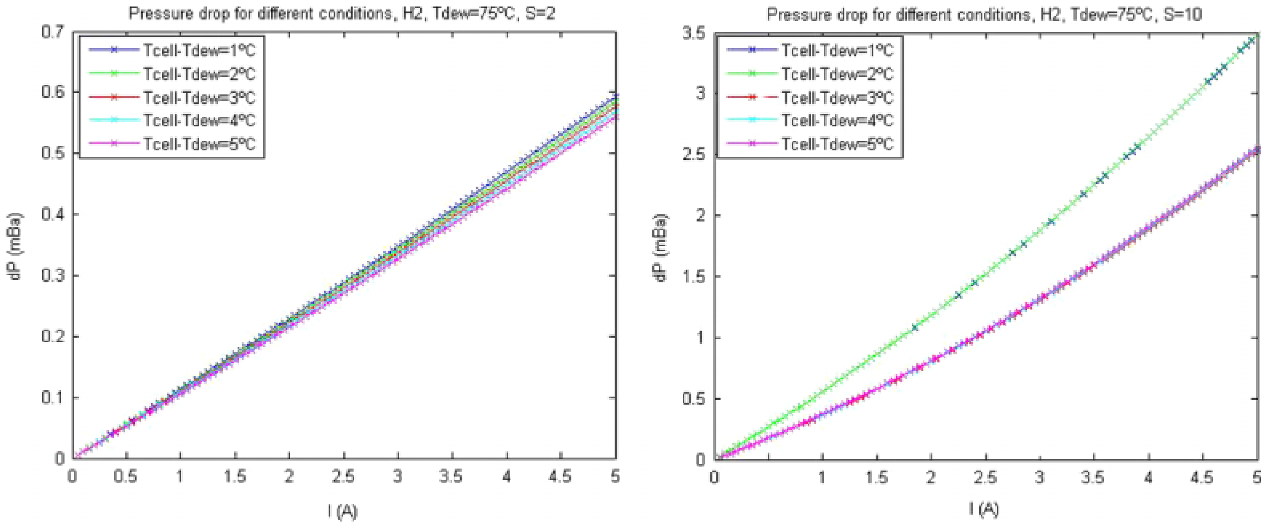

Figure 11. Pressure drop against current, fixed stoichiometry (analog for Air). This figure is available in colour online at www.apjChemEng.com.

Acknowledgements

This work has been funded partially by the projects CICYT DPI2007-62966 and CICYT DPI2004-06871-C02-01 of the Spanish Government.

MODEL AND CONTACT

The implementation in Matlab/Simulink of the model for the single cell used in our laboratory can be found at the following address:http://wikiri.upc.es/wiki/

NOMENCLATURE

A_{ij}	Contact area between nodes i and j (m^2)
c_{p_i}	Thermal capacity of fluid i (J/kgK)
c_{pm}	Thermal capacity of the flow at average conditions (J/kgK)
C_i	Thermal capacity of node i, $C_i = \rho_i V_i c_i$ (J/K)
c_i	Thermal capacity of node i (J/kg K)
D	Channel hydraulic diameter (m)
F	Faraday constant 96485 (C/mol)
g_i^k	Heat generated in node i at time k(W/m^3)
h_i	Convection coefficient of node i (W/m^2K)
h_m	Convection coefficient of the flow, evaluated at average conditions (W/m^2K)
H_r	Relative humidity of the flow
I	Fuel cell current (A)
K_{ij}^k	Thermal transfer coefficient between nodes i and j at discrete time k (W/mK)
K_{wd1}	Quantity of generated water going into the H_2 side
K_{wd2}	Quantity of generated water going into the air side
K_{lin}	Major pressure drop dimensional constant ($1/m^3$)
K_{sing}	Minor pressure drop dimensional constant ($1/m^4$)
K_{w}	Pressure drop constant due to liquid water (1/ms)
K_{ga} (K_{gc})	Percentage of total heat generation due to the reaction, produced in anode (cathode)
l_i	Width of node i in the axis perpendicular to contact area between nodes i and j (subindex mem for membrane) (m)
L	Channel length (m)
$\dot{m}_{xx}$	Mass flow of fluid xx (kg/s)
$\dot{m}_m$	Mass flow of gases at average conditions (kg/s)
M_{xx}	Molar mass of element xx (g/mol)
$\dot{n}_i$	Molar flux of fluid i (mol/s)
P_{xx}	Partial pressure of fluid xx (Pa)
P	Total pressure of gases (Pa)
$P_{\text{st}}(T_{\text{in}})$	Saturation pressure of water at temperature T_{in}
ΔP_{lin}	Pressure drop due to major losses (Pa)
ΔP_{sing}	Pressure drop due to minor losses (Pa)

ΔP_{w}	Pressure drop due to liquid water inside channel (Pa)
Per	Channel hydraulic perimeter (m)
Per_{ww}	Effective channel hydraulic perimeter with liquid water (m)
$\dot{q}^{k}_{\mathrm{ch\_in/out}}$	Heat transfer between gases and in/out channel walls (W)
$\dot{q}^{k}_{\mathrm{ch\_aa}}$	Heat transfer between gases and active area channel walls (W)
$\dot{q}^{k}_{\mathrm{g}}$	Thermal generation inside the active area due to the reaction (W)
$R_{\mathrm{cont\_}ij}$	Contact thermal resistance between nodes i and j (Wm^2/K)
$R_{\mathrm{cont\_an-mem}}$ and $R_{\mathrm{cont\_mem-cat}}$	Contact thermal resistance between anode and membrane (membrane and cathode respectively) (Wm^2/K)
S	Channel cross section (m^2)
S_{ww}	Effective channel cross section with liquid water (m^2)
T_i^k	Temperature of node i (for $i = 1\ldots N$, where N equals the number of cubes inside the mesh), at time k (K)
$T = (T_1 \ldots T_N)^t$	Vector of nodal temperatures
T_{out}	Gas temperature out (K)
T_{ch}	Temperature of the nodes in contact with gases (K)
T_{in}	Gas temperature in (K)
Δt	Time elapsed between instants k and $k+1$ (s)
V_i	Volume of the cube represented by node i (m^3)
V	Voltage given by the fuel cell (V)
v	Velocity of the gas (m/s)
λ_i	Thermal conductivity of fluid i of the flow or thermal conductivity of node i (subindex mem for membrane) (W/mK)
λ_m	Thermal conductivity of the gases at average conditions (W/mK)
η	Fuel cell efficiency
ρ_i	Density of fluid i of the flow or density of node i, what corresponds (kg/m^3)
ρ_m	Density of the gas at average conditions (kg/m^3)
ρ	Density of the gas (kg/m^3)
μ_i	Viscosity of fluid i (Pa·s)
μ	Viscosity of the gas (Pa·s)
∞	Subindex, represents ambient node

REFERENCES

[1] T.E. Springer, T.A. Zawodzinski, S. Gottesfeld. *J. Electrochem. Soc.,* **1991;** *138*(8), 2334–2342.

[2] T.V. Nguyen, R.E. White. *J. Electrochem. Soc.,* **1993;** *140*(8), 2178–2186.

[3] K. Broka, P. Ekdunge. *J. Appl. Electrochem.,* **1997;** *27*(3), 281–289.

[4] M. Coppo, N.P. Siegelb, M.R. Von Spakovskyc. *J. Power Sources,* **2006;** *159*(1), 560–569.

[5] D.M. Bernardi, M.W. Verbrugge. *J. Electrochem. Soc.,* **1992;** *139*(9), 2477–2491.

[6] Y. Shan, S.Y. Choe. *J. Power Sources,* **2005;** *145*(1), 30–39.

[7] S. Um, C.Y. Wang. *J. Power Sources,* **2006;** *156*(2), 211–223.

[8] F.P. Incropera, D.P. DeWitt. *Introduction to Heat Transfer*, Wiley, New York: **1996**.

[9] F.M. White. *Fluid Mechanics*, McGraw-Hill, New York: **1999**.

[10] F. Barbir. *PEM Fuel Cells: Theory and Practice*, Elsevier Inc., New York: **2005**.

[11] M.J. Lampinen, M. Fomino. *J. Electrochem. Soc.,* **1993;** *140*(12), 3537–3546.

[12] H. Ju, H. Meng, C.Y. Wang. *Int. J. Heat Mass Transfer,* **2005;** *48*(7), 1303–1315.

[13] A. Burcat, B. Ruscic. *Third Millennium Ideal Gas and Condensed Phase Thermochemical Database for Combustion*, Technical Report Argonne National Lab, Chicago: **2005**.

[14] F. Barbir, H. Gorgun, X. Wang. *J. Power Sources,* **2005;** *141*(1), 96–101.

[15] L. You, H. Liu. *Int. J. Heat Mass Transfer,* **2002;** *45*(11), 2277–2287.

[16] V. Gurau, H. Liu, S. Kakaç. *AIChE J.,* **1998;** *44*(11), 2410–2422.

Journal of Power Sources 196 (2011) 4251–4263

Contents lists available at ScienceDirect

Journal of Power Sources

journal homepage: www.elsevier.com/locate/jpowsour

Development and experimental validation of a dynamic thermal and water distribution model of an open cathode proton exchange membrane fuel cell

Stephan Strahl, Attila Husar, Maria Serra*

Institut de Robòtica i Informàtica Industrial (CSIC-UPC), Parc Tecnològic de Barcelona, C/Llorens i Artigas 4-6, 08028 Barcelona, Spain

ARTICLE INFO

Article history:
Received 13 August 2010
Received in revised form 14 October 2010
Accepted 25 October 2010
Available online 10 November 2010

Keywords:
Proton exchange membrane fuel cells
Water transport
Electroosmotic drag
Water diffusion
Thermal management

ABSTRACT

Water concentration in proton exchange membrane (PEM) fuel cells strongly influences performance and durability which demands for fundamental understanding of water transport mechanisms. The system efficiency can be significantly improved with greater understanding of water flux dynamics through the membrane and its dependence on the internal conditions of the fuel cell. Therefore, a two-dimensional, non-isothermal, dynamic model of a 100 W open cathode, self-humidified PEM fuel cell system has been developed, that is capable of representing system specific control mechanisms for water and thermal management. The model consists of three coupled submodels based on energy, momentum and water mass balance of the system. The work is based on experimental observations of the investigated fuel cell stack, for which the crucial coefficients for water transport, namely the diffusion and the electroosmotic drag (EOD) coefficient have been determined. The diffusivity of water vapor through the MEA at 30 °C was determined to be $3.3 \times 10^{-8}\ \mathrm{m^2\,s^{-1}}$ and increases by $3 \times 10^{-10}\ \mathrm{m^2\,s^{-1}\,{}^\circ C^{-1}}$ up to 50 °C stack temperature. The EOD coefficient was measured as 0.47–0.48 water molecules per proton at stack currents from 1 to 3 A. Validation of the steady state and the dynamic model by using experimental data, directly obtained from laboratory tests, has shown that the model predictions match the experimental data well.

1. Introduction

For the past 20 years astonishing progress in terms of PEM fuel cell materials, component design, production, and system power density improvements have been achieved. However, there is still a lot to be done in the field of fuel cell system controls, which makes it essential to understand the different physical phenomena within a fuel cell and how they need to be controlled in order to improve efficiency, operating range and durability. The hypothesis is that if the water movement within a PEM fuel cell could be controlled quickly to maintain optimal membrane water content and minimal liquid water, efficiency would be improved. As shown in the experiments of Springer et al. [1], membrane proton conductivity is a strong function of water content. Thus, the performance of PEM fuel cells is sensitive to membrane hydration. Although water is produced during the reaction, the anode catalyst layer is often dehydrated because water is dragged from the anode to the cathode by protons moving through the membrane, which is called electroosmotic drag (EOD).

Besides the EOD, the main water transport mechanism in a PEM fuel cell is diffusion through the membrane due to concentration differences between anode and cathode. The third transport mechanism is hydraulic permeation, which is caused by pressure difference. EOD always transports water from the anode to the cathode whereas diffusion can occur in both directions.

Water is needed to maintain good proton conductivity and therefore has to be kept in the membrane, however liquid water on the catalyst reduces the active area, and in the GDL it hinders the reactant gases from diffusing to the catalyst surface and thus reduces performance. The goal is to maintain an optimal water concentration in the membrane electrode assembly (MEA) by keeping a balance between the two conflicting requirements. Thus, to control water transport within a fuel cell system and thereby optimize the membrane hydration at any operation point, proper dynamic water management strategies have to be developed. This has recently been analyzed by Hussaini and Wang [2].

In order to characterize, understand and manipulate the water transport mechanisms, experimental work is needed as well as a mathematical model that describes the physical phenomena [3].

A 2D isothermal model of the MEA of a PEM fuel cell including the influence of convection in the gas flow channels was developed by Gurau et al. [5]. This model accounts for the concentration variations along the interface between the gas diffusion layer and the catalyst layer, which is related to the gas transport in the coupled domain of the gas flow channel and the gas diffusion layer. However, fluid dispersion in the porous media is disregarded.

---

* Corresponding author. Tel.: +34 93 4015751; fax: +34 93 4015750.
E-mail address: maserra@iri.upc.edu (M. Serra).

0378-7753/$ – see front matter © 2010 Elsevier B.V. All rights reserved.
doi:10.1016/j.jpowsour.2010.10.074

Nomenclature

Symbols

A	cross-sectional area (m^2)
c	concentration ($mol\,m^{-3}$)
C_p	specific heat capacity ($J\,mol^{-1}\,K^{-1}$)
D	diffusion coefficient ($m^2\,s^{-1}$)
ϵ	EOD coefficient
η	efficiency
Φ_{H_2O}	water mass flux ($kg\,s^{-1}\,m^{-2}$)
Φ_q	heat flux ($W\,m^{-2}$)
H_{LHV}	lower heating value H_2 ($kJ\,mol^{-1}$)
I	current (A)
J	molar flux ($mol\,s^{-1}\,m^{-2}$)
k	thermal conductivity ($W\,m^{-1}\,K^{-1}$)
κ	permeability (m^2)
M	molar mass ($kg\,mol^{-1}$)
m	mass (kg)
$\dot{m}$	mass flow rate ($kg\,s^{-1}$)
μ	dynamic viscosity (Pa s)
n_{bpp}	number of bipolar plates
n_{cell}	number of cells
n_{cpp}	number of channels per plate
P	pressure (Pa)
Q	heat energy (W)
ρ	density ($kg\,m^{-3}$)
T	temperature (K)
t	time (s)
v	velocity ($m\,s^{-1}$)
V_{stack}	stack voltage (V)
W	work (W)
x_{H_2O}	humidity mass ratio

Subscripts

act	active
an	anode
ca	cathode
ch	channel
cons	consumed
d	dry
dp	dew point
el	electrical
gen	generated
in	inlet
m	measured
out	outlet
sc	short circuit
tot	total

The amount of waste heat produced by a PEM fuel cell is similar to its electrical power output, depending on its voltage. Moreover it only tolerates a small temperature deviation from its design point for best performance, stability and durability. Therefore a three-dimensional, non-isothermal model was developed by Ju et al. [6]. The model accounts for various heat generation mechanisms and combines them with the electrochemical and mass transport models. A three-dimensional, non-isothermal, two-phase flow model was developed by Wang and Wang [7], which was applied by Basu et al. [8] in order to study the phase-change phenomena in the cathode GDL of a PEM fuel cell and has finally been extended to a complete two-phase model for an entire PEM fuel cell, including two phase flow in the gas channels, by Basu et al. [9].

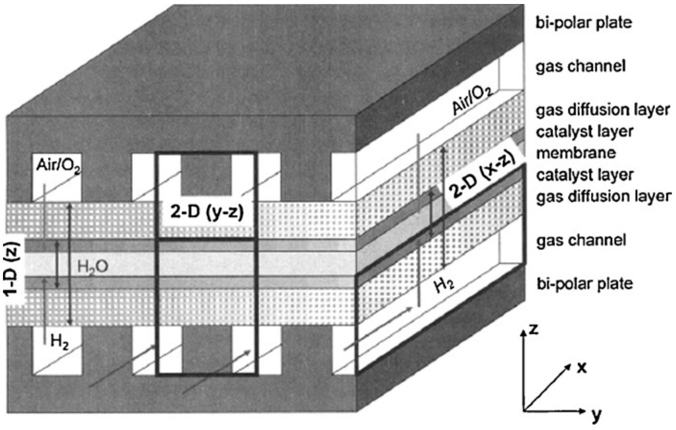

Fig. 1. 1D and 2D modeling domains for a PEM fuel cell [4].

Similar to the model of Gurau et al. [5], but considering fluid dispersion in the porous media, two modeling modes of a 2D isothermal model have already been implemented in COMSOL Multiphysics by Shi and Wang [10]. As defined in Fig. 1 the computational domain of a 2D model can either be a partial cross-section parallel (*x*–*z*-direction) or perpendicular (*y*–*z*-direction) to the gas flow direction in the gas channel. The *y*–*z*-model serves for analysis of fluxes and concentrations in the gas diffusion and catalyst layers and includes the effect of ribs or lands between the channels. This model is also used for investigating fuel cells with interdigitated flow patterns. If the field of study concentrates on the analysis of reactant gases and water vapor concentration along the channel, the *x*–*z*-model is preferred. The two models can be combined to describe the overall behavior of PEM fuel cells in all directions, as shown by Shi and Wang [10].

The water transport equations in most of these models are based on the *ex situ* water transport experiments of a Nafion 117 membrane performed by Springer et al. [1]. These experiments have created a baseline for the industry and show the relationship between EOD and water diffusion through the membrane with respect to membrane water activity and membrane temperature. Even though the diffusion and EOD data for the membrane were accurate, direct application of such data to a real fuel cell may not be appropriate due to the fact that this data was collected *ex situ*, and cannot be considered constant because the coefficients vary significantly depending on the membrane type and on the operating conditions, such as temperature. *In situ* experiments of Husar et al. [11] showed that the EOD of a Nafion 115 membrane increases significantly with temperature and current density and that water diffusivity of membrane is lower than that reported by Springer et al. [1].

A recently published review of water balance in the MEA by Dai et al. [3] states that further work is needed to better understand the fundamentals of water transport in the MEA, not only to improve performance, but also to develop new materials for better water management and to improve durability. In order to develop and simulate dynamic water management strategies that match the application load requirements and the operating conditions, new models need to be based on a broad understanding of water transport in the MEA.

This article describes the developed dynamic thermal and water distribution model, as well as the performed experimental work and the model validation of an open cathode, self-humidified PEM fuel cell.

2. Specific stack characteristics

This work treats the modeling of the water and heat transfer of the commercially available 100 W PEM fuel cell system H-100 from

Horizon Fuel Cells. This open cathode system is self-humidified and air cooled. It includes a cooling fan directly attached to the fuel cell housing, which removes heat from the stack by forced convection and at the same time provides oxygen to the cathode. The anode system has electromagnetic valves on both the inlet and outlet. The outlet valve is usually closed and the pressure is controlled by a forward pressure regulator. It mainly runs in a dead-ended mode, however a periodical hydrogen purge removes water and nitrogen that has crossed over from the cathode that would otherwise hinder the transport of reactant gas to the catalyst layer. A very quick short circuit is applied to the fuel cell to create water and heat in the cathode catalyst layer. With the manufactures' controller the interval of the hydrogen purge and the short circuit is independent of the stack conditions. This means that even if the fuel cell does not require a purge or a short circuit, the system performs it anyway, which reduces efficiency. In order to increase efficiency, without reducing the robustness or operating range of the system, a broad understanding of the water transport inside the fuel cell is necessary, which can be studied by the developed model.

3. Model description

3.1. Modeling strategy

The developed model is used to simulate and study the effects of the dynamic control mechanisms for water management, namely the fan, the periodical hydrogen purge and the short circuit to relate them to the fuel cell performance. By controlling the concentration of water vapor and the additional creation of water due to the short circuit, membrane hydration and fuel cell flooding can be managed. As water distribution and transport is dependent on temperature the model has to include not only the mass balance but also the energy balance of the H-100 fuel cell system. Since this model concentrates on the water transport within the cell, the current density distribution is not modeled. In order to facilitate the model, the current density at the cathode catalyst layer is assumed to be constant in the direction along the flow channel.

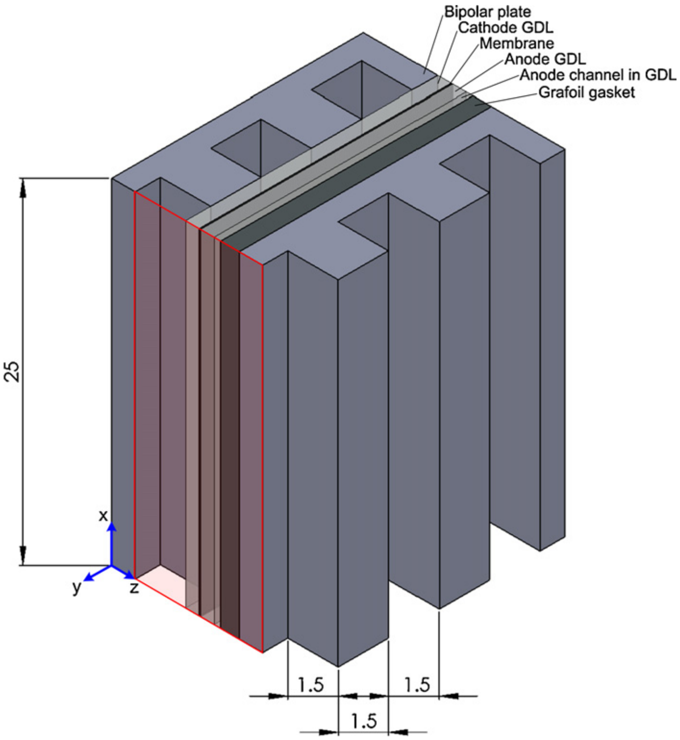

Fig. 2. H-100 stack configuration and modeled section.

To visualize the simulation results, the mathematical model is implemented in COMSOL Multiphysics, a finite element analysis software environment. By means of COMSOL the model can be solved numerically for the specific geometry.

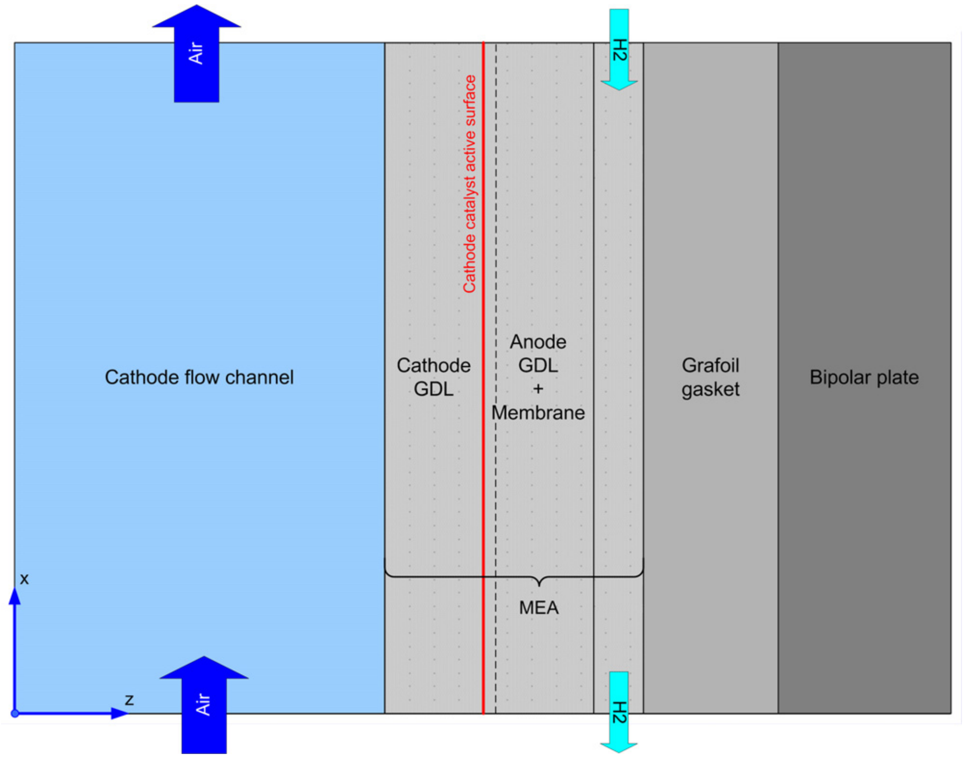

Fig. 3. Model geometric subdomains.

The trade off between accuracy and computing capacity should be considered in choosing the model dimension. Within this work a 2D model is developed that provides better simulation accuracy than 1D models and has a higher computational efficiency than 3D models, which also already exist in the literature [6,7,9].

Referring to Fig. 2, the 2D model describes water and heat propagation and distribution in the *x*–*z*-cross-section of a single cell within the stack. The cross-section can either go through a rib of a bipolar plate or through a channel. Since the primary objective of the model is to describe the effects of water transport, the air mass flow through the channel plays an important role and so the second option for the cross-section location is chosen. A 2D thermal analysis in the *y*–*z*-cross-section has shown that the temperature difference at the channel walls in the same plane is negligible, due to the relatively high thermal conductivity of the solid sections and the fully developed flow through the channel. Thus, the heat removal through the two land sides of one channel, that do not appear in the 2D model in the *x*-*z*-cross-section, is assumed to be equal to the heat removal through the other two channel walls. This simplification is valid in this model, because the channel is square and the thickness of the land is equal to the side of the square, as shown in Fig. 2. Considering also that the *x*–*z*-model is infinite in the *y*-direction, which means that there is an infinite channel without any land, the effective heat removal area in both models is equal. Thus the overall heat removal from the cell can be modeled by just one 2D model in the *x*–*z*-cross-section.

Fig. 3 shows the geometry in the *x*–*z*-plane of the modeled cell within the H-100 stack referred to the cross-section marked in red in Fig. 2. The modeled sub-domains for the simulation of water propagation and distribution are the cathode flow channel, the cathode GDL (including a microporous layer) and two anode GDL's (including a microporous layer). To simulate the heat transfer within the cell, the Grafoil gasket and the bipolar plate also have to be considered, due to conductive heat transfer. The right boundary of the bipolar plate is equal to the left boundary of the cathode flow channel in terms of heat transfer, because only one repeating unit of the stack is modeled.

In terms of modeling, the material properties and dimensions of the components, as well as the anode channel configuration have to be known. The thicknesses of the different layers are listed in Table 1. The channel length is 25 mm.

Since the material of the membrane is unknown, a bulk diffusion coefficient for the whole MEA was determined experimentally. The MEA on the cathode side includes the GDL and the microporous diffusion layer and the cathode catalyst layer. On the anode side the MEA includes the membrane, anode catalyst layer, microporous diffusion layer, and two GDL's. To clarify, the membrane is included in the first anode GDL, which is denoted by the dashed line in Fig. 3. Thus, in terms of water transport and generation the more important cathode catalyst boundary still remains.

According to the model geometry, Fig. 4 shows a schematic of the different physical phenomena that occur within the fuel cell, how they are coupled to each other and how they are treated in the model.

Table 1
H-100 component thicknesses.

Component	Thickness (mm)
Bipolar plate web	0.70
Grafoil gasket	0.55
Anode GDL (flow channel)	0.20
Anode GDL (cover)	0.20
Microporous layer	0.20
Membrane	0.05
Cathode GDL	0.20
Cathode flow channel	1.50

The heart of the model is the water transport submodel, which describes the distribution of water vapor concentration in the MEA and the flow channels. In order to describe convective transport, the water transport submodel is coupled to the momentum transport sub models of anode and cathode, which themselves are linked with the water transport submodel because the density of the reactant gases is dependent on the amount of water in the gas. Since density is also dependent on temperature, the energy transport submodel has to be included, as well. As shown in Section 4, the diffusion coefficient is also a function of temperature, which links the diffusive mass transport to the temperature distribution. The water transport from anode to cathode due to the electroosmotic drag effect is a function of the stack current, which is set by the external load.

The energy transport model, which describes the temperature distribution within the cell includes not only conductive heat transfer through the MEA, the Grafoil gasket and the bipolar plate, but also the convective cooling by the fan. Therefore it is coupled to the velocity field in the cathode channel, obtained by the momentum transport submodel, as described in Section 3.2.2.

Depending on the external load, a certain amount of heat and water is generated at the cathode catalyst surface due to the electrochemical reaction. This generation can be described by the stack current and voltage that is set by the external load. The resulting fluxes of water and heat are treated as an input to the water and energy transport submodel, respectively. The different submodels are explained in the following sections.

A further submodel that describes charge transfer and polarization curve affected by the different types of voltage losses is not included in this work, because the needed parameters to determine voltage losses, such as exchange current density and charge transfer coefficient, are difficult to validate with *in situ* testing.

This model considers that water enters and exits the fuel cell in the vapor state on both anode and cathode. Regarding the cathode, water vapor that enters the cell has the relative humidity of the environment. On the cathode outlet there is always a stoichiometry greater than ten that does not allow the gas to reach 50% relative humidity at an outlet gas temperature of approximately 45 °C, which has also been verified by experiments. Thus, a single-phase model on the cathode side is accurate. The only controversial part would be the anode where the water could condense. Since the anode reaction is orders of magnitude faster than the cathode reaction and hydrogen's diffusivity is much higher than oxygen's, the effects of liquid water on the anode can be neglected for the sake of model simplification. So the model properly predicts water and temperature distribution in the flow channels and the GDL, even without including two-phase flow.

Table 2 shows how the COMSOL application modes are applied to the specific subdomains. These application modes are linked to the different submodels, which are explained in the following section.

3.2. Mathematical model description

3.2.1. Energy transport

The amount of energy brought into the fuel cell system is given by the lower heating value of hydrogen, because it is assumed that all of the product water leaves the stack as vapor. The energy output is split into electrical energy and heat, thus the energy balance of the system is given by:

$$W_{H_2} = W_{el} + Q_{tot} \tag{1}$$

The total generated heat Q_{tot} can be determined using the fuel cell efficiency, which is defined by the ratio of the energy output and the energy input of the system. According to Eq. (1) this is the ratio

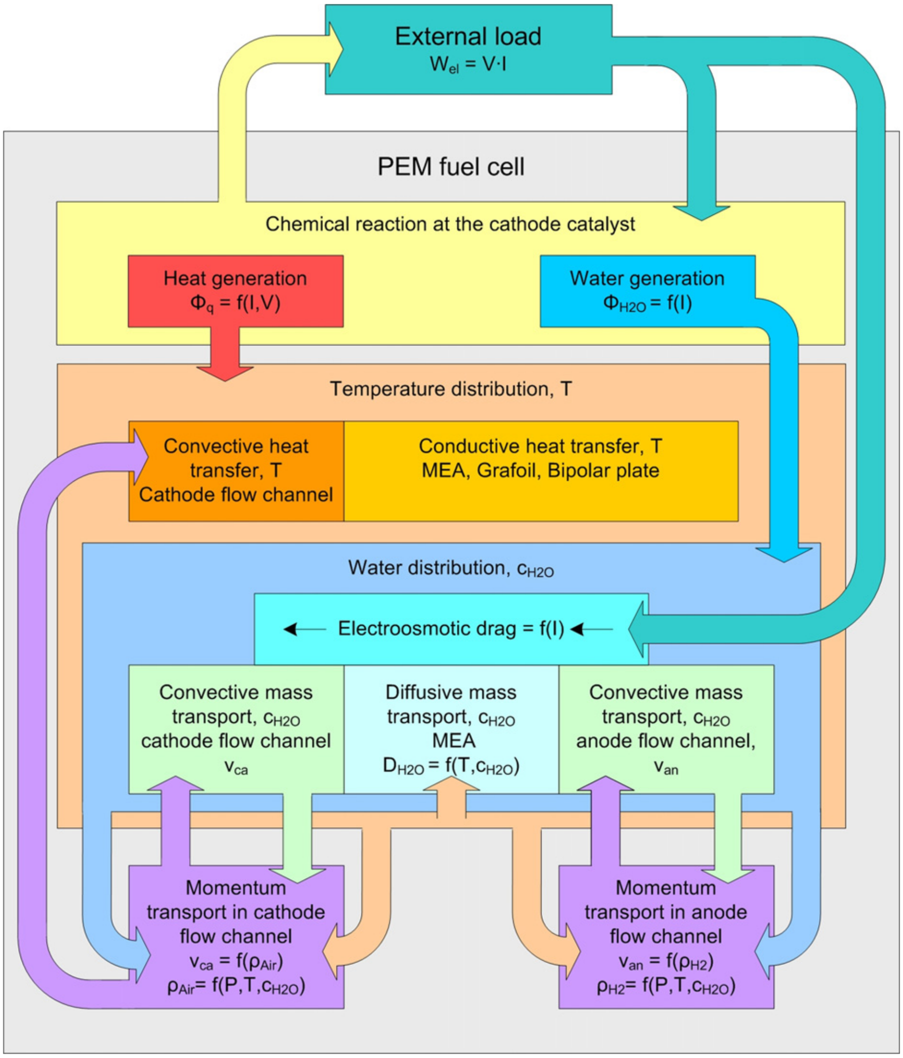

Fig. 4. Model schematic.

of useful electrical work and the work of the consumed hydrogen:

$$\eta = \frac{W_{el}}{W_{H_2}} \tag{2}$$

The work of the consumed dry hydrogen at 25 °C can be calculated using hydrogen's lower heating value [4]:

$$W_{H_2} = \frac{H_{LHV}}{2 \cdot F} \cdot I \cdot n_{cell} \quad [\mathrm{W}] \tag{3}$$

Combining Eqs. (2), and (3) leads to the fuel cell stack efficiency:

$$\eta_{LHV,stack} = \frac{V_{stack}}{1.254 \cdot n_{cell}} \tag{4}$$

Current and voltage values that are used to calculate efficiency are obtained by in-house experimental data of the studied fuel cell stack. The stack efficiency can then be used to describe the total generated heat energy by including Eq. (4) into (1):

$$Q_{tot} = W_{H_2} - W_{el} = W_{el} \cdot \left(\frac{1}{\eta_{LHV,stack}} - 1 \right) \quad [\mathrm{W}] \tag{5}$$

Assuming that all the generated heat energy is released on the cathode catalyst layer, the heat flux through this boundary is determined by the generated heat divided by the active area:

$$\Phi_q = \frac{Q_{tot}}{A_{act}} \quad [\mathrm{W\,m^{-2}}] \tag{6}$$

Heat is transferred by two mechanisms within the fuel cell. The cathode flow channel is dominated by forced convection due to the fan, whereas the heat transfer through the MEA and the bipolar plate is mainly by conduction, which can be seen in the heat transfer simulation results in Fig. 5. Although there is also convection due to

Table 2
COMSOL application modes used in the different model subdomains.

	General heat transfer	Incompressible Navier–Stokes	Darcy's law	Convection and diffusion
Cathode flow channel	X	X		X
Cathode GDL	X			X
Anode GDL + membrane	X		X	X
Anode channel in GDL	X		X	X
Bipolar plate + Grafoil	X			

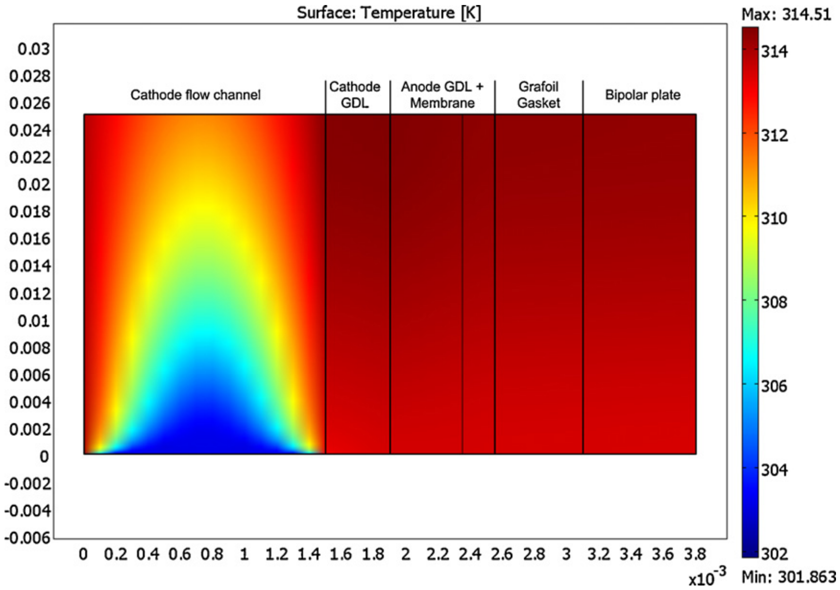

Fig. 5. Typical temperature distribution in the cell and the cathode flow channel (*x* and *y* axis dimensions are in meters).

the diffusing reactants, this transport can be considered negligible because of the high thermal conductivity of the GDL material [6].

Several thermal analyses and models of non-insulated PEM fuel cells e.g. by Mller and Stefanopoulou [12] have shown that the heat loss to the environment by convection and radiation is between 10% and 20% of the total waste heat. Since the fuel cell stack used to validate the model is encased in a plastic support structure, it is assumed that the heat loss to the environment is minimal and thus neglected. Therefore, only heat removal from the system by convective heat transport through the cathode gas channel is considered.

Using conservation of energy, the heat equation that describes conduction and convection within the fuel cell results in [4]:

$$(\rho C_p)\cdot\frac{\delta T}{\delta t}+(\rho C_p)\cdot\vec{v}\cdot\nabla T=\nabla(k\cdot\nabla T)+S_e \tag{7}$$

The first term of the left-hand side describes the heating rate and the second term the heat flux due to convection. The first term on the right-hand side accounts for conductive heat flux through the media with the thermal conductivity k, described by Fourier's law. The source term S_e represents heat flux due to other heat sources or sinks, which in this case is the source heat flux through the catalyst surface, described by Eq. (6).

The velocity vector $\vec{v}$ is obtained by solving the Navier–Stokes equation for momentum transport within the cathode flow channel, which is explained in Section 3.2.2.

The input parameters of the model are the inlet air temperature of the cathode, which is necessary to determine the heat removal from the cell by convection, as well as the cell voltage and current that are used to calculate heat generation at the cathode catalyst as already described in Section 3.2.1. The submodel schematic, including all inputs and outputs, is shown in Fig. 6.

The energy model is coupled with every other sub-model because temperature has a significant effect on the fluid properties, such as densities of the reactant gases, their dynamic viscosities and also on the diffusivity of water through the MEA.

In the H-100 system heat is produced due to the electrochemical reaction, as well as periodically due to the short circuit that is applied every 10 s, as described in Section 2.

During a short circuit the useful electrical energy is zero. This means that all the energy is transformed into heat, which increases temperature inside the fuel cell stack. Nevertheless some energy is lost due to circuit and contact resistance, but is neglected at this point. Thus, knowing the short circuit current, as defined later in Section 3.2.4, the released heat of one cell can be calculated using Eq. (3):

$$W_{H_2}=\frac{H_{LHV}}{2\cdot F}\cdot I_{sc}(t)=Q_{sc}\quad[\mathrm{W}] \tag{8}$$

3.2.2. *Cathode momentum transport*

In order to describe convective mass transport and heat transfer through the cathode flow channel forced by the fan, the momentum transport has to be determined.

The Reynolds number for the H-100 cathode flow channels at maximum flow velocity turned out to be 120. Knowing that the air flow through the channels is laminar and that the pressure difference along the channels and the change in fluid density are also very small, the Navier–Stokes equation for an incompressible fluid can be used to model the momentum transfer through the cathode flow channels [13]:

$$\rho\left(\frac{\partial\vec{v}}{\partial t}+\vec{v}\cdot\nabla\vec{v}\right)=\nabla\{-P\vec{I}+\mu[\nabla\vec{v}+(\nabla\vec{v})^{\mathrm{T}}]\} \tag{9}$$

By solving this equation numerically, the velocity field in the cathode flow channel can be obtained. Fig. 7 shows a schematic with all input and output parameters of the submodel.

Since the velocity is dependent on the gas density, which is a function of temperature, pressure and water concentration, this model has to be coupled with the energy and water transport submodel. The boundary conditions for the model are an inlet velocity v_0 and a constant outlet pressure.

As the cathode air flow determines the amount of heat that is removed from the stack, it has to be controlled by the fan according to the stack temperature. Control strategies can be tested in the model simply by changing the inlet boundary condition from a constant velocity to the desired temperature dependent boundary expression, which is then coupled to the energy transport model.

3.2.3. *Anode momentum transport*

As already described in Section 2 the anode is purged periodically every 10 s. This results in a convective flux through the anode GDL which removes product water from the GDL and the catalyst layer. Because this pressure driven convective flux occurs in

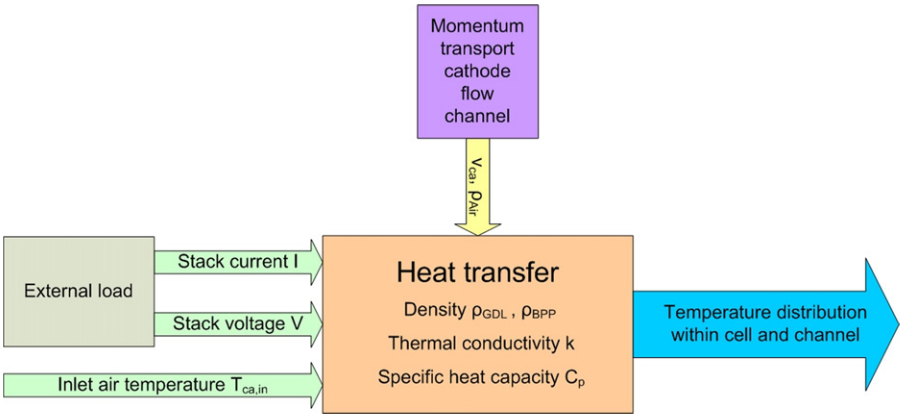

Fig. 6. Schematic of the heat transfer model.

a porous media, the velocity field can be calculated by Darcy's law [13]:

$$\vec{v} = \frac{-\kappa}{\mu}\nabla P \tag{10}$$

where κ denotes the hydraulic permeability of the porous medium and μ the dynamic viscosity of the fluid.

The anode inlet gas velocity is determined by the measured mass flow rate. Thus, knowing the velocity and pressure difference from inlet to outlet, the permeability of the GDL, including the microporous layer, turned out to be $10^{-12}\,m^2$, which accords to the work of Shi et al. [14] and also is used in the models of Shi and Wang [15] and Meng and Wang [16]. The calculated velocity vector is coupled to the water transport model in the anode GDL during a purge to describe the convective mass transport. Fig. 8 summarizes the inlet and outlet parameters of the model.

Just as in the cathode flow model, the anode flow model also has to be coupled to the energy and water transport model due to the changes in gas density.

3.2.4. *Water transport*

In order to determine the water transfer rate, which is required for proper water management in the fuel cell and to validate experimental and modeling work, the water mass balance across the fuel cell is needed. The full water mass balance equation is:

$$\dot{m}_{H_2O,ca,in} + \dot{m}_{H_2O,an,in} + \dot{m}_{H_2O,gen} = \dot{m}_{H_2O,ca,out} + \dot{m}_{H_2O,an,out} \tag{11}$$

This equates the water that enters and is generated in the fuel cell to the water that leaves the fuel cell. Water that enters and exits the cell at the cathode is assumed to be in the vapor form, as already explained in Section 3.1. The only controversial mass flow would be the anode outlet, where the water could condense. However, this is solved by placing a gas line heater at the exit of the anode, which heats the gas up to about 70 °C before measuring the dew point temperature which allows for the measurement of all the water leaving the anode. Consequently, the mass flow of water is in the vapor form at the location where the dew point temperatures are measured.

Generally the mass flow rate of water vapor can be expressed as a fraction of the dry gas mass flow rate:

$$\dot{m}_{H_2O,i,j} = \dot{m}_{i,j_d} \cdot x_{H_2O,i,j} \qquad [\mathrm{kg\,s^{-1}}] \tag{12}$$

where i stands for anode or cathode and j for inlet or outlet. The determination of the five different terms in Eq. (11), according to the measurable variables of the test station, is explained below.

1. **Anode inlet:** The total anode inlet mass flow rate is a sum of the hydrogen mass flow rate and the water vapor mass flow rate, if hydrogen is humidified:

   $$\dot{m}_{an,in} = \dot{m}_{H_2,an,in} + \dot{m}_{H_2O,an,in} \qquad [\mathrm{kg\,s^{-1}}] \tag{13}$$

   Knowing the amount of water vapor entering with the hydrogen by measuring the dew point temperature and the inlet mass flow rate of dry hydrogen, the anode inlet mass flow rate of water vapor can be calculated by Eq. (12):

   $$\dot{m}_{H_2O,an,in} = \dot{m}_{H_2,an,in} \cdot x_{H_2O,an,in} \qquad [\mathrm{kg\,s^{-1}}] \tag{14}$$

2. **Cathode inlet:** The total cathode inlet mass flow rate is a sum of oxygen, nitrogen and water vapor mass flow rate:

   $$\dot{m}_{ca,in} = \dot{m}_{O_2,ca,in} + \dot{m}_{N_2,ca,in} + \dot{m}_{H_2O,ca,in} \qquad [\mathrm{kg\,s^{-1}}] \tag{15}$$

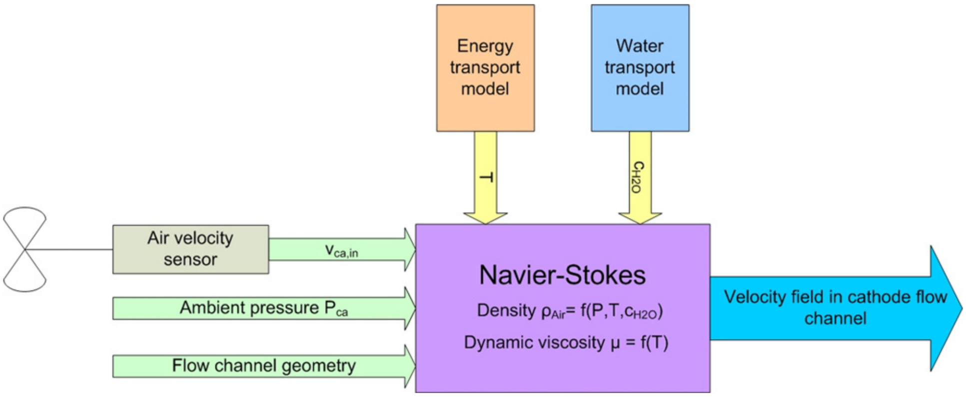

Fig. 7. Schematic of the cathode flow model.

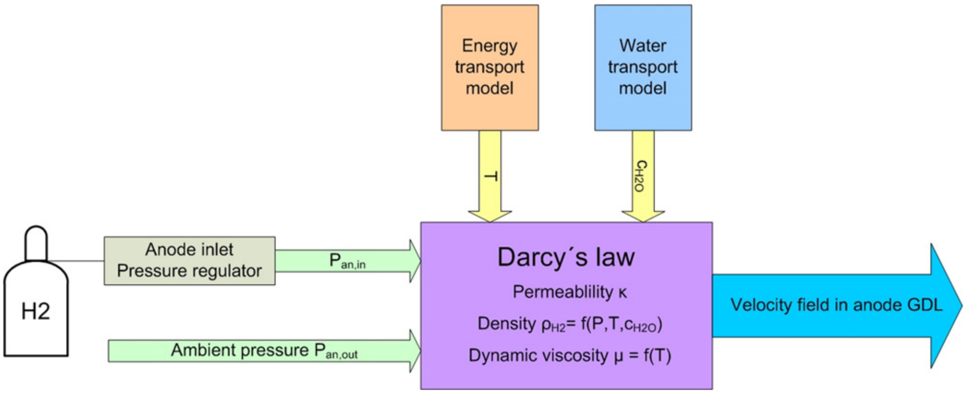

Fig. 8. Schematic of the anode flow model.

Moreover a mass flow rate of a gas stream can be described by the gas density, the velocity and the cross-sectional area, through which gas flows. As the cathode inlet velocity is measured within the test station the cathode inlet mass flow rate is described by:

$$\dot{m}_{ca,in} = \bar{v}_{ca,in} \cdot A_{ca} \cdot \rho_{ca,in} \qquad [\mathrm{kg\,s^{-1}}] \tag{16}$$

where A_{ca} is the cross-sectional area of the fuel cell housing structure within the environmental chamber. Assuming that the median flow velocity $\bar{v}_{ca,in}$ is constant for wet and dry air, because the change in mass flow rate results from the change in density by adding water, the cathode inlet mass flow rate of water vapor can then be calculated by combining Eqs. (16) and (12):

$$\dot{m}_{\mathrm{H_2O},ca,in} = \dot{m}_{air,in,d} \cdot x_{\mathrm{H_2O},ca,in} = \bar{v}_{ca,in} \cdot A_{ca} \cdot \rho_{air,d} \cdot x_{\mathrm{H_2O},ca,in} \qquad [\mathrm{kg\,s^{-1}}] \tag{17}$$

As the cathode inlet air velocity is measured in a housing structure outside the fuel cell stack, but has to be used to model a single channel, the velocity has to be adapted to the smaller flow channel dimensions:

$$\bar{v}_{ca,in} = \frac{A_{housing}}{n_{bpp} \cdot n_{cpp} \cdot A_{ch}} \cdot \bar{v}_m \qquad [\mathrm{m\,s^{-1}}] \tag{18}$$

3. **Anode outlet:** The total anode outlet mass flow is defined as:

$$\dot{m}_{an,out} = \dot{m}_{\mathrm{H_2},an,out} + \dot{m}_{\mathrm{H_2O},an,out} \qquad [\mathrm{kg\,s^{-1}}] \tag{19}$$

This mass flow rate of water vapor can be calculated similar to the inlet flow rate, but adding the fact that hydrogen is consumed inside the fuel cell. Therefore the anode outlet mass flow rate of hydrogen is:

$$\dot{m}_{\mathrm{H_2},an,out} = (\dot{m}_{\mathrm{H_2},an,in} - \dot{m}_{\mathrm{H_2},an,cons}) \qquad [\mathrm{kg\,s^{-1}}] \tag{20}$$

Using Faraday's law, the consumed hydrogen mass flow rate of one cell is found by:

$$\dot{m}_{\mathrm{H_2},an,cons} = \frac{M_{\mathrm{H_2}}}{2F} \cdot I \qquad [\mathrm{kg\,s^{-1}}] \tag{21}$$

Combining Eqs. (12) and (20) the anode outlet mass flow rate of water vapor is described by:

$$\dot{m}_{\mathrm{H_2O},an,out} = (\dot{m}_{\mathrm{H_2},an,in} - \dot{m}_{\mathrm{H_2},an,cons}) \cdot x_{\mathrm{H_2O},an,out} \qquad [\mathrm{kg\,s^{-1}}] \tag{22}$$

4. **Cathode outlet:** Regarding that only oxygen is consumed at the cathode and the amount of nitrogen stays the same, the total cathode outlet mass flow rate results in:

$$\dot{m}_{ca,out} = (\dot{m}_{\mathrm{O_2},ca,in} - \dot{m}_{\mathrm{O_2},ca,cons}) + \dot{m}_{\mathrm{N_2},ca,in} + \dot{m}_{\mathrm{H_2O},ca,out} \qquad [\mathrm{kg\,s^{-1}}] \tag{23}$$

The consumed oxygen mass flow rate of one cell can be calculated using Faraday's law similar to the consumption of hydrogen. The only difference is that the number of electrons per molecule of O_2 is 4.

$$\dot{m}_{\mathrm{O_2},ca,cons} = \frac{M_{\mathrm{O_2}}}{4F} \cdot I \qquad [\mathrm{kg\,s^{-1}}] \tag{24}$$

According to Eq. (12), the cathode outlet mass flow rate of water vapor is determined by the following equation:

$$\dot{m}_{\mathrm{H_2O},ca,out} = \dot{m}_{air,out,d} \cdot x_{\mathrm{H_2O},ca,out} \qquad [\mathrm{kg\,s^{-1}}] \tag{25}$$

where the outlet mass flow rate of dry air can be determined by subtracting the mass flow rate of consumed oxygen from the inlet mass flow rate of dry air:

$$\dot{m}_{air,out,d} = \dot{m}_{air,in,d} - \dot{m}_{\mathrm{O_2},ca,cons} \qquad [\mathrm{kg\,s^{-1}}] \tag{26}$$

5. **Generated water:** The water that is generated in the fuel cell is a product of the reaction of hydrogen and oxygen and is directly proportional to the current passing through the fuel cell stack, based on Faraday's law. Thus, the mass flow rate of generated water results in:

$$\dot{m}_{\mathrm{H_2O},gen} = \frac{M_{\mathrm{H_2O}}}{2F} \cdot I \qquad [\mathrm{kg\,s^{-1}}] \tag{27}$$

As water is only produced at the cathode catalyst surface, the cathode catalyst boundary condition in the 2D model is given by the flux of generated water through the active area:

$$\Phi_{\mathrm{H_2O},gen} = \frac{\dot{m}_{\mathrm{H_2O},gen}}{A_{act}} \qquad [\mathrm{kg\,s^{-1}\,m^{-2}}] \tag{28}$$

Table 3 depicts the different contributions to the water mass balance Eq. (11) at 3 A. As it can be seen, the majority of the water enters and leaves the stack at the cathode side, which is relatively large compared to the generated water at this current.

This water mass balance is used to determine the bulk water vapor diffusion coefficient $D_{\mathrm{H_2O}}$ of the MEA, as described in Section 4 and to validate experimental results.

Since water in a fuel cell is transported by convection, diffusion and is also generated within the cell, the different equations for

Table 3
Contributions to the water mass balance equation at 3 A.

Mass flow rate	Absolute value (mg s^{-1})
$\dot{m}_{\mathrm{H_2O},an,in}$	0.40
$\dot{m}_{\mathrm{H_2O},ca,in}$	60.12
$\dot{m}_{\mathrm{H_2O},an,out}$	−0.52
$\dot{m}_{\mathrm{H_2O},ca,out}$	−65.60
$\dot{m}_{\mathrm{H_2O},gen}$	5.60

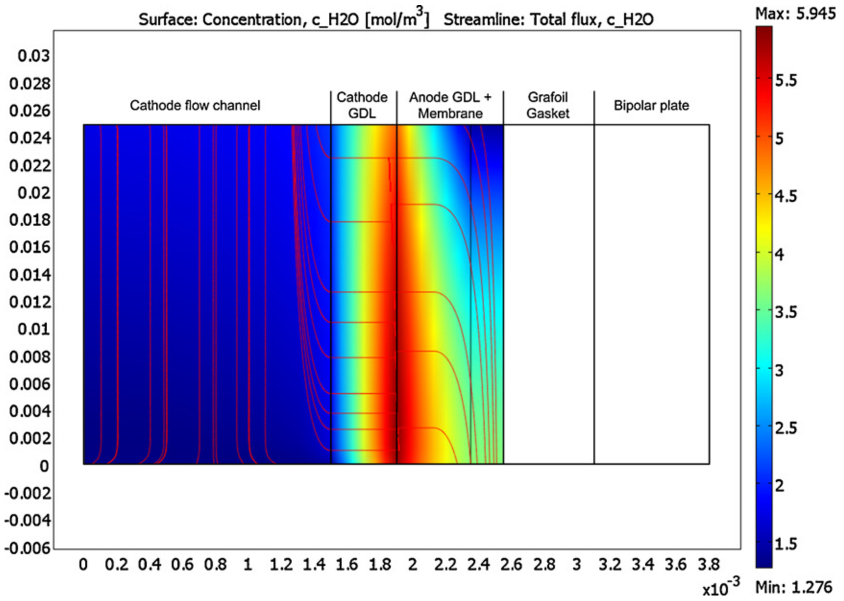

Fig. 9. Typical water concentration distribution for constant anode and cathode flows at 5 A (*x* and *y* axis dimensions are in meters).

each transport mechanisms have been combined in a mass balance equation [13]:

$$\frac{\partial c_{H_2O}}{\partial t} + \nabla(-D_{H_2O}\nabla c_{H_2O}) = \nabla J_{H_2O} - \vec{v}\cdot\nabla c_{H_2O} \quad (29)$$

The first term on the left-hand side of the equation corresponds to the accumulation of water in the system. The second term accounts for the diffusive transport within the MEA, described by Fick's law. The first term on the right-hand side represents a source flux of water due to the chemical reaction and also the EOD. Finally, the second term on the right-hand side accounts for the convective transport due to a velocity field $\vec{v}$. In the cathode flow channel this field is obtained by coupling the Navier–Stokes momentum transport to the equation system, as described in Section 3.2.2, whereas in the anode GDL the momentum transport during a purge is described by Darcy's law, as explained in Section 3.2.3.

Water is also transported by the electroosmotic drag from anode to cathode. This flow rate can also be described by Faraday's law, because the EOD is proportional to current [4]:

$$\dot{m}_{H_2O,EOD} = \epsilon \cdot \frac{M_{H_2O}}{F} \cdot I \qquad [\mathrm{kg\,s^{-1}}] \quad (30)$$

The EOD coefficient ϵ represents the number of water molecules that are dragged from anode to cathode per proton. This coefficient is determined experimentally, as described in Section 4. Regarding the model, the EOD is treated as an internal source flux at the cathode and a sink flux at the anode. A typical water concentration distribution for constant cathode and anode flows is shown in Fig. 9, where the streamlines describe the flux of water from the cathode catalyst layer to the cathode and anode flow channel. As the H-100 is an open cathode stack, the cathode inlet conditions are ambient. At the anode dry, pure hydrogen enters without humidification.

Fig. 10 summarizes all input and output parameters of the model, as well as the influences of the other submodels.

During a short circuit heat and water are produced at the cathode catalyst layer. This mass flow rate of generated water during a short circuit can be calculated using Eq. (27) and replacing the stack current by the short circuit current. As the short circuit current is

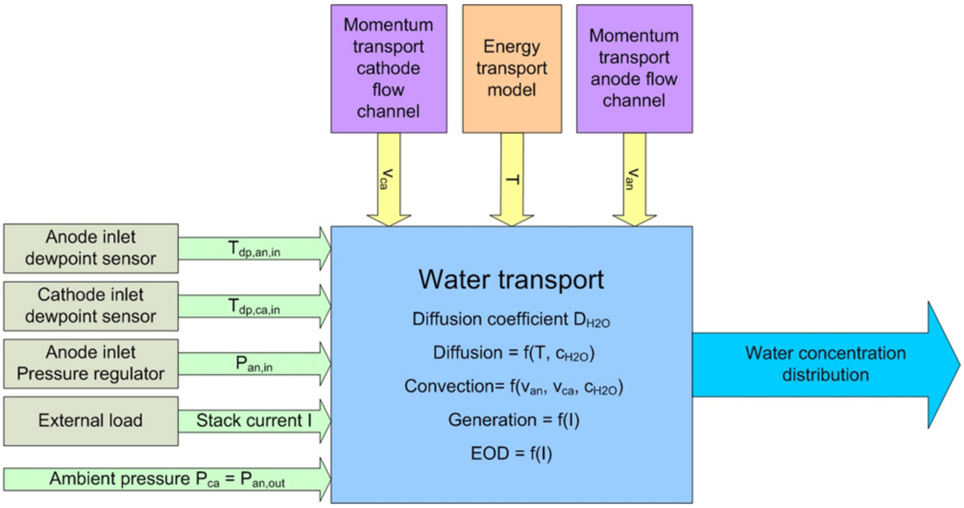

Fig. 10. Schematic of the water transport model.

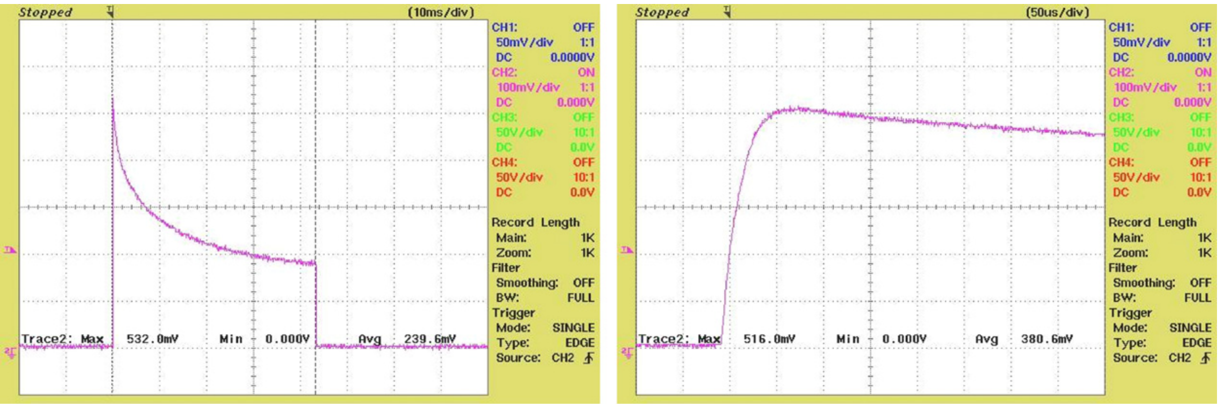

(a) Short circuit duration (b) Rising edge

Fig. 11. *I*–*t*-plot of a short circuit. (a) Short circuit duration and (b) rising edge.

a function of time, the root mean square (RMS) current is used to calculate the mass flow rate

$$\dot{m}_{H_2O,gen,sc} = \frac{M_{H_2O}}{2F} \cdot I_{sc} \qquad [\mathrm{kg\,s^{-1}}] \tag{31}$$

where

$$I_{sc} = \sqrt{\frac{1}{t_{sc}} \int_0^{t_{sc}} (I_{sc}(t))^2 dt} \qquad [\mathrm{A}] \tag{32}$$

The RMS short circuit current of the measured *I*–*t*-curve, shown in Fig. 11, results in 23 A.

Table 4 lists the additional model input parameters, such as physical properties, dimensions and constants, which are used in the model.

4. Experimental determination of coefficients

The diffusion coefficient of water vapor through the MEA (as stated in Section 3.1 also includes all the diffusion layers) is dependent on temperature and water content. In order to develop a mathematical relation between diffusion, temperature and water content, water diffusion has to be separated from the other water transport mechanisms, namely EOD and hydraulic permeation. As the experiments of Husar et al. [11] have shown, water transfer due to hydraulic permeation is at least an order of magnitude lower than that due to the two other transport mechanisms, and therefore can be neglected. To separate diffusion from the EOD, the fuel cell is disconnected from the external circuit and nitrogen is used instead of hydrogen, which also guarantees that no water can be generated due to possible crossover of hydrogen, which would generate water at the cathode side. The experiment was carried out with a dry anode and a wet cathode. The diffusive water mass flux across the membrane is the outlet water mass flux at the dry side which should equal the difference between inlet to outlet water mass flux of the wet side. Since the H-100 is an open cathode fuel cell it is difficult to perform a similar diffusion experiment in the opposite direction, with a wet anode and a dry cathode. However, random tests at stable points where the anode humidity was higher than at the cathode side have shown a direction independence of the diffusion coefficient. The dew point temperature of the wet cathode was kept constant at 20 °C, which means that the partial pressure of water vapor in air does not change with temperature, unlike with using a constant relative humidity. The ambient temperature was increased from 30 to 50 °C with a step size of 10 °C by using an environmental chamber. At each point enough time was given for the anode dew point temperature to become stable, so that a steady state can be assumed. The chamber temperature then equals the stack temperature. Moreover, the maximum cathode flow rate was applied in order to minimize the concentration difference from inlet to outlet at the wet side.

Fig. 12 shows the membrane diffusivity of water vapor at different temperatures. Compared to the work of Springer et al. [1] the experimentally obtained diffusion coefficient is smaller. This might be due to the different membrane types and thickness used

Table 4
Physical parameters and properties.

Description	Value	Unit
Active catalyst area, A_{act}	0.00225	$\mathrm{m^2}$
Bipolar plate density, ρ_{BPP}	1850	$\mathrm{kg\,m^{-3}}$
Bipolar plate thermal conductivity, k_{BPP}	14	$\mathrm{W\,K^{-1}\,m^{-1}}$
Cross-section channel, A_{ch}	1.5×10^{-6}	$\mathrm{m^2}$
Faraday constant, F	96487	$\mathrm{C\,mol^{-1}}$
GDL density, ρ_{GDL}	440	$\mathrm{kg\,m^{-3}}$
GDL permeability, κ_{GDL}	1×10^{-12}	$\mathrm{m^2}$
GDL porosity, ϵ_{GDL}	0.78	
GDL thermal conductivity inplane, $k_{GDL,in}$	21	$\mathrm{W\,K^{-1}\,m^{-1}}$
GDL thermal conductivity through-plane, $k_{GDL,through}$	1.7	$\mathrm{W\,K^{-1}\,m^{-1}}$
GDL thickness, z_{GDL}	4×10^{-4}	m
Number of bipolar plates, n_{bpp}	21	
Number of cells, n_{cell}	20	
Number of channels per plate, n_{cpp}	51	
Universal gas constant, R	8.314	$\mathrm{J\,mol^{-1}\,K^{-1}}$

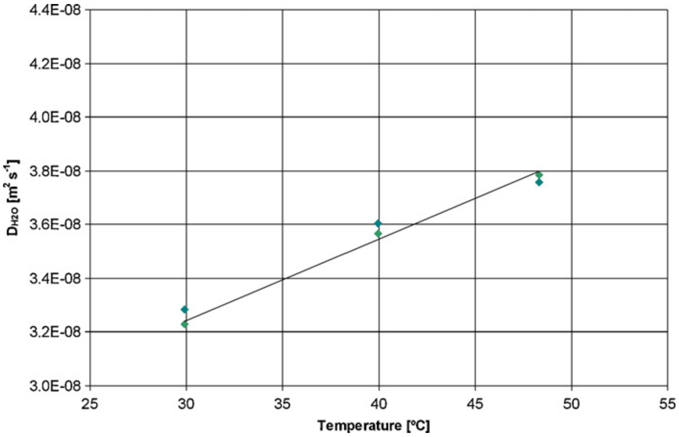

Fig. 12. Membrane diffusivity as a function of stack temperature.

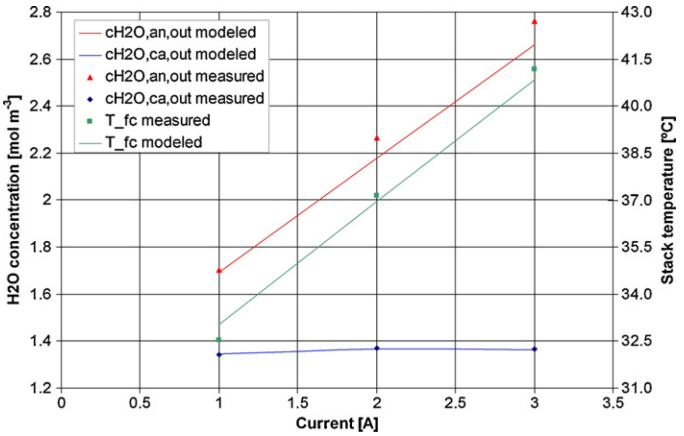

Fig. 13. Anode and cathode outlet water concentration as a function of current.

in this work. However, similar results were found by McKay and Stefanopoulou [17], who also performed *in situ* measurements of the diffusion coefficient with a fuel cell stack.

In order to determine the EOD coefficient experimentally, diffusive water transport through the membrane has to be minimized. This can be obtained by keeping the water concentration on both sides equal and as close to 100% relative humidity as possible, which is achieved by setting the same dew point temperature for the anode and cathode inlets. The measured EOD coefficient slightly increases from 0.47 to 0.48 by increasing the stack current from 1 to 3 A, which is in accordance with the data of Husar et al. [11], but their test was performed at higher current densities and using a thicker membrane.

To determine a specific heat capacity for the stack, a constant current is drawn for a short period of time, and the stack temperature evolution is measured. The test resulted in a specific heat capacity of 1260 J kg^{-1} K^{-1}. A similar value is also used in the heat transfer model of He et al. [18].

5. Results and discussion

5.1. Steady-state validation

By validating the steady-state model, the general model settings such as the boundary conditions, applied physical phenomena or experimentally determined coefficients can be checked. Therefore, experimental data of the H-100 fuel cell stack, directly obtained from laboratory tests, were compared to the simulation results. The initial conditions were a humidified anode and cathode, and a constant fan flow rate. Even though the regular working conditions of the H-100 suggest a dry anode, these tests were performed in order to check the model behavior even under conditions that do not appear in a normal operation. The stack current was stepwise increased from 1 to 3 A. Fig. 13 shows the measured and modeled values of the cathode and anode outlet water concentrations, as well as the fuel cell stack temperature at different currents.

5.2. Dynamic validation

The model has also been compared to dynamic experiments performed with the studied PEM fuel cell stack. These tests have shown that the model is able to give a proper dynamic representation of the actual stack behavior. Fig. 14 shows the comparison of the simulated cathode outlet water concentration with the measurement data, when changing the cooling fan velocity at a constant working point of 5 A.

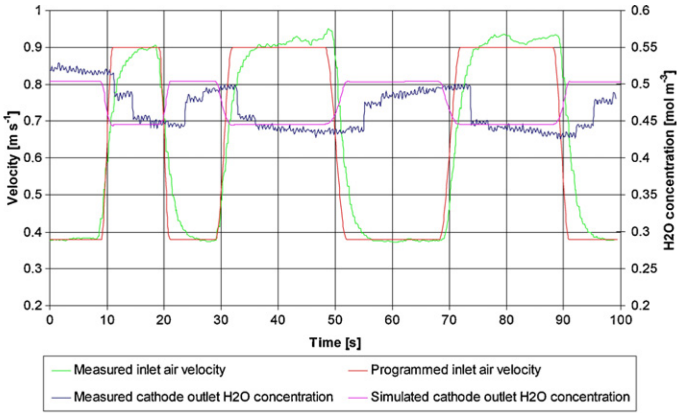

Fig. 14. Dynamic validation—humidity fan test.

The test results show that there is a delay in the cathode outlet dew point measurement, which is due to the response time of the dew point sensor used in this experiment. However, disregarding this unavoidable measurement error, the simulated cathode outlet water concentration gives a good representation of the experimental results.

The second validation parameter is the stack temperature, which was also measured and simulated within the same test. The comparison is illustrated in Fig. 15.

A delay in the measured stack temperature can be noticed here as well. This is not only due to the response time of the sensor but also due to the differences between the programmed velocity curve and the measured curve, which shows a smaller slope at low velocities and therefore the temperature changes slower than in the model. Regarding the temperature gradients, the model matches the experiment, especially during the cooling phase. The modeled fuel cell stack temperature increases faster than the measured temperature when the fan velocity is reduced. The slower increase in the measured temperature could be caused by small amounts of convective and radiative heat removal from the stack, which is not included in the model.

The conclusion of both tests is that the model demonstrates an accurate dynamic representation of the fan.

5.3. Sensitivity analysis

In order to quantify the sensitivity of the input variables of the model, a sensitivity analysis was performed at different current set points. Table 5 shows the model input variable settings and

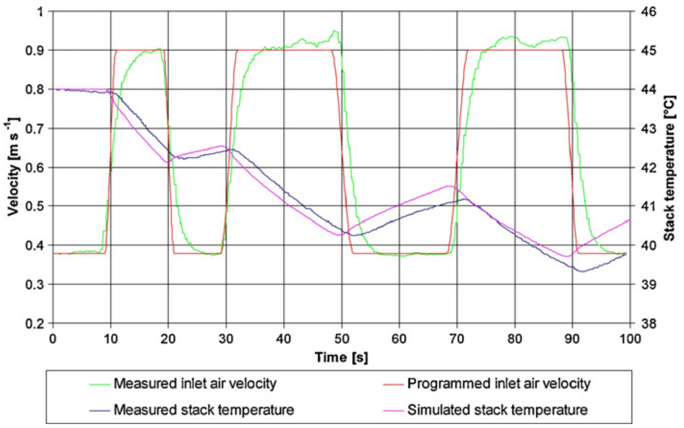

Fig. 15. Dynamic validation—temperature fan test.

Table 5
Input and output variable values and input variable variations.

	T_{ca} (°C)	T_{an} (°C)	$x_{H_2O,ca}$	$x_{H_2O,an}$	v_{ca} ($m\,s^{-1}$)	I_{stack} (A)	V_{stack} (V)
in	30.00	30.00	0.01475	0.23937	0.4	3.0	13.5
out	35.84	38.10	0.01577	0.50157	-	-	-
$\Delta\xi_{in}$	1.0	-	0.00096	0.01424	0.1	0.1	0.1

Table 6
Sensitivity matrix at 3 A.

ξ_{in}	$T_{ca,out}$ (°C)	$s(T_{ca,out})$ (%)	$T_{an,out}$ (°C)	$s(T_{an,out})$ (%)	$x_{H_2O,ca,out}$	$s(x_{H_2O,ca,out})$ (%)	$x_{H_2O,an,out}$	$s(x_{H_2O,an,out})$ (%)
$T_{ca,in}$	36.86	2.85	39.10	2.62	0.015788	0.13	0.502341	0.15
$x_{H_2O,ca,in}$	35.84	0.00	38.10	0.00	0.016744	6.20	0.509306	1.54
$x_{H_2O,an,in}$	35.84	0.00	38.10	0.00	0.015789	0.14	0.509386	1.56
$v_{ca,in}$	34.84	−2.80	37.30	−2.10	0.015570	−1.25	0.499355	−0.44
I_{stack}	36.04	0.56	38.37	0.71	0.015802	0.22	0.510875	1.85
V_{stack}	35.79	−0.14	38.03	−0.18	0.015765	−0.02	0.501492	−0.02

the resulting output variable values at a stack current of 3 A. It also includes the variable variations for the sensitivity analysis. The variation of the anode and cathode inlet water mass fraction represents a variation in the measured inlet dew point temperature of 1 °C, from 20 to 21 °C at the cathode and from 25 to 26 °C at the anode. The big difference between anode and cathode water mass fraction is not only due to the difference in dew point temperature but rather due to the much higher gas flow rate at the cathode. Since the anode inlet temperature has no effect it is not included in this analysis.

By changing the input variables (ξ_{in}), according to the variable variations ($\Delta\xi_{in}$), defined in Table 5, the impact of input signal offsets or variable deviations on each output variable can be observed. Table 6 shows the sensitivity matrix, depicting the resulting output variable values for each input variable variation with the respective relative sensitivity s.

As a result it can be seen that increasing the cathode inlet dew point temperature by 1 °C has almost the same effect on the anode outlet water mass fraction as increasing the anode inlet dew point temperature, however not vice versa. Also the stack current has a similar effect on the anode outlet water mass fraction. Moreover, an increase of the cathode inlet air velocity of 0.1 $m\,s^{-1}$ has the same effect as a 1 °C change in the ambient temperature at these conditions. These observations indicate that the cathode mass flux dominates the energy and mass balance in this stack. All variables show very low sensitivity to a variation of the stack voltage, but are sensitive to a change in the stack current. Repeating the experiment at higher and lower stack currents leads to similar variable sensitivities.

6. Conclusion

A two-dimensional, non-isothermal, dynamic model of a 100 W open cathode, self-humidified PEM fuel cell system has been developed with respect to water and heat transport within the cell. The crucial coefficients for water transport, namely the diffusion and the EOD coefficient, have been determined experimentally. The diffusivity of water vapor through the membrane at 30 °C was determined to be $3.3 \times 10^{-8}\,m^2\,s^{-1}$ and increases by $3 \times 10^{-10}\,m^2\,s^{-1}\,{}^{\circ}C^{-1}$ with increasing temperature to 50 °C. The EOD coefficient was found to be 0.47–0.48 water molecules per proton at stack currents from 1 to 3 A. Moreover, the bulk specific heat capacity for one cell unit, consisting of a MEA plus a bipolar plate, was experimentally determined to be $1260\,J\,kg^{-1}\,K^{-1}$. The model has been validated by using experimental data directly obtained from laboratory tests with the investigated fuel cell stack, which has shown that the model predictions match the experimental data well. The model is kept simple and is capable of representing system specific control mechanisms for water and heat management, as demonstrated within the dynamic validation. As it combines most of the physical phenomena that occur within a PEM fuel cell, it permits for a comprehensive study of these control mechanisms. However, the model can still be improved by including charge transfer, two phase flow characteristics as well as temperature driven water transport. Moreover, further experiments are needed to observe the dynamic effect of water storage in the membrane and the anode GDL, and finally include them in the model. The developed model is intended to be used to simulate and study the effects of water transport and its influence on the system performance, and to develop new water management control strategies, that are strongly demanded, as recent papers have shown. The model is easy to handle by the user-friendly CFD software COMSOL Multiphysics, and can be easily extended. Furthermore, it is applicable to other PEM fuel cell systems, following the developed modeling strategy and performing the experiments in order to determine the specific coefficients.

Acknowledgements

All the experimental tests were performed at the Fuel Cells Laboratory of the *Institut de Robótica i Informática Industrial* (CSIC-UPC, Barcelona) and only possible due to its advanced equipment and proficient technical staff. This work is partially funded by the project of CICYT DPI2007-62966 MICINN, DPI2010-15274 MICINN and the project AECID A/026279/09 and supported from a predoctoral scholarship JAE-intro from CSIC.

References

[1] T.E. Springer, T.A. Zawodzinski, S. Goftesfeld, Journal of the Electrochemical Society 138 (1991) 2334–2342.
[2] I. Hussaini, C. Wang, Journal of Power Sources 195 (2010) 3822–3829.
[3] W. Dai, H. Wanga, X.-Z. Yuan, J.J. Martin, D. Yang, J. Qiao, J. Mab, International Journal of Hydrogen Energy 34 (2009) 9461–9478.
[4] F. Barbir, PEM Fuel Cells: Theory and Practice, Elsevier Academic Press, 2005.
[5] V. Gurau, H. Liu, S. Kakac, AIChE Journal 44 (1998) 2410–2422.
[6] H. Ju, H. Meng, C.-Y. Wang, International Journal of Heat and Mass Transfer 48 (2005) 1303–1315.
[7] Y. Wang, C.-Y. Wang, Journal of the Electrochemical Society 153 (2006) A1193–A1200.
[8] S. Basu, C.-Y. Wang, K.S. Chen, Journal of the Electrochemical Society 156 (2009) B748–B756.
[9] S. Basu, J. Li, C.-Y. Wang, Journal of Power Sources 187 (2009) 431–443.
[10] Z. Shi, X. Wang, Two-dimensional PEM fuel cells modeling using comsol multiphysics, in: G. Petrone, G. Cammarata (Eds.), Modeling and Simulaton, InTech Education and Publishing, 2008, pp. 679–688.

[11] A. Husar, A. Higier, H. Liu, Journal of Power Sources 183 (2008) 240–246.

[12] E.A. Müller, A.G. Stefanopoulou, Excerpt from the Third International Conference on Fuel Cell Science, Engineering and Technology 2005, Ypsilanti, MI, USA, 2005.

[13] COMSOL, COMSOL Multiphysics Version 3.5 Documentation, Chemical Engineering Module, 2008.

[14] Y. Shi, J. Xiao, M. Pana, R. Yuan, Journal of Power Sources 160 (2006) 277–283.

[15] Z. Shi, X. Wang, Excerpt from the Proceedings of the COMSOL Conference 2007, Boston, 2007.

[16] H. Meng, C.-Y. Wang, Journal of the Electrochemical Society 152 (2005) 1733–1741.

[17] D. McKay, A. Stefanopoulou, Proceedings of the American Control Conference, 2004.

[18] G. He, Y. Yamazaki, A. Abudula, Journal of Power Sources 195 (2010) 1551–1560.

Journal of Power Sources 196 (2011) 4298–4305

Contents lists available at ScienceDirect

Journal of Power Sources

journal homepage: www.elsevier.com/locate/jpowsour

LPV observer design for PEM fuel cell system: Application to fault detection☆

S. de Lira[a,*,1], V. Puig[a,1], J. Quevedo[a,1], A. Husar[b,2]

[a] Sistemas Avanzados de Control (SAC), Universitat Politécnica de Catalunya (UPC), Rambla Sant Nebridi 10, 08222 Terrassa, Spain
[b] Instituto de Robótica i Informática Industrial (IRI), (CSIC-UPC) Parc Tecnológic de Barcelona, Edifici U, Carrer Llorens i Artigas, 4-6, Floor 2, 08028 Barcelona, Spain

ARTICLE INFO

Article history:
Received 31 July 2010
Received in revised form 14 October 2010
Accepted 17 November 2010
Available online 25 November 2010

Keywords:
PEM fuel cell
Modelling
LPV
Observer
Fault detection

ABSTRACT

In this paper, the modelling of an energy generation system based on *polymer electrolyte membrane fuel cell* (PEMFC) system through a parameter varying approach (LPV model), that takes in to account model parameter variation with the operating point, is presented. This model has been obtained through a Jacobian linearization of the PEMFC non-linear dynamic model that was previously calibrated using real data from lab. In order to illustrate the use of the LPV model obtained its application to model-based fault detection is used. For this purposes a set of common fault scenarios, which could appear during a normal PEMFC operation, is used as case study.

1. Introduction

Low-temperature PEM fuel cells are considered as sources for rapid medium of energy generation, making these equipment suitable for automobile applications. The supply of raw materials (usually air or pure oxygen) is normally performed using an air compressor or blower and hydrogen stored in tanks. The system uses additional equipment to carry materials reaction to the optimum operating conditions, such as cooling systemsand humidifier. During the chemical reaction that is taking place into the stack, where the energy is generated, different phenomena occur, such as thermal, fluid-mechanical and electrolytic.

The complex and non linear dynamics of the power generation systems based on fuel cell technology lead to the use of linear models that includes parameter varying with operating point not only for advanced control techniques but also for fault diagnosis algorithms based on models. The use of LPV models is an alternative to the approaches presented in previous works [1,2] addressing methodologies for monitoring and fault diagnosis based on a theoretical non-linear dynamic model proposed by Pukrushpan [3,4].

Within the recent decade, state of art and background about control of LPV systems has been developed [5–10]. Because of a LPV system can be considered as a parametrized family of linear systems that change with the operating point conditions, then LPV technique allows a systematic approach for control and fault diagnosis system design. At the cost of conservatism the approach can be applied to an even wider range of systems known as quasi-LPV systems, where varying parameters are scheduled with state variables.

Since LPV models are structured as similar as a linear time-invariant (LTI) state space system, the control and fault diagnosis design methods can easily be extended. The main contribution of this paper is to obtain a linear parameter varying model for a typical PEMFC and illustrate its use for robust fault detection using interval observers.

2. Fuel cell modelling

The model proposed in [11], is a non-linear dynamic model calibrated using real data from laboratory using a *lsq*-non linear fitting approach [12,13]. This model is able to reproduce the behaviour of a commercial PEMFC (Ballard 1.2 kW, Nexa©) prototype, which has been identified in a wide range of operating conditions. Fig. 1 shows the dynamic model layout.

2.1. Dynamic non-linear model

The model is considered as SIMO system, where the input (u) is the stack current (I_{st}) and the outputs (y) are battery temperature (T_{st}), stack voltage (v_{st}), oxygen consumption ratio (λ_{O_2}), speed

---

☆ This work has been partially funded by the grant CICYT HYFA DPI2008-01996 of Spanish Ministry of Education and by a grant from Consejo Nacional de Ciencia y Tecnologia (CONA-CyT), México. The authors wish also to thank to the Instituto de Robotica i Informatica Industrial (IRI/UPC-CSIC) for its know how sharing, specially to J. Riera, M. Serra and D. Feroldi.

* Corresponding author. Tel.: +34 622111233; fax: +34 934015750.
E-mail address: salvador.de.lira@upc.edu (S. de Lira).
[1] http://websac.upc.es.
[2] http://www.iri.upc.edu.

0378-7753/$ – see front matter © 2010 Elsevier B.V. All rights reserved.
doi:10.1016/j.jpowsour.2010.11.084

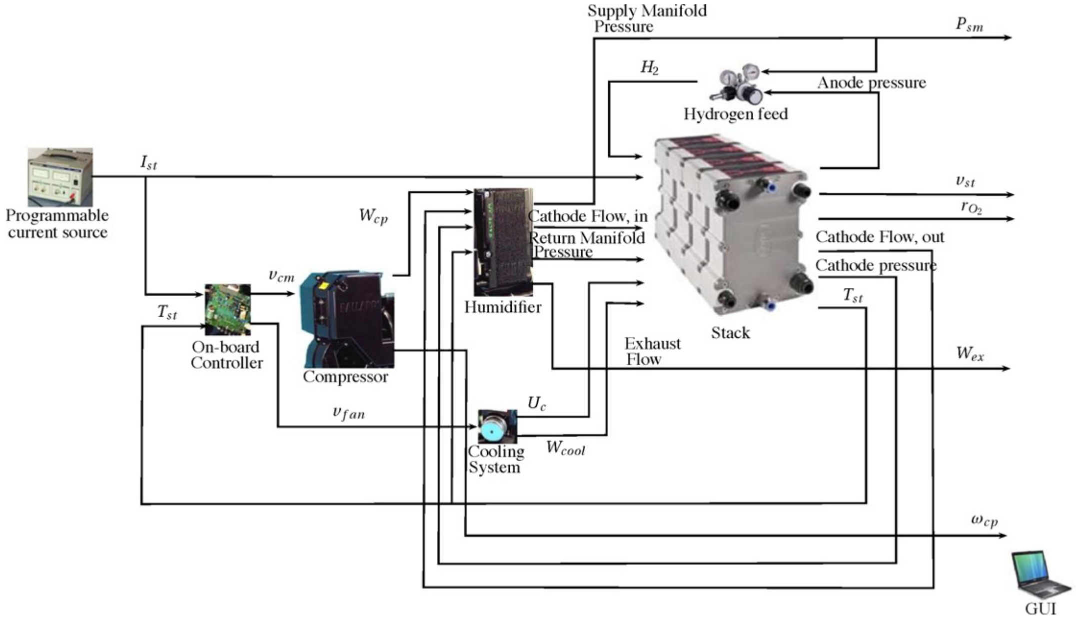

Fig. 1. Nexa© PEMFC simulator schematic.

engine (ω_{cp}) and inlet pressure to the cathode (P_{sm}). The voltage from the compressor (v_{cm}) is controlled using a static feed-forward controller. Fig. 2 shows the layout of each subsystem embedded into the PEMFC dynamic model.

The proposed model consists often state, and the state equations are listed in the following

$$\begin{aligned}
&\dot{\omega}_{cp} = \frac{1}{J_{cp}\omega_{cp}}(\tau_{cm} - \tau_{cp}),\\
&\dot{P}_{rm} = \frac{R_{air}T_{rm}}{V_{rm}}(W_{ca,o} - W_{rm,o}),\\
&\dot{m}_{rm} = W_{ca} - W_{rm,o},\\
&\dot{P}_{sm} = \frac{\gamma R_a}{V_{sm}}(W_{cp}T_{cp} - W_{sm,o}T_{sm}),\\
&\dot{m}_{sm} = W_{cp} - W_{sm,o},\\
&\dot{m}_{H_2} = W_{H_2,i} - W_{H_2,o} - W_{H_2,r-W_{H_2,nl}},\\
&\dot{m}_{w,an} = W_{v_{an},i} - W_{v_{an},o} - W_{v_{mbr}},\\
&\dot{m}_{N_2} = W_{N_2,i} - W_{N_2,o},\\
&\dot{m}_{O_2} = W_{O_2,i} - W_{O_2,o} - W_{O_2,r},\\
&m_{st}C_{st}\dot{T}_{st} = H_{reac} - P_{elec} - Q_{rad} - \dot{Q}_{conv}.
\end{aligned} \tag{1}$$

The state variables (**x**) of this dynamic model are the following: mass of oxygen (m_{O_2}), nitrogen (m_{N_2}), hydrogen (m_{H_2}), cathode water flow ($m_{w,ca}$), stack temperature (T_{st}), angular velocity of the compressor (ω_{cp}), supply pressure (P_{sm}) and return pressure (P_{rm}) of the humidifier, inlet flow (m_{sm}) and outlet flow (m_{rm}) of humidifier. The subindex in the variables *i*, *o*, *r*, *nl* means, input, output, reaction and natural, respectively. In the heat balance the subindex *reac*, *elec*, *rad* and *conv* are related respectively to reaction, electric, radiation and convection.

The system perturbation (**z**) that have been considered are related to the weather conditions (T_{amb}, P_{atm}).

The model output equations are:

- *Stack voltage*:

$$v_{st} = n_{fc}\cdot(E - v_{act} - v_{oh} - v_{con}). \tag{2}$$

- *Oxygen excess ratio*:

$$\lambda_{O_2} = \frac{W_{O_2,i}}{W_{O_2,r}} = \frac{x_{O_2}\cdot W_{cp}}{(M_{O_2}\cdot n_{fc}\cdot I_{st})/4\cdot F}. \tag{3}$$

- *Compressor speed motor*:

$$\omega_{cp} = \frac{U_{cp}\cdot 60}{d_c\cdot\pi}, \tag{4}$$

where v_{st}, total stack voltage (V); E, open circuit voltage (V); v_{act}, activation voltage loss (V); v_{oh}, ohmic voltage lose (V); v_{con}, concentration voltage loss (V); n_{fc}, amount of cells; λ_{O_2}, oxygen excess ratio; I_{st}, stack current (A); F, Faraday constant (col/mol); W, mass flow (g/s); U_{cp}, compressor blade (KRPM); d_c, compressor diameter blade (%); η, compressor efficiency (%); M_{O_2}, oxygen molar weight (g/mol); M_{H_2}, hydrogen molar weight (g/mol); x_{O_2}, oxygen fraction (%); φ_i, humidity ($i = ca, an$) (%).

3. Linear parameter varying model

Exist different ways to obtain LPV models. Some methods use non-linear equations of the system to derive a LPV model such as state transformation, substitution of functions and methods using the well known Jacobian linearization [14–16]. Another kind of method uses multi-model identification that consists basically in two different steps: (1) a set of LTI model is identified at different equilibrium points by classical methods (*on-line* or *off-line*), (2) then, the following step is to get a multi-model by an interpolation law that allows to commute among local LTI model at each operating point [17,18].

3.1. Problem formulation

The type of LPV system, which is considered in this paper, assumes an affine dependence with a parameter vector $\tilde{\vartheta}_k$ and can be described in discrete time state space as:

$$\begin{aligned}
\mathbf{x}_{k+1} &= \mathbf{A}(\tilde{\vartheta}_k)\mathbf{x}_k + \mathbf{B}(\tilde{\vartheta}_k)\mathbf{u}_k + \mathbf{w}_k,\\
\mathbf{y}_k &= \mathbf{C}(\tilde{\vartheta}_k)\mathbf{x}_k + \mathbf{D}(\tilde{\vartheta}_k)\mathbf{u}_k + \mathbf{v}_k,
\end{aligned} \tag{5}$$

where $\mathbf{x}_k \in \mathbb{R}^{n_x}$, $\mathbf{u}_k \in \mathbb{R}^{n_u}$ and $\mathbf{y}_k \in \mathbb{R}^{n_y}$ are, respectively, the state, input, and output vectors. The process and measurement noises are $\mathbf{w}_k \in \mathbb{R}^{n_x}$ and $\mathbf{v}_k \in \mathbb{R}^{n_y}$ respectively. Both are considered unknown but bounded as $\mathbf{v}_k \in \mathbb{V}^{n_x}$ and $\mathbf{w}_k \in \mathbb{W}$ which are interval boxes.

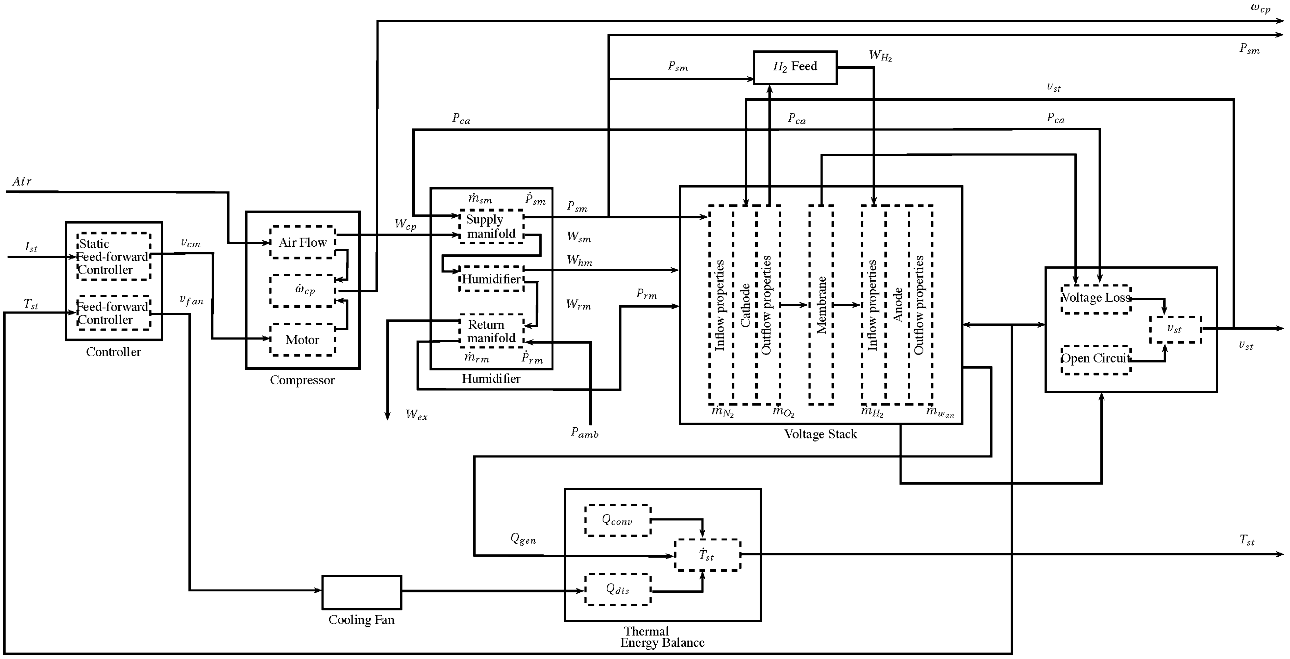

Fig. 2. Nexa© PEM fuel cell dynamic model diagram.

$\tilde{\vartheta}_k \in \Theta$ is the vector of time-varying parameters that change with the operating point scheduled by some measured system variablesp_k ($p_k := p(k)$) that can be estimated using some known function:

$$\tilde{\vartheta}_k = f(p_k), \tag{6}$$

where

$$\Theta = \{\tilde{\vartheta}_k \in \mathbb{R}^{n_\vartheta} | \underline{\tilde{\vartheta}}_k \leq \tilde{\vartheta}_k \leq \bar{\tilde{\vartheta}}_k\}. \tag{7}$$

The system described in Eq. (5) could be seen as a linear model parameterized by a monitored variable through Eq. (7) [5,19,20,21]. In practice, the model in Eq. (6) by a polytope of dimension is N described as an array of matrices described by

$$\begin{aligned}\begin{bmatrix}\mathbf{A}(\tilde{\vartheta}_k) & \mathbf{B}(\tilde{\vartheta}_k)\\ \mathbf{C}(\tilde{\vartheta}_k) & \mathbf{D}(\tilde{\vartheta}_k)\end{bmatrix} &\in \left\{\begin{bmatrix}\mathbf{A}_j(\vartheta^j) & \mathbf{B}_j(\vartheta^j)\\ \mathbf{C}_j(\vartheta^j) & \mathbf{D}_j(\vartheta^j)\end{bmatrix}\right\}\\ &\cong \sum_{j=1}^{N} \alpha_j(p_k)\cdot\begin{bmatrix}\mathbf{A}_j(\vartheta^j) & \mathbf{B}_j(\vartheta^j)\\ \mathbf{C}_j(\vartheta^j) & \mathbf{D}_j(\vartheta^j)\end{bmatrix},\end{aligned} \tag{8}$$

where $\mathbf{A}_j$, $\mathbf{B}_j$, $\mathbf{C}_j$and $\mathbf{D}_j$ are the state matrices for each jth model obtained by linearization of the non-linear model around the jth operating point. Using Eq. (8), the Eq. (5) can be approximated as follows:

$$\begin{aligned}\mathbf{x}_{k+1} &= \sum_{j=1}^{N} \alpha^j(p_k)\cdot[\mathbf{A}_j(\vartheta^j) \quad \mathbf{B}_j(\vartheta^j)]\cdot\begin{bmatrix}\mathbf{x}_k\\ \mathbf{u}_k\end{bmatrix},\\ \mathbf{y}_k &= \sum_{j=1}^{N} \alpha^j(p_k)\cdot[\mathbf{C}_j(\vartheta^j) \quad \mathbf{D}_j(\vartheta^j)]\cdot\begin{bmatrix}\mathbf{x}_k\\ \mathbf{u}_k\end{bmatrix}.\end{aligned} \tag{9}$$

3.2. PEMFC LPV structure

Using the PEMFC non-linear dynamic model presented in Section 2.1 and using the Jacobian linearization approach, the non-linear model is possible to transform it into a LPV model in state space form, as in Eq. (9) with the following system matrices structure

$$\mathbf{A}_j = \begin{bmatrix} a_{11} & 0 & 0 & a_{14} & 0 & 0 & 0 & 0 & 0 & 0\\ 0 & a_{22} & a_{23} & a_{24} & a_{25} & 0 & 0 & a_{28} & a_{29} & a_{210}\\ 0 & a_{32} & 0 & a_{34} & a_{35} & 0 & 0 & a_{38} & a_{39} & a_{310}\\ a_{41} & 0 & 0 & a_{44} & a_{45} & 0 & 0 & a_{48} & a_{49} & a_{410}\\ a_{51} & 0 & 0 & a_{54} & 0 & 0 & 0 & a_{58} & a_{59} & a_{510}\\ 0 & 0 & 0 & a_{64} & 0 & a_{66} & a_{67} & 0 & 0 & a_{610}\\ 0 & 0 & 0 & a_{74} & 0 & a_{76} & a_{77} & 0 & 0 & a_{710}\\ 0 & a_{82} & 0 & a_{84} & a_{85} & 0 & 0 & a_{88} & a_{89} & a_{810}\\ 0 & a_{92} & 0 & a_{94} & a_{95} & 0 & 0 & a_{98} & a_{99} & a_{910}\\ 0 & 0 & 0 & 0 & 0 & a_{106} & a_{107} & 0 & a_{109} & 0 \end{bmatrix},$$

$$\mathbf{C}_j = \begin{bmatrix} c_{11} & 0 & 0 & 0 & 0 & 0 & 0 & 0 & 0 & 0\\ 0 & 0 & 0 & c_{24} & 0 & 0 & 0 & 0 & 0 & 0\\ 0 & 0 & 0 & c_{34} & c_{35} & 0 & 0 & c_{38} & c_{39} & c_{310}\\ 0 & 0 & 0 & 0 & 0 & c_{46} & c_{47} & c_{48} & c_{49} & c_{410} \end{bmatrix},$$

$$\mathbf{B}_j = \begin{bmatrix} b_{11} & b_{12}\\ 0 & 0\\ 0 & 0\\ 0 & 0\\ 0 & 0\\ b_{71} & 0\\ b_{81} & 0\\ 0 & 0\\ b_{91} & 0\\ b_{101} & 0 \end{bmatrix}, \quad \mathrm{D}_j = \begin{bmatrix} 0 & 0\\ 0 & 0\\ d_{31} & 0\\ d_{41} & 0 \end{bmatrix} \tag{10}$$

where

- States: $x = [\omega_{cp}\ P_{om}\ m_{om}\ P_{sm}\ m_{sm}\ m_{H_2}\ m_{w,an}\ m_{N_2}\ m_{O_2}\ T_{st}]^T$.
- Inputs: $u = [I_{st}\ v_{cm}]^T$ where the scheduling variable is I_{st}.
- Outputs: $y = [P_{sm}\ v_{st}\ \lambda_{O_2}\ \omega_{cp}]$.
- Perturbations: $z = [T_{amb}\ P_{atm}]$.

In this case the scheduling variable is the current (I_{st}). Thus Eq. (6) is $\tilde{\vartheta}_k = f(I_{st,k})$ and the varying parameters (a_{ij}, b_{ij}, c_{ij} and d_{ij})

of the system matrices. Consequently the system in Eq. (9) can be particularized as follows.

$$\begin{aligned} \mathbf{x}_{k+1} &= \sum_{j=1}^{N} \alpha^j(I_{st,k}) \cdot [\mathbf{A}_j(\vartheta^j) \quad \mathbf{B}_j(\vartheta^j)] \cdot \begin{bmatrix} \mathbf{x}_k \\ \mathbf{u}_k \end{bmatrix}, \\ \mathbf{y}_k &= \sum_{j=1}^{N} \alpha^j(I_{st,k}) \cdot [\mathbf{C}_j(\vartheta^j) \quad \mathbf{D}_j(\vartheta^j)] \cdot \begin{bmatrix} \mathbf{x}_k \\ \mathbf{u}_k \end{bmatrix}. \end{aligned} \tag{11}$$

4. Linear parameter varying observer

4.1. Definition

Using the PEMFC LPV model obtained in previous section, a discrete time LPV observer for state estimation with *Luenberger observer* structure can be expressed as

$$\begin{aligned} \hat{\mathbf{x}}_{k+1} &= \mathbf{A}(\tilde{\vartheta}_k)\hat{\mathbf{x}}_k + \mathbf{B}(\tilde{\vartheta}_k)\mathbf{u}_k + \mathbf{L}(\tilde{\vartheta}_k)(\mathbf{y}_k - \hat{\mathbf{y}}_k) + \mathbf{w}_k, \\ \hat{\mathbf{y}}_k &= \mathbf{C}(\tilde{\vartheta}_k)\hat{\mathbf{x}}_k + \mathbf{D}(\tilde{\vartheta}_k)\mathbf{u}_k + \mathbf{v}_k. \end{aligned} \tag{12}$$

Using Eq. (11) the observer can be alternatively expressed as

$$\begin{aligned} \hat{\mathbf{x}}_{k+1} &= \sum_{j=1}^{N} \alpha^j(I_{st,k})[\mathbf{A}_j^o(\vartheta^j) \quad \mathbf{B}_j(\vartheta^j)] \cdot \begin{bmatrix} \hat{\mathbf{x}}_k \\ \mathbf{u}_k \end{bmatrix}, \\ \hat{\mathbf{y}}_k &= \sum_{j=1}^{N} \alpha^j(I_{st,k})[\mathbf{C}_j(\vartheta^j) \quad \mathbf{D}_j(\vartheta^j)] \cdot \begin{bmatrix} \hat{\mathbf{x}}_k \\ \mathbf{u}_k \end{bmatrix}, \end{aligned} \tag{13}$$

where

$$\mathbf{A}_j^o = \mathbf{A}_j(\vartheta^j) - \mathbf{L}_j(\vartheta^j) \cdot \mathbf{C}_j(\vartheta^j).$$

The observer gain (**L**) should be designed to guarantee closed loop stability for all operating points, i.e. $\tilde{\vartheta}_k \in \Theta$. This is achieved through LMI formulation for pole-placement within a wide class of pole clustering regions, defined by an affix $(-q, 0)$ and a radius r such that $(-q+r) < 0$ [22].

4.2. Observability analysis

The observer design implies the fulfilment of the observability condition that is related to the number of states that can be inferred (or estimated) based on the available measured outputs. For the study of the system observability degree at each operating point (ϑ) the following conditions are used

$$\text{rank}\left(\begin{bmatrix} \lambda_i I - \mathbf{A} \\ \mathbf{C} \end{bmatrix}\right); \qquad \text{cond}\left(\begin{bmatrix} \lambda_i \mathbf{I} - \mathbf{A} \\ \mathbf{C} \end{bmatrix}\right). \tag{14}$$

As discussed in [4], a given system eigenvalue λ_i is unobservable if the rank condition indicates a rank loss. On the other hand, a large condition number implies that the corresponding eigenvalue is weakly observable.

5. Application to fault detection

In order to test the proposed modelling methodology for fault detection, a common set of faults have been selected as benchmark. This set of fault was included in the model (Ballard, Nexa©) [11] in simulation environment in the MATLAB/SIMULINK© (see Fig. 1).

5.1. Model analysis

The stability of the PEMFC system, described in LPV form by Eq. (5), at each operating point is verified if all the eigenvalues of the system are negative. In the case of the a operating point corresponding to $I_{st} = 15$ A, the stability of the system can be verified by the eigenvalues shown in Table 1. On the other hand, although the system is observable using the observability matrix test, the observability of the system could be further analyzed with conditions showed in Eq. (14).

Table 1
Eigenvalues, rank and condition number for the observability analysis of the polytopic LPV system at $I_{st} = 15$ A.

State	λ_i	Rank	Cond
ω_{cp}	−1.00E+04	10	1.11E−03
P_{rm}	−543.8	10	27.92
m_{rm}	−388	10	31.87
P_{sm}	−49.9	10	404.82
m_{sm}	−13.14	10	2.22E+03
m_{H_2}	−4.88	10	1.04E+04
m_{an}	−1.72	10	5.23E+04
m_{N_2}	−1.26	10	7.53E+04
m_{O_2}	−0.003	10	1.90E+07
T_{st}	−2.50E−07	10	3.31E+11

Table 2
Eigenvalues, rank and condition number for the observability analysis of the reduced polytopic LPV system at $I_{st} = 15$ A.

State	λ_i	Rank	Cond
x_1	−26.81	4	30.4
x_2	−4.91	4	11.5
x_3	−2.21	4	88.94
x_4	−3.50E−03	4	3.80E+03

From Table 1, it is clear to see that there are states (ω_{cp}, P_{sm}, m_{sm}, P_{rm}, m_{rm}) which contain fast dynamics compared to others such as the temperature (T_{st}) or oxygen mass (m_{O_2}). Both types of dynamics could decrease the observability performance of the system producing problems with the state estimation using the observer (Table 2). This can be verified by looking at condition number introduced in Eq. (14). To solve this problem, the order of the model should be reduced as proposed in [23]. Table 1 shows that the eigenvalues of the four first states present a higher value than the rest of them. This means that the model can be reduced to a four order state space model instead of the original ten order state space. The reduced system is observable and the condition number has improved with respect to the values presented in Table 3.

In order to test the behaviour of the reduced model compared to the complete model, both models were implemented in simulation. Fig. 3 shows the simulation results of the complete and reduced PEMFC LPV model under a sequents of operating point changes in current demand (I_{st}). This figure shows also the measured outputs for comparison with those generated in simulation. Fig. 4 shows

Table 3
Description of the fault scenarios implemented in FGB.

ID	Fault description	Type	Magnitude
f_1	There is a suddenly increase of friction in the mechanical component part of the compressor	Parametric abrupt	$\Delta k_R = 60\%$
f_2	Degradation in the stack cells stack is presented because of contact-sensitivity reactions against to a reaction killer	Parametric abrupt	40%
f_3	Hydrogen leak in the anode is presented because of seal degradation.	Parametric abrupt	$A_{nl,f} = 2\text{E}+2$
f_4	A suddenly leak of hydrogen is presented at the anode inlet manifold	Parametric abrupt	80%
f_5	A suddenly leak of air is presented at the inlet outlet supply manifold inlet manifold	Parametric abrupt	10%

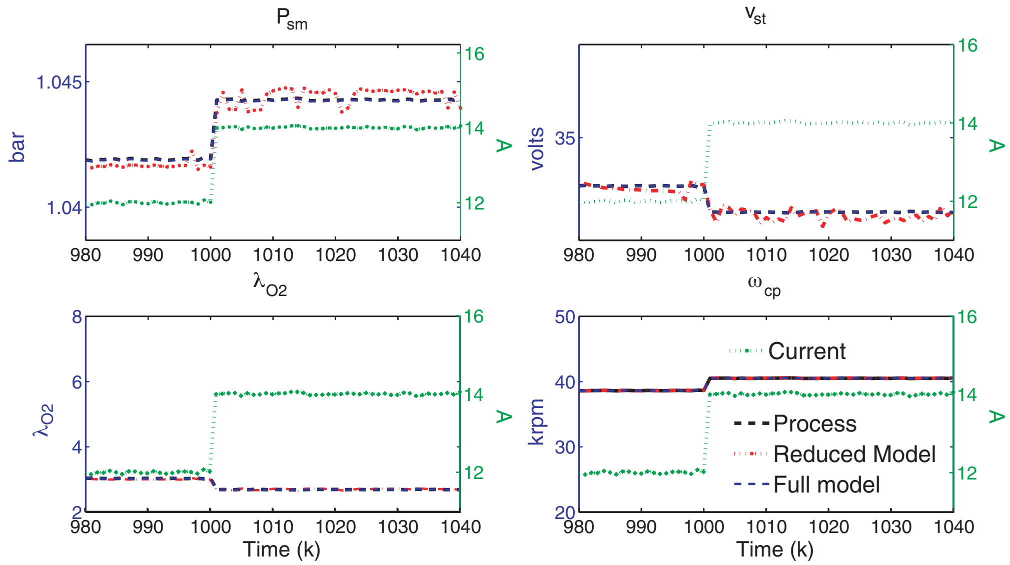

Fig. 3. Comparison of process output signal between real and reduced polytope LPV models.

the model error between the models and the measured outputs of the real process. From either of the two previous figures, it can be noticed that the reduced model presents better performance than the complete one. This result justifies the model reduction since improves the observability and numerical conditioning properties.

5.2. Fault benchmark

The usefulness of LPV model and observer proposed in this paper is illustrated in fault detection. For this purpose, a set of common possible fault scenarios is considered and implemented using the simulator presented in Fig. 1 by adding a fault generator block (FGB) (see Fig. 7). Table 3 describes the set of faults which were considered as case study. In the following section, it is described how the faults were included in simulation.

5.2.1. Fault 1

The fault f_1 is simulated with an increment, ΔR_{cm}, in the compressor motor resistance R_{cm}. The fault effect is translated in a change in the compressor torque τ_{cm} affecting directly the state variable ω_{cp}

$$\tau_{cm} = \frac{\eta_{cm} k_t}{R_{cm} + \Delta R_{cm}} (v_{cm} - k_v \omega_{cm}), \tag{15}$$

where η_{cm} is the motor mechanical efficiency, k_t and k_v are motor constants, and ω_{cm} is the compressor speed. Furthermore, the parameter is related with the state of P_{sm} because its dynamics are governed by the compressor inlet air flow

$$W_{ca,i} = (k_{sm} + \Delta k_{sm})(P_{sm} - P_{cp}), \tag{16}$$

where P_{cp} is the compressor pressure and P_{sm} is the supply manifold pressure. The amount of flow that is feed into the cathode is related

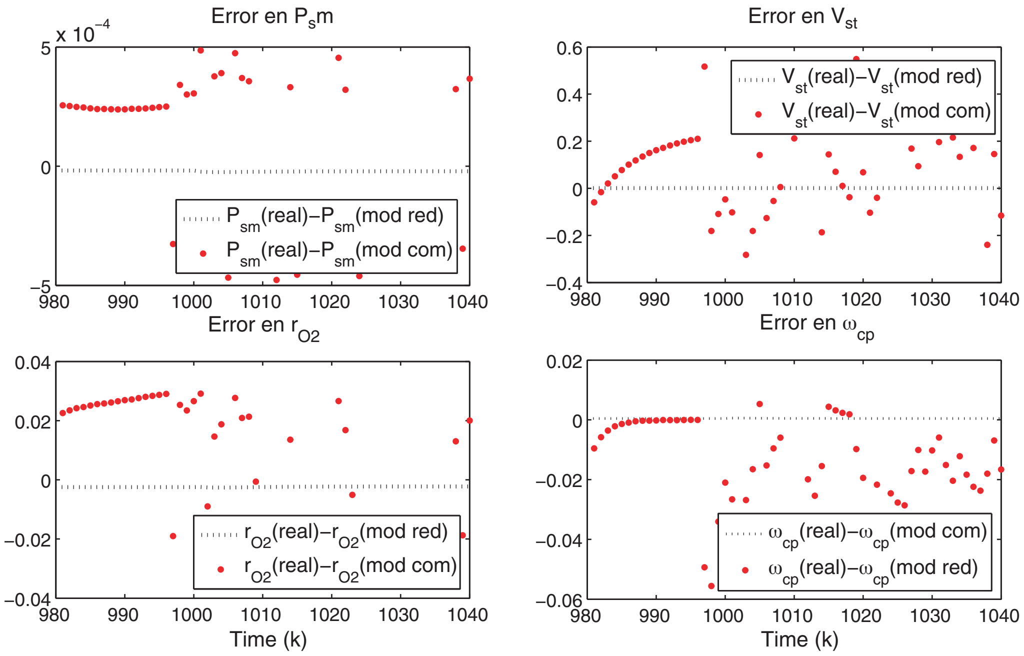

Fig. 4. Model residuals (reduced model and real process data).

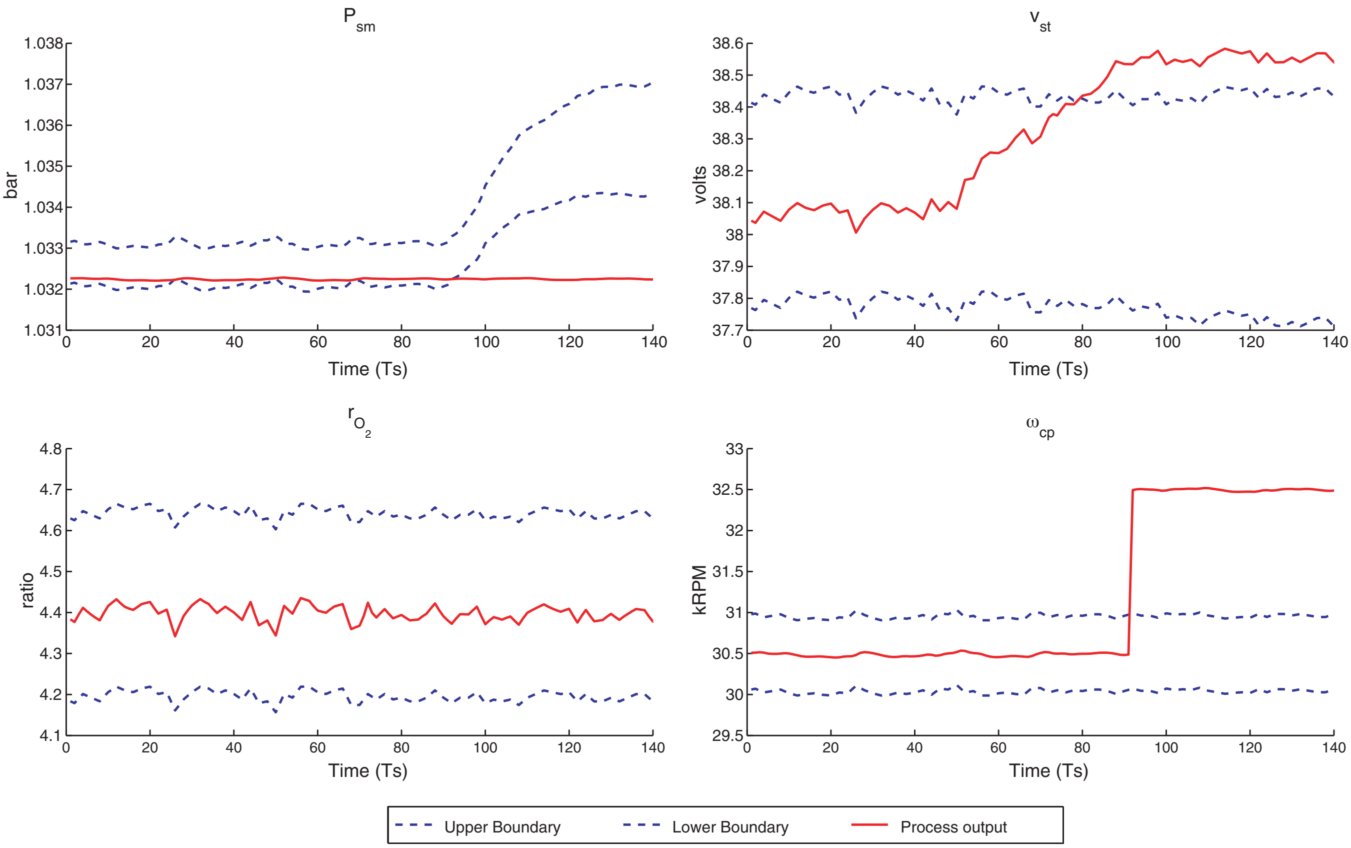

Fig. 5. Confidence intervals for predicted outputs against real measurements in faultily operation (f_2, f_4).

to pressure with a linear constant k_{sm}. It is possible to simulate a reduction in the supply manifold as a change in k_{sm} as Δk_{sm}. Thus, the air mass flow is affected by the fault and consequently, the total mass balance across the PEMFC changes.

5.2.2. *Fault 2*

Fault f_2 is presented as any contamination in the reaction into the stack reducing the chemical reaction efficiency by decreasing of catalysis active area. The current density, i, is defined as current per area in a single cell, which is equals to stack current I_{st} (A), per cell active area, A_{fc} (cm^2). If the stack is mead of a set of cells in series architecture.

$$i = \frac{I_{st}}{A_{fc} \cdot \Delta A_{fc}}, \tag{17}$$

where ΔA_{fc} is the active contaminated area.

Because of the major voltage drops are associated with current density for non-linear relations, see [24], current density is an important issue for total stack voltage

$$v_{st} = n_{fc} \times [E - v_{act} - v_{ohm} - v_{conc}], \tag{18}$$

where E is the open circuit voltage; v_{act}, v_{ohm} and v_{conc} are activation loss, ohmic loss and concentration loss, respectively, then is clear that fault f_2 will have a direct action over the output of stack voltage.

5.2.3. *Fault 3*

The term $W_{H_2,nl}$ introduced in Eq. (10) represents the natural leak from the anode of the fuel cell stack. This leak is always present due to the physical stack sealing design. It is assumed that the natural leak is governed by a standard orifice relation through an effective area, A_{nl}. This parameter has been obtained in [25]. In order to simulate a degradation in the seal a change in A_{nl} is used as $A_{nl,f} = A_{nl} f_3$.

$$W_{H_2,nl} = \frac{A_{nl,f} P_{an}}{\sqrt{R_{an}\phi_{an}}} P_r^{1/\gamma} \left(\frac{2\gamma}{\gamma - 1} [1 - P_r^{(\gamma-1)/\gamma}] \right)^{1/2}, \tag{19}$$

where $P_r = P_{an}/P_{atm}$ is the pressure ratio across the assumed leak and the anode gas constant, R_{an}, is calculated through the universal gas constant, R as follows

$$R_{an} = \frac{R}{y_{H_2} M_{H_2} + (1 - y_{H_2}) M_{H_2O}}, \tag{20}$$

where the molar fraction of hydrogen in the anode is given by

$$y_{H_2} = \frac{P_{an} - \phi_{an} P_{sat_{T=st}}}{P_{an}}. \tag{21}$$

5.2.4. *Fault 4*

This fault introduces a leak of hydrogen and is simulated as a change in the mass balance in the hydrogen inlet flow as follows

$$W_{H_2,f} = W_{H_2,i} - W_{H_2,if_4}. \tag{22}$$

5.2.5. *Fault 5*

This fault appears as a leak of air at the cathode inlet flow. Because this fault is considered as a leak, it is introduced in the mass balance, as fault f_4, as follows

$$W_{hm,f} = W_{hm,i} - W_{hm,if_5}. \tag{23}$$

Note that the amount of air that does not enter into the system will not only create an abrupt change in the total mass balance, where m_{O_2}, m_{N_2} state variable are mainly involved, but also a system pressure change.

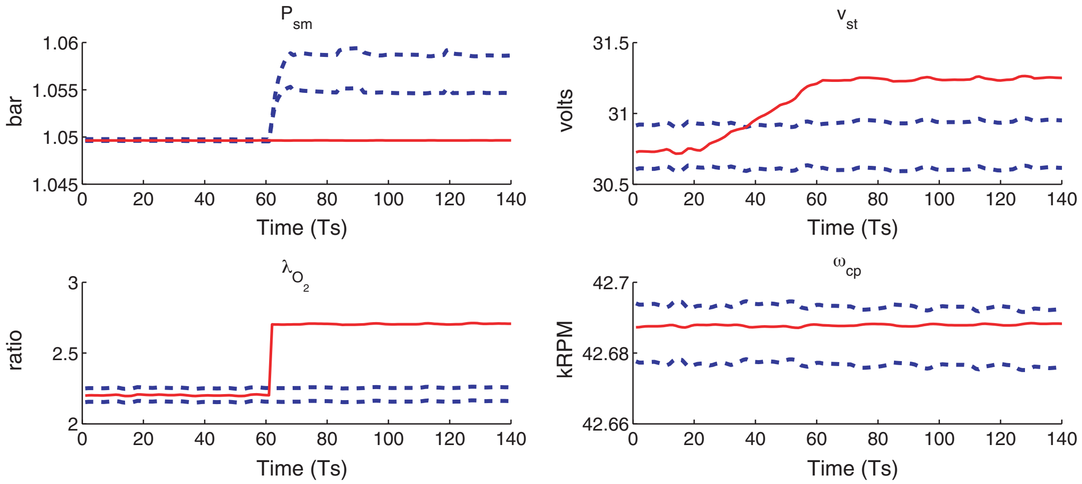

Fig. 6. Confidence intervals for predicted outputs against real measurements in faultily operation (f_2, f_4).

5.3. Fault detection systems

The fault diagnosis system (FDS) based on the LPV observer proposed in this paper has been implemented using MATLAB/SIMULINK environment [26]. The simulator of fuel cell model (Ballard Nexa©) presented in Section 2.1 is used as virtual reality for the fault detection case study. The FGB and FDS subsystems blocks were added to the PEM FC simulator to create the fault scenarios presented in the previous section.

5.3.1. Fault detection process (FDP)

Using the measured inputs and outputs presented in Section 2.1 and using the structural analysis methodology [27], the following set of residuals can be obtained as:

$$\begin{aligned} r_1 &= P_{sm} - \hat{P}_{sm}, \\ r_2 &= \omega_{cp} - \hat{\omega}_{cp}, \\ r_3 &= \lambda_{O_2} - \hat{\lambda}_{O_2}, \\ r_4 &= v_{st} - \hat{v}_{st}. \end{aligned} \tag{24}$$

The residuals are defined conceptually as the differences the process measurements and output estimation from the LPV observer as described in Section 3.2. From the model analysis in Section 5.1, the reduced model offers a better performance when implementing the LPV observer than the complete model. Thus the reduced model is used for creating the PEMFC LPV model.

Fig. 5 shows the measured and the confidence intervals for predicted outputs considering noise and process noise. Notice that when the f_2 is introduced at $k = 50$ in the PEMFC system, at the time $k = 85$ the sensor measurements cross the boundaries of confidence intervals of predicted outputs. This allows detecting the fault.

Fig. 6 shows PEMFC process behaviour compared with the adaptive thresholding generated the interval observer. The process suffers a degradation in supply pressure (P_{sm}) sensor fault over the time starting from $k = 20$ and ends in $k = 60$, the measurement cross the upper boundary at $k = 40$. Note that the other variables do not cross their thresholds. Later appears a sensor offset in λ_{O_2}, that leads the measurement to cross the upper bound at $k = 60$. The effect of this second fault additionally acts over the interval estimation of ω_{cp} (Fig. 7).

The confidence intervals for predicted outputs are computed using zonotope-based algorithm proposed in [28], which offers an efficient way of taking into account model uncertainty when estimating the state using an LPV observer.

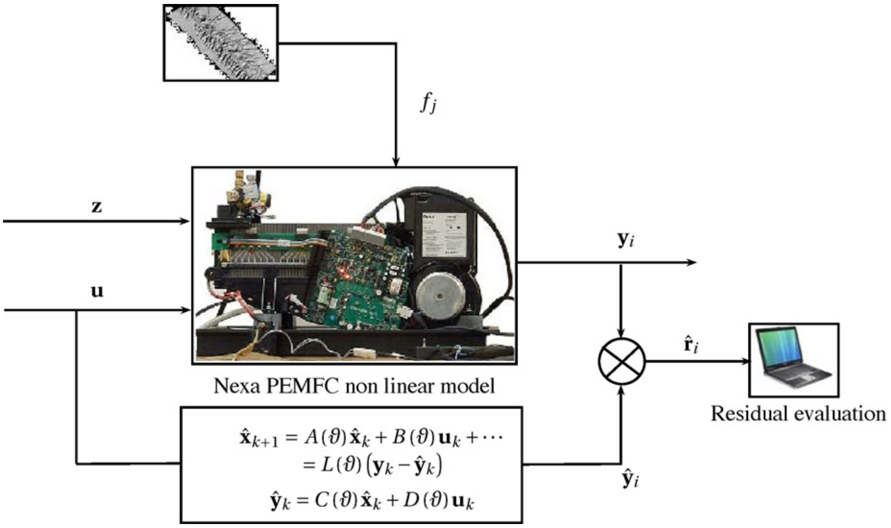

Fig. 7. Fault generator block (FGB) and fault diagnosis system (FDS) implementation diagram.

6. Conclusions

In this paper, an LPV model is introduced as a means to approximate a PEMFC that presents a highly non-linear behaviour using a model with linear structure but with parameters that vary with the operating point. This model can be obtained from the linearization of non-linear model which has been calibrated above a set of data from a commercial PEMFC model (Ballard, Nexa©) around a set of operating points. In addition to the LPV model, the paper proposes the design of an LPV observer to estimate PEMFC system states. To illustrate the usefulness of the LPV model and observer, the application to fault detection is used. The paper also analysis the observability of the LPV model obtained concluding that the complete LPV model contains dynamics that are very different that create numerical difficulties in the observation implementation. These difficulties can be overcome by model reduction neglecting system fast dynamics. The application of the LPV observer to fault detection is shown using a simulator developed using an experimentally calibrated nonlinear model of a typical PEMFC (Nexa© Power Module). A set of common fault scenarios have been defined and implemented in the simulator to test the LPV observer in fault detection. Finally, the paper presents how the observer can satisfactorily detect faults in some of the fault scenarios defined. As an extension of the research presented in this paper, an algorithm that allows not only detect faults but also isolate them is being developed based also in the LPV observer developed. Some preliminary results have already been obtained that show promising results in this line.

References

[1] D. Feroldi, M. Serra, J. Riera, Journal of Power Sources 169 (2007) 205Ű–212Ű.
[2] T. Escobet, D. Feroldi, S. de Lira, V. Puig, J. Quevedo, J. Riera, M. Serra, Journal of Power Sources (2009) 205–212.
[3] J. Pukrushpan, H. Peng, A. Stefanopoulou, Journal of Dynamics Systems, Measurement, and Control 126 (2002) 14–25.
[4] T. Pukrushpan, A.G. Stefanopoulou, Automotive Research Center, Department of Mechanical Engineering 126 (2004) 14–25.
[5] P. Apkarian, P. Gahinet, IEEE Transactions on Automatic Control 40 (1995) 853–863.
[6] P. Falugi, L. Giarre, L. Chisci, G. Zappa, in: IFAC Workshop on Periodic Control Systems, 2001, pp. 33–38.
[7] J.S. Humbert, A.J. Krener, International Journal of Control 71 (1998) 805–821.
[8] J.S. Shamma, M. Athans, Automatica 27 (1991) 559–564.
[9] J. Shamma, Linearization and Gain Scheduling, W. Levine Control Handbook, CRC Press Edition, Boca Raton, 1996.
[10] J. Shamma, D. Xiong, Automatica 35 (1999) 1081–1089.
[11] S. de Lira, V. Puig, J. Quevedo, National Congress of Fuel Cells, CONAPICCE, Sevilla, Spain, 2010.
[12] D. Marquardt, SIAM Journal Applied Mathematics 11 (1963) 431–441.
[13] J. Dennis, Nonlinear Least-Squares: State of the Art in Numerical Analysis, D. Jacobs ed., Academic Press, 1977, pp. 269–312.
[14] C. Mehendale, M.G. Karolos, American Control Conference, 2006, pp. 14–16.
[15] L. Fabien, Z. Jing-Yun, P. Borne, Communications & Control 1 (2006) 73–84.
[16] C. Mehendale, M.G. Karolos, 43rd IEEE Conference on Decision and Control, Atlantis, Paradise Island, Bahamas, 2004, pp. 14–17.
[17] P. Barahyi, D. Tikk, Y. Yam, R. Patton, From differential equations to PDC controller design via numerical transformation, Computers in Industry 51 (2003) 281–297.
[18] B. Bamieh, L. Giarre, Identification for linear parameter varying models, the 38th IEEE Control and Decision Conference, 2 (1999) 1505-1510.
[19] B. Bamieh, L. Giarre, Identification For a General Class of LPV Models, the IFAC systemidentification (2000).
[20] B. Bamieh, L. Giarre, Identification for a General Class of LPV Models, the IFAC System Identification, 2000.
[21] B. Bamieh, L. Giarre, International Journal of Robust and Nonlinear Control 12 (2002) 841–853.
[22] M. Chilali, P. Gahinet, IEEE Transactions on Automatic Control 41 (1996) 358–367.
[23] R Moore, Interval Analysis, Prentice-Hall, Englewood Cliffs, 1966.
[24] J. Larminie, A. Dicks, Fuel Cell Systems Explained, John Wiley & Sons Inc., 2003.
[25] A. Ingimundarson, A.G. Stefanopoulou, D.A. McKay, IEEE Transactions on Automatic Control 16 (2005) 1004–1012.
[26] C. Spiegel, PEM Fuel Cell: Modeling and Simulation Using MATLAB, Elsevier, 2008.
[27] M. Blanke, M. Kinnaert, J. Lunze, M. Staroswiecki, Diagnosis Fault-tolerant Control, Springer-Verlag, Berlin/Heidelberg, 2003.
[28] S. De Lira, J. Quevedo, V. Puig, 20th International Workshop on Principles of Fault Diagnosis, DX, Stockholm, pp. 91-98.

Control-Oriented Modeling and Experimental Validation of a PEMFC Generation System

Cristian Kunusch, *Member, IEEE*, Paul F. Puleston, Miguel A. Mayosky, *Senior Member, IEEE*, and Attila P. Husar

***Abstract*—An experimentally validated control-oriented model that reproduces the most typical features of a laboratory proton exchange membrane fuel cell generation system, is presented in this paper. The proposed representation is a 7th order fully analytical nonlinear model of ordinary differential equations, primarily focused on the system gases dynamics. The complete model is developed following a modular procedure, combining theoretical modeling techniques and empirical analysis based on experimental data. The presented methods can be used as a general modeling guideline for control-oriented purposes, being possible to adapt to other fuel-cell-based systems with similar characteristics.**

***Index Terms*—Control-oriented model, experimental validation, fuel-cells systems, nonlinear systems.**

I. INTRODUCTION

FUEL cells represent a radically different approach to energy conversion, one that could replace conventional power generation technologies in a wide variety of applications, from automotive and stationary power systems to portable appliances. In particular, a proton exchange membrane (PEM) fuel cell is an electrochemical device that converts hydrogen chemical energy into electric power energy, without the intermediate production of mechanical work and with water and heat as the only byproducts [1]. Then, considering that hydrogen production from water electrolysis can be performed using renewable energy (solar, wind, geothermal, etc.), PEM fuel cells emerge as one of the cleanest and most promising alternatives to reduce fossil fuel dependency [2].

In this context, improvements in this field require interdisciplinary work and the development of new technologies in many areas. From the automation control point of view, the natural step is to face the challenge of designing and implementing efficient control strategies for the actual fuel-cell-based energy generation systems. Like in most control design procedures, the first and decisive stage is to obtain a reliable and adequate mathematical description of the system. In this particular case, a control-oriented nonlinear model is a key requirement for the development of a control algorithm capable to avoid transient power deterioration and irreversible damages in cell membranes [3].

Furthermore, critical characteristics of PEM fuel cell (PEMFC) based systems such as its viability, robustness, and efficiency may be strongly related to their proper control. Hence, several model-based control strategies have been reported in the past few years [3]–[7]. As a matter of fact, modeling PEMFC systems is a particular difficult task, due to the interactions among different subsystems, especially as far as control purposes are concerned. Previous literature models like the ones presented in [8] and [9] are electrochemical characterizations based on empirical relationships that do not consider the dynamics of the different gasses. On the other hand, works such as [3], [10]–[12] present extended equations, including gasses dynamics and temperature effects within the stack, however, only [10] and [11] have proposed fully analytical control-oriented models. In [11], only a three state air supply subsystem is explained and validated, the humidifier is not included in the model and the characterization of the other subsystems is merely outlined. [10] is probably the first and the most accurate validated control engineering model developed for a PEM fuel-cell system, being the base of numerous works such as [3], [13], [14]. Nevertheless, such accuracy entails a certain degree of complexity, making this model not directly suitable for nonlinear control design.

The goal of the current work is therefore to present a fully validated, fully analytical model of the fuel cell flow dynamics specially developed for nonlinear control purposes. The model retains parameters that have physical significance, so that it can be adapted to other systems. It adequately describes the interaction between the different subsystems (i.e., the fuel cell stack, the reactant supply system and the humidity management unit) from a control point of view.

As a result, based on the use of some general physical laws, the proposed PEMFC control-oriented model presents relevant contributions from the automatic control point of view. On the one hand, the systematic procedure developed in the paper makes it a useful general guideline to evaluate other existing modeling schemes and develop new models. On the other hand, the nonlinear control design suitability of the model and the explicit set of state-space equations make it easy to reproduce and directly apply sophisticated control algorithms, such as model predictive control and variable structure control. It is noteworthy to mention that the authors, using the proposed model, have already obtained encouraging results applying oxygen stoichiometry control by means of homogeneous second order sliding mode design (preliminary results can be found in [15]).

Manuscript received October 1, 2010; revised January 7, 2011; accepted February 21, 2011. Date of publication April 21, 2011; date of current version August 19, 2011. This research was supported by the CICYT project DPI2010-15274 (MICINN-España), the Agencia Española de Cooperación Internacional (AECI) under the project A/026279/09, the CSIC JAE-DOC Research Programme, Universidad Nacional de La Plata (UNLP), CONICET, and CICpBA. Paper no. TEC-00387-2010.

C. Kunusch and A. P. Husar are Automatic Control Systems, Institut de Robòtica i Informàtica Industrial (CSIC-UPC), Barcelona, Spain (e-mail: ckunusch@iri.upc.edu; ahusar@iri.upc.edu).

P. F. Puleston and M. A. Mayosky are with the Facultad Ingenieria - LEICI, University of La Plata, La Plata, Buenos Aires, Argentina (e-mail: puleston@ing.unlp.edu.ar; mayosky@ing.unlp.edu.ar).

Digital Object Identifier 10.1109/TEC.2011.2124462

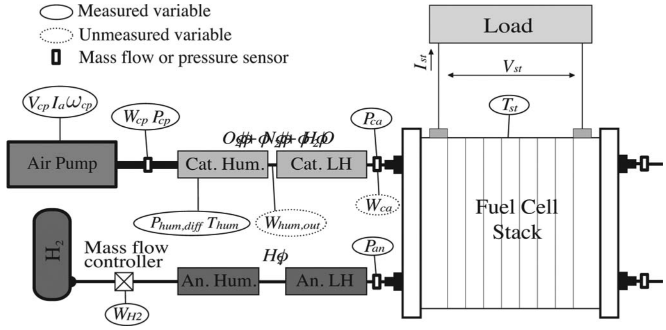

Fig. 1. Fuel-cell system diagram.

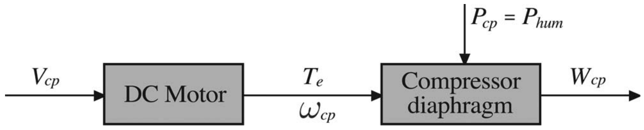

Fig. 2. Schematic diagram of the compressor subsystem.

More particularly, the laboratory test plant under study in this proposal mainly comprises a fuel-cell stack, an air compressor, a hydrogen storage tank, humidifiers, and line heaters (see schematic representation in Fig. 1).

The modeling process is conducted following a modular methodology, combining a theoretical approach, together with empirical analysis based on experimental data. The work is organized in a way such that the fundamentals of the proposed combined methods can be used as a general modeling guideline, being easy to adapt to different fuel-cell systems with few modifications. In fact, every subsystem is modeled in terms of physical laws and only adjusting some specific parameters. For instance, following the procedure below, changes in the gas humidification subsystems, the air vacuum pump or even in case of stack replacement would just require to follow the proposed steps and only reprocess some indicated data.

II. AIR COMPRESSOR SUBSYSTEM

The air compressor is a 12 V dc oil-free KNF diaphragm vacuum pump, which is based on a simple principle: An elastic diaphragm, fixed on its perimeter, moves up and down its central point by means of an eccentric. On the down-stroke, it draws the air or gas being handled through the inlet valve. On the up-stroke the diaphragm forces the gas through the exhaust valve and out of the head. The compression chamber is hermetically separated from the drive mechanism by the diaphragm. The pump transfers, evacuates, and compresses completely oil-free gas and is driven by a 15 W dc motor.

The equations that describe the behavior of the system are obtained by analyzing the air compressor as two coupled subsystems. The first one embodies the permanent magnet dc motor dynamics and, the second one, represents the compressing diaphragm nonlinear characteristics (Fig. 2).

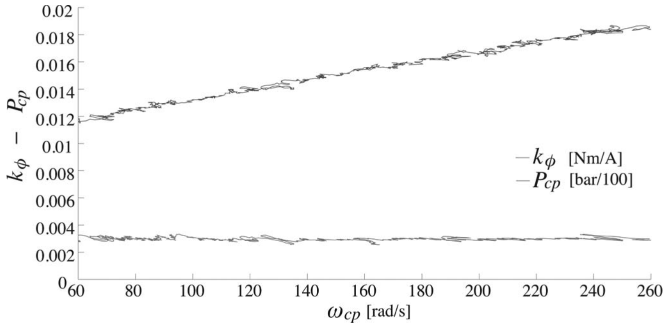

Fig. 3. k_ϕ versus ω_{cp} (experimental data).

A. Air Compressor Motor Dynamic Equations

The following equations summarize the dynamic model of the compressor dc motor:

$$V_{\mathrm{cp}}(t) = L\frac{di_a(t)}{dt} + Ri_a(t) + k_\phi \omega_{\mathrm{cp}}(t) \tag{1}$$

$$J\frac{d\omega_{\mathrm{cp}}}{dt} = T_e(t) - T_l(\omega_{\mathrm{cp}}(t), P_{\mathrm{cp}}(t)) \tag{2}$$

with

$$T_e(t) = k_\phi i_a(t) \tag{3}$$

where V_{cp} is the armature voltage, i_a the armature current, L and R the electrical inductance and resistance of the stator winding, k_ϕ the motor constant, ω_{cp} the shaft angular speed, P_{cp} the absolute pressure at the compressor output, J the inertia, T_e the electrical torque, and T_l is a nonlinear function that groups together the effects of the motor and diaphragm friction and the pneumatic load. The computations of the electrical and mechanical parameters of the compressor and the load torque function T_l are developed in a systematic procedure.

To start with, the electrical resistance and inductance of the stator winding can be directly measured through an electronic impedance meter. Then, the k_ϕ value is determined using the electrical equation of the motor (1) in steady state operation

$$L\frac{di_a(t)}{dt} = V_{\mathrm{cp}} - Ri_a - k_\phi \omega_{\mathrm{cp}} = 0. \tag{4}$$

From (4), $k_\phi = \frac{V_{\mathrm{cp}} - R.i_a}{\omega_{\mathrm{cp}}}$ can be computed by measuring i_a and ω_{cp} at different equilibria. Fig. 3 shows that for various compressor pressures (P_{cp}) the value of k_ϕ remains constant.

The next step deals with the characterization of the load torque function T_l, that lumps the friction and the pneumatic loads. In a first approach, it can be modeled as a nonlinear static function of ω_{cp} and P_{cp}. For modeling purposes, this load torque expression was divided into two terms

$$T_l(\omega_{\mathrm{cp}}, P_{\mathrm{cp}}) = T_{l,\mathrm{amb}}(\omega_{\mathrm{cp}}) + T_l'(\omega_{\mathrm{cp}}, P_{\mathrm{cp}}). \tag{5}$$

The former corresponds to the load torque of the system operating at ambient pressure. The latter takes into account the extra torque that appears when the diaphragm vacuum pump operates at pressures higher than the ambient.

The experimental values of the load torque can be computed using data obtained from steady state operation tests. Under

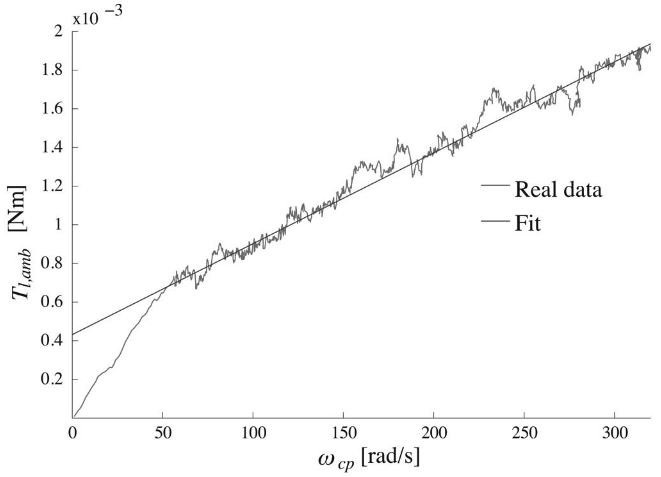

Fig. 4. $T_{l,\mathrm{amb}}$ versus ω_{cp}: measured data and linear approximation.

these conditions $\dot{\omega}(t)$ is zero, thus (2) gives

$$T_e(t) = k_\phi i_a(t) = T_l(\omega_{\mathrm{cp}}, P_{\mathrm{cp}}) \tag{6}$$

and T_l can be readily inferred from direct measurement of the current i_a.

Then, with the assistance of (2), the values of the first term of (5), $T_{l,\mathrm{amb}}$, are obtained conducting experiments at ambient pressure and different shaft speeds. Analyzing the data (see Fig. 4), it can be concluded that $T_{l,\mathrm{amb}}$ can be well approximated by a linear expression, such as

$$T_{l,\mathrm{amb}}(\omega_{\mathrm{cp}}) = A_0 + A_1\omega_{\mathrm{cp}} \tag{7}$$

where A_0 and A_1 are parameters determined experimentally that can be found in the Appendix.

To find the expression of the second term of (5), T_l', a new set of experiments is required, with the compressor working at different speeds and compressor pressures, covering its entire range of operation (60 rad/s $< \omega_{\mathrm{cp}} <$ 360 rad/s, 1 bar $< P_{\mathrm{cp}} <$ 2.5 bar). Then, from (6), (5), and (7), T_l' can be written in terms of the current i_a and the speed ω_{cp}, both measurable variables

$$\begin{aligned} T_l'(\omega_{\mathrm{cp}}, P_{\mathrm{cp}}) &= T_l(\omega_{\mathrm{cp}}, P_{\mathrm{cp}}) - T_{l,\mathrm{amb}}(\omega_{\mathrm{cp}}) \\ &= k_\phi i_a - A_0 - A_1\omega_{\mathrm{cp}}. \end{aligned} \tag{8}$$

Combining (8) with the data gathered in the experiments, the following bivariate quadratic function can be obtained by means of polynomial regression modeling tools (e.g., polyfitn [16])

$$\begin{aligned} T_l' = A_{00} &+ A_{10}\omega_{\mathrm{cp}} + A_{20}\omega_{\mathrm{cp}}^2 + A_{01}P_{\mathrm{cp}} \\ &+ A_{11}\omega_{\mathrm{cp}}P_{\mathrm{cp}} + A_{02}P_{\mathrm{cp}}^2 \end{aligned} \tag{9}$$

with A_{ij} constant coefficients.

In Fig. 5, two surfaces are displayed. The first one (colored surface), results from the interpolation of experimental data (dots and crosses). The second one (grey surface), depicts the quadratic approximation (9) that best fits the obtained data.

Note that with this approach, losses due to deviations from the isentropic compression and unmodeled friction terms are now incorporated into the model [10].

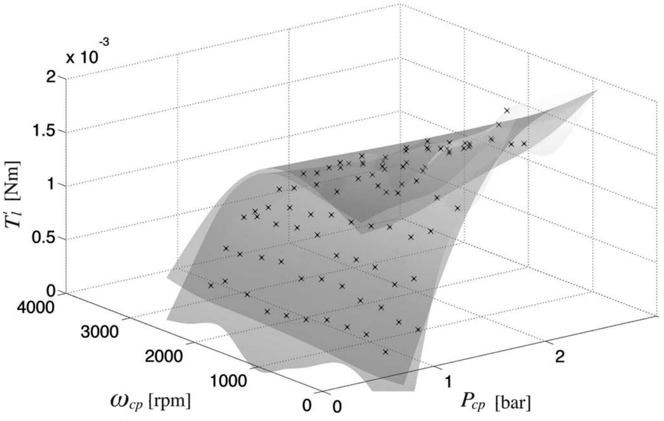

Fig. 5. T_l' surface interpolation from real data (colored surface) and polynomial approximation (grey surface).

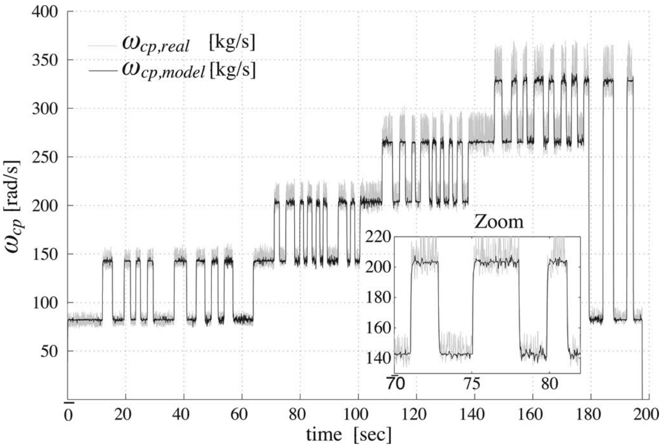

Fig. 6. Validation of the dc motor model dynamics.

The following parameter to be estimated is the motor inertia. Considering the practical impossibility to directly measure J, its value can be determined by adjusting the dynamic response of the model variable $\omega_{\mathrm{cp}}(t)$ to the experimental data. In the validation test presented in Fig. 6, step variations are applied to the compressor input voltage. It can be seen that the angular speed matches, even dynamically, the experimental values. This result is verified in a broad span of working conditions, indicating that the developed model is capable to predict the motor behavior in an extended range of operation. In fact, the approximation error of ω_{cp} remains below 3 % in all the tested working conditions.

B. Diaphragm Vacuum Pump Characteristics

The next modeling stage required to complete the compressor model is the characterization of the map that relates the output flow W_{cp} with the internal variable ω_{cp} and compressor pressure P_{cp}.

To this end, several steady state tests exploring different operating conditions have been conducted in order to gather data from the mass flow meter, the tachometer, and the pressure transducer, respectively. Then, following a fitting procedure similar to the one performed with T_l', an approximating bivariate

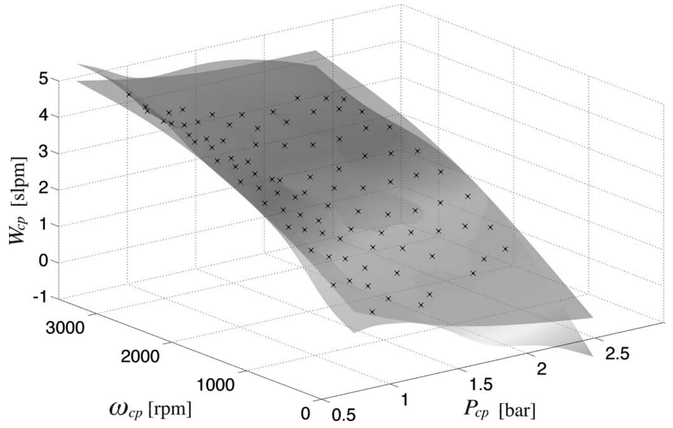

Fig. 7. $W_{\rm cp}$ surface interpolation from real data (colored surface) and polynomial approximation (gray surface).

function is obtained

$$W_{\rm cp} = B_{00} + B_{10}\omega_{\rm cp} + B_{20}\omega_{\rm cp}^2 + B_{01}P_{\rm cp} + B_{11}\omega_{\rm cp}P_{\rm cp} + B_{02}P_{\rm cp}^2 \qquad (10)$$

with $B_{\rm ij}$ constant values.

In Fig. 7 the $W_{\rm cp}$ approximated surface corresponding to (10) is shown (gray surface), as well as the spline interpolation of the real data (colored surface).

The parameters and coefficients of the compressor under study can be found in the Appendix.

C. Air Compression

The air dynamics corresponding to the compression process inside the diaphragm pump can be fully modeled using the principles of mass and momentum conservation. Nevertheless, a reasonable good approximation from the control viewpoint can be obtained by including this extra dynamics in the motor inertia and readjusting the value of J determined in Section II.A. The new value of this equivalent inertia is computed from experimental tests and validated in the overall operating range. The obtained value of the gathered inertia (J_g) of the vacuum pump plus the dc motor was $J_g = 1.2 \times 10^{-6}$ Nm.

Fig. 8 presents the time evolution of the compressor air flow of the FC system under consideration. It can be observed that, even during transients, the model provides a very good approximation of the experimental data. This result is also verified at different air compressor flows and pressures.

III. AIR HUMIDIFICATION SUBSYSTEM

Cellkraft P-series humidifiers based on exchange membranes are used to maintain proper humidity conditions inside the cells, which is crucial to ensure the optimal operation of PEM membranes. Gas humidification at flows rates up to 10 slpm and pressures close to 10 bar can be achieved with this sort of devices. The line heaters and stack temperatures are controlled by a power station via decentralized PID controllers, allowing for independent gas conditions to the stack.

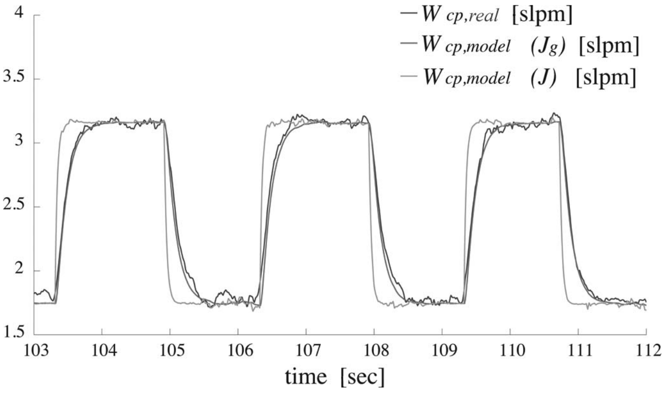

Fig. 8. Compressor dynamics.

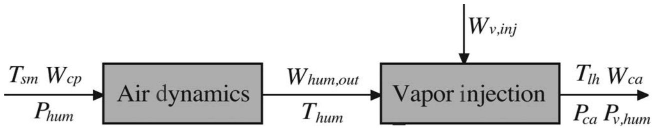

Fig. 9. Schematic diagram of the humidification subsystem.

The operating principle of the membrane humidification technique is feeding deionized temperature-controlled water and the gas to be humidified to each side of a polymeric membrane, respectively. During the process, a humidity gradient is established across the membrane, allowing the transference of water towards the circulating gas by diffusion. The degree of humidification is regulated by adjusting the water temperature within the humidifier. The closed loop control of moisture can be performed by two different methods, i.e. controlling either the dew point of the gas or the water temperature [17], the temperature control method was implemented for the following experiments.

Prior to entering the stack, the humidified gas circulates through a line heater. The purpose of this device is twofold. On the one hand, by rising the gas temperature, condensation inside the cathode channels is prevented. On the other hand, regulation of the differential temperature (between the humidifier and line heater) allows to control the relative humidity of the cathode inlet gas flow.

To obtain the equations that govern the humidification subsystem, the modeling process is divided into two steps. First, it is assumed that the subsystem dynamics is dominated by the air humidifier pressure change, without taking into account the effect of the vapor injected to the gas (see Fig. 9). Then, as a second stage, the effect of the vapor flow injected to the gas is taken into consideration by adding a nonlinear static term, function of the gas temperature, pressure, and speed conditions.

Step 1:

Under the aforementioned assumptions and considering that the humidifier pressure is the compressor load pressure ($P_{\rm cp} = P_{\rm hum}$), the equations of the cathode humidifier dynamics are given by the following expressions:

$$\frac{dm_{\rm hum}}{dt} = W_{\rm cp} - W_{\rm hum} \qquad (11)$$

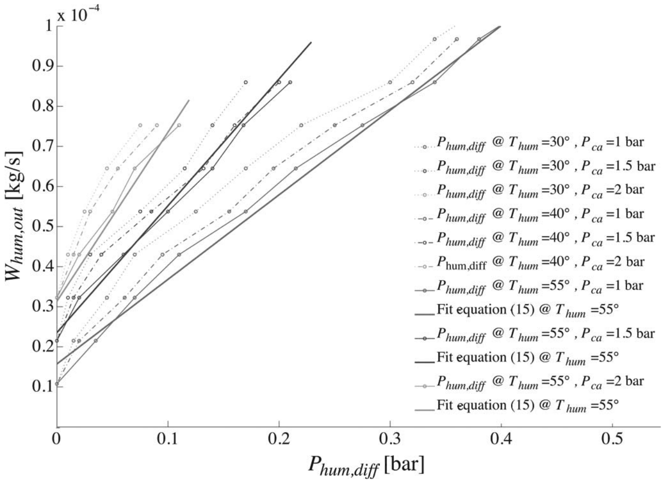

Fig. 10. Humidifier characteristics (fits and real data).

$$\frac{dP_{\rm hum}}{dt} = \frac{R_a}{V_{\rm hum}}\left(W_{\rm cp}T_{\rm cp} - W_{\rm hum}T_{\rm hum}\right) \tag{12}$$

$$W_{\rm hum} = f(T_{\rm hum}, P_{\rm ca}, P_{\rm hum,diff}) \tag{13}$$

with

$$P_{\rm hum,diff} = P_{\rm hum} - P_{\rm ca} \tag{14}$$

where $m_{\rm hum}$ and $P_{\rm hum}$ are the mass and pressure of air inside the humidifier, $W_{\rm hum}$ is the flow of air that leaves the humidifier, $V_{\rm hum}$ is the volume of the humidifier, $T_{\rm hum}$ is the gas temperature inside the humidifier, $P_{\rm hum,diff}$ is the humidification subsystem pressure drop and $P_{\rm ca}$ is the cathode inlet pressure.

The right-hand side of (13) corresponds to a non linear nozzle function, strongly dependent on the humidifier gas temperature, the cathode pressure, and the humidifier pressure drop (see Fig. 10). It could be approximated by a trivariate function or a family of bivariate functions (parametrised by $T_{\rm hum}$), obtained through experimental data gathered from tests performed at different operating temperatures and pressures. In particular, the current laboratory test plant is set to operate at constant stack temperature of $60\,^\circ$C and humidifier temperature of $55\,^\circ$C, respectively, regulated through external controllers. The former is a recommended operation temperature for the equipment, whereas the latter is adjusted to obtain high relative humidity of the cathode inlet flow (>79%), while preventing vapor condensation. Then, considering a constant humidifier working temperature, the nozzle function can be well approximated by the following bivariate function:

$$W_{\rm hum} = C_0 + C_1 P_{\rm hum,diff} P_{\rm ca} + C_2 P_{\rm ca} \tag{15}$$

where the coefficients C_0, C_1, and C_2 are experimentally determined from the tests (see thick solid lines in Fig. 10).

Step 2:

In this step, the vapor injected to the air stream ($W_{v,\rm inj}$) is incorporated to the model. Then, the total humidified air flow entering the cathode ($W_{\rm ca}$) is given by:

$$W_{\rm ca} = W_{\rm hum} + W_{v,\rm inj}. \tag{16}$$

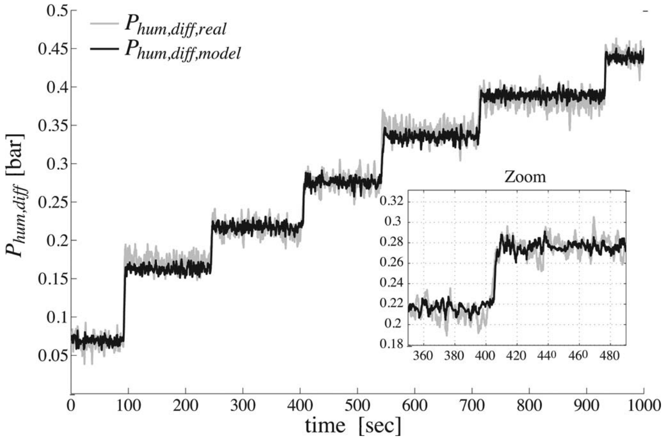

Fig. 11. Humidifier dynamic validation.

Assuming that the humidifying closed loop system of the device efficiently regulates the gas relative humidity, the computation of the injected water to the air flow can be described by

$$W_{v,\rm inj} = \frac{G_v RH_{\rm hum} P_{\rm sat}(T_{\rm hum}) W_{a,\rm hum}}{G_a P_a} - W_{v,\rm hum} \tag{17}$$

being G_v the vapor molar mass, G_a the dry air molar mass, and $P_{\rm sat}(T_{\rm hum})$ the vapor saturation pressure at the humidifier temperature. $RH_{\rm hum}$ is the relative humidity of the gas exiting the humidifier, which in normal operating conditions can be considered a known value, in accordance with the humidifier technical specifications (usually, close to 100%). The dry air partial pressure (P_a), the dry air output flow of the humidifier ($W_{a,\rm hum}$), and the flow of vapor due to ambient moisture entering the humidifier ($W_{v,\rm hum}$), are variables that depend on the ambient conditions and can be directly computed using the following relationships:

$$W_{a,\rm hum} = \frac{1}{1+\omega_{\rm hum}} W_{\rm hum,out} \tag{18}$$

$$W_{v,\rm hum} = W_{\rm hum} - W_{a,\rm hum} \tag{19}$$

with

$$\omega_{\rm hum} = \frac{G_v}{G_a}\frac{P_{\rm sat}(T_{\rm amb})RH_{\rm amb}}{P_{\rm amb} - P_{\rm sat}(T_{\rm amb})RH_{\rm amb}} \tag{20}$$

where $\omega_{\rm hum}$ is the ambient humidity ratio, $T_{\rm amb}$ the ambient temperature, $P_{\rm amb}$ the ambient pressure and $RH_{\rm amb}$ the ambient relative humidity.

At this point, there is only one parameter left to be estimated to complete the humidification subsystem model. This is the humidifier volume ($V_{\rm hum}$), present in the dynamic equation (12). An adequate estimation of this parameter can be attained by adjusting the transient response of the modeled $P_{\rm hum}$ to match the experimental data (tests varying the compressor air flow at fixed humidifier temperature are considered). It is important to note that the estimated value does not exactly correspond to the real humidifier volume. It can be interpreted as the volume of an equivalent humidification subsystem, that allows for modeling errors and unmodeled dynamics. Fig. 11 shows that highly satisfactory dynamic validation results are achieved (refer to the Appendix for estimated parameters).

A final remark is pertinent to close this section. It was previously mentioned that regulation of the line heater temperature allows controlling the relative humidity of the gas. Then, in accordance with the Dalton's law, the effect of the increase of temperature (from T_{hum} to T_{lh}) on the partial pressures, and the relative humidity of the cathode inlet gas flow can be easily computed through

$$P_{i,\mathrm{lh}} = \frac{T_{\mathrm{lh}}}{T_{\mathrm{hum}}} P_{i,\mathrm{hum}} \tag{21}$$

$$RH_{\mathrm{lh}} = \frac{P_{v,\mathrm{lh}}}{P_{\mathrm{sat}}(T_{\mathrm{lh}})} \tag{22}$$

where i stands for O_2, N_2, and vapor, respectively, and $P_{\mathrm{sat}}(T_{\mathrm{lh}})$ is the vapor saturation pressure at the line heater temperature T_{lh}.

IV. FUEL CELL STACK FLOW SUBSYSTEM

The stack is an EFC50-ST ElectroChem, which is a laboratory PEM fuel-cell system designed for the study of membrane electrode assemblies and fuel cell operation. The system consists of a 7 cell stack with Nafion 115 membranes, platinum catalyst loading of 1 mg·cm^{-2}, Toray carbon fiber papers as gas diffusion layers and 50 cm^2 of active area. This unit generates 50 W under nominal operation conditions and can provide up to 100 W peak power during transients.

A. Cathode Channels

The dynamic mass balance within the stack channels depends on the gases partial pressures, on the water transported by the membrane, and on the electric current drained from the stack (I_{st}). The cathode state variables are the masses of the circulating elements, i.e. oxygen ($m_{o_2,\mathrm{ca}}$), nitrogen ($m_{N_2,\mathrm{ca}}$), and vapor ($m_{v,\mathrm{ca}}$). Then, the dynamic equations that govern the behavior of the gases inside the cathode are given by

$$\frac{dm_{o_2,\mathrm{ca}}}{dt} = W_{o_2,\mathrm{ca}} - W_{o_2,\mathrm{ca,out}} - W_{o_2,\mathrm{react}} \tag{23}$$

$$\frac{dm_{N_2,\mathrm{ca}}}{dt} = W_{N_2,\mathrm{ca}} - W_{N_2,\mathrm{ca,out}} \tag{24}$$

$$\frac{dm_{v,\mathrm{ca}}}{dt} = W_{v,\mathrm{ca}} - W_{v,\mathrm{ca,out}} + W_{v,\mathrm{ca,gen}} + W_{v,\mathrm{mem}} \tag{25}$$

while the following relationships hold for the cathode input and output flows (W_{ca} and $W_{\mathrm{ca,out}}$)

$$W_{\mathrm{ca}} = W_{o_2,\mathrm{ca}} + W_{N_2,\mathrm{ca}} + W_{v,\mathrm{ca}} \tag{26}$$

$$W_{\mathrm{ca,out}} = W_{o_2,\mathrm{ca,out}} + W_{N_2,\mathrm{ca,out}} + W_{v,\mathrm{ca,out}} \tag{27}$$

being $W_{o_2,\mathrm{ca}}$, $W_{N_2,\mathrm{ca}}$, $W_{v,\mathrm{ca}}$, $W_{o_2,\mathrm{ca,out}}$, $W_{N_2,\mathrm{ca,out}}$, and $W_{v,\mathrm{ca,out}}$ the input and output flows of oxygen, nitrogen, and vapor, $W_{o_2,\mathrm{react}}$ the flow of oxygen that reacts in the cathode, $W_{v,\mathrm{ca,gen}}$ the flow of vapor generated in the reaction, and $W_{v,\mathrm{mem}}$ the flow of water transferred across the membrane (comprising an electro-osmotic drag term and a back-diffusion term).

Subsequently, the calculation of the flow terms that constitute the right-hand sides of (23)–(25), must be addressed.

To begin with, the amount of reduced oxygen and generated vapor in the cathode reaction is computed from the stack current, according to the following two electrochemical principles:

$$W_{o_2,\mathrm{react}} = G_{o_2} \frac{nI_{\mathrm{st}}}{4F} \tag{28}$$

$$W_{v,\mathrm{ca,gen}} = G_v \frac{nI_{\mathrm{st}}}{2F} \tag{29}$$

where n is the number of cells of the stack, G_{o_2} and G_v are the molar masses of oxygen and vapor, respectively, and F is the Faraday constant.

Next, the components of the cathode input and output flows are considered. First, assuming knowledge of W_{ca} from (16), the partial input flows $W_{o_2,\mathrm{ca}}$, $W_{N_2,\mathrm{ca}}$ and $W_{v,\mathrm{ca}}$ are readily calculated using (26)

$$W_{o_2,\mathrm{ca}} = X_{o_2,\mathrm{ca}} \frac{1}{1+\omega_{\mathrm{ca}}} W_{\mathrm{ca}} \tag{30}$$

$$W_{N_2,\mathrm{ca}} = (1 - X_{o_2,\mathrm{ca}}) \frac{1}{1+\omega_{\mathrm{ca}}} W_{\mathrm{ca}} \tag{31}$$

$$W_{v,\mathrm{ca}} = W_{\mathrm{ca}} - W_{N_2,\mathrm{ca}} - W_{o_2,\mathrm{ca}} \tag{32}$$

where ω_{ca} is the humidity ratio and $X_{o_2,\mathrm{ca}}$ the mass mole fraction of the input air flow, given by

$$\omega_{\mathrm{ca}} = \frac{G_v P_{v,\mathrm{lh}}}{G_a (P_{o_2,\mathrm{lh}} + P_{N_2,\mathrm{lh}})} \tag{33}$$

$$X_{o_2,\mathrm{ca}} = \frac{y_{o_2,\mathrm{amb}} G_{o_2}}{y_{o_2,\mathrm{amb}} G_{o_2} + (1 - y_{o_2,\mathrm{amb}}) G_{N_2}} \tag{34}$$

being $y_{o_2,\mathrm{amb}}$ the ambient oxygen mole fraction.

Second, using (27), the partial output flows $W_{o_2,\mathrm{ca,out}}$, $W_{N_2,\mathrm{ca,out}}$ and $W_{v,\mathrm{ca,out}}$ can be obtained following a similar procedure

$$W_{o_2,\mathrm{ca,out}} = X_{o_2,\mathrm{ca,out}} \frac{1}{1+\omega_{\mathrm{ca,out}}} W_{\mathrm{ca,out}} \tag{35}$$

$$W_{N_2,\mathrm{ca,out}} = (1 - X_{o_2,\mathrm{ca,out}}) \frac{1}{1+\omega_{\mathrm{ca,out}}} W_{\mathrm{ca,out}} \tag{36}$$

$$W_{v,\mathrm{ca,out}} = W_{\mathrm{ca,out}} - W_{o_2,\mathrm{ca,out}} - W_{N_2,\mathrm{ca,out}} \tag{37}$$

with the output humidity ratio and mass mole fraction

$$\omega_{\mathrm{ca,out}} = \frac{G_v P_{v,\mathrm{ca}}}{G_a (P_{o_2,\mathrm{ca}} + P_{N_2,\mathrm{ca}})} \tag{38}$$

$$X_{o_2,\mathrm{ca,out}} = \frac{y_{o_2,\mathrm{out}} G_{o_2}}{y_{o_2,\mathrm{out}} G_{o_2} + (1 - y_{o_2,\mathrm{out}}) G_{N_2}} \tag{39}$$

$$y_{o_2,\mathrm{out}} = \frac{P_{o_2}}{P_{\mathrm{ca}}} \tag{40}$$

with $y_{o_2,\mathrm{out}}$ the cathode oxygen mole fraction.

However, for these computations the cathode output flow $W_{\mathrm{ca,out}}$ is not yet available, given that it is not measurable due to its high vapor content. It must be indirectly obtained, making use of the pressure drop measurement. The relationship between the output flow and the pressure drop can be modeled as a linear nozzle equation

$$W_{\mathrm{ca,out}} = K_{\mathrm{ca,out}}(P_{\mathrm{ca}} - P_{\mathrm{rm,ca}}) \tag{41}$$

where $P_{\mathrm{rm,ca}}$ is the return manifold pressure, governed through a mechanical back pressure regulator.

Then, to compute $W_{\mathrm{ca,out}}$ it is necessary to determine $K_{\mathrm{ca,out}}$. To estimate this parameter, experimental data of the pressure drop, and the cathode output flow is required. The former is available from the differential pressure transducer but, as it was previously said, no direct measurement of $W_{\mathrm{ca,out}}$ is feasible due to its high relative humidity. However, under appropriate experimental conditions, its steady state values can be inferred from measurements of the compressor flow W_{cp}. The estimation test conditions are: (a) steady state operation, (b) equally humidified reactant gases, and (c) nil stack current. On the one hand, $I_{\mathrm{st}} = 0$ guarantees that the liquid water ($W_{l,\mathrm{ca,out}}$) and the reaction flows ($W_{o_2,\mathrm{react}}$ and $W_{v,\mathrm{ca,gen}}$) remain zero. On the other hand, considering anode and cathode gases at similar relative humidities ensures that at steady state operation there is no water concentration gradient across the membrane, so the effect of $W_{v,\mathrm{mem}}$ can be neglected. Therefore, under these testing conditions $W_{\mathrm{ca,out}}$ is equal to W_{ca} [see (23)–(25)]. Then, using (11), (16), and (17), data of W_{cp} allows the computation of $W_{\mathrm{ca,out}}$ and, consequently, the estimation of the nozzle restriction.

Note that the partial pressures of the gases inside the cathode, required in (33), can be obtained from the stack temperature and the masses of oxygen, nitrogen and vapor. Using the Dalton's law, the cathode partial pressures and relative humidity are

$$P_{i,\mathrm{ca}} = \frac{m_{i,\mathrm{ca}} R_i T_{\mathrm{st}}}{V_{\mathrm{ca}}} \tag{42}$$

$$RH_{\mathrm{ca}} = \frac{P_{v,\mathrm{ca}}}{P_{\mathrm{sat}}(T_{\mathrm{st}})} \tag{43}$$

where subscript i stands for O_2, N_2, and v, respectively, and V_{ca} is the cathode volume.

The last flow term of (23)–(25) to be computed is the water transferred across the membrane. To this end, the anode relative humidity is required, so the anode flow model will be addressed first and, subsequently, the calculation of $W_{v,\mathrm{mem}}$ will be resumed.

B. Anode Channels

In this type of PEMFC systems the input hydrogen flow is independently regulated, thus it is assumed as a known constant input W_{an}. Under this condition, the dynamics of the anode channel can be modeled by

$$\frac{dm_{H_2,\mathrm{an}}}{dt} = W_{H_2,\mathrm{an}} - W_{H_2,\mathrm{an,out}} - W_{H_2,\mathrm{react}} \tag{44}$$

$$\frac{dm_{v,\mathrm{an}}}{dt} = W_{v,\mathrm{an}} - W_{v,\mathrm{an,out}} - W_{v,\mathrm{mem}} \tag{45}$$

while the following equations hold for the anode input and output flows

$$W_{\mathrm{an}} = W_{H_2,\mathrm{an}} + W_{v,\mathrm{an}} \tag{46}$$

$$W_{\mathrm{an,out}} = W_{H_2,\mathrm{an,out}} + W_{v,\mathrm{an,out}} \tag{47}$$

being $W_{H_2,\mathrm{an}}$, $W_{v,\mathrm{an}}$, $W_{H_2,\mathrm{ca,out}}$, and $W_{v,\mathrm{an,out}}$ the input and output flows of hydrogen and vapor, respectively, $W_{H_2,\mathrm{react}}$ the flow of hydrogen consumed in the reaction and $W_{v,\mathrm{mem}}$ the aforementioned flow of water transferred to the cathode. In this particular case, no liquid water is supposed to be condensed in the anode channels, given that in normal working conditions the relative humidity of the anode is always below 100%. On the other hand, the hydrogen consumed in the reaction is

$$W_{H_2,\mathrm{react}} = G_{H_2} \frac{n I_{\mathrm{st}}}{2F} \tag{48}$$

where G_{H_2} stands for the molar mass of hydrogen.

Analogously to the cathode channel, the components of the anode input and output flows must be calculated. The partial input flows $W_{H_2,\mathrm{an}}$ and $W_{v,\mathrm{an}}$ are obtained through

$$W_{H_2,\mathrm{an}} = \frac{1}{1+\omega_{\mathrm{an}}} W_{\mathrm{an}} \tag{49}$$

$$W_{v,\mathrm{an}} = W_{\mathrm{an}} - W_{H_2,\mathrm{an}} \tag{50}$$

$$\omega_{\mathrm{an}} = \frac{G_v P_{v,\mathrm{lh,an}}}{G_{H_2} P_{H_2,\mathrm{lh,an}}} \tag{51}$$

where ω_{an} is the humidity ratio of the anode input gas, $P_{\mathrm{lh,an}}$ the anode input pressure, and $P_{v,\mathrm{lh,an}}$ the anode input vapor pressure, that can be obtained using the Dalton's law.

Besides, the partial output flows $W_{H_2,\mathrm{an,out}}$ and $W_{v,\mathrm{an,out}}$ are computed as follows:

$$W_{H_2,\mathrm{an,out}} = \frac{1}{1+\omega_{\mathrm{an,out}}} W_{\mathrm{an,out}} \tag{52}$$

$$W_{v,\mathrm{an,out}} = W_{\mathrm{an,out}} - W_{H_2,\mathrm{an,out}} \tag{53}$$

$$\omega_{\mathrm{an,out}} = \frac{G_v P_{v,\mathrm{an}}}{G_{H_2} P_{H_2,\mathrm{an}}} \tag{54}$$

where $\omega_{\mathrm{an,out}}$ is the humidity ratio of the gas inside the anode, P_{an} the anode pressure, and $P_{v,\mathrm{an}}$ the anode vapor pressure.

C. Membrane Water Transport

Now the calculation of $W_{v,\mathrm{mem}}$ can be taken up again. The flow of water across the membrane is modeled assuming linear concentration gradients from channels inlet to outlet and across the membrane thickness. Then, it can be expressed as [9]

$$W_{v,\mathrm{mem}} = \left[n_d \frac{i}{F} + D_w \frac{c_{v,\mathrm{ca}} - c_{v,\mathrm{an}}}{t_m} \right] G_v A_{\mathrm{fc}} n \tag{55}$$

where i is the stack current density, A_{fc} the fuel cell active area, t_m the membrane dry thickness, and $c_{v,\mathrm{ca}}$ and $c_{v,\mathrm{an}}$ the water concentration at the membrane surfaces on the cathode and anode sides, respectively. The term n_d is the electro-osmotic drag coefficient (number of water molecules carried by each proton) and D_w the back-diffusion coefficient of the membrane. The water concentration terms are determined from the membrane water contents on the cathode (λ_{ca}) and anode (λ_{an}) sides

$$c_{v,\mathrm{ca}} = \frac{\rho_{m,\mathrm{dry}}}{G_{m,\mathrm{dry}}} \lambda_{\mathrm{ca}} \tag{56}$$

$$c_{v,\mathrm{an}} = \frac{\rho_{m,\mathrm{dry}}}{G_{m,\mathrm{dry}}} \lambda_{\mathrm{an}} \tag{57}$$

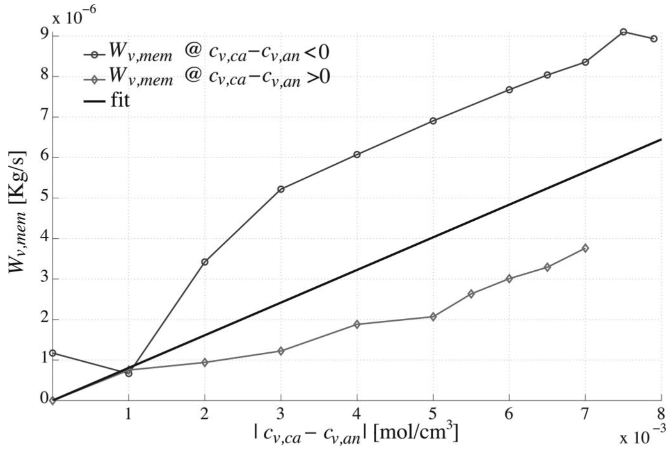

Fig. 12. Experimental and estimated membrane water diffusion characterisation.

where $\rho_{m,\mathrm{dry}}$ is the membrane dry density and $G_{m,\mathrm{dry}}$ the membrane dry molecular weight. The water content in the membrane is defined as the ratio of water molecules to the number of charge sites. When no liquid water is present in the channels, the ratio can be estimated at both sides using the following equation [9]:

$$\lambda_j = a_0 + a_1 RH_j + a_2 RH_j^2 + a_3 RH_j^3 \tag{58}$$

being RH_j the gas relative humidity and subscript j referring to cathode or anode ($j = ca, an$), respectively.

The next step is to estimate the apparent diffusion coefficient D_w of expression (55). Two different experiments can be set-up to compute this parameter, either a cathode or an anode drying test. In both cases, the stack current must be set to zero ($I_{\mathrm{st}} = 0$) in order to cancel the stack current density i in (55). For the former, a long term cathode drying procedure is conducted, decreasing the cathode humidifier temperature from 55 °C to 40 °C, while setting the temperatures of the anode humidifier, both line heaters and the stack at 60 °C. With this test, a water concentration gradient is established between the channels and an increasing extra flow in the cathode output can be detected due to the membrane contribution.

The second test is conducted analogously to the first one, but in this case the anode channel is dried out, keeping the other variables at similar stationary conditions. Following this simple procedure, the D_w coefficient can be directly determined without using humidity sensors or a more specific equipment. Fig. 12 displays the data gathered from both tests (the average value obtained for the back-diffusion coefficient is given in the Appendix).

Finally, the electro-osmotic coefficient n_d is characterized through the widely accepted expression developed in [18] and reported in [3] and [19]

$$n_d = n_0 + n_1 \lambda_m + n_2 \lambda_m^2 \tag{59}$$

where λ_m is the average membrane water content, which can be derived from (58) considering

$$RH_m = (RH_{\mathrm{ca}} + RH_{\mathrm{an}})/2. \tag{60}$$

V. CONTROL-ORIENTED STATE SPACE MODEL

The final modeling phase, previous to the controller design stage, deals with the rearrangement of the equations presented in Sections II–IV, in order to obtain an state space model, suitable for nonlinear control design purposes. This procedure comprises both, coupling all the presented differential equations with its auxiliary equations in order to represent the system only in terms of the space states, external inputs (I_{st}, $W_{\mathrm{an,in}}$, and V_{cp}), and constants, as well as taking into account any possible assumptions that lead to order reduction. In this particular case, the latter assumptions involve taking $T_{\mathrm{cp}} = T_{\mathrm{hum}}$ and $di_a/dt = 0$, which in turn, are assumptions based on different tests that have revealed that (11) and (12) are linearly coupled within the PEMFC operating range and the time constant of the variable I_{st} can be neglected respect to the rest of the system dynamics. Another possible assumption that can be performed in these type of PEMFC systems is to consider the anode line dynamics decoupled with the cathode line, because its only interaction depend on the term $W_{v,\mathrm{mem}}$. Further information about how the overall state space equations were obtained can be found in [2].

Then, taking state $x \in \mathbb{R}^7$, control input $u = V_{\mathrm{cp}} \in \mathbb{R}^1$, and the model parameters and operating conditions in Tables I–V of the appendix, the PEMFC generation system under study can be described in the form $\dot{x} = f(x, I_{\mathrm{st}}) + g.u$, accordingly to the following set of state space equations, as shown in (61)–(67) with the parameters of Table VI.

VI. CONCLUSION

The control-oriented model derived in this paper reproduces the most typical features of a laboratory PEM fuel cell arrangement, which is a complex system that combines mechanical, electrical, pneumatic and electrochemical subsystems. The proposed representation is a 7th order nonlinear model primarily focused on the fuel cell fluid dynamics, presenting the following features, required for control design: continuous, smooth dynamic vector fields and bounded uncertainty. The complete model in state-space representation is presented and discussed considering modular subsystems. It is important to stress that the presented model validation covers the entire operation range of the fuel cell-based system under study, even though an overall test could not be displayed due to space limitations.

Important control problems found in PEM fuel cells such as the ones presented in [3], [5], [10], and [20] (H_2/O_2 stoichiometry regulation, total and partial pressures control, H_2 consumption minimization, etc.), can be approached using the developed control model.

The mixed methodology used in this paper is not an example on identification nor a theoretical exercise. Guided by the knowledge of the processes and reactions that take place in the real fuel-cell system, the different components were modeled using available information and simple experiments. Therefore, the proposed strategy can be used as a general guide for control-oriented modeling in PEM fuel-cell systems with similar features. Moreover, the reactant flow model developed in this work can be successfully complemented with the work developed by the authors in a recent publication [21], where a complete characterization of the stack output voltage in terms of its operating conditions (flows, pressures, current densities) was presented.

$$\begin{aligned}\dot{x}_1 ={}& (m_1(u(t) - m_2 x_1) - x_1 m_3 + A_0 + A_{00} + A_{10}(x_2 m_5 + m_6) + A_{20}(x_2 m_5 + m_6)^2 + A_{01} x_1 \\ & + A_{11}(x_2 m_5 + m_6) x_1 + A_{02} {x_1}^2) m_4 \end{aligned} \tag{61}$$

$$\begin{aligned}\dot{x}_2 ={}& B_{00} + B_{10}(x_2 m_5 + m_6) + B_{20}(x_2 m_5 + m_6)^2 + B_{01} x_1 + B_{11}(x_2 m_5 + m_6) x_1 + B_{02} {x_1}^2 \\ & - b_1(x)^3 C_3 - b_1(x)^2 C_2 - b_1(x) C_1 - C_0 \end{aligned} \tag{62}$$

$$\begin{aligned}\dot{x}_3 ={}& \Bigg(m_9 (b_1(x)^3 C_3 + b_1(x)^2 C_2 + b_1(x) C_1 + C_0) {G_a}^{-1} (x_2 m_5 - m_{10})^{-1} \left(1 + \frac{m_{11}}{x_2 m_5 - m_{10}}\right)^{-1} \\ & + \left(b_1(x)^3 C_3 + b_1(x)^2 C_2 + b_1(x) C_1 + C_0\right) \left(1 + \frac{m_{11}}{x_2 m_5 - m_{10}}\right)^{-1} \Bigg) X_{o2,\mathrm{ca,in}} \left(1 + \frac{m_{14}}{(x_3 R_{o2} + x_4 R_{N2} + x_5 R_v) m_8 - m_{12}}\right)^{-1} \\ & - K_{\mathrm{ca}} ((x_3 R_{o2} + x_4 R_{N2} + x_5 R_v) m_8 - P_{\mathrm{amb}}) x_3 R_{o2} G_{o2} \Bigg(1 + G_v x_5 R_v \left(\frac{x_3 R_{o2} G_{o2}}{x_3 R_{o2} + x_4 R_{N2}} + \left(1 - \frac{x_3 R_{o2}}{x_3 R_{o2} + x_4 R_{N2}}\right) G_{N2} \right)^{-1} \\ & \times (x_3 R_{o2} + x_4 R_{N2})^{-1} \Bigg)^{-1} (x_3 R_{o2} + x_4 R_{N2})^{-1} \left(\frac{x_3 R_{o2} G_{o2}}{x_3 R_{o2} + x_4 R_{N2}} + \left(1 - \frac{x_3 R_{o2}}{x_3 R_{o2} + x_4 R_{N2}}\right) G_{N2} \right)^{-1} - 1/4 \frac{G_{o2} n I_{\mathrm{st}}}{F} \end{aligned} \tag{63}$$

$$\begin{aligned}\dot{x}_4 ={}& \Bigg(m_9 (b_1(x)^3 C_3 + b_1(x)^2 C_2 + b_1(x) C_1 + C_0) {G_a}^{-1} (x_2 m_5 - m_{10})^{-1} \left(1 + \frac{m_{11}}{x_2 m_5 - m_{10}}\right)^{-1} \\ & + (b_1(x)^3 C_3 + b_1(x)^2 C_2 + b_1(x) C_1 + C_0) \left(1 + \frac{m_{11}}{x_2 m_5 - m_{10}}\right)^{-1} \Bigg) \left(1 - X_{o2,\mathrm{ca,in}}\right) \left(1 + \frac{G_v m_{12}}{G_a\,(b_2(x) - m_{12})}\right)^{-1} \\ & - \Bigg(1 - x_3 m_8 G_{o2} b_3(x)^{-1} \left(\frac{x_3 m_8 G_{o2}}{b_3(x)} + \left(1 - \frac{x_3 m_8}{b_3(x)}\right) G_{N2} \right)^{-1} \Bigg) \\ & \times K_{\mathrm{ca,n}}\,(b_2(x) - P_{\mathrm{amb}}) \Bigg(1 + G_v x_5 R_v m_8 \left(\frac{x_3 m_8 G_{o2}}{b_3(x)} + \left(1 - \frac{x_3 m_8}{b_3(x)}\right) G_{N2} \right)^{-1} (x_3 R_{o2} m_8 + x_4 R_{N2} m_8)^{-1} \Bigg)^{-1} \end{aligned} \tag{64}$$

$$\begin{aligned}\dot{x}_5 ={}& G_v m_{12} (b_1(x)^3 C_3 + b_1(x)^2 C_2 + b_1(x) C_1 + C_0) {G_a}^{-1} (x_2 m_5 - m_{10})^{-1} \left(1 + \frac{G_v m_{10}}{G_a\,(x_2 m_5 - m_{10})}\right)^{-1} + \frac{b_4(x)}{b_5(x)} \\ & - \left(\frac{G_v m_{12} b_4(x)}{G_a\,(x_2 m_5 - m_{10})\, b_5(x)} + \frac{b_4(x)}{b_5(x)} \right) \left(1 + \frac{G_v m_{12}}{G_a\,(b_2(x) - m_{12})}\right)^{-1} - K_{\mathrm{ca,out}}\,(b_2(x) - P_{\mathrm{amb}}) + K_{\mathrm{ca,out}}\,(b_2(x) - P_{\mathrm{amb}}) \\ & \times \left(1 + G_v x_5 R_v m_8 b_3(x)^{-1} \left(\frac{x_3 m_8 G_{o2}}{b_3(x)} + \left(1 - \frac{x_3 m_8}{b_3(x)}\right) G_{N2} \right)^{-1} {R_{o2}}^{-1} \right)^{-1} + 1/2 \frac{G_v n I_{\mathrm{st}}}{F} \\ & + \Bigg((n_0 + n_1 (a_0 + a_1 b_6(x) + a_2 b_6(x)^2 + a_3 b_6(x)^3) + n_2 (a_0 + a_1 b_6(x) + a_2 b_6(x)^2 + a_3 b_6(x)^3)^2) I_{\mathrm{st}} / A_{\mathrm{fc}} / F \\ & - D_w \left(\frac{(a_0 + a_1 x_5 m_{16} + a_2 {x_5}^2 {m_{16}}^2 + a_3 {x_5}^3 {m_{16}}^3) \rho_{m,\mathrm{dry}}}{G_{m,\mathrm{dry}}} - \frac{(a_0 + a_1 x_7 m_{15} + a_2 {x_7}^2 {m_{15}}^2 + a_3 {x_7}^3 {m_{15}}^3) \rho_{m,\mathrm{dry}}}{G_{m,\mathrm{dry}}} \right) {t_m}^{-1} \Bigg) G_v A_{\mathrm{fc}} n \end{aligned} \tag{65}$$

$$\dot{x}_6 = W_{\mathrm{an,in}} \left(1 + \frac{G_v m_{17}}{G_{H_2}\,(b_7(x) - m_{17})}\right)^{-1} - K_{\mathrm{an,out}}\,(b_7(x) - P_{\mathrm{amb}}) \left(1 + \frac{G_v x_7 m_{19}}{G_{H_2} x_6 m_{20}}\right)^{-1} - 1/2 \frac{G_{H_2} n I_{\mathrm{st}}}{F} \tag{66}$$

$$\begin{aligned}\dot{x}_7 ={}& W_{\mathrm{an,in}} - W_{\mathrm{an,in}} \left(1 + \frac{G_v m_{17}}{G_{H_2}\,(b_7 - m_{17})}\right)^{-1} - K_{\mathrm{an,out}}\,(b_7(x) - P_{\mathrm{amb}}) + K_{\mathrm{an,out}}\,(b_7(x) - P_{\mathrm{amb}}) \left(1 + \frac{G_v x_7 m_{19}}{G_{H_2} x_6 m_{20}}\right)^{-1} \\ & - \Bigg((n_0 + n_1 (a_0 + a_1 b_6(x) + a_2 b_6(x)^2 + a_3 b_6(x)^3) + n_2 (a_0 + a_1 b_6(x) + a_2 b_6(x)^2 + a_3 b_6(x)^3)^2) I_{\mathrm{st}} / A_{\mathrm{fc}} / F \\ & - D_w \left(\frac{(a_0 + a_1 x_5 m_{16} + a_2 {x_5}^2 {m_{16}}^2 + a_3 {x_5}^3 {m_{16}}^3) \rho_{m,\mathrm{dry}}}{G_{m,\mathrm{dry}}} - \frac{(a_0 + a_1 x_7 m_{15} + a_2 {x_7}^2 {m_{15}}^2 + a_3 {x_7}^3 {m_{15}}^3) \rho_{m,\mathrm{dry}}}{G_{m,\mathrm{dry}}} \right) {t_m}^{-1} \Bigg) G_v A_{\mathrm{fc}} n \end{aligned} \tag{67}$$

Due to the fact that the model was primarily developed for model-based control studies, a system level approach was considered and only dynamic effects with time constants in the range of 10^{-2} s to 10^{0} s were taken into account.

The developed nonlinear model accurately describes the steady state and dynamical behavior of the studied fuel-cell stack and its associate devices.

APPENDIX

AUXILIARY FUNCTIONS

$$b_1(x) = x_3 m_5 - (x_4 R_{O_2} + x_5 R_{N_2} + x_6 R_v)\, m_8$$

$$b_2(x) = (x_4 R_{O_2} + x_5 R_{N_2} + x_6 R_v)\, m_8$$

$$b_3(x) = \frac{x_4 R_{O_2} m_8 + x_5 R_{N_2} m_8}{R_{O_2}}$$

$$b_4(x) = C_0 + C_1 b_1(x) b_2(x) + C_2 b_2(x)$$

$$b_5(x) = 1 + \frac{G_v m_{10}}{G_a\,(x_3 m_5 - m_{10})}$$

$$b_6(x) = \frac{x_8 m_{15}}{2} + \frac{x_6 m_{16}}{2}$$

$$b_7(x) = (x_7 R_{H_2} + x_8 R_v)\, m_{18}$$

TABLES

TABLE I
COMPRESSOR PARAMETERS

Parameter	Value
Electrical inductance (L)	2.12 mH
Electrical resistance (R)	2.03 Ω
Torque constant (k_ϕ)	0.0031 Nm/A
Motor inertia (J)	2 x 10^{-7} Nm
Compressor gathered inertia (J_g)	1.2 x 10^{-6} Nm
Load torque coefficient (A_0)	4.10 x 10^{-4} Nm
Load torque coefficient (A_1)	3.92 x 10^{-6} Nms

TABLE II
GENERAL PHYSICAL CONSTANTS

Parameter	Value
Air gas constant (R_a)	286.9 Nm/kg/°K
Vapour molar mass (G_v)	0.01802 kg/mol
Dry air molar mass (G_a)	0.029 kg/mol
Oxygen molar mass (G_{o_2})	32 x 10^{-3} kg/mol
Nitrogen molar mass (G_{N_2})	28 x 10^{-3} kg/mol
Hydrogen molar mass (G_{H_2})	2.01 x 10^{-3} kg/mol
Air gas constant (R_a)	286.9 Nm/kg/°K
Oxygen gas constant (R_{o_2})	259.8 Nm/kg/°K
Nitrogen gas constant (R_{N_2})	296.8 Nm/kg/°K
Vapour gas constant (R_v)	461.5 Nm/kg/°K
Hydrogen gas constant (R_{H_2})	4.124 x 10^{3} Nm/kg/°K
Faraday constant (F)	96485 C/mol

TABLE III
POLYNOMIAL COEFFICIENTS OF EQUATIONS (10) AND (11)

Parameter	Value
A_{00}	0
A_{10}	0.0058 Nms
A_{20}	-0.0013 Nms^2
A_{01}	3.25 x 10^{-6} Nm/bar
A_{11}	-2.80 x 10^{-6} Nms/bar
A_{02}	-1.37 x 10^{-9} Nms/bar^2
B_{00}	4.83 x 10^{-5} kg/s
B_{10}	-5.42 x 10^{-5} kg/s^2
B_{20}	8.79 x 10^{-6} kg/s^3
B_{01}	3.49 x 10^{-7} kg/s^2/bar
B_{11}	3.55 x 10^{-13} kg/s
B_{02}	-4.11 x 10^{-10} kg/s/bar

TABLE IV
OPERATING CONDITIONS

Parameter	Value
Humidifier temperature (T_{hum})	55 °C
Line heater temperature (T_{lh})	60 °C
Fuel cell stack temperature (T_{st})	60 °C
Humidifier relative humidity (RH_{hum})	0.95
Ambient relative humidity (RH_{amb})	0.5
Ambient pressure (P_{amb})	1 bar
Ambient temperature (T_{amb})	25 °C
Ambient oxygen mole fraction ($y_{o_2,amb}$)	25 °C
Hydrogen input flow ($W_{H_2,an}$)	2 slpm

TABLE V
AIR HUMIDIFIER AND FUEL CELL STACK PARAMETERS

Parameter	Value
Humidifier volume (V_{hum})	2 x 10^{-4} m^3
Humidifier restriction coefficient (C_0)	1.048 x 10^{-7} kg/s
Humidifier restriction coefficient (C_1)	2.109 x 10^{-4} kg/s/bar^2
Humidifier restriction coefficient (C_2)	1.562 x 10^{-5} kg/s/bar
Number of fuel cells (n)	7
Cathode restriction constant ($K_{ca,out}$)	0.0094 kg/s/bar
Cathode volume (V_{ca})	4 x 10^{-4} m^3
Membrane effective area (A_{fc})	50 cm^2
Membrane dry thickness (t_m)	0.0127 cm
Membrane dry density($\rho_{m,dry}$)	0.002 kg/cm^3
Membrane dry molecular weight($G_{m,dry}$)	1.1 kg/mol
Membrane diffusion coefficient (D_w)	5.43 x 10^{-6} cm^2/s
Membrane water content coefficient (a_0)	0.043 $[H_2O/SO_3]$
Membrane water content coefficient (a_1)	17.81 $[H_2O/SO_3]$
Membrane water content coefficient (a_2)	-39.85 $[H_2O/SO_3]$
Membrane water content coefficient (a_3)	36.0 $[H_2O/SO_3]$
Electro-osmotic coefficient (n_0)	-3.4x10^{-19} $[H_2O/H^+]$
Electro-osmotic coefficient (n_1)	0.05 $[H_2O/H^+]$
Electro-osmotic coefficient (n_2)	0.0029 $[H_2O/H^+]$

TABLE VI
STATE SPACE MODEL COEFFICIENTS

$m_1 = k_\phi/R$
$m_2 = k_\phi 30/\pi$
$m_3 = A_1 30/\pi$
$m_4 = \pi/30/J$
$m_5 = T_{sm} R_a/V_{hum}$
$m_6 = -P_{sat}(T_{sm}) RH_{amb} + RH_{hum,ca} P_{sat}(T_{hum,ca})$
$m_8 = T_{st}/V_{ca}$
$m_9 = G_v RH_{hum,ca} P_{sat}(T_{hum,ca})$
$m_{10} = P_{sat}(T_{sm})\ RH_{amb}$
$m_{11} = G_v P_{sat}(T_{sm}) RH_{amb}/G_a$
$m_{12} = RH_{hum,ca} P_{sat}(T_{hum,ca})$
$m_{13} = R_o T_{st} G_O$
$m_{14} = G_v RH_{hum,ca} P_{sat}(T_{hum,ca})/G_{a,ca,in}$
$m_{15} = T_{st} R_v/V_{an}/P_{sat}(T_{lh,an})$
$m_{16} = R_v T_{st}/V_{ca}/P_{sat}(T_{lh,ca})$
$m_{17} = RH_{an,in} P_{sat}(T_{lh,an})$
$m_{18} = T_{st}/V_{an}$
$m_{19} = T_{st} R_v/V_{an}$
$m_{20} = T_{st} R_h/V_{an}$

ACKNOWLEDGMENT

All the laboratory tests were performed at the Fuel Cells Laboratory of the Institut de Robòtica i Informàtica Industrial (CSIC-UPC, Barcelona, Spain) and were only possible due to its advanced equipment and proficient technical staff.

REFERENCES

[1] J. Larminie and A. Dicks, *Fuel Cell Systems Explained*, 2nd ed. Hoboken, NJ: John Wiley & Sons Inc, 2003.

[2] C. Kunusch, "Modelling and nonlinear control of pem fuel cell systems," Ph.D. dissertation, Elect. Dept., Nat. Univ. of La Plata, Mar. 2009.

[3] J. Pukrushpan, A. Stefanopoulou, and H. Peng, *Control of Fuel Cell Power Systems*. New York: Springer, 2004.

[4] R. Talj, D. Hissel, R. Ortega, M. Becherif, and M. Hilairet, "Experimental validation of a PEM fuel-cell reduced-order model and a moto-compressor Higher Order Sliding-Mode control," *IEEE Trans. Ind. Electron.*, vol. 57, no. 6, pp. 1906–1913, Jun. 2010.

[5] C. Kunusch, P. Puleston, M. Mayosky, and J. Riera, "Sliding mode strategy for PEM fuel cells stacks breathing control using a Super-Twisting algorithm," *IEEE Trans. Control Syst. Technol.*, vol. 17, no. 1, pp. 167–174, Jan. 2009.

[6] W. K. Na and B. Gou, "Feedback-linearization-based nonlinear control for PEM fuel cells," *IEEE Trans. Energy Convers.*, vol. 23, no. 1, pp. 179–190, Mar. 2008.

[7] J. Zhang, G. Liu, W. Yu, and M. Ouyang, "Adaptive control of the airflow of a PEM fuel cell system," *J. Power Sources*, vol. 179, no. 2, pp. 649–659, 2008.

[8] J. Amphlett, R. Baumert, R. Mann, B. Peppley, and P. Roberge, "Performance modelling of the ballard mark iv solid polymer electrolyte fuel cell," *J. Electrochem. Soc.*, vol. 142, no. 1, pp. 9–15, 1995.

[9] T. Springer, T. Zawodzinski, and S. Gottesfeld, "Polymer electrolyte fuel cell model," *J. Electrochem. Soc.*, vol. 138, no. 8, pp. 2334–2342, 1991.

[10] P. Rodatz, "Dynamics of the polymer electrolyte fuel cell: Experiments and model-based analysis," Ph.D. dissertation, Swiss Federal Inst. of Technol., Zurich, 2003.

[11] F. Grasser and A. Rufer, "A fully analytical PEM fuel cell system model for control applications," *IEEE Trans. Ind. Appl.*, vol. 43, no. 6, pp. 1499–1506, Nov./Dec. 2007.

[12] F. Gao, B. Blunier, M. Simoes, and A. Miraoui, "Pem fuel cell stack modeling for real-time emulation in hardware-in-the-loop applications," *IEEE Trans. Energy Convers.*, vol. 26, no. 1, PP, 184–194, Mar. 2011.

[13] M. Khan and M. Iqbal, "Modelling and analysis of electro-chemical, thermal, and reactant flow dynamics for a pem fuel cell system," *Fuel cells*, vol. 5, no. 4, pp. 463–475, 2005.

[14] C. Bao, M. Ouyang, and B. Yi, "Modeling and control of air stream and hydrogen flow with recirculation in a pem fuel cell system–i. control-oriented modeling," *Int. J. Hydrogen Energy*, vol. 31, no. 13, pp. 1879–1896, 2006.

[15] C. Kunusch, P. Puleston, M. Mayosky, and A. Dávila, "Efficiency optimisation of an experimental PEM fuel cell system via Super Twisting control," in *Proc. 11th Int. Workshop Variable Struct. Syst.*, Mexico, DF, Mexico., Jun. 2010, pp. 319–324.

[16] J. D'Errico, "Polyfitn (n-d polynomial regression model)," 2006. [Online]. Available: http://www.mathworks.com/matlabcentral/fileexchange

[17] Cellkraft, *P-10 humidifier manual: v 2.0*, 2007.

[18] S. Dutta, S. Shimpalee, and J. Van Zee, "Numerical prediction of mass-exchange between cathode and anode channels in a pem fuel cell," *Int. J. Heat Mass Transfer*, vol. 44, pp. 2029–2042, 2001.

[19] D. McKay, W. Ott, and A. Stefanopoulou, "Modeling, parameter identification, and validation of reactant and water dynamics for a fuel cell stack," in *ASME Int. Mech. Eng. Congr. Exposition*, 2005.

[20] C. Ramos-Paja, C. Bordons, A. Romero, R. Giral, and L. Martinez-Salamero, "Minimum fuel consumption strategy for pem fuel cells," *IEEE Trans. Ind. Electron.*, vol. 56, no. 3, pp. 685–696, Mar. 2009.

[21] C. Kunusch, P. Puleston, M. Mayosky, and J. Moré, "Characterization and experimental results in PEM fuel cell electrical behaviour," *Int. J. Hydrogen Energy*, vol. 35, pp. 5876–5881, 2010.

Cristian Kunusch (M'05) received the Diploma in electronic engineering, M.Sc. degree in engineering, both in 2003, and the Ph.D. degree in engineering and automation, in 2009, all from the National University of La Plata, Argentina.

He was an Assistant Professor of Automatic Control (2003–2009) at the National University of La Plata, Argentina. Currently, he is an Associate Researcher at the Institut de Robòtica i Informàtica Industrial (CSIC-UPC), Barcelona, Spain. His current work addresses the control and automation issues associated with (PEM) fuel cells systems.

Paul F. Puleston received the B.S.E.E. degree (with first class honors) and the Ph.D. degree from the National University of La Plata, Argentina, in 1988 and 1997, respectively.

During 1999–2000, he was a Research Associate at the Engineering Department, Leicester University, U.K. He is currently a Full Professor at the Electrical Engineering Department, National University of La Plata. He was awarded the Gold Medal "Ing. Antonio Marin" of the National Academy of Engineering, in 2002. His research interests include automatic control and renewable energy systems.

Prof. Puleston is a Research Member of the National Council for Scientific and Technical Research, Argentina.

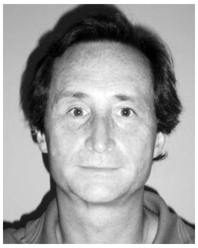

Miguel A. Mayosky (M'97–SM'98) was born in La Plata, Argentina, in 1960. He received the Engineer on Electronics degree (First Class Award) from the University of La Plata (UNLP), La Plata, Argentina, and the Ph.D. degree (*cum Laude*) in computer science from the Autonomous University of Barcelona, Spain, in 1983 and 1990, respectively.

He is currently a Full Professor of Automatic Control Systems at the School of Engineering, UNLP, and also a member of the Research Staff of the Buenos Aires Scientific Research Commission (CICpBA). His research activities involve real-time data acquisition and control systems, instrumentation for high energy physics experiments, and embedded computer architectures.

Prof. Mayosky was President of the Argentina Chapter of the IEEE Computational Intelligence Society (2005-2006).

Attila P. Husar received the Bachelors' and M.Sc. degrees in mechanical engineering from the University of Miami, Coral Gables, FL, and is currently a Ph.D. candidate at the Universitat Politcnica de Catalunya (UPC), Barcelona, Spain, where he has designed and built different proton exchange membrane fuel cell (PEMFC) test stations.

He has spent his 14-year engineering career directly involved in the development of PEM fuel cells and fuel-cell systems. Before returning to school for the Ph.D. degree, he worked at Energy Partners, West Palm Beach, FL. He led fuel-cell engineering team that designed and built fuel cells and fuel-cell systems and put them in practical applications. He is the author or coauthor of more than 20 publications in international scientific journals on fuel cells and conference proceedings.

ARTICLE IN PRESS

INTERNATIONAL JOURNAL OF HYDROGEN ENERGY XXX (2012) 1–7

Available online at www.sciencedirect.com

SciVerse ScienceDirect

journal homepage: www.elsevier.com/locate/he

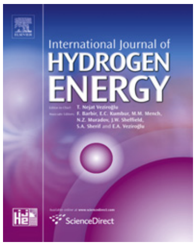

Experimental characterization methodology for the identification of voltage losses of PEMFC: Applied to an open cathode stack

A. Husar[*], *S. Strahl*, *J. Riera*

Institut de Robòtica i Informàtica Industrial (CSIC-UPC), C/ Llorens i Artigas 4-6, 08028 Barcelona, Spain

ARTICLE INFO

Article history:
Received 9 September 2011
Received in revised form
22 November 2011
Accepted 24 November 2011
Available online xxx

Keywords:
Activation losses
Mass transport losses
Ohmic losses
PEMFC
Open cathode

ABSTRACT

The objective of this study is to describe the methodology used to isolate the main voltage loss indicators through a simple and effective treatment of a current interrupt and current sweep. The voltage loss indicators are activation polarization, mass transport, and ohmic losses. The indicators for these losses are the Tafel slope, mass transport resistance and ohmic resistance respectively. The use of this methodology to isolate the individual voltage losses works quite well. Even though there may be some inaccuracies, the trends can be clearly seen. This methodology can be used in any PEMFC system to monitor the state of health of the fuel cell. If this method were to be automated and implemented on a periodic basis, then an on-line measurement of the individual voltage losses could be monitored. The data analysis indicates that a major objective of the controller will be to minimize the mass transport losses by implementing proper temperature control.

1. Introduction

Remarkable progress has been made in polymer electrolyte membrane fuel cell (PEMFC) materials, component design, production and system power density. However, there is still significant work to be done in order to understand the different physical phenomena within a working fuel cell and how they need to be controlled in order to improve efficiency, operating range and stability [6]. This experimental study is focused on identifying the major voltage losses in a PEMFC with a simple, yet effective, method using only current, voltage, and PEMFC stack temperature measurements. In the literature simple methodologies have been suggested as a way to decompose the i-V performance curves and therefore isolate individual losses [1,10]. The major losses to be identified are activation, mass transport and ohmic resistance. For each of these losses, indicators have been determined. The experimental methodology used to extract the individual indicators is based on two dynamic tests: current interrupt and current sweep. The extraction methods are explained and the results using these methods are presented.

First, the fuel cell voltage loss model will be explained in Section 2 followed by the experimental methodology for dissecting the i–V curve in Section 3. Section 4 describes the experimental setup and test conditions followed by a discussion of results and the conclusions.

The objective is to isolate and identify the main voltage loss indicators with a simple and effective treatment of a current interrupt and current sweep.

---

[*] *Corresponding author.*
E-mail address: ahusar@iri.upc.edu (A. Husar).

0360-3199/$ – see front matter Copyright © 2011, Hydrogen Energy Publications, LLC. Published by Elsevier Ltd. All rights reserved.
doi:10.1016/j.ijhydene.2011.11.130

Please cite this article in press as: Husar A, et al., Experimental characterization methodology for the identification of voltage losses of PEMFC: Applied to an open cathode stack, International Journal of Hydrogen Energy (2012), doi:10.1016/j.ijhydene.2011.11.130

2. Fuel cell voltage losses model

In the widely published [8] basic fuel cell model used in this work, the fuel cell voltage $V_{(fc)}$ is equal to the thermodynamic reversible potential ($E_{(T,P)}$) of a PEM fuel cell minus the three major losses: activation (ΔV_{act}), mass transport (ΔV_{mt}) and ohmic (ΔV_{ohm}).

$$V_{fc} = E_{(T,P)} - \Delta V_{act} - \Delta V_{mt} - \Delta V_{ohm}\ [V] \tag{1}$$

The thermodynamic reversible potential is represented by the following equation [8]:

$$E_{(T,P)} = -\left(\frac{\Delta H}{nF} - \frac{T\Delta S}{nF}\right) - \frac{RT}{nF}\ln\left(\frac{\Pi a_{prod}^{\upsilon_i}}{\Pi a_{react}^{\upsilon_i}}\right) \tag{2}$$

where ΔH is the change in enthalpy and ΔS is the change in entropy of the reaction at standard temperature and pressure, which in this study is considered to be 25 °C and 1 atm and has a value of −285,826 J/mol and −163 J/mol/K respectively. If more accuracy is needed then equations can be introduced to make the enthalpy and entropy a function of temperature. n represents the number of electrons transferred per mole, which in this case is 2 for H_2, F is Faraday's constant and R is the universal gas constant. T is the fuel cell operating temperature. a_{prod} and a_{react} are the activities at the inlet conditions, which are: partial pressure of H_2O vapour (the product) and H_2 and O_2 (the reactant) divided by the total gas pressure that enters the fuel cell. υ_i is the corresponding stoichiometric coefficient of each species participating in the reaction, which is 1 for all of them except for O_2, which is $\upsilon_{O_2} = 1/2$.

2.1. *Activation polarization losses*

A certain proportion of energy is needed to start the chemical reaction. This phenomenon produces a nonlinear voltage drop called activation polarization. These losses occur on both anode and cathode catalysts. However, the oxygen reduction reaction kinetics is much slower than hydrogen oxidation reaction, thus the reduction reaction produces a much larger magnitude of activation polarization loss. The oxidation reaction on the anode is much faster and practically constant through out the current range. If only a single reaction is considered then the voltage loss due to activation polarization can be described by the Tafel equation [2]:

$$\Delta V_{act} = \frac{RT}{\alpha nF}\ln\left(\frac{i}{i_0}\right) = 2.3\frac{RT}{\alpha nF}\log\left(\frac{i}{i_0}\right)\ [V] \tag{3}$$

The parameter α is the charge transfer coefficient and expresses how the change in the electrical potential across the reaction interface changes the reaction rate. It depends on the type of reaction and the electrode material. Its value is theoretically between 0 and 1 depending on the catalyst material [5]. It physically represents the fraction of additional energy that goes toward the cathodic reduction reaction at an electrode. The charge transfer coefficient can also be thought of as a symmetry coefficient of the electrode reaction and it is typically considered to be around 0.5 with hydrogen and oxygen reacting on a platinum catalyst [7]. The exchange current density i_0 [A/cm^2] is the rate at which the reaction proceeds (simultaneously in both directions) at equilibrium potential ($E_{(T,P)}$) when the net current equals zero [2]. The exchange current density is a measure of the effectiveness of the electrode in promoting the electrochemical reaction where the higher the exchange current density, the lower the overall activation losses. The fuel cell current density is denoted by i [A/cm^2]. The activation losses are generally the dominant effect on the fuel cell voltage, as is shown in Fig. 1.

When the fuel cell is not connected to an external circuit (open circuit voltage), the fuel cell voltage would be expected to be close to the thermodynamic potential, relative to the ambient conditions and reactant partial pressure. However, the measured fuel cell voltage is much lower, usually less than 1 V/cell, which can be attributed to hydrogen crossover and internal currents. These losses arise because the membrane in a PEMFC is slightly electronically conductive and permeable to gasses. These losses can be considered as an internal current. The amount of current that these losses represent is rather small compared to normal operating currents. However, these internal current losses have a large effect on the voltage when the external current is very small. In this study these losses are considered part of the activation losses [2] and should not affect the results.

The Tafel slope is the main indicator for activation losses and will be explained in more detail in Section 3.3.

2.2. *Ohmic losses*

The resistance to the flow of electrons through the electrically conductive fuel cell components and to the flow of ions through the membrane causes a voltage drop, which can be expressed by Ohm's law:

$$\Delta V_{ohm} = i \cdot R_{ohm}\ [V] \tag{4}$$

The internal cell resistance R_{ohm} is in [Ω-cm^2]. The electric and contact resistance can be considered constant with respect to current and temperature. Thus any change in the resistance is only dependent on membrane water concentration and membrane temperature [9].

R_{ohm} is the indicator for membrane ionic resistance.

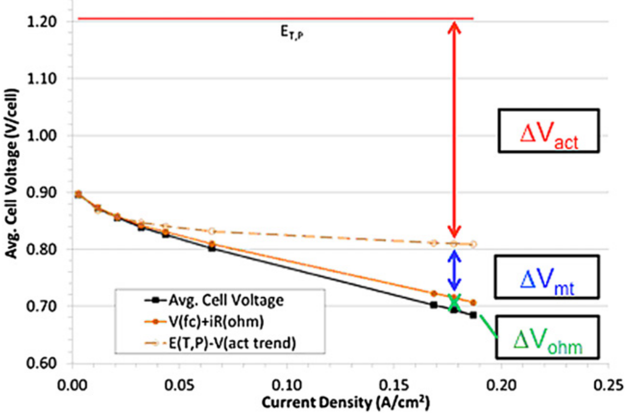

Fig. 1 – Graphical representation of Eq. (1) depicting the three main losses at a given current (graph based on real data 4 A at 32.2° C).

Please cite this article in press as: Husar A, et al., Experimental characterization methodology for the identification of voltage losses of PEMFC: Applied to an open cathode stack, International Journal of Hydrogen Energy (2012), doi:10.1016/j.ijhydene.2011.11.130

2.3. *Mass transport losses*

The consumption of reactant gases at the catalyst layers leads to concentration gradients and thus changes the partial pressure of the reactants, which affects the fuel cell voltage as seen previously in Eq. (2). Referring to Faraday's law of electrolysis, the transferred charge and the molar flux of a reactant J are proportional to the current density [2]:

$$J = \frac{i}{nF} \quad [\mathrm{mol\ s^{-1} m^{-2}}] \tag{5}$$

The higher the current density, the lower the reactant concentration is at the catalyst layer.

The current density at which the reactant concentration reaches zero is called the limiting current density (i_L). Considering this relationship between reactant mass transport and current density, the mass transport losses can be expressed as [2]:

$$\Delta V_{conc} = \frac{RT}{\alpha nF} \ln\left(\frac{i_L}{i_L - i}\right) \tag{6}$$

However this expression for mass transport losses does not represent the experimental values well [8]. In a forced flow open cathode fuel cell where the air reactant stoichiometry is always over 10 and the maximum current drawn from the stack is relatively low (0.27 A/cm^2) it is assumed that the mass transport losses are neglected for current densities of less than 0.04 A/cm^2 and are considered linear beyond that current density. High current densities are not possible with open cathode stack due to the lack of humidification and the standard operating conditions, hence the mass transport losses seem linear.

$$\begin{aligned} &\Delta V_{mt} = 0 \text{ if } i < 0.04\ \mathrm{A/cm^2} \\ &\Delta V_{mt} = R_{mt}(i - 0.04) \ \text{ if } i \geq 0.04\ \mathrm{A/cm^2} \end{aligned} \tag{7}$$

3. Experimental methodology applied to open cathode PEMFC

The following experimental approach is used to isolate the individual losses in the fuel cell stack. The data presented in the following section is an example of real data treated using this method. The main difficulty is to isolate mass transport from activation losses.

As the Nyquist plots from Electrical Impedance Spectroscopy (EIS) only give linear information at the measured point of operation, another method to determine the nonlinear losses caused by the activation are described.

Although the data used in this explanation corresponds to an open cathode fuel cell, the methodology is valid for all PEMFC.

3.1. *Current interrupt*

The purpose of the current interrupt (CI) is to obtain the ohmic resistance (R_{ohm}) of the fuel cell in a fast and accurate manner. The principal concept is to isolate the resistance that is outside of the RC circuit, which should be seen as an instantaneous jump in voltage when the load is removed, because it has no capacitive component. The developed algorithm detects the jump in voltage when the load is disconnected and separates the curve in two straight lines to generate the point where the instantaneous voltage increase stops, as illustrated in Fig. 2. The algorithm detects the jump by looking for 3 consecutive points of rising voltage and then uses the first point as the vertical line. Then looks for the point after the jump where the difference between the points is less than 0.002 V and then creates a line using the following 10 points.

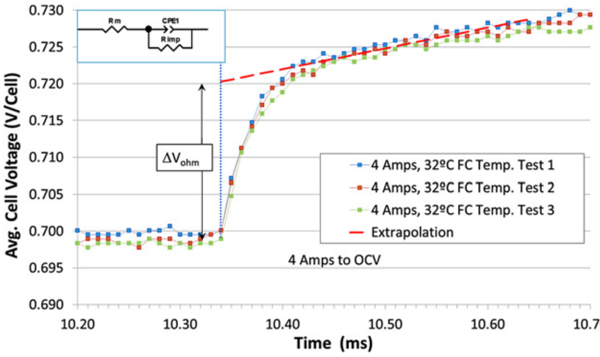

Fig. 2 – CI data for 3 tests at the same operating condition to show repeatability. Ohmic resistance using CI is 0.121 Ω-cm^2.

EIS data has been compared to the ohmic resistance measurement via the current interrupt method in order to calibrate the detection algorithm to the EIS results, shown in Fig. 3.

3.2. *Current sweep*

The purpose of the current sweep is to obtain an i–V curve of the fuel cell with minimal changes to the internal conditions. This is done by quickly passing through specifically selected current set points.

In this study current sweeps were performed when the fuel cell reached steady state conditions, however it is not necessary. The time constant of the system was determined from the EIS bode diagram and is determined to be in the order of $\tau = 120$ ms. It is interesting to note that the time constant of

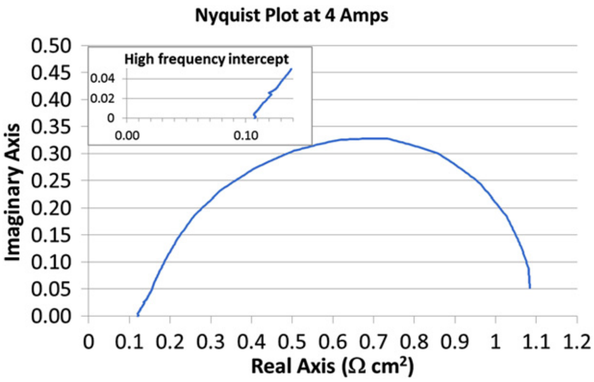

Fig. 3 – Nyquist plot at the same conditions (4 A) as the CI data. Ohmic resistance using EIS is 0.119 Ω-cm^2.

Please cite this article in press as: Husar A, et al., Experimental characterization methodology for the identification of voltage losses of PEMFC: Applied to an open cathode stack, International Journal of Hydrogen Energy (2012), doi:10.1016/j.ijhydene.2011.11.130

the fuel cell increases as the current decreases. The time needed for the voltage to stable out at a current set point of 0 A/cm^2 is much longer than at the other currents, which can be clearly seen in Fig. 4.

In this study the fuel cell is left at each current set point for only 300 ms, which provided enough time for the fuel cell to stable out.

As can be seen in Fig. 4 there are 10 current rest points, 4 points with a difference to the operating current of 5% of the operating current and 6 points in the nonlinear region at lower current densities. The 4 points around the operating condition give a good reading of the linear slope of the fuel cell. The 6 points at the low current densities give a good reading on the nonlinear region of the fuel cell. The black line in Fig. 1 shows the plot of the extracted current sweep (i–V) from Fig. 4.

The rest time at each set point has to be kept to a minimum due to the nature of the open cathode system where the water content and the temperature in the fuel cell are driven by the current. The total time for the current sweep could be reduced to less than 1 s if necessary. However it can be noted in this test that even at a total of 3 s, the voltage before and after the test are the same.

3.3. *Breakdown of the current sweep*

Using the resistance data from the CI and assuming that mass transport losses are negligible ($\Delta V_{mt} = 0$) at current densities of less then 0.04 A/cm^2 (the nonlinear part of the sweep), Eq. (1) was solved for ΔV_{act}.

$$\Delta V_{act} = E_{T,P} - V_{fc} - iR_{ohm} \tag{8}$$

A logarithmic function is fitted to the data from 0.00 to 0.04 A/cm^2 as shown in Fig. 5. The slope of this line in the logarithmic scale is the Tafel slope, and the intercept on the *x*-axis is the exchange current density.

$$\text{Tafel slope} = \frac{RT}{n\alpha F} \tag{9}$$

Using the fitted Tafel slope and exchange current density the line was extrapolated out to the steady state current set point. Thus the difference between the thermodynamic reversible potential ($E_{T,P}$) and the extrapolated curve gives activation losses (ΔV_{act}) seen in Fig. 1.

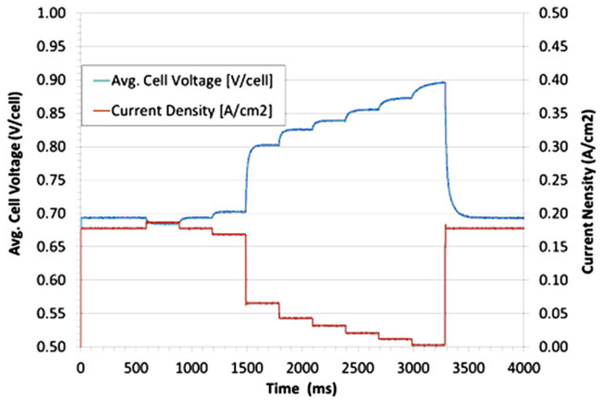

Fig. 4 – Average cell voltage and current density dynamic of a current sweep with 300 ms at each point. Note that the voltage before and after the test is the same.

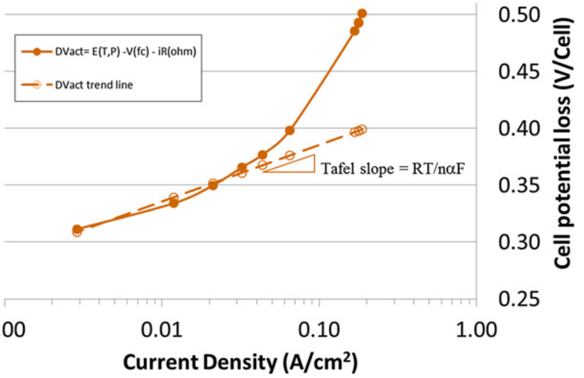

Fig. 5 – The solid line represents the real data (E_{TP}–V_{fc}–iR_{ohm}). The linear extrapolation of the lower current density points is represented by the dotted line. Note that it is in a logarithmic scale.

Now looking back at Eq. (1) all the variables are known except for (ΔV_{mt}), which now can be solved. With this, the breakdown of the individual losses can be plotted, as shown in Fig. 6.

The *x*-axis intercept of the mass transport losses are artificially set to 0.04 A/cm^2 due to the assumption that there are no mass transport losses at the lower current densities. This can be seen in Fig. 5 where the dotted trend line separates from the solid line.

Take note that the losses calculated using this method is only valid for the current and temperature at which the sweep and CI were taken, which in this case is 4 A and 32.2 °C.

If this method is automated and implemented on a periodic basis then an on-line measurement of the individual voltage losses could be monitored.

3.4. *Experimental setup & operating conditions*

A Horizon® H-100 open cathode, 20 cell, 22.5 cm^2 active area fuel cell stack in an environmental chamber was tested. The only active control mechanism employed is

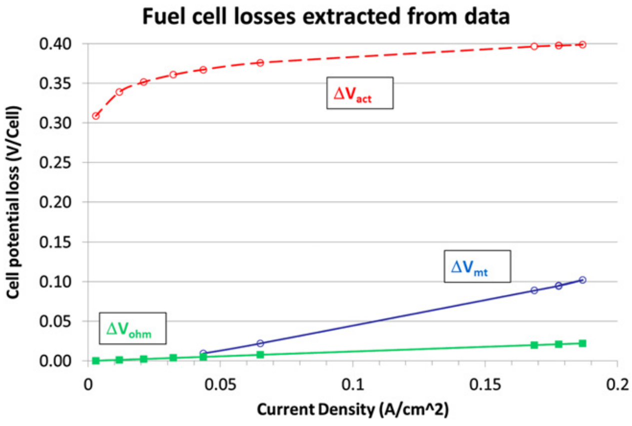

Fig. 6 – The graph depicts the breakdown of the voltage losses from experimental data.

Please cite this article in press as: Husar A, et al., Experimental characterization methodology for the identification of voltage losses of PEMFC: Applied to an open cathode stack, International Journal of Hydrogen Energy (2012), doi:10.1016/j.ijhydene.2011.11.130

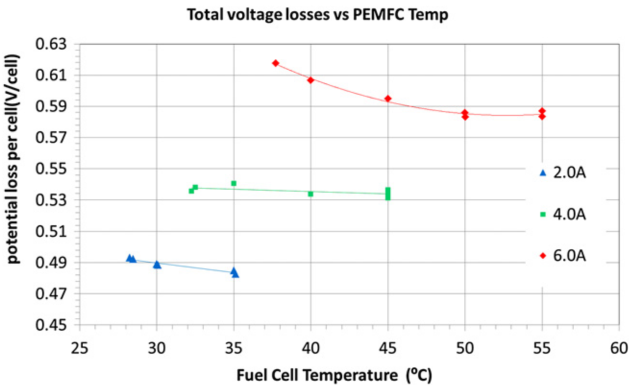

Fig. 7 – The graph shows the evolution of total voltage loss at three different currents 2, 4, 6 A as a function of fuel cell temperature with constant environmental conditions.

a single fan that both cools and provides the oxygen needed for the reaction. All the other control mechanisms are disconnected and a constant pure, dry hydrogen flow is supplied to the stack.

The ambient conditions set in the environmental chamber were 25 °C with 90%RH. The steady state current densities of 0.09, 0.18, and 0.27 A/cm^2 correspond to 2, 4 and 6 A. The combined cathode and cooling fan was set to control a constant fuel cell temperature. The fuel cell temperature set points are: from a minimum temperature, 30, 35, 40, 45, 50, 55 °C. Pure dry hydrogen was supplied to the anode at 0.36, 0.71 and 1.07 SLPM as the steady state current was increased from 2, to 4 and 6 A respectively.

LabVIEW data acquisition software was used in conjunction with analog to digital converter (ADC) of National Instruments to measure the stack voltage. The hall-effect-based current sensor ACS713 from Allegro MicroSystems measures the current in the load circuit. The switch used to perform the current interrupt was an intelligent power highside switch IPS6021 from International Rectifier. Finally, the data acquisition card used for the high frequency test was a PCI-DAS 4020/12 from Measurement Computing, where the sampling rate can be set from 1 kHz to 20 MHz.

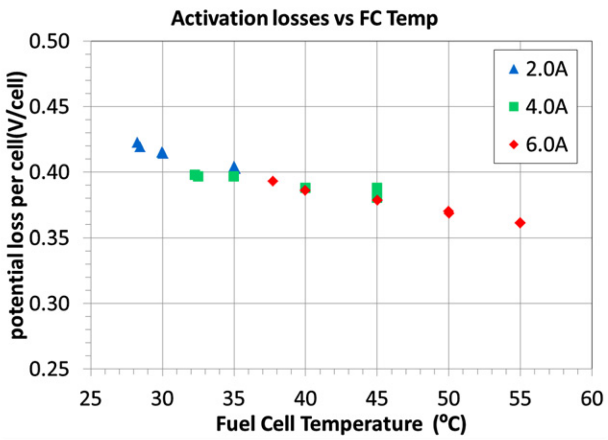

Fig. 8 – Activation losses of the fuel cell stack.

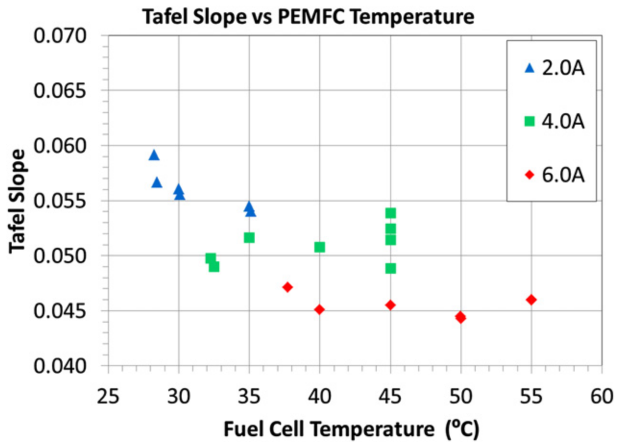

Fig. 9 – Tafel slope as activation indicator.

4. Results and discussion

In this section several results are discussed, with respect to current and ambient temperature.

The load on the stack obviously has the largest influence on the fuel cell voltage loss as seen in Fig. 7. It is interesting to note that at all three currents the voltage losses decrease with an increase in temperature but it is only the 6 A curve that has a nonlinear decrease. The source of the nonlinearity will be discussed in Section 4.2 and 4.3 and shows the practicality of this methodology as a diagnostic tool.

The next sections will discuss the evolution of the individual voltage losses at the different currents and fuel cell operating temperature.

4.1. *Activation losses evaluation*

The activation losses are shown in Fig. 8. They decrease linearly with fuel cell temperature in these ranges of currents and temperatures. The reason for the linear decrease in activation losses is due to the decrease in thermodynamic reversible potential ($E_{(T,P)}$) which decreases with fuel cell temperature, thus causing the activation losses to decrease.

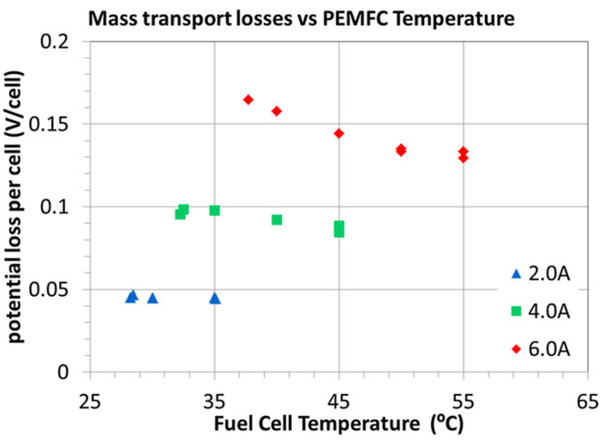

Fig. 10 – Mass transport losses.

Please cite this article in press as: Husar A, et al., Experimental characterization methodology for the identification of voltage losses of PEMFC: Applied to an open cathode stack, International Journal of Hydrogen Energy (2012), doi:10.1016/j.ijhydene.2011.11.130

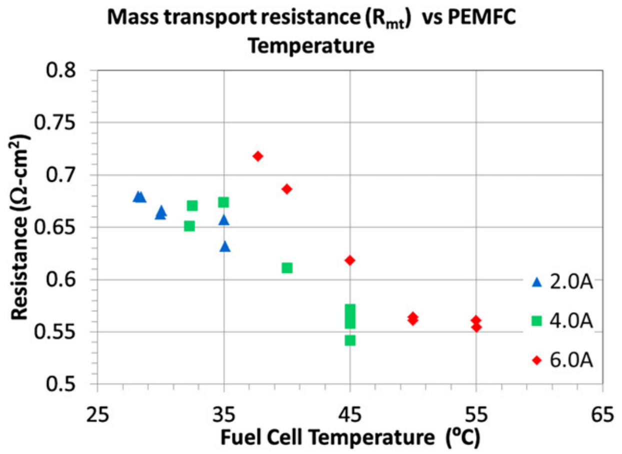

Fig. 11 – Linear mass transport indicator represented as a resistance for 2, 4 and 6 A.

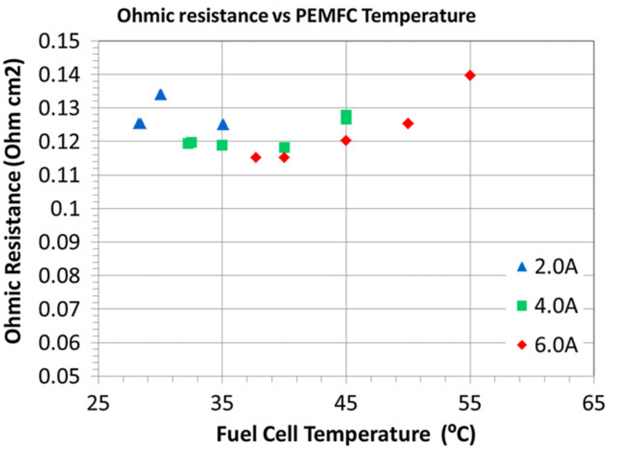

Fig. 13 – Ohmic resistance as the ohmic indicator.

However, the original current sweep data does not show this decrease. The low current density current sweep data for the same current at different temperatures are identical to each other at less than 0.04 A/cm^2. Thus this is only a theoretical decrease in activation losses due to the order in which the data was decomposed.

The Tafel slope, being the indicator for activation losses, reflects the linearity as it seems to remain relatively constant with respect to temperature at each current tested, as shown in Fig. 9.

4.2. *Mass transport losses evaluation*

The mass transport losses increase greatly with the increase in current (see Fig. 10), which is expected according to Eqns. (5) and (6). All the measurement errors are incorporated into this indicator due to the order in which the voltage loss decomposition was done. However, an interesting trend is seen with regard to temperature. There is a general linear decrease in mass transport losses with the increase in fuel cell temperature and seems to be linear for temperatures lower than 50 °C. However, when temperatures go beyond 50 °C, there seems to be stabling out of the losses. This can be seen dramatically in the mass transport indicator shown in Fig. 11.

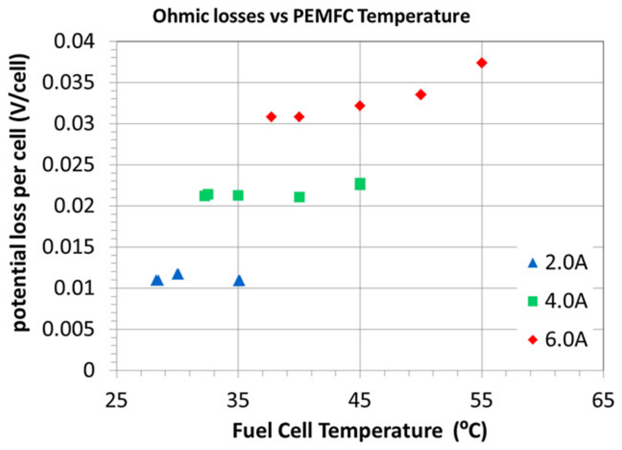

Fig. 12 – Ohmic losses with respect to current and temperature.

This elbow in the 6 A data suggests that there is a change in state of the diffusion and/or catalyst layers. This could possibly be due to the evaporation of most of the liquid water in these layers allowing for maximum diffusion flux. There is a possible trade-off of maximizing diffusion with increased membrane resistance, as will be shown in the ohmic losses section.

4.3. *Ohmic resistance losses evaluation*

Ohmic losses increase with an increase in current and temperature. There seems to be a distinct upward trend as the fuel cell reaches 45 °C (Fig. 12). This may indicate that beyond this temperature and inlet relative humidity the membrane is not fully saturated, which reinforces the hypothesis that there is no more liquid water in the diffusion and/or catalyst layers.

Even though the ohmic losses are relatively small compared to the other losses in the fuel cell, there may be some undesirable long-term degradation caused by a dry membrane.

The Ohmic resistance ranges from 0.115 to 0.140 (Ω-cm^2). This is comparable to studies in the literature which indicate ranges from 0.100 to 0.182 (Ω-cm^2) for Nafion 212 and 117 respectively [3,4]. Fuel cell resistance R_{ohm} is relatively constant at each current for temperatures below 45° C (Fig. 13).

5. Conclusions

The proposed methodology in this work to isolate the individual voltage losses functions quite well. Even though there may be some inaccuracies, the trends are clearly seen. This methodology can be used to monitor any PEMFC state of health with respect to activation, mass transport, and ohmic losses.

It must be noted that all the power generated during the sweep would be lost. Thus it will affect the intended performance of the system. Capacitors could be placed in parallel with the fuel cell to supply the needed power during the sweep. The efficiency loss due to the sweep will be dependent on the frequency and the duration of the sweeps. This analysis has not been done but it is strongly dependent on the fuel cells design

Please cite this article in press as: Husar A, et al., Experimental characterization methodology for the identification of voltage losses of PEMFC: Applied to an open cathode stack, International Journal of Hydrogen Energy (2012), doi:10.1016/j.ijhydene.2011.11.130

and its sensibility to the operating conditions. An optimization analysis of the sweep, in order to minimize the frequency and the duration of the sweeps, would also need to be done.

If this method is automated and implemented on a periodic base, then an on-line measurement of the individual voltage losses could be monitored.

Through analysis of the open cathode fuel cell data it is clear that a major objective of the controller will be to minimize the losses through proper control of the temperature by means of the fan.

Future work will be dedicated to determining how the hydrogen purge rate, inlet temperatures and relative humidity affect the individual losses.

Acknowledgements

All the experimental tests were performed at the Fuel Cells Laboratory of the *Institut de Robótica i Informática Industrial* (CSIC-UPC, Barcelona) and are only possible due to its advanced equipment and proficient technical staff. This work is partially funded by the project of CICYT DPI2010-15274 MICINN and CICYT DPI2011-25649 MICINN.

REFERENCES

[1] Baghalha M, Stumper J, Eikerling M. Model-based deconvolution of potential losses in a PEM fuel cell. ECS Trans 2010;28:159–67.

[2] Barbir F. PEM fuel cells: theory and practice. Elsevier Academic Press; 2005.

[3] Büchi FN, Scherer GG. In-situ resistance measurements of Nation 117 membranes in polymer electrolyte fuel cells. J Electroanalytical Chem 1996;404:37–43.

[4] Hou J. A study on polarization hysteresis in PEM fuel cells by galvanostatic step sweep. Int J Hydrogen Energy 2011;36(12): 7199–206.

[5] Larminie J. Fuel cell systems explained. 2nd ed. John Wiley & Sons Ltd; 2003.

[6] Li H, Tang Y, Wang Z, Shi Z, Wu S, Song D, et al. A review of water flooding issues in the proton exchange membrane fuel cell. J Power Sources 2008;178:103–17.

[7] Mench MM. Fuel cell engines. John Wiley & Sons, Inc; 2008.

[8] O'Hayre R. Fuel cell fundamentals. John Wiley & Sons Ltd; 2009.

[9] Springer TE, Zawodzinski TA, Gottesfeld S. Polymer electrolyte fuel cell model. J Electrochem Soc 1991;138(8).

[10] Wu J, Yuan XZ, Wang H, Blanco M, Martin JJ, Zhang J. Int J Hydrogen Energy 2008;33(6):1735–46.

Please cite this article in press as: Husar A, et al., Experimental characterization methodology for the identification of voltage losses of PEMFC: Applied to an open cathode stack, International Journal of Hydrogen Energy (2012), doi:10.1016/j.ijhydene.2011.11.130